

NIST-GCR-97-706

**A STUDY OF ENTRAINMENT AND FLOW
PATTERNS IN POOL FIRES USING PARTICLE
IMAGING VELOCIMETRY**

X.C.Zhou and J.P.Gore



United States Department of Commerce
Technology Administration
National Institute of Standards and Technology

NIST-GCR-97-706

**A STUDY OF ENTRAINMENT AND FLOW
PATTERNS IN POOL FIRES USING PARTICLE
IMAGING VELOCIMETRY**

X.C.Zhou and J.P.Gore

Purdue University
W.Lafayette,IN 47907-1003

March 1996



U.S. Department of Commerce
William M. Daley, Secretary
Technology Administration
Mary L. Good, *Under Secretary for Technology*
National Institute of Standards and Technology
Arati Prabhakar, *Director*

Notice

This report was prepared for the Center for Fire Research of the Building and Fire Research Laboratory of the National Institute of Standards and Technology, under Grant Number 60NANB2D1291. The statements and conclusions contained in this report are those of the authors and do not necessarily reflect the views of the U.S. Department of Commerce, the National Institute of Standards and Technology, the Building and Fire Research Laboratory, and the Center for Fire Research.

A STUDY OF ENTRAINMENT AND FLOW PATTERNS IN POOL FIRES USING
PARTICLE IMAGING VELOCIMETRY

March 1996

sponsored by

U.S. DEPARTMENT OF COMMERCE

NATIONAL INSTITUTE OF STANDARDS AND TECHNOLOGY

BUILDING AND FIRE RESEARCH LABORATORY

CENTER FOR FIRE RESEARCH

EXECUTIVE SUMMARY

An experimental and theoretical study of the flow fields induced by pool fires was completed. Pool burners of three diameters, namely 7.1 cm, 15 cm and 30 cm, were used. For the two smaller pool burners, the effects of a 51 cm sheet metal floor around the pool at the surface were also studied. Three fuel, methanol, toluene and heptane were burned as representatives of alcohols, paraffins and aromatics. The velocity field induced by the 7.1 cm toluene pool fire with the metal floor was mapped with a Laser Doppler Velocimetry (LDV) system. The transient characteristics of the velocities were studied by analyzing their discrete Probability Density Functions (PDFs) and their Power Spectral Densities (PSDs). The instantaneous fire induced flow fields around all the pool fires were studied using Particle Imaging Velocimetry (PIV). The PIV data for the 7.1 cm toluene pool fire were confirmed using the LDV data. Following a favorable comparison, PIV, which is a faster technique, was used for the remaining fires. The mean flow patterns were obtained by averaging 100 instantaneous velocity vector plots. Air entrainment rates were calculated based on the mean velocity fields and normalized using the fire Froude number, which was shown to be the appropriate nondimensional number using the governing equations for the buoyant diffusion flames. A theoretical model was utilized to predict the entrainment flow field with the volumetric heat release rate distribution and vorticity distribution assumed to be known a priori. Important conclusions of the present study are:

- 1) Although air is always entrained into the flame on an average, instantaneous radially outward velocities were observed, showing that air is sometimes pushed away from the flame. PDFs of the vertical velocities show that the vertical velocity of the ambient air is rarely over 50 cm/s, but the vertical velocity of the flame gas can be

much higher. The PSDs of the velocities show that the far-field entrainment flow field does not respond to the periodic pulsations of the pool fire.

- 2) A floor around the pool fires changes the mean entrainment patterns as well as qualitative features of the instantaneous entrainment flow. When there is a floor around the 7.1 cm pool fire, the entrainment flow starts far away from the flame and is very irregular, with occasional vortices in the flow. In the absence of a floor, there is a layer of air at very high convection speed enveloping the flame while the ambient is rather quiescent. The mean velocity vector plots show that in the presence of the floor the entrained air originates from very large radial distances. Without floor, the entrained air originates from radial locations closer to the pool fire edge. A substantial amount of air is also entrained from vertical locations below the vertical location of the fuel surface.
- 3) The qualitative effect of pool size on the entrainment is shown by the fact that even without a floor the entrainment flow fields of the 30 cm pool fires start far away from the pool edge. The instantaneous flow patterns are highly transient compared to those of the 7.1 cm fires. Near the flame bulge, the flow can even be outward or downward. The mean velocity vector plots show that at $r = 27$ cm, the magnitudes of the radial velocity components are comparable to those of the vertical velocity components.
- 4) As expected from fundamental fluid mechanical considerations, the mean vorticity field estimated using the velocity data show an irrotational flow field surrounding the fire with a layer of intense vorticity generation concentrated near the flame sheet. This intense vorticity region causes an inflow of ambient air. The volumetric expansion caused by the combustion process counteracts the inward vorticity-induced motion. However, at larger radial locations, the flow induced by vorticity dominates the field.
- 5) Air entrainment rates are evaluated based on the mean velocity field, and the results are compared with data and a correlation in the literature. Only one correlation from the literature was selected for comparison because it utilizes nondimensional groups that can be derived from fundamental equations as shown in Appendix A. Different

choices of entrainment boundaries lead to qualitative as well as quantitative differences in air entrainment rates. The large scatter in the existing entrainment correlations can be attributed to the differences in explicit or implicit definitions of entrainment implied by the different measurement techniques. Fuel type has little effect on the dimensionless air entrainment rates normalized by the fire Froude number, mass based stoichiometric ratio, and the fuel consumption rate. Without floor, the normalized air entrainment rates of the 15 cm and 30 cm pool fires collapse into a common correlation for the three fuels. The normalized entrainment rates for the 7.1 cm pool fires collapse into a separate correlation for the three fuels. This correlation has approximately 20% higher normalized entrainment rates compared to that for the larger fires. A 51 cm floor around the 7.1 cm pool fires lowers the normalized air entrainment rates by about 20%.

A kinematic model for the pool fire induced flow field was adapted from Baum and McCaffrey (1988). The flow field is decomposed into irrotational flow and incompressible flow components. The source terms in the governing equations are estimated by analyzing the velocity and temperature distribution correlations for buoyant diffusion flames. The boundary conditions on the outer edge of the computational domain are approximated with asymptotic values. The governing differential equations are discretized by a control volume method and the resulting system of algebraic equations is solved using the Gauss-Seidel iteration method. A multigrid scheme is used to accelerate convergence of the iterations. The grid dependence of the numerical model is tested by comparing the results computed on computational domains of different sizes and using different grid spacings. Vorticity generated by the density gradient inside the flame plays a dominant role in determining the flow pattern. Heat release from combustion causes an approximately hemispherical expansion pattern in the presence of a floor.

There is qualitative agreement between the mean velocity measurements and the predictions of the entrainment flow fields. Reasonable quantitative agreement between measurements and predictions can be obtained by adjusting the radius of the $1/e$ point in the velocity and temperature profiles within the fire. This adjustment affects the input

distribution of volumetric heat release rate and vorticity arbitrarily. Measurements of the volumetric heat release rate field and the vorticity field are needed to remove the arbitrary adjustment discussed above. Measurements of volumetric heat release rate and vorticity distributions in fires have always been challenging since instruments for measuring these quantities directly are not available. Particle Imaging Velocimetry (PIV) in surrogate gaseous fires with a pulsed laser for obtaining accurate estimates of vorticity is being considered. Estimates of local heat release rate can be obtained using mean gas species concentration data obtained by sampling and gas chromatography.

The measurements of detailed velocity and gas species distributions in the present fires will also be useful for an evaluation of numerical simulations of the entire flowfield including the fire being developed at NIST.

TABLE OF CONTENTS

	Page
EXECUTIVE SUMMARY	iv
LIST OF TABLES	x
LIST OF FIGURES	xi
LIST OF SYMBOLS	xx
CHAPTER 1 INTRODUCTION	1
1.1 Existing Measurements of Entrainment Rates	2
1.1.1 Entrainment Data Based on Axial Velocity and Temperature	2
1.1.2 Measurement of Entrainment Using a Steady State Mass Balance	5
1.1.3 Measurement of Entrainment Using a Stably Stratified Layer	6
1.1.4 Direct Measurements of Fire Induced Flow Field	7
1.1.5 Summary of Correlations	8
1.2 Analytical and Numerical Work	10
1.3 An Example of the Application of Existing Correlations	11
1.4 Specific Objectives	12
CHAPTER 2 EXPERIMENTAL METHODS	16
2.1 Laser Doppler Velocimetry (LDV)	16
2.1.1 Experimental Apparatus	17
2.1.2 The Instrumentation	18
2.1.3 Interface Height and the Background Velocity	20
2.2 Particle Imaging Velocimetry (PIV)	22
2.2.1 Experimental Apparatus	23
2.2.2 The Instrumentation	23
2.3 Study of Flame Geometry	24
CHAPTER 3 THEORETICAL METHODS	38
3.1 The Governing Differential Equations	39
3.2 The Heat Release Rate Distribution and the Vorticity Field inside the Flame ..	43

	Page
3.3 Boundary Conditions.....	48
3.4 Numerical Scheme	50
3.4.1 Numerical Solution.....	50
3.4.2 Multigrid Scheme for Accelerated Solution	52
3.4.3 The Effect of Computational Domain Sizes and Grid Spacing	55
3.4.4 The Irrotational Velocity and the Incompressible Velocity	58
CHAPTER 4 LDV RESULTS AND DISCUSSION.....	80
4.1 The Mean Entrainment Flow Field and the Vorticity Distribution	80
4.2 The Transient Characteristics of the Entrainment Phenomena	84
4.3 Entrainment Rates Based on the Mean Entrainment Flow Field.....	86
4.4 The Predicted Entrainment Velocity Field.....	88
CHAPTER 5 PIV RESULTS AND DISCUSSION	118
5.1 Instantaneous Entrainment Flow Structure	118
5.2 The Mean Entrainment Flow Fields.....	127
5.3 Air Entrainment Rates	129
5.4 Comparison of Prediction and Measurement of Entrainment Velocity	131
CHAPTER 6 SUMMARY, CONCLUSIONS AND RECOMMENDATIONS	181
6.1 Conclusions.....	181
6.2 Recommendations for Future Work.....	183
LIST OF REFERENCES	185
APPENDICES	
Appendix A Dimensionless Numbers	190
Appendix B Estimation of Combustion Efficiency	193
Appendix C Properties of LDV Probe and Measuring Volumes	196
Appendix D Uncertainty Analysis of LDV Measurement	199
Appendix E Some Parameters of PIV Measurement.....	200
Appendix F LDV Measurement Data	205

LIST OF TABLES

Table	Page
1.1 Correlations of buoyant diffusion flame air entrainment	10
3.1 Parameters of the correlations of buoyant diffusion flame structure	44
4.1 Radii of the visible flame boundary	81
5.1 Test conditions for pool fires	119
F.1 Data of the mean velocity around the 7.1 cm toluene pool fire with a floor.....	205

LIST OF FIGURES

Figure	Page
1.1 A sketch of the entrainment measurement apparatus used by Ricou and Spalding (1961).	14
1.2 A sketch of the entrainment measurement apparatus used by Zukoski and coworkers (1980).	14
1.3 Estimates of air entrainment rates based on existing engineering correlations summarized in Table 1.1	15
2.1 A sketch of the experimental apparatus for measuring fire-induced flow field velocities using LDV	25
2.2 A schematic of the pool fire burner.....	26
2.3 A sketch of the fuel supply system.....	27
2.4 The change of interface height with pool position.....	28
2.5 Discrete PDF of background radial velocity at three different heights at $r = 6.5$ cm	29
2.6 Discrete PDF of background vertical velocity at three different heights at $r = 6.5$ cm	30
2.7 Discrete PDF of background radial velocity at three different heights at $r = 9.5$ cm	31
2.8 Discrete PDF of background vertical velocity at three different heights at $r = 9.5$ cm	32
2.9 Discrete PDF of background radial velocity at three different heights at $r = 12.5$ cm	33

Figure	Page
2.10 Discrete PDF of background vertical velocity at three different heights at $r = 12.5$ cm	34
2.11 A schematic of the enclosure and seeding system used in PIV measurement of pool fire induced flow	35
2.12 A sketch of the Particle Imaging Velocimetry (PIV) system	36
2.13 Measurements and prediction of the vertical velocity of an air jet as a function of radial location at three different heights	37
3.1a Sketch of the computational domain of the flow field induced by pool fire with a floor.....	61
3.1b Sketch of the computational domain of the flow field induced by pool fire without a floor.....	62
3.2 The flame radius $R(z)$ as a function of height as per the correlation of Baum and McCaffrey (1988).	63
3.3 The vorticity distribution at $z = 0.5$ cm, 20.5 cm and 42.5 cm estimated according to McCaffrey's flame structure correlations	63
3.4 The volumetric heat release rate distribution at $z = 0.5$ cm and 12.5 cm estimated according to McCaffrey's flame structure correlations.....	64
3.5 Discretization of the computational domain and designation of the control volume surfaces and grid points.....	65
3.6 A typical element in the discretized computational domain.....	66
3.7 The pattern of coarse control volume block encompassing fine control volume grid cells	67
3.8 Flow chart of the computer code.....	68
3.9a The predicted axial velocity at $z = 42.5$ cm by using Eqs. 3.46 and 3.47	69
3.9b The predicted axial velocity at $z = 42.5$ cm by using Eqs. 3.48 and 3.49 for boundary nodes.....	69

Figure	Page
3.10a Comparison of the predicted axial velocities at $z = 0.5$ cm using computational domains of different sizes	70
3.10b Comparison of the predicted radial velocities at $z = 0.5$ cm using computational domains of different sizes	70
3.11a Comparison of the predicted axial velocities at $z = 42.5$ cm using computational domains of different sizes	71
3.11b Comparison of the predicted radial velocities at $z = 42.5$ cm using computational domains of different sizes	71
3.12a Comparison of the predicted axial velocities at $z = 0.5$ cm using different radial grid spacings	72
3.12b Comparison of the predicted radial velocities at $z = 0.5$ cm using different radial grid spacings	72
3.13a Comparison of the predicted axial velocities at $z = 42.5$ cm using different radial grid spacings	73
3.13b Comparison of the predicted radial velocities at $z = 42.5$ cm using different radial grid spacings	73
3.14a Comparison of the predicted axial velocities at $r = 7.5$ cm using different axial grid spacings.....	74
3.14b Comparison of the predicted radial velocities at $r = 7.5$ cm using different axial grid spacings.....	74
3.15a Comparison of the predicted axial velocities at $r = 3.5$ cm using different axial grid spacings.....	75
3.15b Comparison of the predicted radial velocities at $r = 3.5$ cm using different axial grid spacings	75
3.16a Comparison of the predicted axial velocities at $r = 0.5$ cm using different axial grid spacings.....	76
3.16b Comparison of the predicted radial velocities at $r = 0.5$ cm using different axial grid spacings.....	76

Figure	Page
3.17a Decomposition of the radial velocities at $z = 0.5$ cm into irrotational velocity due to heat release and incompressible velocity caused by vorticity.....	77
3.17b Decomposition of the radial velocities at $z = 42.5$ cm into irrotational velocity due to heat release and incompressible velocity caused by vorticity.....	77
3.18a Decomposition of the axial velocities at $z = 0.5$ cm into irrotational velocity due to heat release and incompressible velocity caused by vorticity.....	78
3.18b Decomposition of the axial velocities at $z = 42.5$ cm into irrotational velocity due to heat release and incompressible velocity caused by vorticity.....	78
3.19 Decomposition of the radial velocities at $r = 0.5$ cm into irrotational velocity due to heat release and incompressible velocity caused by vorticity.....	79
4.1 The mean velocity vectors around a 7.1 cm toluene pool fire obtained using LDV	92
4.2 Azimuthal vorticity distribution in the near region of the flame evaluated based on mean velocity measurements	93
4.3 Vorticity distribution as a function of radial position at three different heights.....	94
4.4 Vertical velocity distribution as a function a radial position at three different heights.....	95
4.5 Discrete PDF of radial entrainment velocity at three different heights at $r = 3.5$ cm	96
4.6 Discrete PDF of vertical entrainment velocity at three different heights at $r = 3.5$ cm	97
4.7 Discrete PDF of the vertical velocity at $z = 9$ cm, $r = 3.5$ cm.....	98
4.8 Discrete PDF of radial entrainment velocity at three different heights at $r = 4.5$ cm	99
4.9 Discrete PDF of vertical entrainment velocity at three different heights at $r = 4.5$ cm	100

Figure	Page
4.10 Discrete PDF of radial entrainment velocity at three different heights at $r = 11.5$ cm	101
4.11 Discrete PDF of vertical entrainment velocity at three different heights at $r = 11.5$ cm	102
4.12 Discrete PDF of vertical entrainment velocity at $z = 22$ cm at $r = 11.5$ cm.....	103
4.13 Power Spectrum Density of radial velocities at three different heights at $r = 4.5$ cm	104
4.14 Power Spectrum Density of vertical velocities at three different heights at $r = 4.5$ cm	105
4.15 Power Spectrum Density of radial velocities at three different heights at $r = 11.5$ cm	106
4.16 Power Spectrum Density of vertical velocities at three different heights at $r = 11.5$ cm	107
4.17 Comparison of present experimental data concerning entrainment mass-flow rate with past measurements and a correlation from the literature	108
4.18 The predicted velocity field in the near region of a pool fire at heat release rate of 3.04 kW and radiative loss fraction of 30%	109
4.19 The predicted expansion velocity field in the near region of a pool fire at heat release rate of 3.04 kW and radiative loss fraction of 30%	110
4.20 The predicted incompressible velocity field in the near region of a pool fire at heat release rate of 3.04 kW and radiative loss fraction of 30%	111
4.21 Comparison of predicted vertical velocities with measurements at three different heights	112
4.22 Comparison of predicted radial velocities with measurements at three different heights.....	113
4.23 Comparison of measured visible flame boundary with the predicted flame radius as a function of height.....	114

Figure	Page
4.24	Comparison of measurements with the predictions of radial velocities computed with measured visible flame boundary at three different heights..... 115
4.25	Comparison of measurements with the predictions of axial velocities computed with measured visible flame boundary at three different heights..... 116
4.26	The predicted velocity field computed with measured visible flame boundary 117
5.1	Instantaneous velocity vectors around a 7.1 cm toluene pool fire with a floor obtained using PIV showing the strong entrainment upstream and downstream of a flame bulge..... 132
5.2	Instantaneous velocity vectors around a 7.1 cm toluene pool fire with a floor obtained using PIV showing the vertical phase of the transient flow 133
5.3	Instantaneous velocity vectors around a 7.1 cm toluene pool fire with a floor obtained using PIV showing the extrainment phase of the flow 134
5.4	Instantaneous velocity vectors around a 7.1 cm toluene pool fire with a floor obtained using PIV showing vortex in the negative direction..... 135
5.5	An instantaneous velocity field of the flow induced by a 7.1 cm toluene pool fire without a floor..... 136
5.6	An instantaneous velocity field of the flow induced by a 7.1 cm toluene pool fire without a floor..... 137
5.7	Instantaneous velocity vectors around a 15 cm toluene pool fire with a 51 cm sheet metal floor138
5.8	Instantaneous velocity vectors around a 15 cm toluene pool fire with a 51 cm sheet metal floor 139
5.9	Instantaneous velocity vectors around a 15 cm toluene pool fire with a 51 cm sheet metal floor 140
5.10	Instantaneous velocity vectors around a 15 cm toluene pool fire with a 51 cm sheet metal floor 141
5.11	Instantaneous velocity vectors around a 15 cm toluene pool fire with a 51 cm sheet metal floor 142

Figure	Page
5.12 Instantaneous velocity vectors around a 15 cm toluene pool fire without a floor	143
5.13 Instantaneous velocity vectors around a 15 cm toluene pool fire without a floor	144
5.14 Instantaneous velocity vectors around a 15 cm toluene pool fire without a floor	145
5.15 Instantaneous velocity vectors around a 15 cm toluene pool fire without a floor	146
5.16 Instantaneous velocity vectors around a 15 cm toluene pool fire without a floor	147
5.17 Instantaneous velocity vectors around a 15 cm toluene pool fire without a floor	148
5.18 Instantaneous velocity vectors around a 15 cm heptane pool fire with a 51 cm sheet metal floor	149
5.19 Instantaneous velocity vectors around a 15 cm heptane pool fire with a 51 cm sheet metal floor	150
5.20 Instantaneous velocity vectors around a 15 cm heptane pool fire with a 51 cm sheet metal floor	151
5.21 Instantaneous velocity vectors around a 15 cm heptane pool fire with a 51 cm sheet metal floor	152
5.22 Instantaneous velocity vectors around a 15 cm heptane pool fire with a 51 cm sheet metal floor	153
5.23 Instantaneous velocity vectors around a 15 cm heptane pool fire without a floor	154
5.24 Instantaneous velocity vectors around a 15 cm heptane pool fire without a floor	155
5.25 Instantaneous velocity vectors around a 30 cm toluene pool fire without a floor obtained using PIV showing the strong entrainment at the radial location of pool burner	156

Figure	Page
5.26 Instantaneous velocity vectors around a 30 cm toluene pool fire without a floor obtained using PIV showing the vertical and extrainment phase of the transient flow.....	157
5.27 Instantaneous velocity vectors around a 30 cm toluene pool fire without a floor obtained using PIV showing the downward flow after a flame bulge...	158
5.28 Instantaneous velocity vectors around a 30 cm toluene pool fire without a floor obtained using PIV showing the flow about a flame bulge	159
5.29 Instantaneous velocity vectors around a 30 cm heptane pool fire without a floor obtained using PIV.....	160
5.30 Instantaneous velocity vectors around a 30 cm heptane pool fire without a floor obtained using PIV.....	161
5.31 Instantaneous velocity vectors around a 30 cm heptane pool fire without a floor obtained using PIV.....	162
5.32 The mean entrainment flow field of a 7.1 cm toluene pool fire with a floor obtained using PIV.....	163
5.33 Radial velocity measurements near a 7.1 cm toluene pool fire with a floor using LDV and PIV instruments	164
5.34 Vertical velocity measurements around a 7.1 cm toluene pool fire with a floor using LDV and PIV instruments	165
5.35 The mean velocity field around a 7.1 cm toluene pool fire without a floor obtained using PIV	166
5.36 The mean velocity field around a 15 cm toluene pool fire without a floor obtained using PIV	167
5.37 The mean velocity field around a 15 cm heptane pool fire without a floor obtained using PIV	168
5.38 The mean velocity field around a 15 cm toluene pool fire with a floor obtained using PIV	169
5.39 The mean velocity field around a 15 cm heptane pool fire with a floor obtained using PIV	170

Figure	Page
5.40 The mean entrainment flow field around a 30 cm toluene pool fire without a floor obtained using PIV	171
5.41 The mean entrainment flow field around a 30 cm heptane pool fire without a floor obtained using PIV	172
5.42 Normalized air entrainment rate for three 7.1 cm pool fires without a floor as a function of normalized distance above the fuel surface	173
5.43 Normalized air entrainment rate for three 15 cm pool fires without a floor as a function of normalized distance above the fuel surface	174
5.44 Normalized air entrainment rate for three 30 cm pool fires without a floor as a function of normalized distance above the fuel surface	175
5.45 Normalized air entrainment rate for three 7.1 cm pool fires with a floor as a function of normalized distance above the fuel surface	176
5.46 Normalized air entrainment rate for three 15 cm pool fires with a floor as a function of normalized distance above the fuel surface	177
5.47 Flame radius profile used in predicting the entrainment flow field of a 30 cm toluene pool fire without a floor	178
5.48 Measurements and prediction of radial velocity around a 30 cm toluene pool fire with adjusted flame radius profile in predictions.....	179
5.49 Predictions of velocity vectors around a 30 cm toluene pool fire with adjusted flame radius	180

LIST OF SYMBOLS

Symbol	Description
C_p	specific heat of constant pressure, kJ/kg·K
D	burner diameter, m
\hat{e}_r	unit vector in radial direction
\hat{e}_z	unit vector in axial direction
Fr_f	fire Froude number
g	gravitational acceleration, m/s ²
$H(z)$	energy convected through a cross section of the fire per unit time, kW
L	length, m
\dot{m}	mass flow rate in axial direction, kg/s
\dot{m}_{ent}	air entrainment rate, kg/s
\dot{m}_f	fuel consumption rate, kg/s
\tilde{P}	perturbation to the hydrostatic pressure
P_0	thermodynamic pressure
Q	heat release rate, kW
Q_0	total heat release rate, kW
$Q(\vec{r})$	volumetric heat release rate distribution, kW / m ³
R	burner radius, m; universal gas constant, kJ/kg-mole·K
$R(z)$	flame radius as a function of height, m
r	radial position, m
\vec{r}	position vector in the cylindrical coordinate system
S	mass stiochiometric ratio

T	temperature, K
$U(z)$	centerline axial velocity as a function of z , m/s
U_r	radial velocity, m/s
U_z	axial velocity, m/s
\vec{V}	the total velocity vector field, m/s
\bar{V}	the velocity vector due to expansion, m/s
\tilde{V}	the velocity vector caused by vorticity, m/s
W	the molecular weight of the mixture, kg/kg-mole
X	mole fraction
Y	mass fraction
X_A	combustion efficiency
X_R	radiative loss fraction
z	axial position, m

Greek Symbol

ϕ	the potential function
ψ	the stream function
η_s	soot generation factor, kg/kg carbon in the fuel
η_{CO}	CO generation factor, kg/kg carbon in the fuel
η_{CO_2}	CO ₂ generation factor, kg/kg carbon in the fuel
ρ	density, kg / m ³
$\bar{\omega}(\vec{r})$	distribution of azimuthal vorticity, 1/s
$\omega_p(\vec{r})$	distribution of azimuthal vorticity in plume, 1/s
ξ	ratio of velocity width to temperature width
Θ	dimensionless centerline excess temperature
Ω	vorticity in the outer region, 1/s

Superscript

* dimensionless values

Subscript

d nondimensionalizing parameters

∞ ambient properties

i species i

CHAPTER 1 INTRODUCTION

Studies of buoyant diffusion flames are of practical interest in fire safety. In early stages of most accidental fires, a liquid or solid material is evaporated or sublimated to produce combustible gases, which accelerate gradually due to buoyancy effects and subsequently mix with ambient air by entrainment and diffusion to sustain combustion. It is a complex phenomenon involving pyrolysis and oxidation, mass and heat diffusion, radiative and convective heat transfer, and fluid dynamics including turbulent transport. Due to their importance in models of hazard, egress time, possibility of flashover and suppression techniques, various aspects of buoyant diffusion flames, such as flame heights, temperature distribution, velocity distribution, soot generation, radiation and entrainment rate have been studied experimentally, analytically, and numerically. For a given combustible material, radiation and entrainment affect flame shape and size, degree of partial mixing, and consequently smoke production, burning rate, and spread rate of a fire significantly.

Past work concerning entrainment rates has not been conclusive. In fact, fundamental differences regarding the very definition of entrainment, originating in the surface across which it is defined, exist. In the fluid mechanics literature, the entrainment rate is defined as the increase in the axial mass flow rate with distance from the injector surface. For an axisymmetric flow this definition can be expressed as:

$$\dot{m}_{\text{ent}} = 2\pi \frac{d}{dz} \int_0^R r \rho U_z dr \quad (1.1)$$

where z is the distance from the injector surface, r is the radial distance from the axis, ρ is the local density, R tends to infinity, and U_z is the velocity in the axial direction. If a

radial location at which the axial velocity is zero can be found at each z , then the integral in eq. (1.1) can be evaluated by equating R to the radius of this location. Various implicit and explicit approximations for the location R have been made in the past, resulting in large differences among data. As a result, there are considerable uncertainties in existing empirical correlations for the rate of air entrainment into buoyant diffusion flames. The lack of knowledge concerning air entrainment rates inhibits understanding of physical processes and model development. A literature survey and a description of the specific objectives of the present study are given in the remainder of this chapter.

1.1 Existing Measurements of Entrainment Rates

A variety of techniques have been used to measure the rate of entrainment of air into buoyant diffusion flames. The measuring techniques can be roughly classified into four categories.

1.1.1 Entrainment Data Based on Axial Velocity and Temperature

Measurements of axial velocity and temperature profiles inside the flame are used for calculation of the axial flow rate by either direct radial integration or integration of curve fits for velocity and density. McCaffrey (1979) reported the first use of this method to measure the entrainment rate in the near field of buoyant diffusion flames produced by burning natural gas above a 30 cm by 30 cm square porous refractory burner.

Measurements of mean temperature with thermocouples and mean velocity with a bi-directional pressure probe were made. The probe had a relatively large measuring area (1.6 cm diameter) in order to spatially average the signals. Neglecting the cross-correlation between density and velocity, a correlation for mass flow rate in the axial direction was obtained as:

$$\dot{m} = 0.055zQ^{1/2} \quad (1.2)$$

where 0.055 is a constant with units of $(\text{kg} / \text{s}) / \text{m} \cdot (\text{kW})^{1/2}$.

Cox and Chitty (1980) carried out measurements of velocity in the flame established over a burner identical to that of McCaffrey (1979) by analyzing the cross-correlation function of signals obtained by two closely spaced thermal sensors. Temperature was measured with thermocouples. A correlation for the mass flow rate very close to the fuel surface was obtained as:

$$\dot{m} = 0.008z^{1/2}Q^{4/5} \quad (1.3)$$

McCaffrey and Cox (1982) modified their correlations using new estimates of the transverse variation of axial velocities. An energy balance was used in conjunction with measured radiative heat loss fractions to estimate the new velocity correlations. The updated correlation for mass flow rate was given as:

$$\dot{m} = 0.053z^{1.3}Q^{0.48} \quad (1.4)$$

Yumoto and Koseki (1982) measured velocities along the axis of a 30 cm heptane pool fire with a Pitot tube and mapped the mean temperature distribution with a matrix of 80 chromel-alumel thermocouples. Gas samples withdrawn at different locations along the flame axis were analyzed with gas chromatography. In their study, air entrainment was calculated based on two assumptions: (1) axial velocity and temperature are constant over any horizontal plane in the flame; and (2) the flame has a cylindrical form with a diameter equal to that of the burner. The authors reported that the air entrained up to 100 cm is 9.4 times the air requirement for stoichiometric combustion.

Koseki and Yumoto (1988) studied entrainment into heptane pool fires with five burners of different sizes ranging from 0.3 m to 6 m diameter, with the same experimental techniques and theoretical assumptions as in their previous study. The data were correlated, and for the 0.3 m heptane pool fire, the total air entrainment as a function of height was expressed as:

$$\dot{m}_{\text{ent}} = 3.26(z/R)^{0.56}S \quad (1.5)$$

where S is the mass based stoichiometric ratio and R is the burner radius. It is noted that the mass flow rate in the axial direction \dot{m} differs from the entrained mass flow rate only by the burning rate of fuel \dot{m}_f .

Simultaneous measurements of velocity and temperature in a 30.5 cm acetone pool fire were performed by Weckman (1989) using a single component Laser Doppler Velocimeter (LDV) and thermocouples. The data were sufficiently resolved to be incorporated into a control volume analysis of the flow field. The fluxes of mass, momentum and energy were calculated for discrete control volumes around a measurement location. The total flux crossing a horizontal plane was calculated as the sum of the mass flow rates for the discrete control volumes intersected by the plane. Measured values of rms of temperature, rms of velocity and the cross-correlation between temperature and velocity were substituted into the discretized equations to account for turbulent transport. The scaled data agreed well with the correlation proposed by Delichatsios (1987).

The differences in the estimates of air entrainment rates occur as a result of differences in the selection of the value for R which should tend to infinity as per the definition of eq. (1.1). Koseki and Yumoto (1988), Yumoto and Koseki (1982), and Weckman (1989) selected R to be equal to the radius of the visible flame or plume edge. This selection leads to the neglect of the fire-induced flow in the ambient. McCaffrey (1979), Cox and Chitty (1980), and McCaffrey and Cox (1982) approximated the axial velocity distribution and density distribution using analytical expressions and carried out the integration of eq. (1.1) under the limit of R tending to infinity.

In addition to the ambiguity associated with the selection of R , several difficulties are encountered in the use of eq. (1.1). The conversion of temperature data to density requires information concerning molecular weight distribution within the fire which is only approximately known. The most significant difficulty with the use of eq. (1.1) is that the experimental uncertainties and noise in the U_z data are the largest at the largest radial locations and eq. (1.1) has the effect of magnifying the effect of these uncertainties and noise.

1.1.2 Measurement of Entrainment Using a Steady State Mass Balance

Ricou and Spalding (1961) developed a technique based on direct measurement of the air flow rate needed to meet the entrainment requirement of forced and buoyant jets. The jets were enclosed in a double-walled chamber with the inner wall being made of a fine-grade filter cloth as shown in Fig. 1.1. The base of the chamber was closed. The jet flow exited the chamber through an orifice selected to yield a high pressure sensitivity to excess or deficit flow through the inner wall. The orifice was made large enough to avoid interference with the jet flow at the exit. Air entrainment rates were measured for the far field of burning jets, momentum-controlled jets, and buoyant plumes. The authors observed that the entrainment rates for buoyant jets are greater than those for non-buoyant jets with identical exit momentum.

Delichatsios and Orloff (1984) measured air entrainment rates for turbulent buoyant propane/air jet diffusion flames with nozzle diameters of 12 mm and 23 mm and heat release rates of 21 kW, 31 kW, and 45 kW using a version of the Ricou and Spalding technique. The flow rate of air was measured using a tracer. A known quantity of ethylene tracer gas was injected into the air supply line and its concentration inside the enclosure was accurately measured to determine the air flow rate. The expression for air entrainment from the best linear fit of the data was given as:

$$\dot{m}_{\text{ent}} = 0.034 \rho_{\infty} g^{1/2} z^{5/2} \quad (1.6)$$

The dependence on heat release rate and burner size observed in earlier correlations does not appear in eq. (1.6).

The main limitations of the Ricou and Spalding (1961) technique are that: (1) entrainment rates near the burner exit can not be measured due to the need for measuring very small mass flow rates, and (2) the downstream orifice affects the flow field significantly in the case of elliptic flows such as buoyant pool fires. Majority of the data obtained by Ricou and Spalding (1961) and the successful correlation of entrainment rate were for forced jets. Since the effect of the chamber on the entrainment flow field is not known, the accuracy of the measurement of local air entrainment rates cannot be determined. Hill (1972) made a modification to the Ricou & Spalding technique by

shortening the chamber and opening both ends so that the local entrainment rates could be measured directly by moving the chamber axially. However, Hill's technique has never been applied to measure the air entrainment rate of diffusion flames.

1.1.3 Measurement of Entrainment Using a Stably Stratified Layer

The entrainment rate of air can be obtained by sampling stably stratified combustion products in a hood and solving a set of global mass balance equations to obtain the equivalence ratio. This method was pioneered by Zukoski and coworkers (Zukoski et al, 1980; Cetegen et al, 1982 and 1984; Toner et al, 1987; Zukoski, 1994). Their apparatus consisted of a large steel hood placed over the flames stabilized on 10, 19, and 50 cm diameter natural gas burners with heat release rates ranging from 20 to 100 kW as shown in Fig. 1.2. The hot gases accumulate within the hood and spill from under the bottom edge. An interface between the combustion products spilling out of the hood and the ambient atmosphere develops in the process. The mass flux in the fire plume at the interface is calculated from the fuel flow rate and the fuel-air ratio of the gases inside the hood which is determined from a chemical analysis of gas samples withdrawn from the hood after reaching steady state. Zukoski (1994) pointed out that the presence of the stably stratified interface between hot combustion products and ambient air forces the velocity to remain horizontal near this boundary, and this constraint might affect the inflowing gas and cause the entrainment rate at a given height to be a function of the interface height. Some velocity measurements done in the past show that the entrainment processes are affected by the presence of the interface. The measurements of velocity in the vicinity of buoyant diffusion flames performed by Thomas et al. (1965), and Walker and Moss (1984) showed significant vertical velocities even at a considerable distance from the fire plume. In addition, the vertical velocity component at a given radial location increased with height. The limited size of a hood may impede these vertical flows. The best fit to data given by Zukoski (1994) shows that the plume mass flow rate at an elevation z above a burner with a diameter D can be correlated as:

$$\dot{m} = 0.62zD \quad (1.7)$$

Selection of an appropriate size for the hood is not straightforward. In fact, Zukoski and coworkers used two different sizes of hood for measurements in the near and far field regions of the pool fires.

Beyler (1983) applied a variation of the above technique to measure the entrainment rates of propane fueled flames and methanol pool fires established on 13 and 19 cm diameter burners. Instead of letting the collected hot gases spill from the bottom surface of the stratified layer, they were drawn from a peripheral slot opened on the side wall near the top of the hood and sent through a flat plate orifice meter to measure the collected gas flow rate. It was intended as a better simulation of a building fire with ventilation. Based on these data, a curve fit for the entrainment data for the 19 cm propane flames is:

$$\dot{m}_{\text{ent}} = 0.073(z + 0.06)^{1.25} \quad (1.8)$$

which is different from Zukoski's results by a factor of two to three. Neither correlation shows any dependence on heat release rate in contrast to the work discussed earlier.

A common limitation of the three experimental methods discussed above is that information about the details of the entrainment flow field are not measured. Direct measurement of velocities in the fire induced flow field allows calculations of entrainment flow across any desired interface. The disadvantage of this technique is the need for seeding of ambient and the large amount of measurement effort.

1.1.4 Direct Measurements of Fire Induced Flow Field

Thomas et al. (1965) measured the velocity field of entrained air flow induced by 91 cm diameter fires burning various fuels. The pool was surrounded by a 276 cm diameter floor. Photographs of the flow seeded with thistledown were taken using a camera with a rotating shutter. The velocities of the thistledown were deduced from the number of interruptions in the trace left by the image of thistledown on the picture. The volumetric flow rate of air through cylindrical surfaces at different radial locations were

calculated as a function of height using the horizontal velocity data. Since there was considerable upward velocity at the level of the visible flame height even at the farthest measuring point away from the flame, the authors concluded that the total entrained air flow towards the fire must be underestimated using their data. The limitations imposed by light source and image quality affected the accuracy of their measurement.

1.1.5 Summary of Correlations

Delichatsios (1987) proposed a semi-empirical set of correlations to predict the air entrainment rates of buoyant jet flames and pool fires. Five parameters controlling fire dynamics were identified: the burner diameter, the ambient density, the mass based stoichiometric ratio S , the total buoyancy flow, and the buoyancy force per unit mass of combustion products at the adiabatic temperature at stoichiometric conditions. General correlations forms were obtained based on dimensional analysis of these parameters, and were further refined by examining the flame shapes. The coefficients in the correlations were determined by comparison with the experimental data of Cetegen et al. (1984), Beyler (1983), and Delichatsios and Orloff (1984). The correlations for air entrainment in three regions along the height of a pool fire are:

$$\text{near the pool surface, } \frac{\dot{m}_{\text{ent}}}{(S+1)\dot{m}_f} \text{Fr}_f = 0.086 \left(\frac{z}{D} \right)^{1/2} \quad (1.9a)$$

$$\text{in the middle region, } \frac{\dot{m}_{\text{ent}}}{(S+1)\dot{m}_f} \text{Fr}_f = 0.093 \left(\frac{z}{D} \right)^{3/2} \quad (1.9b)$$

$$\text{in the plume, } \frac{\dot{m}_{\text{ent}}}{(S+1)\dot{m}_f} \text{Fr}_f = 0.018 \left(\frac{z}{D} \right)^{5/2} \quad (1.9c)$$

where \dot{m}_f is the fuel burning rate and Fr_f is the fire Froude number. The Froude number is the ratio of the inertia force to the buoyancy force, and Delichatsios showed that with the approximation of adiabatic temperature it could be evaluated as:

$$\text{Fr}_f = \frac{\dot{m}_f \Delta H_c}{\rho_\infty [\Delta H_c / (S+1)] D^2 \sqrt{\{\Delta H_c / [(S+1) C_p T_\infty]\} g D (X_A - X_R)}} \quad (1.10)$$

where ΔH_c is the combustion enthalpy of the fuel, X_A is the combustion efficiency and X_R is the radiative loss fraction. According to these correlations, the air entrainment rate changes when different types of fuels are burned, because Fr_f is a function of heating values of the fuel, stiochiometric mass ratio, combustion efficiency and radiative loss fraction. However, the entrainment rate is independent of the heat release rate when burning the same fuel, as Fr_f is linearly proportional to the fuel consumption rate.

As discussed in Appendix A, the fire Froude number can be derived from the governing mass, momentum and energy conservation equations in the buoyancy-dominated, fast chemistry limit. Therefore it should be the appropriate nondimensional parameter for correlating entrainment rates of buoyant diffusion flames.

The available correlations discussed above are summarized in Table 1.1. The correlations by McCaffrey (1979), Cox and Chitty (1980), McCaffrey and Cox (1982) and Zukoski (1994) were originally given as the mass flow rate in the fire plume, and fuel flow rates are subtracted from these to yield the air entrainment rate. The air entrainment rates according to the correlations in Table 1.1 are the total air entrainment up to a given axial location, instead of the local air entrainment rate at the given axial location.

Table 1.1 Correlations of buoyant diffusion flame air entrainment.

Author(s)	Year	Correlation Formula	Dependent on Burner size?	Dependent on Heat Release?
McCaffrey	1979	$\dot{m}_{ent} = 0.055zQ^{1/2} - \dot{m}_f$	No	Yes
Cox and Chitty	1980	$\dot{m}_{ent} = 0.008z^{1/2}Q^{4/5} - \dot{m}_f$	No	Yes
McCaffrey and Cox	1982	$\dot{m}_{ent} = 0.053z^{1.3}Q^{0.48} - \dot{m}_f$	No	Yes
Koseki and Yumoto	1988	$\dot{m}_{ent} = 3.26(z/R)^{0.56}S$	Yes	No, but dependent on fuel type
Delichatsios and Orloff	1984	$\dot{m}_{ent} = 0.034\rho_\infty g^{1/2}z^{5/2}$	No	No
Zukoski	1994	$\dot{m}_{ent} = 0.62zD - \dot{m}_f$	Yes	very weakly
Beyler	1983	$\dot{m}_{ent} = 0.073(z + 0.06)^{1.25}$	Yes	No
Delichatsios	1987	$\frac{\dot{m}_{ent}}{(S+1)\dot{m}_f} Fr_f = 0.086 \left(\frac{z}{D} \right)^{1/2}$ $\frac{\dot{m}_{ent}}{(S+1)\dot{m}_f} Fr_f = 0.093 \left(\frac{z}{D} \right)^{3/2}$ $\frac{\dot{m}_{ent}}{(S+1)\dot{m}_f} Fr_f = 0.018 \left(\frac{z}{D} \right)^{5/2}$	Yes	No, but dependent on fuel type

1.2 Analytical and Numerical Work

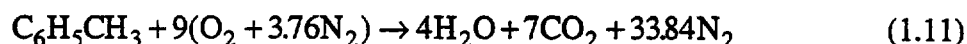
In addition to the experimental work discussed above, a few studies involving analyses and computations of the entrainment flow field have been reported. Taylor (1958) calculated the flow field outside a thermal jet with the assumption that the entrainment flow was caused by a line of sinks distributed along the axis of the jet. The strength of each sink was determined using the breadth and velocity of the jet at different heights obtained by solving mean continuity and momentum equations with a mixing length closure.

Morton (1965) gave a theoretical treatment for the entrainment by diffusion flames by using the theories of weakly buoyant plumes. The local entrainment function for weakly buoyant plumes was modified to make allowances for the larger variation in density and the cooling effect of radiation.

Baum and McCaffrey (1989) developed a kinematic approach to predict the flow field induced by unconfined fires in a semi-infinite environment. The vorticity generation rate and the heat release rate, obtained from McCaffrey's (1983) correlations of flame structure, were regarded as the driving forces for the fire induced flow, both inside and outside the fire plume. The flow field was decomposed into an irrotational flow and an incompressible flow, and the resulting partial differential equations were discretized and solved using a finite difference method. The predicted velocities were qualitatively similar to those observed by Adams et al. (1973) in large scale experiments. However, the magnitude of the predicted velocities was approximately a factor of two higher than those measured by Adams et al. (1973).

1.3 An Example of the Application of Existing Correlations

In the following, an example demonstrating the current state of the correlations for entrainment into a pool fire is presented. A 7.1 cm pool fire burning toluene in air is considered following Klassen (1992). Stoichiometric combustion of toluene can be represented as:



Mass:	92	288	947.52	72	308	947.52
-------	----	-----	--------	----	-----	--------

$Y_i(\%)$:				5.4	23.3	71.4
-------------	--	--	--	-----	------	------

$C_{p,i}(\text{kJ} / \text{kg} \cdot \text{K})$:				1.87	0.84	1.04
---	--	--	--	------	------	------

Hence, $S = 13.4$, $C_p = \sum C_{p,i} Y_i = 1.04(\text{kJ} / \text{kg} \cdot \text{K})$. The radiative heat loss fraction X_R is 0.30 (Klassen, 1992), and the combustion efficiency X_A is 88%, according to the estimation presented in Appendix B. The heat of combustion of toluene $\Delta H_c = 41628$

kJ/kg (CRC Handbook of Chemistry and Physics, 1975). Since $\dot{m}_f = 83 \text{ mg/s}$ (Klassen, 1992) and $\rho_\infty = 1.2 \text{ kg/m}^3$, $T_\infty = 293 \text{ K}$, the Froude number of the fire is 0.097.

Air entrainment rates for this fire as estimated using the various correlations summarized in Table 1.1 are plotted in Fig. 1.3 as a function of height above the fuel surface. There are significant qualitative and quantitative differences among the correlations as observed in Table 1.1 and Fig. 1.3. The correlations by McCaffrey (1979), Cox and Chitty (1980) and McCaffrey and Cox (1982) suggest that air entrainment rate depends on the heat release rate, while the correlations of Koseki and Yumoto (1988), and Zukoski (1994) suggest a dependence on the burner size. All of the correlations show a dependence on axial distance, but with different exponents. The different definitions of air entrainment implied by the specific measurement techniques, the interference of the flow field by the measuring equipment, and the uncertainty of each measurement technique contribute to the large discrepancy among different correlations. Thus it is clear that the state of current engineering correlations of entrainment is such that systematic further work is needed.

1.4 Specific Objectives

As discussed above, existing correlations of air entrainment lead to remarkably different estimates for the same fire. Our understanding of the entrainment process is rather limited because most of the experiments did not provide information about the entrainment flow field itself. More systematic measurements of the entrainment velocity and rational models are needed to deepen our understanding of the physical processes. Engineering correlations with more certainty than that exhibited in Fig. 1.3 are needed.

Based on this background, the specific objectives of the present study are:

(1) Measure the mean and the fluctuating velocity field around a 7.1 cm toluene pool fire using a Laser Doppler Velocimeter (LDV),

(2) Measure the mean and the instantaneous velocity field around different pool fires applying Particle Imaging Velocimetry (PIV) to study the effect of fire size, fuel type and floor on air entrainment,

(3) Utilize a kinematic model to predict the entrainment velocity field of pool fires, and compare the predicted entrainment velocity field with the present measurements,

(4) Compare the result of the present investigation with previous data and correlations and propose explanations for the discrepancies among different studies.

The experimental methods used in this study are described in Chapter 2, followed by a discussion of the theoretical methods in Chapter 3. In Chapter 4, experimental data from LDV measurements, their comparison with existing correlation, and existing data are presented. The results of the kinematic analysis are also compared with the data. The results are discussed in terms of the definition of entrainment rate and the adequacy of the present descriptions of the heat release rate and the vorticity generation rate distributions in the fires. In Chapter 5, experimental data from PIV measurements of air entrainment velocity field are discussed, with emphasis on instantaneous entrainment flow structures. Toluene, heptane and methanol burning in 7.1, 15 and 30 cm pool burners are considered. For the two smaller pool burners, the effect of a floor around the pool on the entrainment flow fields is also studied. The conclusions and recommendations of the study are presented in Chapter 6.

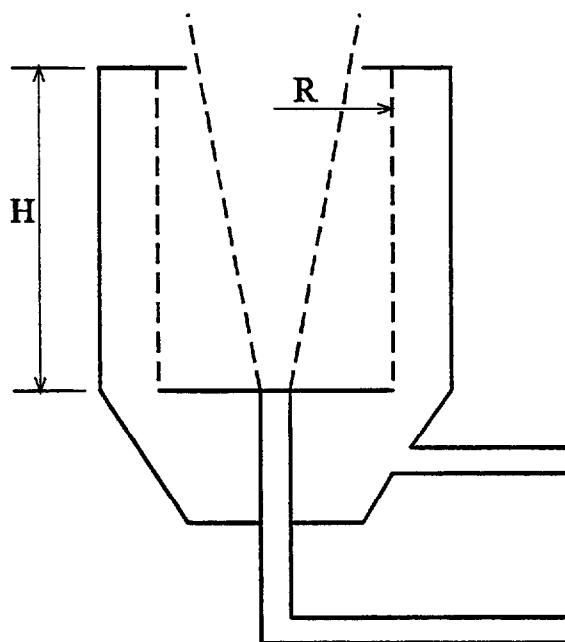


Figure 1.1 A sketch of the entrainment measurement apparatus used by Ricou and Spalding (1961).

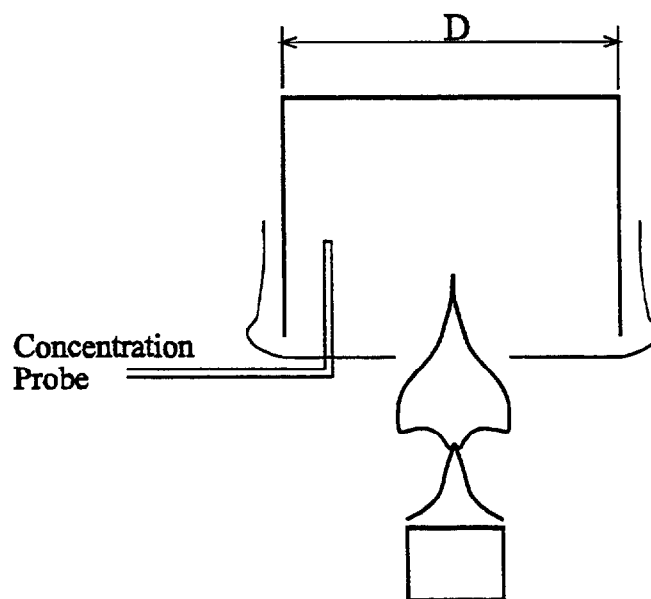


Figure 1.2 A sketch of the entrainment measurement apparatus used by Zukoski and coworkers (1980).

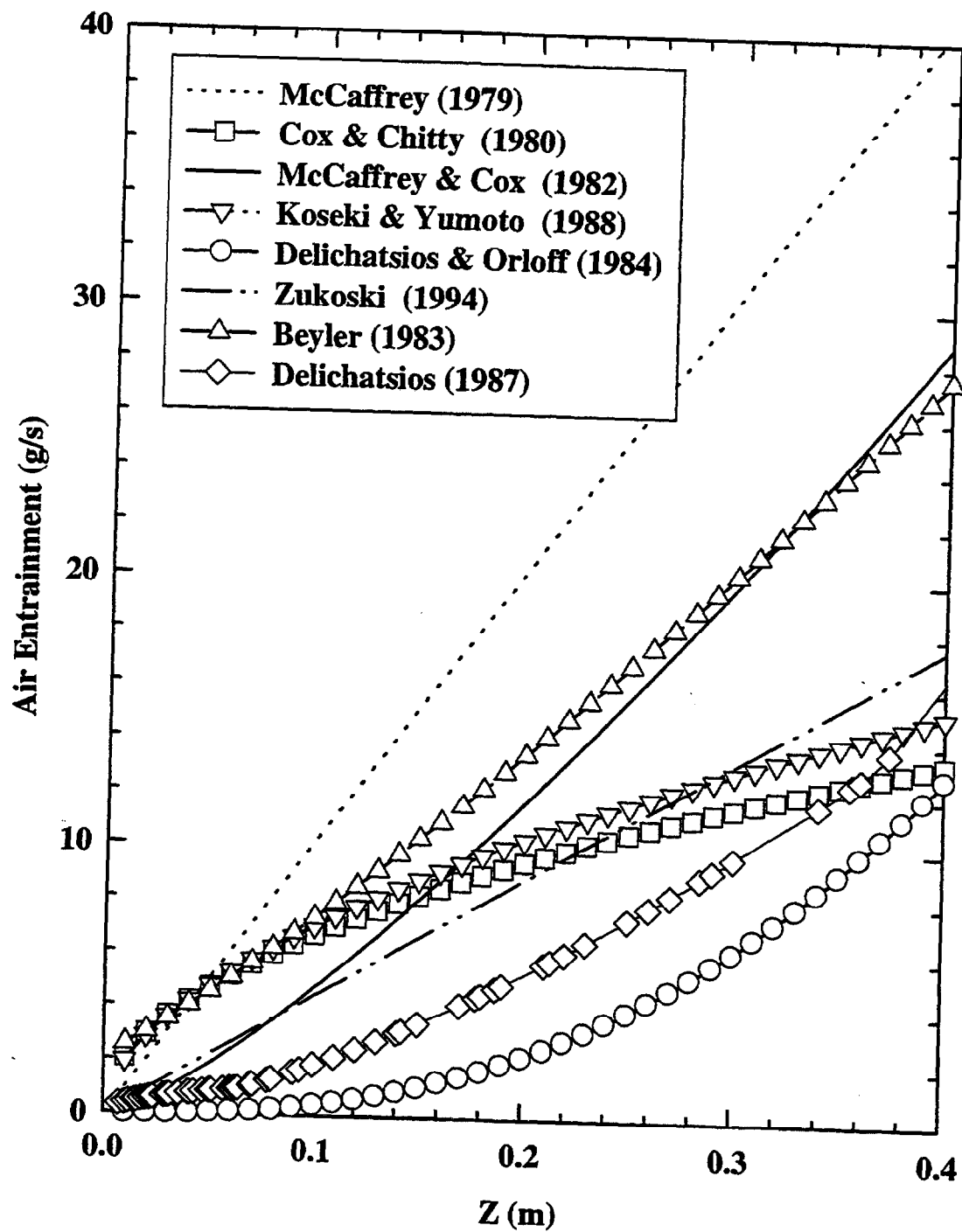


Figure 1.3 Estimates of air entrainment rates based on existing engineering correlations summarized in Table 1.1.

CHAPTER 2 EXPERIMENTAL METHODS

In order to improve our understanding of the fire-induced flow field, it is necessary to avoid the difficulties associated with the effects of the exit orifice or the sampling hood on the flow field as well as to allow calculations of entrainment rates over various possible surfaces. Therefore, non-intrusive optical velocimetry techniques, namely, Laser Doppler Velocimetry (LDV) and Particle Imaging Velocimetry (PIV), are applied in this study to investigate the entrainment flow fields of pool fires. First, detailed velocity field measurements surrounding a 7.1 cm toluene pool fire were obtained using LDV. The fire was enclosed in a large enclosure to allow seeding of the surrounding air with smoke particles. The low concentration level of smoke did not cause measurable vitiation. The enclosure prevented the ambient disturbances from affecting the flow field. The LDV is a more established technique and hence was used for obtaining baseline data. However, LDV is much more time consuming and use of the faster PIV technique was essential to complete the measurements in a reasonable time frame. PIV was used to study the instantaneous flow structures and the mean velocity field induced by nine different pool fires. Validity of the PIV technique was first confirmed by comparison of the measurements of velocity field around the 7.1 cm toluene pool fire with the LDV data.

2.1 Laser Doppler Velocimetry (LDV)

Configuration of the experimental apparatus and technical details of LDV measurements are summarized in this section. Control of the boundary conditions is also discussed.

2.1.1 Experimental Apparatus

A 7.1 cm inner diameter pool burner made of copper with a cooling jacket was used. The burner was established in the center of a Plexiglas enclosure. Figure 2.1 shows a sketch of the experimental apparatus. A schematic diagram of the burner is shown in Fig. 2.2. Both the inner wall and the outer wall, which together comprise the water jacket, are 2 mm thick. There are two ports connected to the water jacket, with the lower port serving as the cooling water inlet. Nakakuki (1994) concluded that for small uncooled burners, heat transferred by convection from the burner to the liquid fuel was dominant compared with direct conductive heat transfer and radiative heat transfer from the flame to the liquid. Hence the burning rate of small pool fires is mainly determined by the temperature of the burner, which is controlled in the present experiments by adjusting the cooling water flow rate using a needle valve and a rotameter. Another factor affecting the energy transfer from the flame to the liquid fuel in the burner is the contact area between the fuel and the metal pool. The contact area changes with the lip height defined as the distance between the fuel surface and the top edge of the burner. Preliminary experiments showed that the lip height affected the flame geometry as well as the burning rate. For a fixed cooling water flow rate, the burning rate decreased with increasing lip height and the flame became smaller but steadier. The lip height was maintained at 2 mm during all the velocity measurements. During the experiments, a sheet metal floor with outer diameter of 51 cm was placed on the shoulder of the burner to simulate a floor flush with the fire source. Toluene was supplied at the bottom of the pool using a fuel supply system which is shown schematically in Fig. 2.3. The fuel flow rate is controlled by a stainless steel metering valve and a rotameter. The rotameter was calibrated using a stop watch and an electronic scale. The flow rate at a certain rotameter reading was determined by measuring the time needed to flow a certain amount of toluene through the fuel supply system at that rotameter reading. Repeated calibrations proved that accuracy of the measurement of the fuel flow rate was better than 5%. The toluene reservoir tank was pressurized at 10 psig with nitrogen from a high pressure cylinder via a two stage

pressure regulator to provide the necessary driving force to push the fuel to the burner through the fuel line.

Buoyant diffusion flames are very sensitive to ambient disturbances in the laboratory. McCaffrey (1979), and Weckman and Sobiesiak (1988) noticed that a floor around the burner enhances the sensitivity to ambient disturbances. To protect the flame from ambient disturbances, a Plexiglas enclosure was utilized. The cross section of the enclosure is 100 cm \times 100 cm, and its height is 300 cm. At the bottom around the periphery of the enclosure a 10 cm gap between the Plexiglas panels and the floor allowed fresh air to be drawn in. The gap was filled with wire screen taped to the bottom edge of the Plexiglas panels to damp out disturbances in the incoming air.

An 18 inch diameter ventilation pipe with an exhaust fan in the middle connected the enclosure to the outside atmosphere. The speed of the exhaust fan could be adjusted continuously. The chimney effect in the pipe would draft the hot gases out even if the fan were not run. However, it was observed that running the fan at a low speed kept the flame more steady. At the bottom of the ventilation pipe, a sheet metal damper controlled by a pulley system was utilized. The damper allowed the establishment of an upper layer of hot combustion products at a certain distance above the burner. It was discovered that the distance between the upper layer and the fuel surface (interface height) affected the entrainment flow field. The effect of the interface height was observed to be as large as 20%. Hence, the damper was adjusted carefully to move the interface to the same height each time before velocity measurements were started. Maintaining a constant interface height resulted in a self-consistent data set. However, comparison with measurements and predictions obtained with a different interface height will be affected by the effect described above.

2.1.2 The Instrumentation

The LDV involves a dual-beam, single-channel system (TSI, Model 9100-6) operated in the forward scattering mode. A 1.3 mm diameter laser beam at 514.5 nm

wavelength was obtained from a Lexel 95 Argon-ion CW laser operating in the TEM 00 mode. A TSI beam splitter, Model 9115-1, split the laser beam into two parallel beams of equal intensity, each 25 mm from the optical axis. In order to measure possible reverse flows and flows with very low convective velocity, a frequency shifter system, which consisted of a TSI 9186A electronics module and a TSI 9182-12 optics module, was used to modulate one of the beams at 100 kHz. A convex lens of 604 mm focal length brought the two beams to a focus, forming a probe volume in the form of an ellipsoidal region containing a series of parallel interference fringes. The properties of the ellipsoidal probe volume are discussed in Appendix C. Since the frequencies of the two beams are not identical, the fringe pattern moves at an apparent speed equal to the product of the fringe spacing and the frequency difference between the beams in a direction normal to the fringe plane and towards the lower frequency beam. With the present setting, the velocity of the fringe pattern movement was 62.2 cm/s.

To get a LDV signal of the best quality, an on-axis forward-scatter configuration was used. The receiving optics, TSI Model 9140, focused the signal collected by a convex lens of 604 mm focal length into a photodetector aperture. A 514.5 nm green filter was placed in front of the photodetector to block the flame luminosity which was predominantly yellow. The properties of the measuring volume are determined by the focal length and the size of the receiving lens and the size of the photodetector aperture, as discussed in Appendix C. The photomultiplier system consists of a model 9162 photomultiplier (PMT) with a 0.2 mm aperture and an integral preamplifier, and a model 9165 Power Supply. A counter-type burst processor consisting of a model 1994 input conditioner, a model 1995 Timer and a Model 1992 Readout is utilized to process the PMT output. In the input conditioner, signals with large pedestals were rejected as they came from light scattered by large particles which probably could not follow the flow faithfully. The signals were then passed through a set of band pass filters. The limit of the high pass filter was set at 10 KHz to remove low frequency noise, while the limit of the low pass filter was set at 300 KHz to filter out high frequency noise. When measuring the vertical velocity at higher locations, the low pass filter limit was changed to 600 KHz to

accommodate the much higher velocity to be measured. The filtered signals were amplified and processed by a timer. Effective data rates were monitored using the digital readout. The output voltages, which are proportional to the Doppler frequency, were stored in a PC with a Scientific Solutions Data Acquisition Board. The other settings for the burst processor used in this study were: 8 cycles/burst, 7% comparison, and 10 exponent. An estimation of the uncertainty of LDV measurement is provided in Appendix D.

Since the density of particles large enough to act as tracers in the air is not high enough, artificial seeding was provided by burning incense sticks. A batch of evenly spaced four incense sticks arranged in a sponge filled in a unistrut frame was placed on the floor along each side of the enclosure. Smoke from the lighted incense sticks was carried by the air through the wire screens between the Plexiglas panels and the floor into the enclosure. Inside the enclosure, the smoke mixed quickly with the air in the enclosure and yielded uniform seeding. According to Megaridis (1993), the mean size of the smoke particles was 0.2 micron in diameter. Measurements of oxygen concentrations (using sampling and gas chromatography) in the enclosure away from the fire showed that the burning of incense sticks for seeding purposes caused negligible vitiation of oxygen.

2.1.3 Interface Height and the Background Velocity

The burner was mounted on a transverse system consisting of two unislides which gave two dimensional freedom to the controlled movement of the burner to facilitate mapping of the velocity field of the fire-induced flow. During the experiment, the LDV system remained stationary and the burner was moved in order to map the velocity field in the near region of the pool fire. Since the interface height was determined by the combined effect of the opening of the damper under the ventilation hood, the exhaust fan speed, and the buoyancy inside the hood and the ventilation pipe with respect to the ground, the interface height changed with position of the pool fire. When the pool was lowered, for measurement of velocities at higher positions relative to the burner, and no

adjustment was made to the opening of the damper and the fan speed, the distance between the top surface of the burner and the interface increased temporarily. This meant that more air was entrained by the plume before it entered the upper layer, but the ventilation still remained the same, and consequently the interface lowered. Lower interface position provided larger buoyancy which increased the ventilation. The interface kept lowering down until a new equilibrium between the entrainment and the ventilation was reached. It was a concern whether the interface height, i.e., the distance between the interface and the top surface of the burner, was constant for different pool positions since it is known that the interface height had an effect on the entrainment rate of buoyant flames (Zukoski, 1994). The change in interface heights was measured as the pool was lowered down to different positions. The results of the measurements are plotted in Fig. 2.4. Interface height decreased from about 64 cm to about 59 cm as the pool is lowered from 0 cm to - 40 cm. The change is less than 5% as the pool burner was lowered down by 40 cm. Since the entrainment was not a steady process and the interface height could remain a constant only within a certain limit even when the pool was not moved, no attempts were made to bring the interface height back to 64 cm by adjusting the opening of the damper or the exhaust fan speed when the pool was lowered down.

In order to determine the possible effect of the exhaust fan on the flow field, background velocities were measured with the fan speed and the opening of the damper remaining unchanged after putting out the pool fire. Flow visualization showed that without the pool fire, the air inside the enclosure was very quiescent. Figure 2.5 represents the background radial velocities at three different heights at $r = 6.5$ cm in the form of a discrete PDF (Probability Density Function). The maximum mean radial velocity (mean velocity is denoted with an overbar in the legends of the plots) is 1.3 cm/s at $z = 3$ cm. The fluctuation of the velocity is very limited as shown by the distribution of the PDF and the maximum rms (denoted with an overbar and an apostrophe in the legends). The maximum rms is 0.6 cm/s at $z = 14$ cm. The PDFs of the vertical background velocities at the same locations are shown in Fig. 2.6. The mean vertical velocity maximum in magnitude is -0.5 cm/s at $z = 14$ cm, and the maximum rms is 0.7

cm/s at the same location. Both the mean and rms of these velocities are very small too. PDFs of the background velocities at $r = 9.5$ cm and $r = 12.5$ cm are shown in Figs. 2.7 - 2.10. Both the background radial and vertical velocities at all locations show only a small fluctuation around a mean value very close to zero. It is noted that all the mean radial velocities at measuring locations are positive, suggesting that air is flowing inward towards the centerline of the burner, while all the mean vertical velocities are negative, indicating that the air is flowing downward. It is possible that the configuration of the system does cause some background flow pattern, but it is too weak to be identified by flow visualization.

2.2 Particle Imaging Velocimetry (PIV)

The principle of Particle Imaging Velocimetry is different from that of Laser Doppler Velocimetry in three aspects. First, PIV obtains information about velocity by measuring the displacement of tracers in the flow field during a given time interval, while LDV measures the time needed for the tracer to travel through a given distance (fringe spacing). Secondly, PIV measures the velocity vectors at multiple points and is capable of capturing the instantaneous flow structure. Laser Doppler Velocimetry can only measure velocity (1-D, 2-D, or 3-D) at one point in the flow field. As a result, the mean velocity at one point is obtained by averaging over instantaneous velocity field measurements in PIV measurement (ensemble average), while in LDV measurement, the mean velocity is obtained by averaging over time (stationary average).

A discussion about some of the parameters which affect the resolution and accuracy of PIV measurements is provided in Appendix E.

2.2.1 Experimental Apparatus

Besides the aforesaid 7.1 cm pool burner, two other pool burners of 15 cm and 30 cm diameters were used. The details of the two bigger pool burners are identical to those reported by Klassen (1992).

To accommodate the bigger pool fires, a bigger enclosure ($1.5\text{ m} \times 1.5\text{ m} \times 3\text{ m}$) was built. A sketch of the enclosure is shown in Fig. 2.11. The top 1 m of the enclosure is made of glass in order to establish an upper layer as the downstream boundary condition for the fire. The remaining 2 m of the enclosure is constructed using a fine wire cloth to protect the fire from ambient disturbances. The top of the enclosure is a hole and lid with adjustable opening. Above the enclosure is a ventilation hood ($2.5\text{ m} \times 2.5\text{ m}$) which collects and discharges the combustion products into outer atmosphere.

Three fuels (methanol, heptane and toluene) were considered to obtain data for fires with a range of soot and radiation properties. The lip height (the distance from the fuel surface to the burner edge) is kept at 0.2 cm for 7.1 cm pool fires and 0.5 cm for the 15 cm and 30 cm pool fires. The larger lip height is necessary for the larger pool fires in order to prevent occasional overflow of the liquid over the edge.

2.2.2 The Instrumentation

The Particle Imaging Velocimetry system is model MKIII System supplied by Fluid Flow Diagnostics Inc. Its configuration is shown schematically in Fig. 2.12. A CW Argon-ion laser with a multiline power output of 12 W is used to generate a train of dual pulses of light by passing the laser light beam through a two-slot chopper rotating at a frequency of 100 Hz. Two convex lenses are used to focus the laser beam at the location of the chopper plate to maximize the signal to noise ratio. A cylindrical lens is used to spread the pulsed laser beam into a light sheet to illuminate a planar section of the flow field for two closely spaced short time intervals. The air inside the enclosure is seeded with Al_2O_3 particles of $0.5\text{ }\mu\text{m}$ diameter using a bank of cyclone seeders with a fluidized bed. A Kodak Megaplug 1.4 MB CCD camera and a frame grabber are used to capture

the light scattered from the seeding particles in the view region during the two laser pulses. To eliminate the ambiguity in the direction of motion, a shift in the direction of the mean velocity is introduced by a scanning mirror, which is synchronized to the chopper with a digital delay. The shift is larger in magnitude than the maximum reverse flow velocity to ensure a correct ordering of the two exposures. The double-exposed images are processed with a resolution box of size 32×32 pixels (corresponding to 2.5×2.5 mm in the flow field). An auto-correlation field is obtained by applying Fast Fourier Transform twice to the image. The coordinates of the signal peak in the auto-correlation field represent the displacement between pairs of particle images. The shift is subtracted from the resolved vector field in the analysis stage. The mean velocity field is obtained by averaging 100 instantaneous vector plots.

In order to check the operation of the PIV system, a 1 cm diameter non-reacting air jet seeded with the Al_2O_3 particles and injected vertically upwards in a stagnant environment is used. Figure 2.13 shows radial profiles of streamwise velocity at three axial positions. The PIV data are in reasonable agreement with the LDV data and the correlation of Schlichting (1979). The particle seeding was not adequate near the highest position leading to the maximum discrepancy. However, for the two lower positions, agreement within the instrument uncertainty for both methods is obtained.

2.3 Study of Flame Geometry

Measurements of the flame geometry were obtained using a CCD camera. A video record of a flame was taken with a 1/1000 second shutter speed and a 30 Hz frame rate. The average flame shape was constructed by averaging over 30 frames at a time interval of 1/5 second (6 frames/second). The flame height was obtained as the average of flame heights in 512 frames.

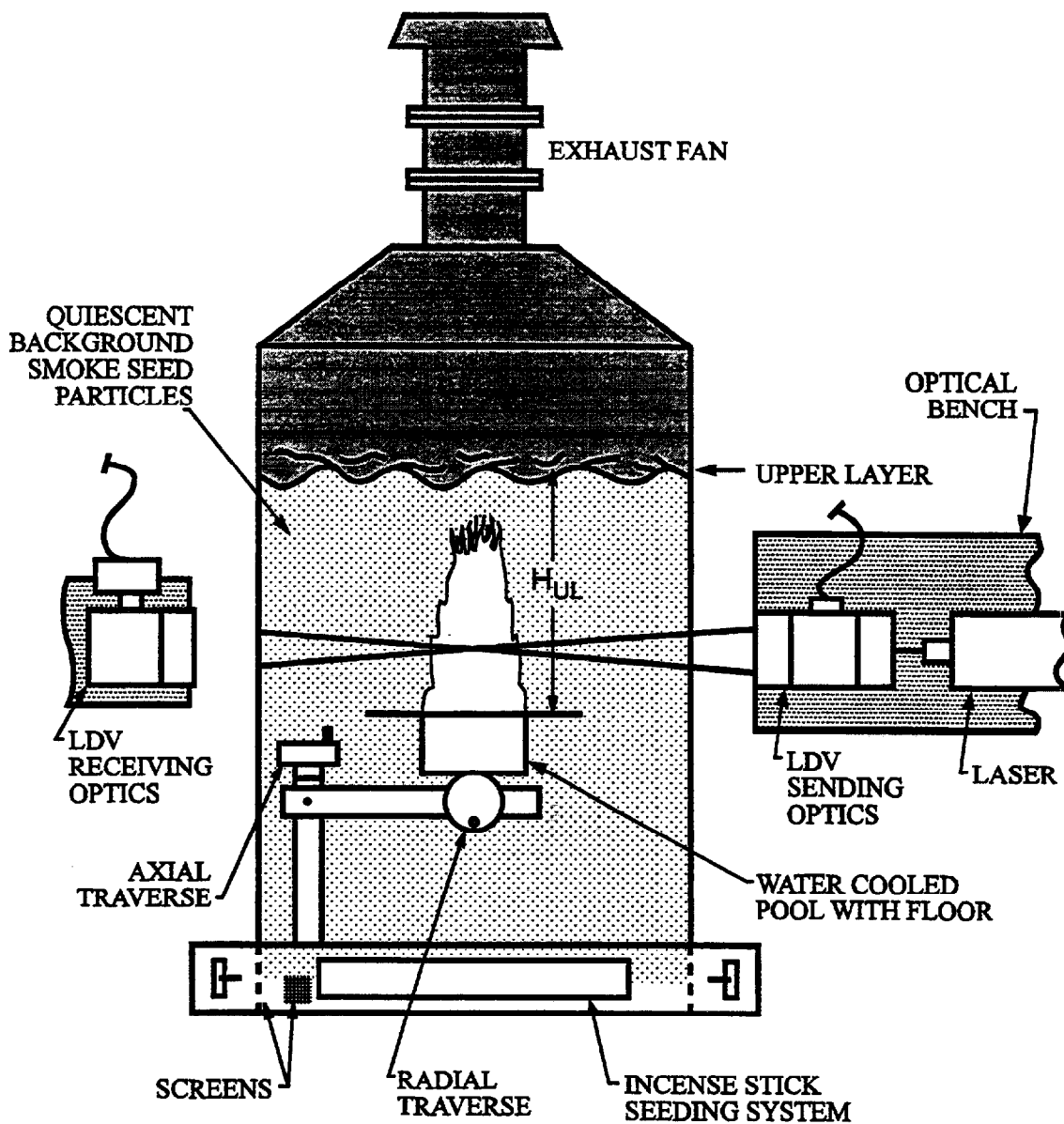


Figure 2.1 A sketch of the experimental apparatus for measuring fire-induced flow field velocities using LDV.

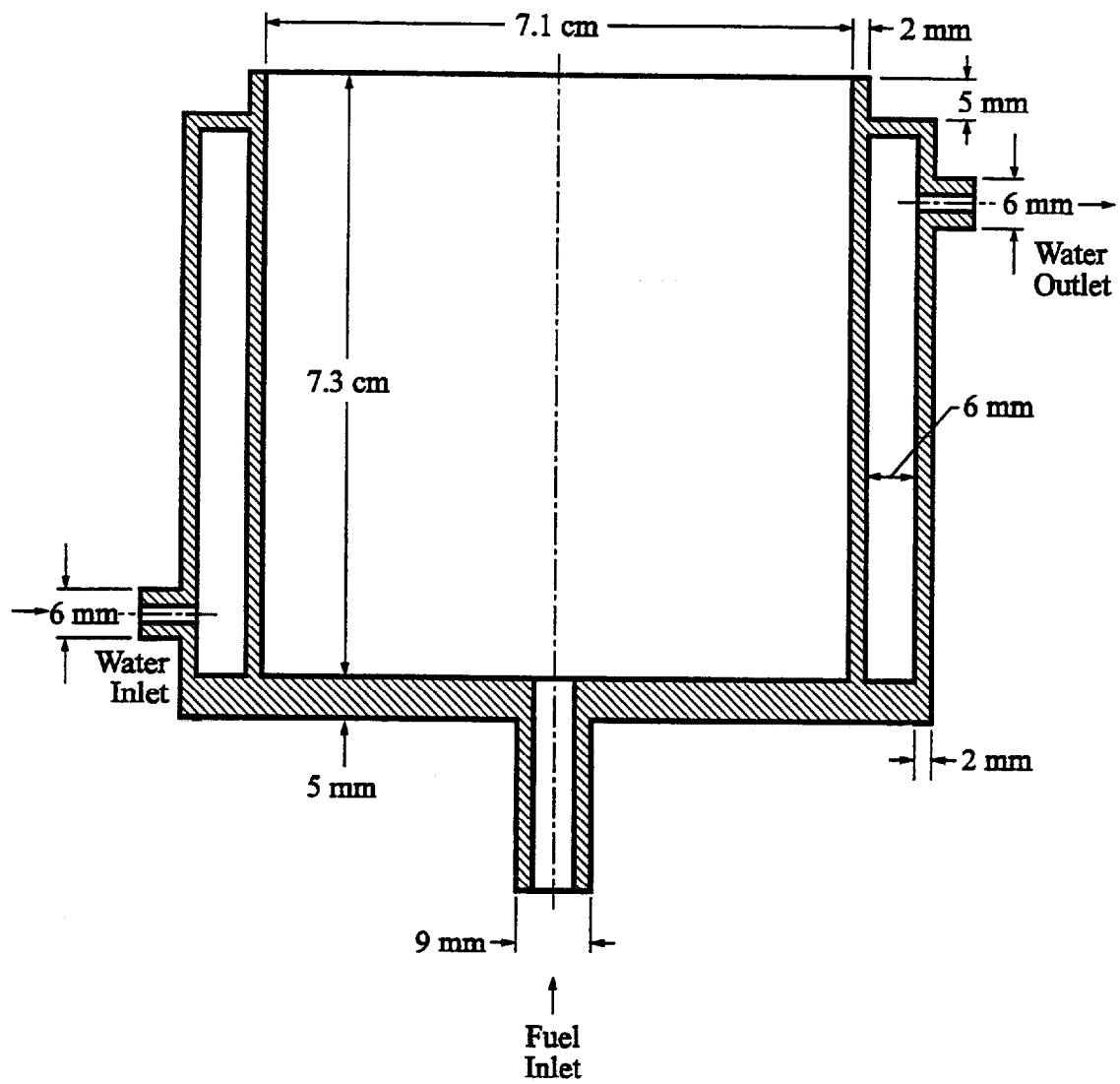


Figure 2.2 A schematic of the pool fire burner.

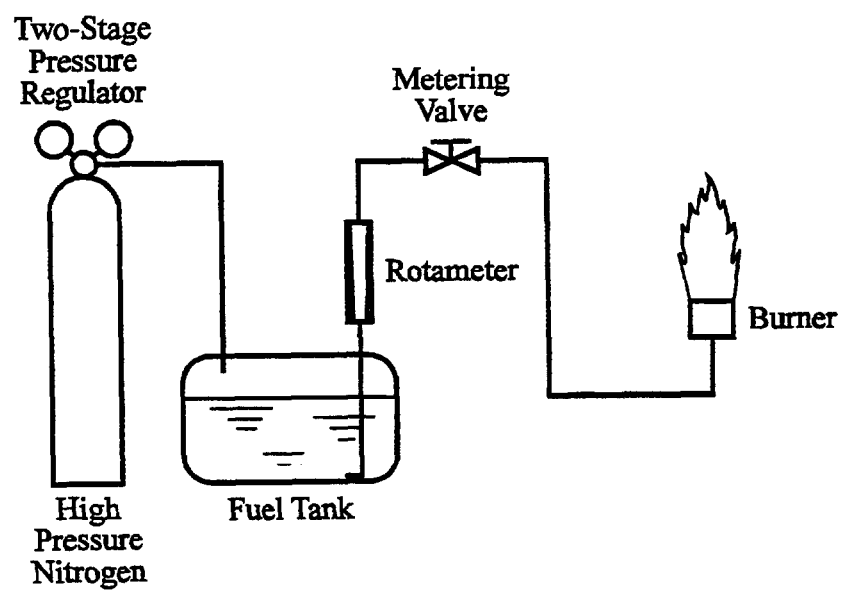


Figure 2.3 A sketch of the fuel supply system.

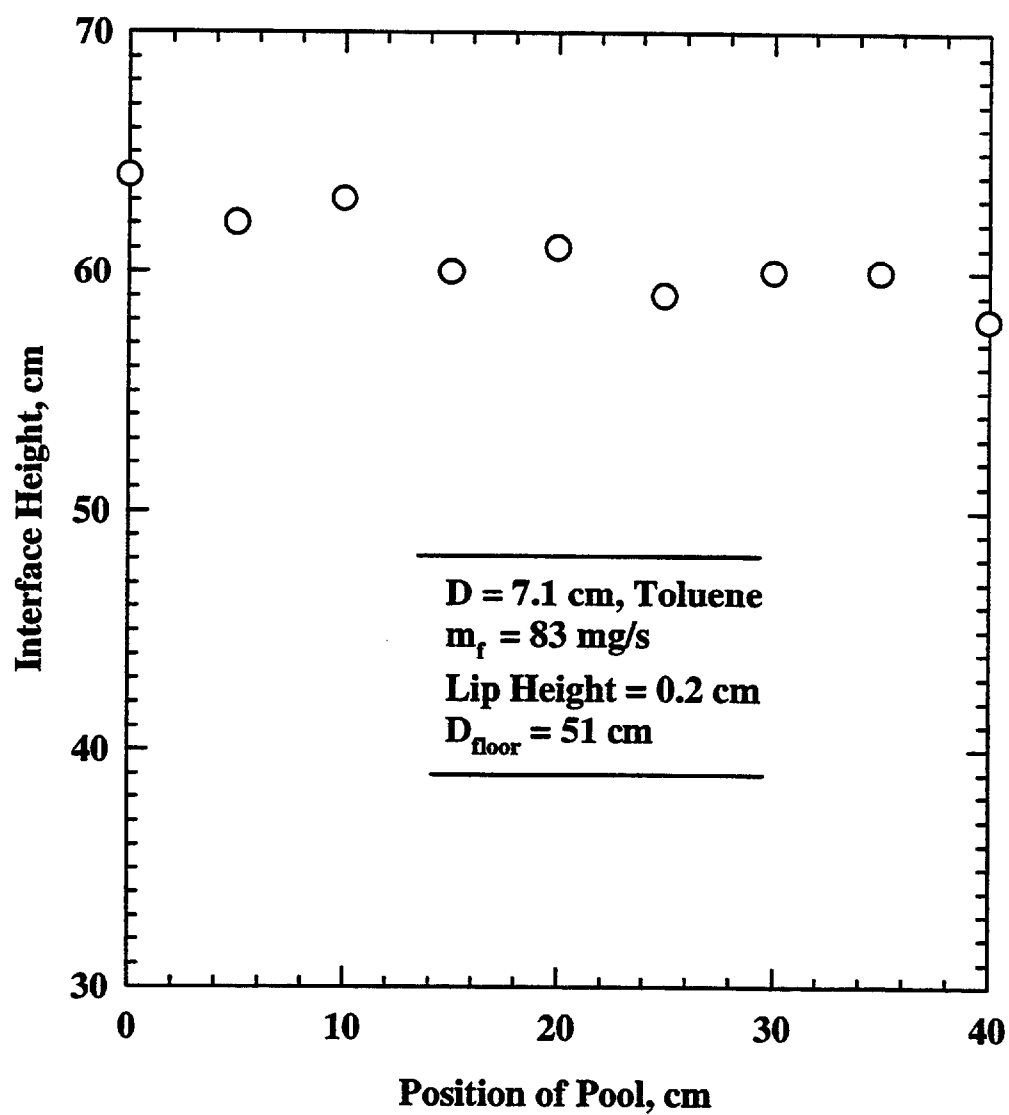


Figure 2.4 The change of interface height with pool position.

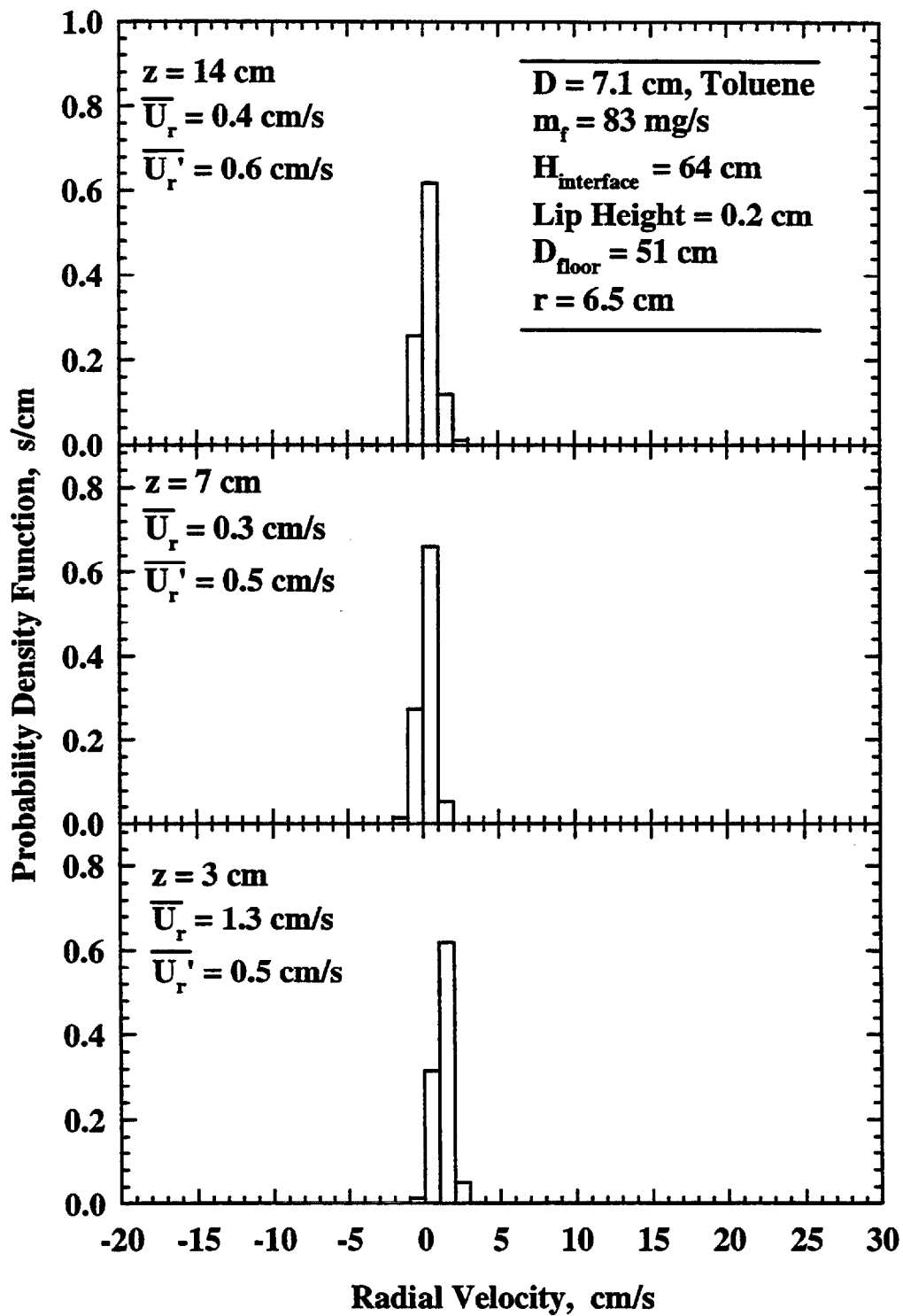


Figure 2.5 Discrete PDF of background radial velocity at three different heights at $r = 6.5$ cm.

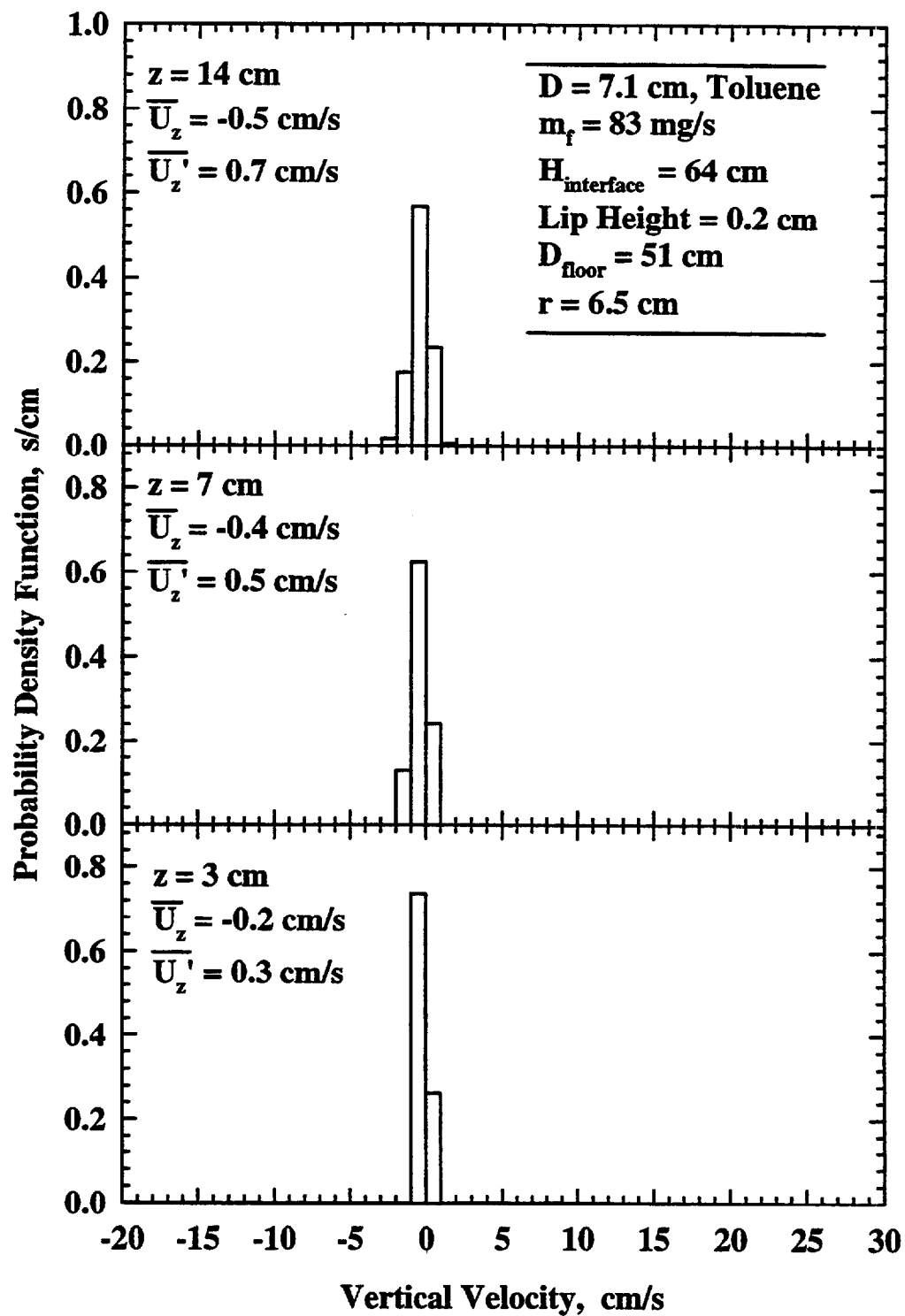


Figure 2.6 Discrete PDF of background vertical velocity at three different heights at $r = 6.5$ cm.

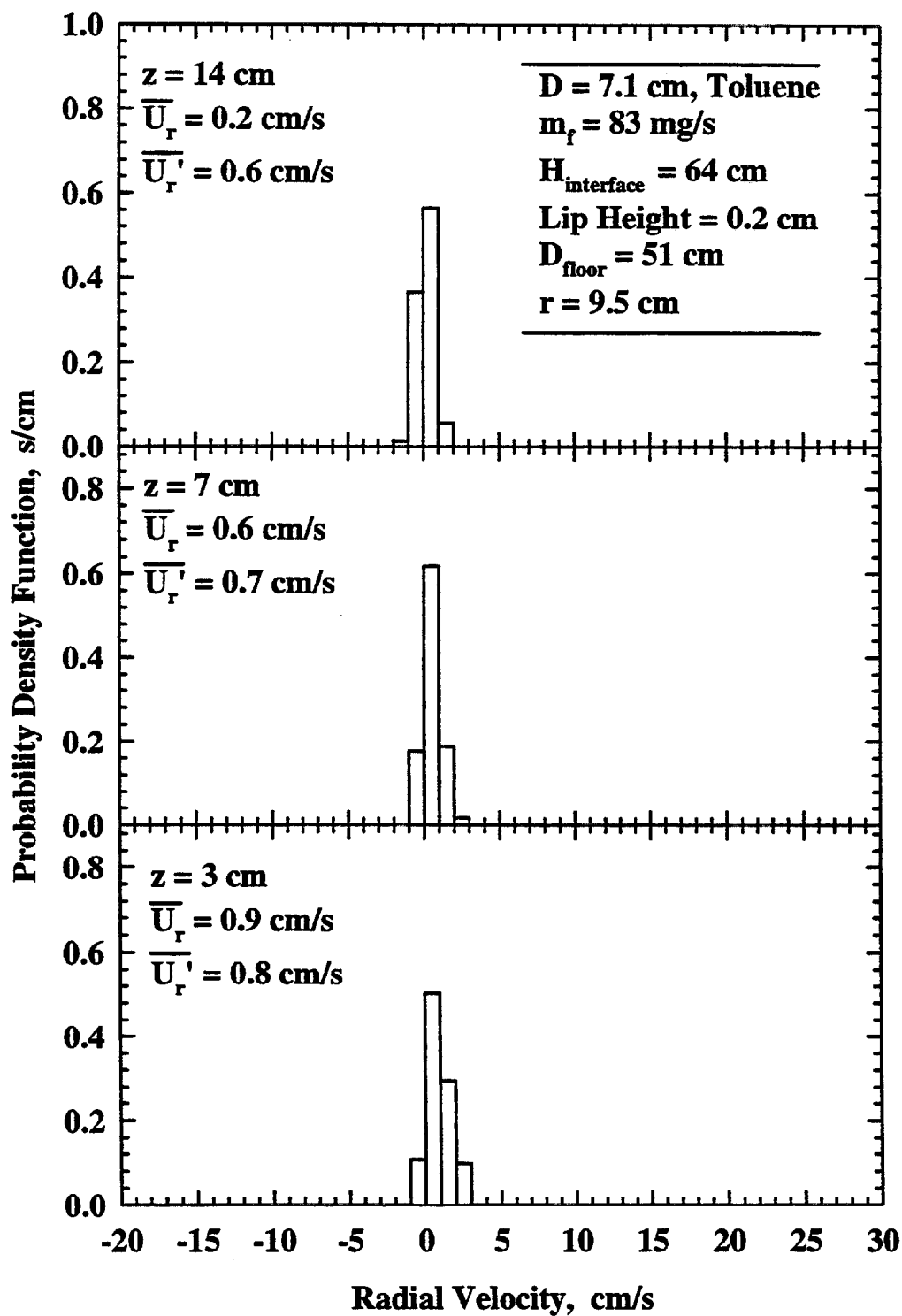


Figure 2.7 Discrete PDF of background radial velocity at three different heights at $r = 9.5$ cm.

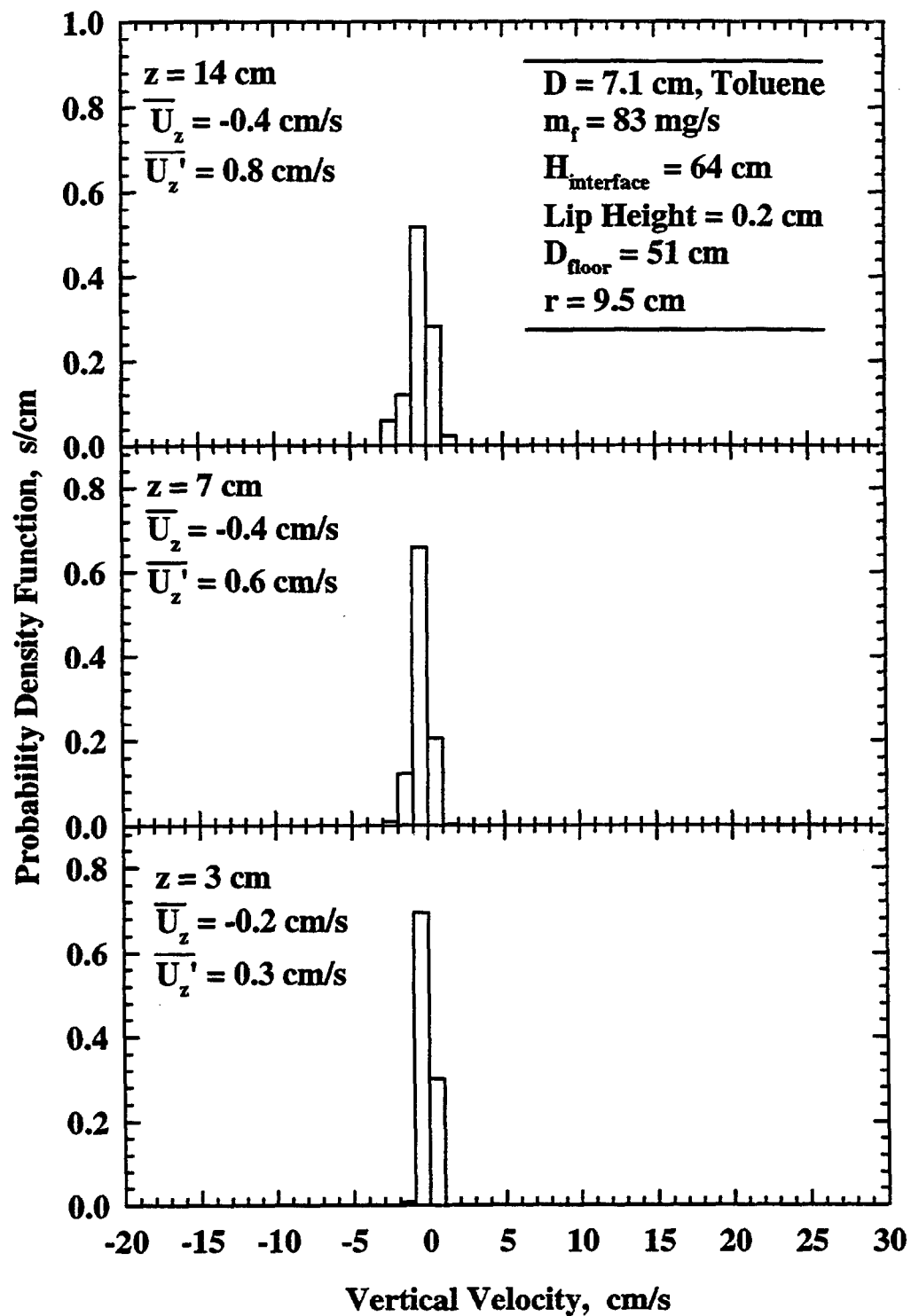


Figure 2.8 Discrete PDF of background vertical velocity at three different heights at $r = 9.5 \text{ cm}$.

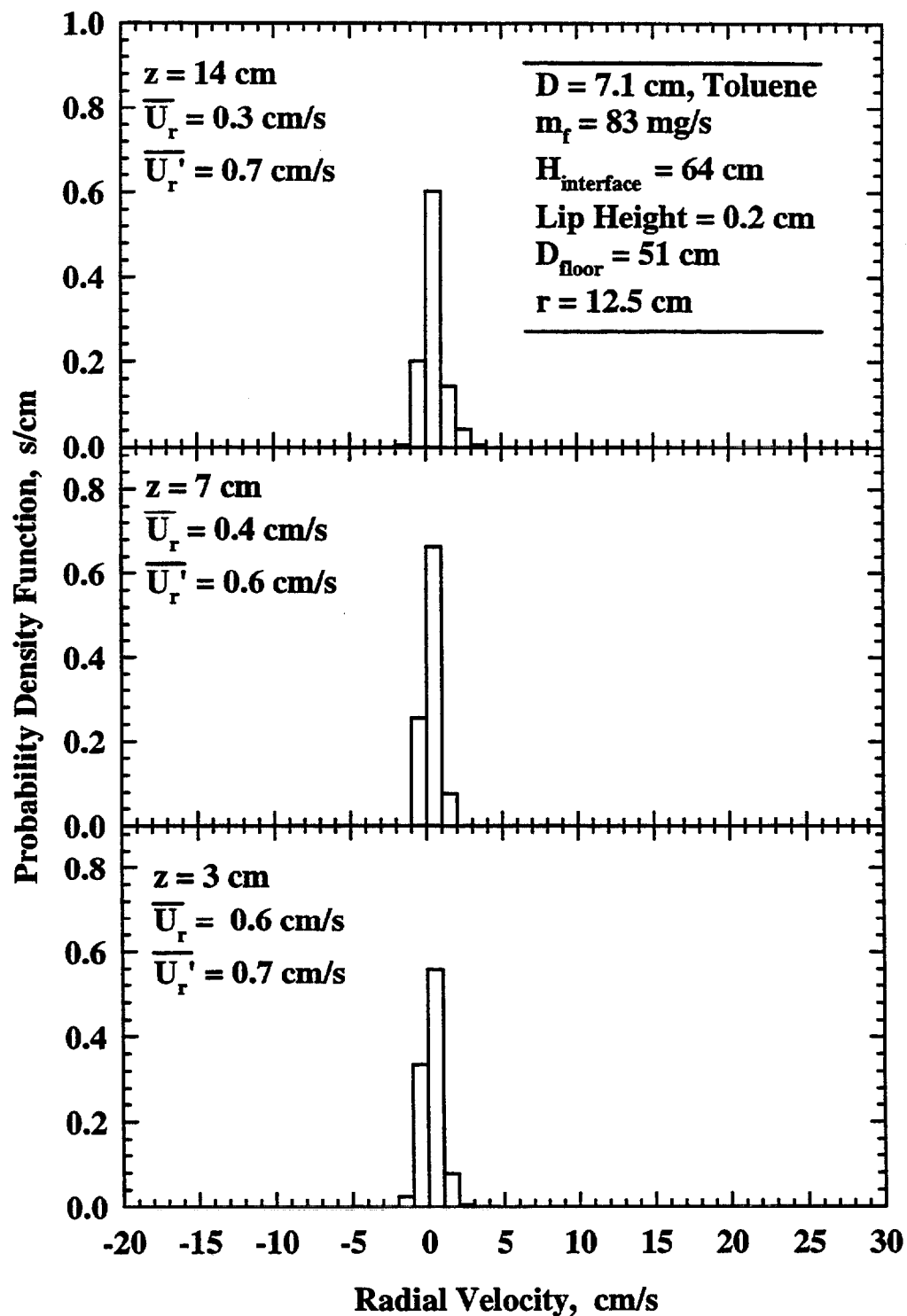


Figure 2.9 Discrete PDF of background radial velocity at three different heights at $r = 12.5$ cm.

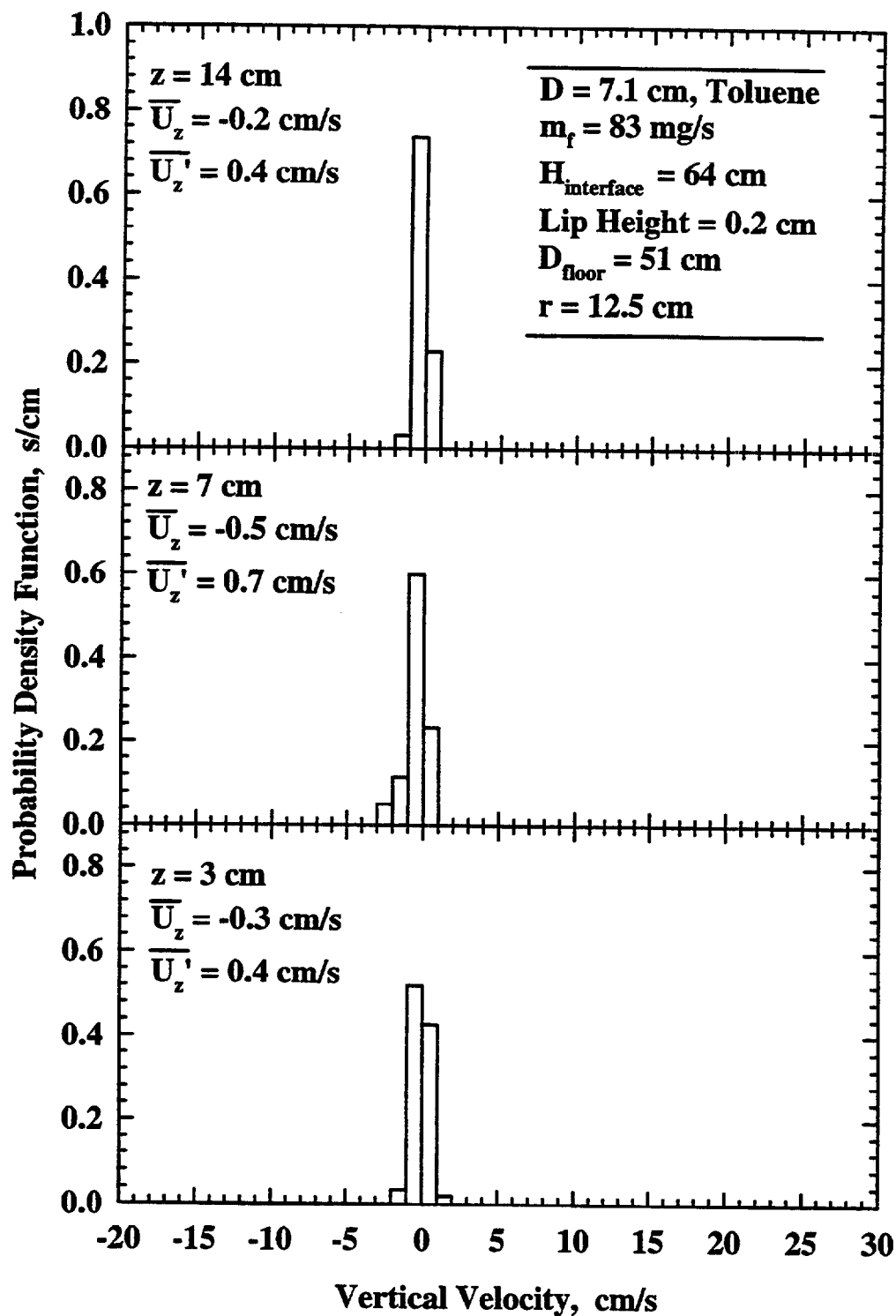


Figure 2.10 Discrete PDF of background vertical velocity at three different heights at $r = 12.5$ cm.

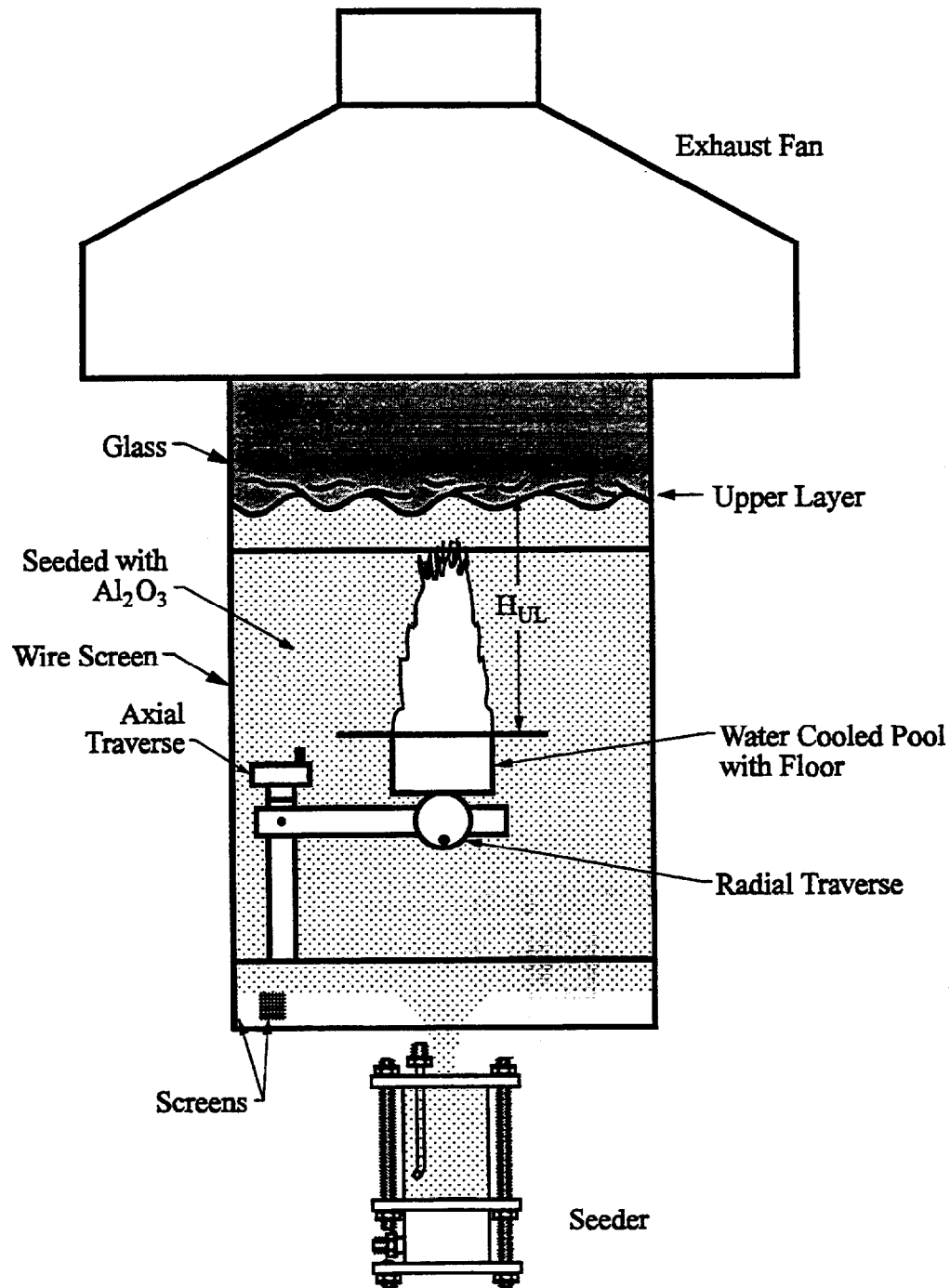


Figure 2.11 A schematic of the enclosure and seeding system used in PIV measurement of pool fire induced flow.

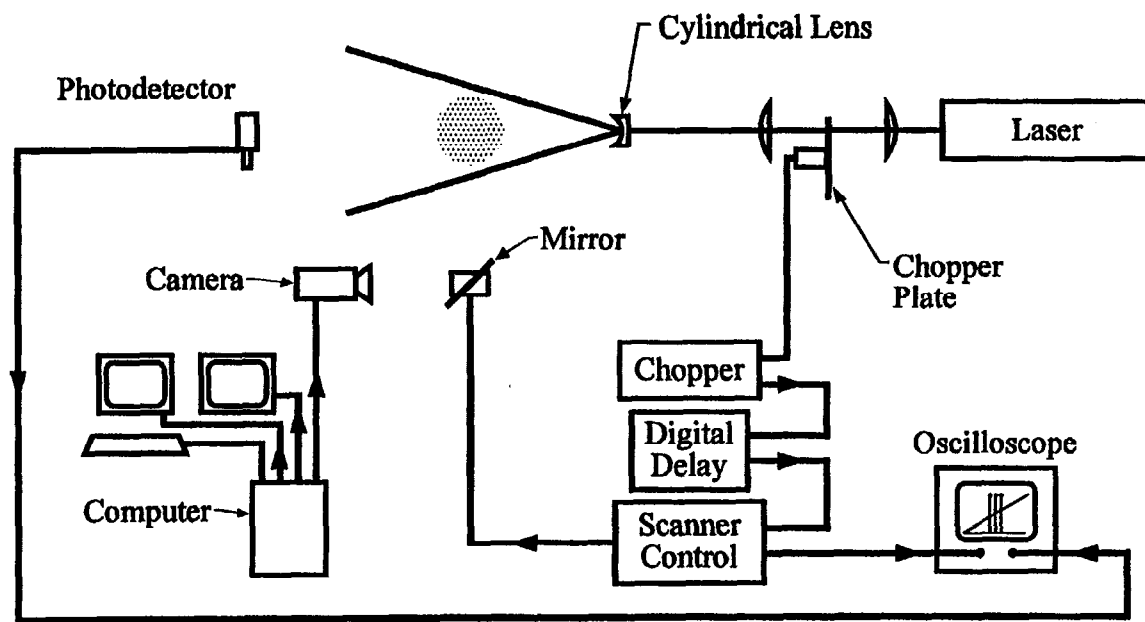


Figure 2.12 A sketch of the Particle Imaging Velocimetry (PIV) system.

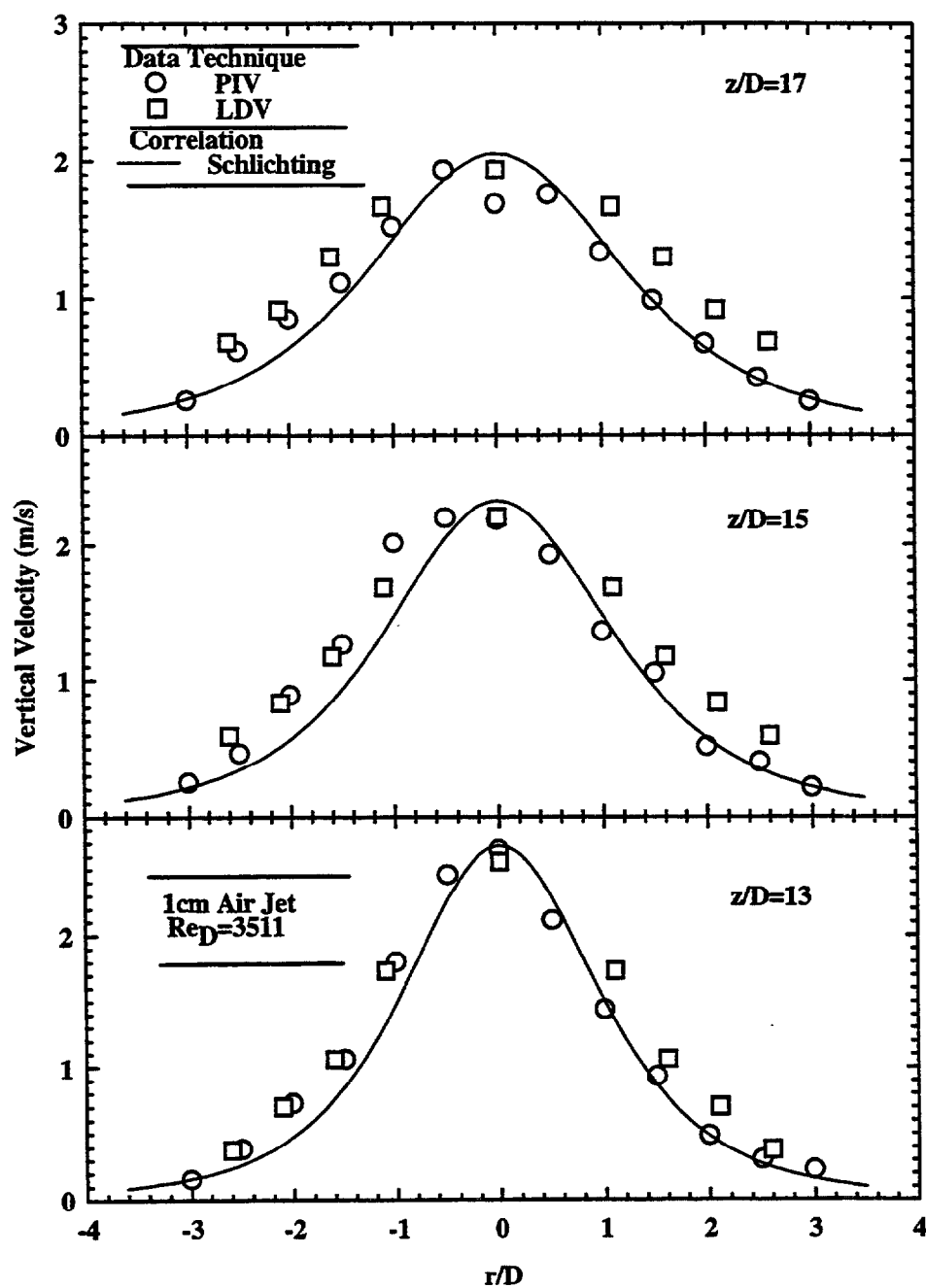


Figure 2.13 Measurements and prediction of the vertical velocity of an air jet as a function of radial location at three different heights.

CHAPTER 3 THEORETICAL METHOD

The existing correlations of entrainment by pool fires have large discrepancies regarding qualitative dependency on various parameters as well as quantitative values. Therefore, a more fundamental approach based on basic conservation laws is explored in the present work. The general treatment follows the work of Baum and McCaffrey (1988) with minor differences involving the treatment of boundary conditions. A numerical model to predict the mean flow pattern induced by buoyant diffusion flames is developed, based upon kinematic relationships between the velocity, the vorticity, and the heat release distribution. Neglect of viscous forces and thermal conduction effects is justified by the fact that even for small fires, the Grashof numbers, which represent the ratio of the inertial forces to viscous forces in natural convection, are large enough for molecular transport phenomena to be important only in wall boundary layers and in the highly convoluted flame sheets (Baum et al., 1983). Furthermore, the analyses are restricted to the resolution of large scale effects only. The governing equations are obtained by decomposing the flow field into its irrotational and incompressible components. The nonhomogeneous source terms in the partial differential equations governing these two components, namely the volumetric heat release rate distribution and the vorticity distribution, are estimated based on correlations of buoyant diffusion flame structure given by McCaffrey (1983). The boundary conditions on the outer edges of the computational domain for the irrotational flow equation are approximated by an asymptotic solution to the potential flow generated by a point source of heat with the same heat release rate as the pool fire, while the boundary conditions on the outer edges for the solenoidal flow are obtained by transforming the original governing equation into spherical coordinates and solving the resulting ordinary differential equation numerically.

The governing equations are discretized using a control volume method (Ramadhyani, 1995). The resulting system of simultaneous algebraic equations are solved by Gauss-Seidel iteration, and the solution process is accelerated by a multigrid scheme. The validity and the accuracy of the numerical model are tested by comparing the velocity predictions computed using domains and discretization grids of different sizes. In the following, the derivation of the equations is discussed. This is followed by a discussion of a model for the source terms involving use of an experimental data set concerning velocity and temperature distributions. The treatment of the boundary conditions is discussed next followed by a presentation of the numerical scheme and the tests for its accuracy and validity.

3.1 The Governing Differential Equations

The mean entrainment flow field $\bar{\mathbf{V}}$ induced by buoyant diffusion flames established on a circular burner is assumed to be axisymmetric without a swirling velocity component. For this reason, an axisymmetric cylindrical coordinate system is established, with its origin at the center of the fuel surface. The coordinate system and the computational domain are shown schematically in Fig. 3.1a (with a floor) and Fig. 3.1b (without a floor). Any flow field can be linearly decomposed into an irrotational component $\bar{\mathbf{V}}$ and an incompressible component $\tilde{\mathbf{V}}$ (Baum and McCaffrey, 1988; Batchelor, 1967):

$$\bar{\mathbf{V}} = \bar{\mathbf{V}} + \tilde{\mathbf{V}} \quad (3.1)$$

In order to automatically satisfy:

$$\nabla \times \bar{\mathbf{V}} = 0 \text{ (irrotational)} \quad (3.2)$$

$$\text{and} \quad \nabla \cdot \tilde{\mathbf{V}} = 0 \text{ (incompressible)} \quad (3.3)$$

in the axisymmetric cylindrical coordinate system used in this study, the irrotational velocity field and the incompressible velocity field can be defined in terms of a potential function ϕ and a stream function ψ as:

$$\bar{\nabla} = \frac{\partial \phi}{\partial z} \hat{e}_z + \frac{\partial \phi}{\partial r} \hat{e}_r \quad (3.4)$$

and

$$\bar{\nabla} = \frac{1}{r} \frac{\partial \psi}{\partial r} \hat{e}_z - \frac{1}{r} \frac{\partial \psi}{\partial z} \hat{e}_r \quad (3.5)$$

where \hat{e}_z and \hat{e}_r are the unit vectors in the axial and the radial directions.

The mass, momentum, and energy conservation equations and state equation for a low Mach number, variable density flow with negligible viscous effects are (Baum and McCaffrey, 1988):

$$\frac{D\rho}{Dt} + \rho \bar{\nabla} \cdot \bar{V} = 0 \quad (3.6a)$$

$$\rho \frac{D\bar{V}}{Dt} + \nabla \bar{P} - (\rho - \rho_\infty) \bar{g} = 0 \quad (3.6b)$$

$$\rho C_p \frac{DT}{Dt} = Q(\bar{r}) \quad (3.6c)$$

$$P_0 = \rho RT / W \quad (3.6d)$$

where ρ , \bar{V} , T , R , g and W are the local density, velocity vector, temperature, the universal gas constant, the gravitational acceleration, and the molecular weight of the mixture. $Q(\bar{r})$ is the volumetric heat release rate distribution in the flow field, defined as the rate at which heat is released by chemical reaction per unit volume per unit time. Stratification of the ambient air is not taken into consideration because of the limited height of the region of interest, and ρ_∞ , the density of the ambient air, is taken to be a constant. It is further assumed that for the low velocity flow, the thermodynamic pressure change in the entrainment flow field is insignificant, and that the molecular weight of the mixture remains constant, so that the only cause of the density change is the change in temperature. Thus, the state equation becomes:

$$\rho T = \rho_\infty T_\infty \quad (3.7)$$

where T_∞ is the room temperature. Substituting eq. (3.6d) into eq. (3.6c) gives:

$$\rho C_p \frac{D\left(\frac{P_0 W}{\rho R}\right)}{Dt} = Q(\bar{r}) \quad (3.8)$$

Expanding the material derivative in eq. (3.8) yields:

$$-C_p \frac{D\rho}{Dt} = \frac{Q(\vec{r})R\rho}{P_0 W} \quad (3.9)$$

Multiplying eq. (3.6a) by specific heat and adding the resulting equation to eq. (eq. 3.9) yields:

$$\nabla \cdot \vec{V} = \frac{Q(\vec{r})}{\rho C_p T} \quad (3.10)$$

Using eq. (3.7), the above equation can be rewritten as:

$$\nabla \cdot \vec{V} = \frac{Q(\vec{r})}{\rho_\infty C_p T_\infty} \quad (3.11)$$

Substituting eq. (3.1) into eq. (3.11) and applying eq. (3.3) yields the governing differential equation for the irrotational flow field as:

$$\nabla \cdot \vec{V} = \frac{Q(\vec{r})}{\rho_\infty C_p T_\infty} \quad (3.12)$$

The physical meaning of eq. (3.12) is that the volumetric expansion rate of any fluid element, $\nabla \cdot \vec{V}$, is proportional to the net rate of heat addition by chemical reaction into the region occupied by that fluid element. It should be noted that although $Q(\vec{r})$ is nonzero only inside the flame, eq. (3.12) holds everywhere in the flow field, with $Q(\vec{r})$ being zero outside the flame.

According to its definition, the vorticity of any fluid element is the curl of its velocity vector (Currie, 1989). Hence

$$\nabla \times \vec{V} = \vec{\omega}(\vec{r}) \quad (3.13)$$

where $\vec{\omega}(\vec{r})$ is the vorticity. Following Baum and McCaffrey (1988), the Curl of the momentum equation is taken and the resulting vorticity transport equation is integrated over a closed loop to yield:

$$\frac{D}{Dt} \oint \vec{\omega} \cdot \vec{n} dA = \frac{D\Gamma}{Dt} = \oint \left(\frac{(\rho - \rho_\infty)\vec{g}}{\rho} - \frac{\nabla \tilde{P}}{\rho} \right) d\vec{r}$$

According to the above equation and Panton (1984), vorticity can be created in an inviscid flow away from a solid boundary through the mechanism of density gradient. When there is a density gradient in the flow, the center of mass of a fluid element, also the gravitational center, does not coincide with its geometric center, through which the pressure acts. The gravitational force and the pressure force are not aligned with each other and this unbalance rotates the fluid element, generating vorticity. As an element of air is drawn from the ambient towards the flame, it contains no vorticity. Upon entering the flame, it encounters a steep density gradient caused by a large temperature change, and an intense vortex sheet shrouding the flame is created (Baum and McCaffrey, 1988). The only nonzero component of vorticity is in the azimuthal direction because the flow field is axisymmetric. For these reasons and using eqs. (3.1) and (3.2), eq. (3.13) can be rewritten as (Baum and McCaffrey, 1988):

$$\nabla \times \tilde{\mathbf{V}} = \omega_p(\tilde{\mathbf{r}}) \quad (3.14)$$

where $\omega_p(\tilde{\mathbf{r}})$ is the azimuthal vorticity distribution within the plume. Similar to eq. (3.12), eq. (3.14) holds throughout the flow field although the vorticity is nonzero only in the region with a density gradient. Equation (3.14) is derived from the momentum equation and satisfies it accurately as long as an accurate description of the vorticity source term can be provided.

Substituting $\tilde{\mathbf{V}}$ in eq. (3.12) using eq. (3.4) gives the differential equation governing the irrotational flow in terms of the potential function ϕ as:

$$\frac{\partial^2 \phi}{\partial z^2} + \frac{1}{r} \frac{\partial}{\partial r} \left(r \frac{\partial \phi}{\partial r} \right) = \frac{Q(\tilde{\mathbf{r}})}{\rho_\infty C_p T_\infty} \quad (3.15)$$

Substituting $\tilde{\mathbf{V}}$ in eq. (3.14) using eq. (3.5) gives the differential equation governing the incompressible flow in terms of the stream function ψ as:

$$\frac{\partial^2 \psi}{\partial z^2} + \frac{\partial^2 \psi}{\partial r^2} - \frac{1}{r} \frac{\partial \psi}{\partial r} = -r \omega_p(\tilde{\mathbf{r}}) \quad (3.16)$$

3.2 The Heat Release Rate Distribution and the Vorticity Field inside the Flame

In order to solve eqs. (3.15) and (3.16), the source terms in the equations, $Q(\bar{r})$ and $\omega_p(\bar{r})$, have to be evaluated first. Since heat release and vorticity generation occur only inside the flame, knowledge of the flame structure is required for this evaluation. The flame structure correlations of McCaffrey (1983) are used in this work following Baum and McCaffrey (1988).

Before analyzing the flame structure correlations to obtain the volumetric heat release rate distribution and the vorticity generation field, it is useful to examine the flame appearance. The buoyant diffusion flames are usually distinctively divided into three regions along the axial direction (McCaffrey, 1983). At the bottom, there is a continuous flame region, where there is always combustion occurring in anchored flame sheets. However, the flame is not necessarily steady. The flame shape changes periodically as lumps of ambient air enter the flame and erupt into large scale structure. As a consequence of the pulsating effect of the continuous flame, some patches of flame break away, marking the beginning of the intermittent region. In this region, the convective energy, $H(z)$, approximately remains unchanged as heat release from combustion just compensates for radiation heat loss. $H(z)$ is the energy convected through a cross section of the fire per unit time. Above the intermittent region is the plume region where combustion has ceased entirely and $H(z)$ decreases very slowly due to energy loss by radiation. McCaffrey (1983) provided correlations for the centerline velocity and centerline excess temperatures for each of the three regions. The correlations, given in eq. (3.17a) and (3.17b) in the original dimensionless form, depend on dimensionless heights only. The general form for all three regions is identical with the coefficients and exponents given in Table 3.1.

$$U^*(Z^*) = A(Z^*)^n \quad (3.17a)$$

$$\Theta = \frac{T - T_\infty}{T_\infty} = B(Z^*)^{2n-1} \quad (3.17b)$$

The length and velocity scales used for obtaining nondimensional distance Z^* and velocity U^* are:

$$\text{Length: } L_d = \left(\frac{Q_0}{\rho_\infty c_p T_\infty \sqrt{g}} \right)^{2/5} \quad (3.18)$$

$$\text{Velocity: } U_d = \sqrt{gL_d} \quad (3.19)$$

where Q_0 is the total heat release rate, $Z^* = Z/L_d$, and $U^* = U/U_d$.

Table 3.1 Parameters of the correlations of buoyant diffusion flame structure

Region	Range of Z^*	n	A	B
Continuous	[0, 1.32]	1/2	2.18	2.91
Intermittent	[1.32, 3.30]	0	2.45	3.81
Plume	[3.30,]	-1/3	3.64	8.41

McCaffrey also hypothesized that both excess temperature and velocity radial profiles are Gaussian. However, the width of the temperature profile is smaller than the width of the velocity profile. The ratio of these widths is denoted as ξ . According to a Gaussian radial distribution, the velocity and excess temperature profiles are:

$$U_z = U(z) \exp\{-[r/R(z)]^2\} \quad (3.20)$$

$$\frac{T - T_\infty}{T_\infty} = \Theta(z) \exp\{-[r/\xi R(z)]^2\} \quad (3.21)$$

where $U(z)$ is the centerline axial velocity as a function of z , and U_z is the axial component of the velocity at each point in the flow field. $R(z)$ is the radius at which the velocity decreases to e^{-1} of its centerline value and is called the “flame radius” by McCaffrey (1983). The radius of the flame $R(z)$ is approximated to be a constant in the continuous flaming region (Baum and McCaffrey, 1988). In the intermittent and plume regions, $R(z)$ is evaluated from a balance of energy assuming that all the combustion is over in the continuous flame region.

$H(z)$ increases with height in the continuous flame region (Baum and McCaffrey, 1988). It can be evaluated using McCaffrey’s correlations as:

$$\begin{aligned}
H(z) &= \int_0^\infty 2\pi\rho U_z (T - T_\infty) C_p r dr \\
&= 2\pi C_p \int_0^\infty \frac{\rho_\infty T_\infty}{T_\infty + (T - T_\infty)} (T - T_\infty) U_z r dr \\
&= \pi C_p \rho_\infty T_\infty R^2(z) U(z) [1 - I_\xi(\Theta)]
\end{aligned} \tag{3.22}$$

where

$$I_\xi(\Theta) = \int_0^1 \frac{dt}{1 + \Theta t^{1/(\xi^* \xi)}} \tag{3.23}$$

In the intermittent and plume regions, $H(z)$ is a constant equal to the total chemical heat release rate minus the fraction that has been radiated away, thus:

$$H(z) = Q_0(1 - X_R) = \pi C_p \rho_\infty T_\infty R^2(z) U(z) [1 - I_\xi(\Theta)] \tag{3.24}$$

where X_R is the radiative heat loss fraction. A little manipulation yields the flame radius as a function of height z in the plume region:

$$R(z) = \left\{ \frac{1 - X_R}{\pi U^*(Z^*) [1 - I_\xi(\Theta)]} \right\}^{1/2} L_d \tag{3.25}$$

In the present study, the model discussed above for the flame radius is used as a first step. However, it was discovered that based on visible flame shapes and comparison between measurements and predictions of entrainment velocities, the model is not appropriate for the present 7.1 cm diameter pool fires. Hence, $R(z)$ based on visible flame shape was also used as an improvement.

The volumetric heat release rate distribution is assumed to have a Gaussian profile following Baum and McCaffrey (1988):

$$Q(\bar{r}) = Q(z) \exp\{-[r / R(z)]^2\} \tag{3.26a}$$

where $Q(z)$ is the volumetric heat release rate along the axis at height z . Using the definitions of $H(z)$ and the volumetric heat release rate, it can be shown that

$$\frac{\Delta H(z)}{\Delta z} = \int_0^\infty 2\pi Q(\bar{r}) (1 - X_R) r dr \tag{3.26b}$$

Substituting eq. (3.26a) into eq. (3.26b) for $Q(\bar{r})$:

$$Q(z) = \frac{\Delta H(z)}{\Delta z} \frac{1}{\pi(1 - X_R)R^2(z)}$$

Substituting $Q(z)$ into eq. (3.26a) yields:

$$Q(\bar{r}) = \frac{\Delta H(z)}{\Delta z} \frac{\exp\{-[r/R(z)]^2\}}{\pi(1 - X_R)R^2(z)} \quad (3.27)$$

Neglecting the component caused by the change of radial velocity in the axial direction, the azimuthal vorticity field is approximately:

$$\omega_p(\bar{r}) = -\frac{\partial U_z}{\partial r} = \frac{2U(z)}{R(z)} \left\{ \frac{r}{R(z)} \exp\{-[r/R(z)]^2\} \right\} \quad (3.28)$$

Equations (3.27) and (3.28) define the volumetric heat release rate distribution and the vorticity distribution for the fire. The error in the vorticity source term caused by this neglect of the radial velocity gradient decreases rapidly with height. It is 50% at $z = 1$ cm and 10% at $z=4$ cm based on the present data for the 7.1 cm toluene fire.

Since these correlations involve numerical integration and dependence on radial and axial coordinates, values of key parameters are plotted to illustrate the flame structure. Figure 3.2 shows a graph of flame radius $R(z)$ as a function of height above the fuel surface according to the correlations. Figure 3.3 shows the source term for vorticity (eq. 3.28) resulting from this flame shape and the velocity distribution given by eqs. (3.17a) and (3.20). Radial distribution of the vorticity source term at a single representative axial location in the continuous flame zone, the intermittent flame zone, and the plume region are shown. As seen from Fig. 3.3, the azimuthal vorticity has a positive value indicating a direction of rotation away from the axis at the top of the vortex. The vorticity in the continuous flame region has a smaller magnitude than that in the plume region. The highest magnitude of vorticity occurs in the intermittent region. This is due to the large values of $U(z)$ in the intermittent region. The dependence of

vorticity on $U(z)$ is stronger than that on $R(z)$. $U(z)$ decreases in the plume region (Baum and McCaffrey, 1988). Figure 3.4 shows the volumetric heat release rate as a function of radial position at the beginning and the end of the continuous flame zone. The volumetric heat release rate distributions in the intermittent flame zone and in the plume region are zero except for some roundoff errors in the evaluation. Thus the volumetric expansion originates primarily in the continuous flame zone.

In order to solve the problem in a dimensionless form, additional scaling parameters are introduced as follows (Baum and McCaffrey, 1988):

$$\text{Vorticity: } \Omega_d = \sqrt{g/L_d} \quad (3.29)$$

$$\text{Volumetric Heat Release Rate: } Q_d = Q_0 / L_d^3 \quad (3.30)$$

$$\text{Stream Function: } \Psi_d = \sqrt{gL_d^3} \quad (3.31)$$

$$\text{Potential Function: } \Phi_d = \sqrt{gL_d^3} \quad (3.32)$$

Nondimensionalizing the governing differential equations (eqs. (3.15) and (3.16)) with the scaling parameters defined in eqs. (3.18-3.19) and (3.29 - 3.32), these can be transformed into nondimensional form as (Baum and McCaffrey, 1988):

$$\frac{\partial^2 \phi}{\partial z^2} + \frac{1}{r} \frac{\partial}{\partial r} \left(r \frac{\partial \phi}{\partial r} \right) = Q(\bar{r}) \quad (3.33)$$

$$\frac{\partial^2 \psi}{\partial z^2} + \frac{\partial^2 \psi}{\partial r^2} - \frac{1}{r} \frac{\partial \psi}{\partial r} = -r\omega_p(\bar{r}) \quad (3.34)$$

where all the variables in eqs. (3.33) and (3.34) are the dimensionless counterparts of those designated with identical symbols in the discussion prior to eq. (3.33).

3.3 Boundary Conditions

When there is a floor around the fire, the velocity component normal to the floor is zero in both the irrotational velocity field and the incompressible velocity field. Thus the gradient of the velocity potential in the z direction is zero, and the stream function is constant along the floor. The velocity potential function can be understood as the driving force for the flow. In a uniform potential field, there is no fluid flow. In a nonuniform potential field, the velocity is along the gradient of the potential. The stream function is constant along a streamline, which is defined as a curve in the flow field to which the local velocity vector is tangent at all points. The flow rate between two streamlines is a constant; hence, the flow velocity is inversely proportional to the distance between two streamlines. The incompressible velocity is equal to the gradient of the stream function in magnitude, but in a direction normal to that of the gradient.

Along the centerline of the flame, because of axisymmetry, there is no radial velocity, hence the gradient of the velocity potential in the r direction is zero, and the stream function is constant along the centerline. Without loss of generality, the values of the stream function along the floor and along the centerline are taken to be zero.

Referring to Fig. 3.1a:

$$\frac{\partial \phi}{\partial z} = 0, \quad \psi = 0, \quad \text{at } z=0 \text{ for all } r \quad (3.35a)$$

$$\frac{\partial \phi}{\partial r} = 0, \quad \psi = 0, \quad \text{at } r=0 \text{ for all } z \quad (3.35b)$$

When there is no floor around the pool fire, because of axisymmetry of velocity along the pool axis, both the radial derivatives of potential function and the values of the stream function along the centerline are zero. Referring to Fig. 3.1b:

$$\frac{\partial \phi}{\partial r} = 0, \quad \psi = 0, \quad \text{at } r=0 \text{ for all } z \quad (3.36)$$

The boundary conditions for the velocity potential at the outer edge of the computational domain are taken to be equal to those of a potential flow caused by a point heat source of equivalent normalized strength $(1 - X_R)$, where X_R is the radiative loss

fraction. The solution to this problem is found in Baum and McCaffrey (1988) and Sneddon (1957). When there is a floor around the pool fire, the potential function in this field is described by

$$\phi = \frac{1 - X_R}{2\pi\sqrt{r^2 + z^2}} \quad (3.37a)$$

In the absence of the floor, the potential function is half that of the value with the floor:

$$\phi = \frac{1 - X_R}{4\pi\sqrt{r^2 + z^2}} \quad (3.37b)$$

The boundary values of the stream function are obtained by transforming eq. (3.34) into an ordinary differential equation in a spherical coordinate system, following Baum and McCaffrey (1988). The axisymmetric spherical coordinate system is also shown in Fig. 3.1a. Substituting:

$$\psi = \zeta^{5/3} F(\mu) \quad (3.38)$$

where $\zeta = \sqrt{r^2 + z^2}$, $\mu = \cos \theta$, and θ is the polar angle, into eq. (3.34) yields:

$$\frac{d^2 F}{d\mu^2} + \frac{10F}{9(1 - \mu^2)} = \Omega(\mu) \quad (3.39)$$

where $\Omega(\mu)$ is the vorticity in the far field, which is obtained by substituting eq. (3.25) into eq. (3.28) and making the necessary transformation. At the floor, μ is equal to zero and along the centerline, μ is equal to unity. The stream function is zero at both locations according to eqs. (3.35a) and (3.35b); hence, the boundary conditions for eq. (3.39) are:

$$F(0) = F(1) = 0 \quad (3.40a)$$

To solve eq. (3.39), the second order derivative in the equation is approximated by central finite differencing and the resulting discretization equation is solved numerically using a Tri-Diagonal Matrix Algorithm (TDMA) subject to boundary conditions represented by eq. (3.40) to obtain a value of $F(\mu)$. The boundary values of the stream function ψ are then evaluated using eq. (3.38).

In the absence of a floor around the pool fire, the boundary conditions for eq. (3.39) change to

$$F(-1) = F(1) = 0 \quad (3.40b)$$

3.4 Numerical Scheme

Implementation of the numerical solution for the governing equations is discussed first, followed by a test of the validity of the numerical model by comparing the results computed on domains of different sizes or different grid spacings. The velocity profiles along constant r and z are explained in terms of the irrotational and the incompressible velocity components.

3.4.1 Numerical Solution

The two elliptic partial differential equations, eqs. (3.33) and (3.34), are solved numerically using a control volume method. The control volume method involves deploying the control surfaces across the computational domain first and then putting the node points midway between neighboring control surfaces (Ramadhyani, 1995). Designation of the control volume surfaces and the grid points, which can greatly facilitate subsequent programming if done carefully, is shown in Fig. 3.5. Attention is paid to the boundaries to take full advantage of the control volume method. A typical control volume element and its neighboring grid points in the discretized computational domain are shown in Fig. 3.6 for a uniform mesh with grid spacings Δr and Δz , in the radial and the axial directions. Integrating eq. (3.33) over the control volume at a grid point P in cylindrical coordinates:

$$\int_s^n \int_e^w \left\{ \frac{\partial^2 \phi}{\partial z^2} + \frac{1}{r} \frac{\partial}{\partial r} \left(r \frac{\partial \phi}{\partial r} \right) \right\} = Q(\bar{r}) \quad (3.41)$$

Assuming constant properties on each surface of the control volume element, the integration can be carried out to obtain:

$$\frac{r_e^2 - r_w^2}{2} \left(\frac{\partial \phi}{\partial z} \Big|_n - \frac{\partial \phi}{\partial z} \Big|_s \right) + \left(r \frac{\partial \phi}{\partial r} \Big|_e - r \frac{\partial \phi}{\partial r} \Big|_w \right) \Delta z_p = Q(\bar{r}) \left(\frac{r_e^2 - r_w^2}{2} \right) \Delta z_p \quad (3.42)$$

Approximating the properties at the control surface by linear interpolation between neighboring nodes, and the derivatives at the control surface with a linear profile, the above equation is changed into an algebraic equation:

$$a_P \phi_P = a_E \phi_E + a_W \phi_W + a_N \phi_N + a_S \phi_S + d_P \quad (3.43a)$$

$$\text{where: } a_E = \Delta z \left(\frac{r_e}{\Delta r_e} \right) \quad (3.43b)$$

$$a_W = \Delta z \left(\frac{r_w}{\Delta r_w} \right) \quad (3.43c)$$

$$a_N = \frac{r_e^2 - r_w^2}{2} \frac{1}{\Delta z_n} \quad (3.43d)$$

$$a_S = \frac{r_e^2 - r_w^2}{2} \frac{1}{\Delta z_s} \quad (3.43e)$$

$$a_P = a_E + a_W + a_N + a_S \quad (3.43f)$$

and the numerical source term:

$$d_P = Q(\bar{r}) \left(\frac{r_e^2 - r_w^2}{2} \right) \Delta z. \quad (3.43g)$$

The capital subscripts E, W, N and S designate the four neighboring grid points, while the lower case subscripts e, w, n, and s denote the four surfaces of the control volume at the point P.

In a similar manner, the stream function equation, eq. (3.34) is discretized to obtain an approximate algebraic equation:

$$a_P \psi_P = a_E \psi_E + a_W \psi_W + a_N \psi_N + a_S \psi_S + d_P \quad (3.44a)$$

where the coefficients are

$$a_E = \Delta z \left(\frac{r_e}{\Delta r_e} - 1 \right) \quad (3.44b)$$

$$a_W = \Delta z \left(\frac{r_w}{\Delta r_w} - 1 \right) \quad (3.44c)$$

$$a_N = \frac{r_e^2 - r_w^2}{2} \frac{1}{\Delta z_n} \quad (3.44d)$$

$$a_S = \frac{r_e^2 - r_w^2}{2} \frac{1}{\Delta z_s} \quad (3.44e)$$

$$a_P = a_E + a_W + a_N + a_S \quad (3.44f)$$

$$\text{and } d_P = \omega_P(\bar{r}) \left(\frac{r_e^3 - r_w^3}{3} \right) \Delta z \quad (3.44g)$$

Equations (3.43) and (3.44) can be solved directly by Gauss-Seidel iteration to get the potential function field and the stream function field. However, due to the large number (at least 200×400) of grid points necessary to cover the large dimensions needed for applying the point source based boundary, convergence can be very slow. To alleviate this problem, a multigrid scheme is applied to accelerate the propagation of information.

3.4.2 Multigrid Scheme for Accelerated Solution

The principle of the multigrid scheme is to iterate over a coarse grid (with fewer grid points) to obtain a correction value for the properties over the fine grids in each coarse grid block. As shown in Fig. 3.7, each coarse control volume contains 5 × 5 fine grid control volumes in the present multigrid scheme. With the coarse grid, the information at the boundaries transfers at a faster rate into the interior region of the computational domain. After adding the correction term for each coarse grid block to the solutions of the fine grid points within that coarse block, a Gauss-Seidel iteration is performed on the fine grids to refine the solution. Multigrid acceleration involves flipping back and forth between the coarse grid and the fine grid. Each time after flipping, the convergence criteria are tightened, until a desired accuracy is obtained for the fine grid solution. The flow chart of the present computer code is depicted in Fig. 3.8. The system of equations for obtaining the correction terms using the coarse grid is obtained by summing the discretized equations for all the fine grid control volumes contained in a coarse grid block. All the fine grid control volumes in a particular coarse

grid block have the same correction term; the inner nodes within a coarse grid block do not contribute to the coefficients in the equations for the correction terms. The general form of the discretization equation for the correction term $\tilde{\phi}$ over the coarse grid block is:

$$c_{i,j} \tilde{\phi}_{i,j} = c_{ip,j} \tilde{\phi}_{ip,j} + c_{im,j} \tilde{\phi}_{im,j} + c_{i,jp} \tilde{\phi}_{i,jp} + c_{i,jm} \tilde{\phi}_{i,jm} + D_{i,j} \quad (3.45)$$

where $c_{ip,j}$ is the sum of the a_E 's of the fine grid points on the right border of the coarse block (i, j), $c_{im,j}$ is the sum of the a_W 's of the fine grid points on the left border of the coarse block, $c_{i,jp}$ is the sum of a_N 's on the upper border, and $c_{i,jm}$ is the sum of a_S 's on the lower border of the coarse block. For the present problem, $c_{i,j}$ is the sum of the four neighboring coefficients. $c_{i,j} = c_{ip,j} + c_{im,j} + c_{i,jp} + c_{i,jm}$. $D_{i,j}$ is a fictitious source term equal to the sum of the residues of all equations on the fine grid control volumes in the coarse block (i, j).

The correction terms for the fine grids on the edge of the computational domain can be taken to be zero for all three kinds of boundary conditions. For Dirichlet boundary conditions, the boundary values are already given; hence, there is no need for any correction. For Neumann boundary conditions, the property gradient is given. When integration of the original differential equation is carried out over the control volume, the coefficients for the boundary grid points are zero as values of the boundary grid point properties have no effect on the discretized equation. This renders the coefficients for the correction terms for boundary grid points to be zero, or alternatively the correction terms themselves can be defined to be zero. By similar argument, the correction terms for the boundary grids under the third kind of boundary condition, which involves both the boundary values and the derivative on the boundary, can be taken to be zero. The multigrid acceleration method equations are similar to those governing a transient heat conduction problem with decreasing internal heat sources and zero boundary temperature. As the internal sources decreases to zero, the temperature at the internal nodes reduces to zero in the heat conduction problem. Similarly, the correction terms for each coarse grid block reduce after each iteration has converged on

the fine grids and the sum of the residues of the discretized equations on the fine grid control volume approaches zero.

The velocity field due to expansion is recovered using the definition of the potential function, eq. (3.4), with the derivative in the equation approximated with central finite differencing. Referring to Fig. 3.6, for an internal node (i, j), the finite difference equations are:

$$\bar{U}_z(i, j) = \frac{\phi(i, j+1) - \phi(i, j-1)}{\Delta z_n(j) + \Delta z_s(j)} \quad (3.46a)$$

$$\bar{U}_r(i, j) = \frac{\phi(i+1, j) - \phi(i-1, j)}{\Delta r_e(i) + \Delta r_w(i)} \quad (3.46b)$$

The velocity field caused by the vorticity generated in the flame is recovered using the definition of the stream function approximated by a central finite difference:

$$\tilde{U}_z(i, j) = \frac{\psi(i+1, j) - \psi(i-1, j)}{\Delta r_e(i) + \Delta r_w(i)} \frac{1}{r_p(i)} \quad (3.47a)$$

$$\tilde{U}_r(i, j) = -\frac{\psi(i, j+1) - \psi(i, j-1)}{\Delta z_s(j) + \Delta z_n(j)} \frac{1}{r_p(i)} \quad (3.47b)$$

For the nodes adjacent to the boundary, however, eqs (3.46) and (3.47) and the properties at neighboring nodes result in false central finite differencing since the distances between the node in question and the neighboring nodes are different. The velocities at these nodes thus obtained are incompatible with the interior velocity field, as demonstrated in Fig. 3.9a, where the predicted axial velocity at $z = 42.5$ is plotted as a function of radial position. The axial velocity according to correlations of McCaffrey (1983) is also plotted. The numerical value at a node close to the axis is very different from the axial velocity according to correlations of McCaffrey (1983). To solve this problem, a property on the interior surface of the boundary control volumes, obtained by linear interpolation, was used to achieve proper central finite differencing. The finite difference equations corresponding to eqs. (3.46) are:

$$\text{along } j = 2 \quad \bar{U}_z(i, 2) = \frac{(\phi(i, 3) + \phi(i, 2)) / 2 - \phi(i, 1)}{z_n(2) - z_s(2)} \quad (3.48a)$$

$$\text{along } i = 2 \quad \bar{U}_r(2, j) = \frac{(\phi(3, j) + \phi(2, j)) / 2 - \phi(1, j)}{r_e(2) - r_w(2)} \quad (3.48b)$$

and those corresponding to eqs (3.47) are:

$$\text{along } i = 2 \quad \tilde{U}_z(2, j) = \frac{(\psi(3, j) + \psi(2, j)) / 2 - \psi(1, j)}{r_e(2) - r_w(2)} \frac{1}{r_p(2)} \quad (3.49a)$$

$$\text{along } j = 2 \quad \tilde{U}_r(i, 2) = -\frac{(\psi(i, 3) + \psi(i, 2)) / 2 - \psi(i, 1)}{z_n(2) - z_s(2)} \frac{1}{r_p(i)} \quad (3.49b)$$

Treating the boundary control volumes with eqs. (3.48) and (3.49) yields improved agreement between the numerical velocity prediction and the velocity profile according to the correlations of McCaffrey (1983), as shown in Fig. 3.9b.

3.4.3 The Effect of Computational Domain Sizes and Grid Spacing

A numerical model is not useful without estimation of its accuracy and validity. The validity of the present numerical model is evaluated by varying the size of the computational domain and the number of grid points for a fixed size of the computational domain and observing the resulting changes in the predicted velocity field. The sensitivity to the size of the computational domain results from the assumption of a point source made in specifying the boundary conditions for the velocity potential and stream function. The sensitivity to grid spacing is common to all numerical representations of continuous functions and their derivatives.

The grid spacing was kept constant and uniform at 1 cm in order to study the effects of the size of the computational domain. The velocity fields were first computed on computational domains of: 100×400 grid cells, which resulted in a computational domain of the size 1 m \times 4 m, as a basis for comparison. Velocity calculations with four additional sizes for the computational domain were completed. The first two of these involved a constant 1 m radial dimension and heights of 2 m and 5 m. Two additional sets of computations were performed with height of the computational domain equal to 4 m and radii of the domain varied from 0.5 m to 2 m. The velocity predictions at $z = 0.5$ cm and 42.5 cm based on the different computational domains are shown in Figs. 3.10

and 3.11. The predicted axial velocities at $z = 0.5$ cm as a function of radial position are plotted in Fig. 3.10a. The five lines representing the predictions based on computational domains of different sizes cannot be distinguished from one another. Checking the values revealed that the maximum difference is 0.01 cm/s between the $0.5 \text{ m} \times 4 \text{ m}$ prediction and the $2 \text{ m} \times 4 \text{ m}$ predictions at $r = 0.5$ cm. The predicted radial velocities at $z = 0.5$ cm are plotted in Fig. 3.10b. The largest difference among the three predictions computed on domains of the same radial dimension of 1 m is 0.02 cm/s at $r = 39.5$ cm, and in the figure, the profiles are indistinguishable. There are appreciable differences between these predictions and those computed on a $2 \text{ m} \times 4 \text{ m}$ domain at large radial positions. At $r = 39.5$ cm, the radial velocity based on the $2 \text{ m} \times 4 \text{ m}$ domain predictions is 0.13 cm/s lower. The differences between the predictions using the $1 \text{ m} \times 4 \text{ m}$ domain and the predictions using the $0.5 \text{ m} \times 4 \text{ m}$ domain are more pronounced. At $r = 39.5$ cm, the difference between predictions based on the two domains is 0.4 cm/s. However, the predictions based on the 5 different domains collapse on a single curve for r smaller than 10 cm.

Comparison of the axial velocity predictions at $z = 42.5$ cm are shown in Fig. 3.11a. The three lines representing the velocity predictions with computational domains with 1 m radial dimension are grouped together, with the largest difference between them less than 0.05 cm/s. Compared to these, the velocity predictions based on the $2 \text{ m} \times 4 \text{ m}$ domain are usually 0.3 cm/s larger, while those based on the $0.5 \text{ m} \times 4 \text{ m}$ domain are approximately 0.8 cm/s smaller. The largest differences between predictions caused by the different computational domain sizes is small compared to the absolute value of velocity which is of the order of 10 cm/s. The predicted radial velocities at $z = 42.5$ cm are plotted in Fig. 3.11b. Similar to those observed in Fig. 3.10b, the three predictions based on a 1 m radial dimension are close to each other, and those based on the 2 m radial dimension are lower, while those based on a 0.5 m radial dimension for the computational domain are higher. The largest difference between the radial velocity predictions at $r = 39.5$ cm is 0.18 cm/s. In the region close to the centerline of the flame, the five predictions agree with one another very well.

It can be concluded that the change in the computational domain size in the axial direction within the range examined here hardly affects the velocity predictions, while the change in the radial dimension can cause some differences at larger radial locations. However, the effect is too small to have any significance within the present range. Based on this, the treatment of the boundary conditions on the outer edges of the computational domain can be considered proper. The computational results reported in the following were obtained using the $1\text{ m} \times 4\text{ m}$ domain.

The mesh size is a crucial parameter in numerical simulation of physical phenomena. As a second test of the model, the grid spacings were changed both radially and axially with the size of the computational domain fixed. The velocity predictions computed on a $1\text{ m} \times 4\text{ m}$ computation domain with a uniform grid spacing of 1 cm serve as a baseline for comparison. The radial grid spacing was decreased by half to $\Delta r = 0.5\text{ cm}$, while the axial computational domain and the grid spacing were maintained at the baseline values. The velocity predictions for the two different radial grid spacings are plotted in Figs. 3.12 and 3.13. The predicted axial velocities at $z = 0.5\text{ cm}$ are plotted in Fig. 3.12a. Near the axis there is a small difference between the velocities obtained using different radial grid spacings. The curve is smoother with smaller grid spacing. However, the solution does not change qualitatively with grid spacing in the present range. The reason is more obvious in Figure 3.12b, where the radial velocities are compared. In the region around the maximum entrainment velocity, the velocity changes rapidly. Because the velocity prediction based on 1 cm grid spacing can not follow the change as quickly, the computed velocity curve with $\Delta r = 1\text{ cm}$ shows abrupt slope changes, while the curve representing the velocity prediction based on a 0.5 cm grid spacing is smooth. The predicted axial velocities at $z = 42.5\text{ cm}$ are shown in Fig. 3.13a. The two velocity predictions agree with each other very well except very near the flame axis. The radial velocities at $z = 42.5\text{ cm}$ are plotted in Fig. 3.13b. There is a small difference between the predictions based on different radial grid spacings only near the flame region where rapid changes in velocity occur.

The effect of axial grid spacing on the velocity predictions was examined by changing the axial grid spacing from 1 cm to 0.8 cm while maintaining the radial grid spacing at 1 cm. The axial velocity predictions at $r = 7.5$ cm as a function of axial distance are plotted in Fig. 3.14a, and the radial velocity predictions are plotted in Fig. 3.14b. There is hardly any difference between the results obtained using the different axial grid spacings. The axial and radial velocities at $r = 3.5$ cm are plotted in Fig. 3.15. There is a very small but perceptible difference in the radial velocity predictions with different axial grid spacings. At $r = 0.5$ cm, there is little difference in axial velocity predictions with different axial grid spacings, as shown in Fig. 3.16a. The curve representing the radial velocity prediction as a function of axial distance computed with $\Delta z = 0.8$ cm in Fig. 3.16b is not only smoother than the curve representing the radial velocity computed with $\Delta z = 1$ cm, but sometimes perceptibly lower. However, the largest difference is only 0.2 cm/s. Based on the above examination of the effects of grid spacing, it is clear that the present discretization is adequate. The computations reported in the following are based on a 1 cm grid spacing.

3.4.4 The Irrotational Velocity and the Incompressible Velocity

The radial velocity at all axial stations shows an interesting pattern. For example at $z = 42.5$ cm shown in Fig. 3.11b, starting from the far field, the radial velocity is negative, showing that the flow is towards the flame as a result of air entrainment. It is by this mechanism that a very strong inward wind can be caused in a conflagration. As it gets near the flame, the absolute value of the radial velocity becomes larger to compensate for the reduction in area, until a maximum is reached. Beyond this point, the radial velocity becomes less, and at about $r = 6$ cm, the velocity becomes positive, i.e., the flow is radially outward. The outward flow velocity becomes higher at radial locations corresponding to increasing heat release, reaches a maximum value at the location of peak heat release, and then goes to zero on the flame centerline.

The predicted radial velocities due to expansion and vorticity are plotted in Figs. 3.17a and 3.17b as a function of radial position for $z = 0.5$ cm and $z = 42.5$. Figure 3.17a shows the velocities for $z = 0.5$ cm. The radial velocity due to expansion shows a trend to go to zero both at the axis and at radii tending to infinity with a local maximum at about $r = 4$ cm. The incompressible radial velocity due to vorticity shows a similar trend, but the net flow velocities are radially inward except for a small unresolved region near the axis. The value of the incompressible velocity is higher than that of the expansion, resulting in a net air entrainment velocity, except for very near the flame axis, where the expansion velocity is higher than the incompressible velocity caused by vorticity and the net velocity is outward. But the radial velocities at $z = 42.5$ cm, plotted in Figure 3.17b, show somewhat different flow pattern of the radial velocity changing with radial position. The irrotational velocity due to heat release changes from 0 cm/s at the flame axis to about 0.2 cm/s at $r = 39.5$ cm, always insignificantly small compared to the incompressible velocity caused by vorticity. The behavior of the total velocity is very similar to that of the incompressible velocity caused by vorticity. The total velocity begins to increase with decreasing radius after $r = 12$ cm, becomes zero at about $r = 4.5$ cm, reaches a maximum at $r = 2.5$ cm, and returns to zero at the axis.

To seek the reason for this changing pattern of the velocity due to vorticity, the vorticity distribution as a function of radial position at $z = 42.5$ cm in Fig. 3.3 is re-examined. The vorticity created by density gradient inside the flame first increases in strength with radial position, reaches a maximum at $r = 4.5$ cm, and returns to zero outside the flame starting at about $r = 16$ cm. The radial position where the vorticity is maximum coincides with the position where the velocity becomes zero. It is clear that the high vorticity layer, which is strongest in a region close to the flame boundary, not only entrains air from the surroundings, but also entrains combustion gases from the interior region. The irrotational and incompressible components of the predicted axial velocities at $z = 0.5$ cm and 42.5 cm are plotted in Figs. 3.18a and 3.18b. At both locations, the axial velocities are dominated by the incompressible flow caused by vorticity. At $z = 0.5$ cm, the maximum axial velocity due to expansion is 0.9 cm/s at $r = 0.5$ cm, while the axial velocity caused by vorticity at the same location reaches a

maximum of 23.3 cm/s. At $z = 42.5$ cm, the maximum axial velocity due to expansion is 0.5 cm/s, while the axial velocity due to vorticity is 225.2 cm/s.

The radial velocity generated by the vorticity field dominates the flow field at locations at larger radius and close to the fuel surface. Figure 3.19 shows the behavior of the radial velocity at a radial location of 0.5 cm to demonstrate the manner in which the net positive outflow is created. In the continuous flame region ($z < 10$ cm), the heat release rate and the corresponding expansion is large, leading to a large irrotational flow as shown in the figure. The velocity component generated by vorticity has a negative value that reduces the net expansion flow. The vorticity source at the relatively low radial position is small in the intermittent and plume regions causing negligible incompressible component of velocity as shown in Fig. 3.19. At the interface between the continuous and intermittent flame regions, a sudden decrease in the magnitude of the incompressible velocity occurs due to a change in the vorticity source. For the location relatively close to axis, the small incompressible velocity component has a positive sign indicating that the region of strong vorticity entrains combustion products from the centerline and air from the outside. The velocity attains a small positive value in the far field as a result of this.

The entrainment flow field of a pool fire is a result of expansion velocity and velocity generated by vorticity. In the continuous flame region, the expansion velocity can be comparable to that caused by vorticity. However, in the intermittent region and the fire plume, the vorticity generated velocity component dominates the flow.

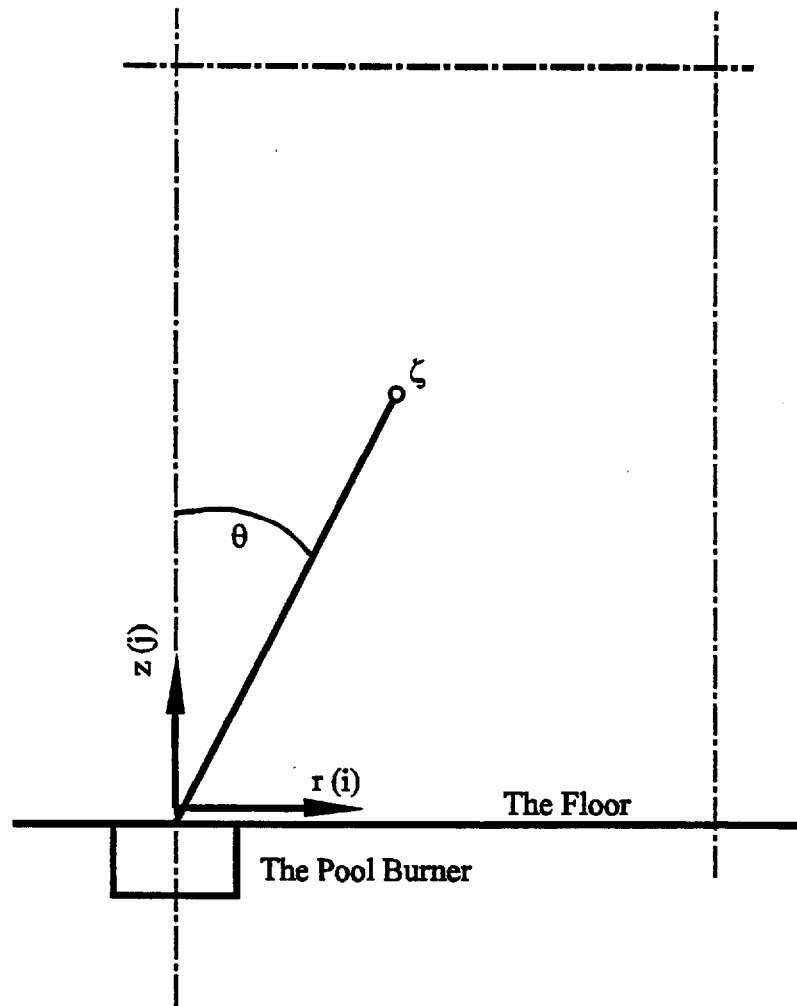


Figure 3.1a Sketch of the computational domain of the flow field induced by pool fire with a floor.

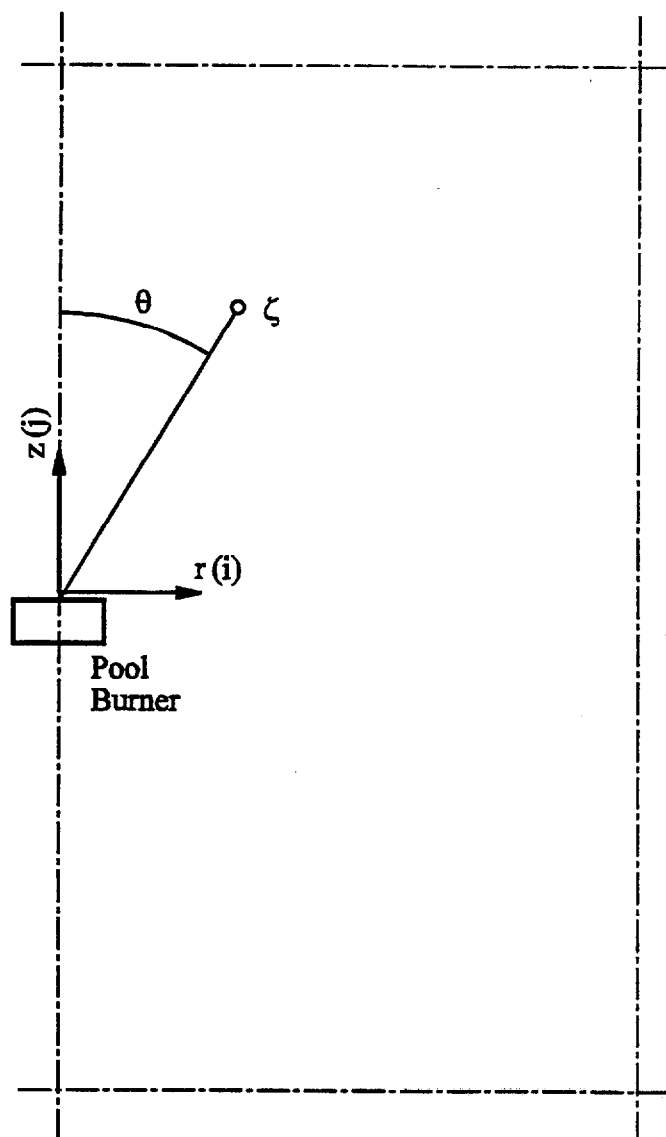


Figure 3.1b Sketch of the computational domain of the flow field induced by pool fire without a floor.

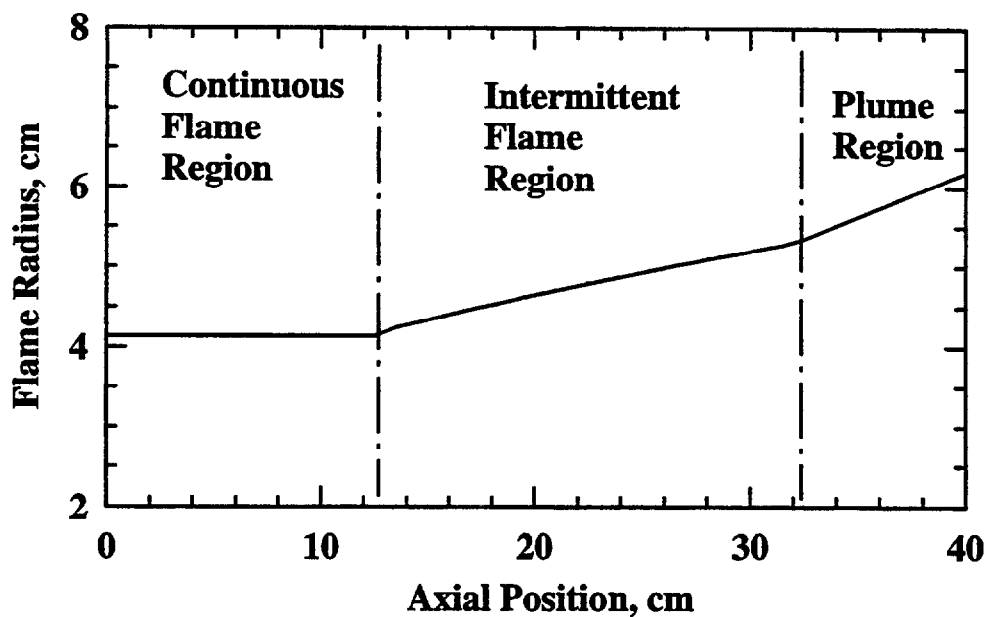


Figure 3.2 The flame radius $R(z)$ as a function of height as per the correlation of Baum and McCaffrey (1988).

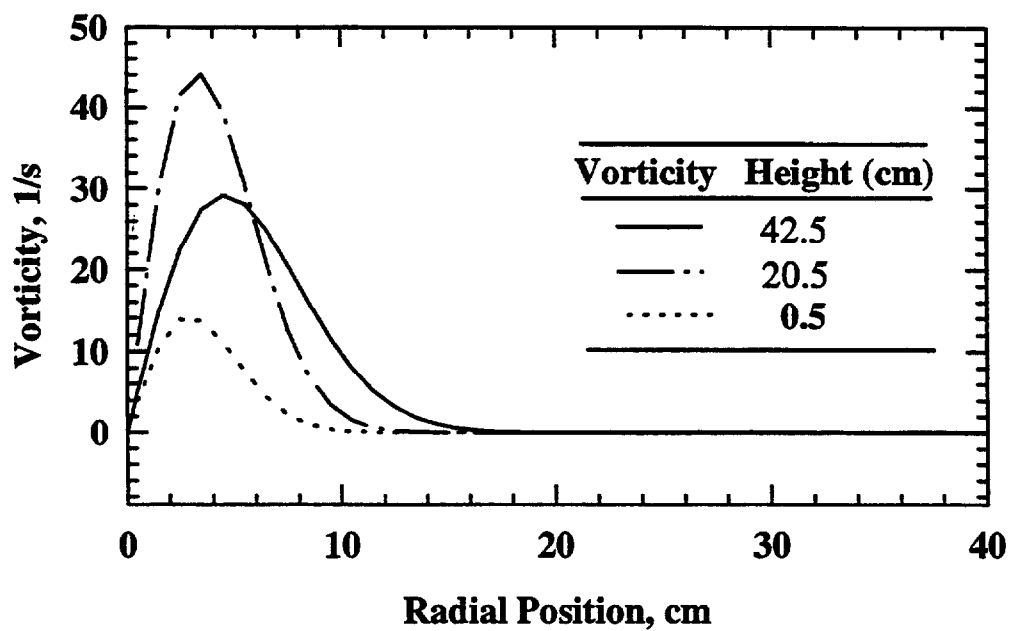


Figure 3.3 The vorticity distribution at $z = 0.5$ cm, 20.5 cm and 42.5 cm estimated according to McCaffrey's flame structure correlations.

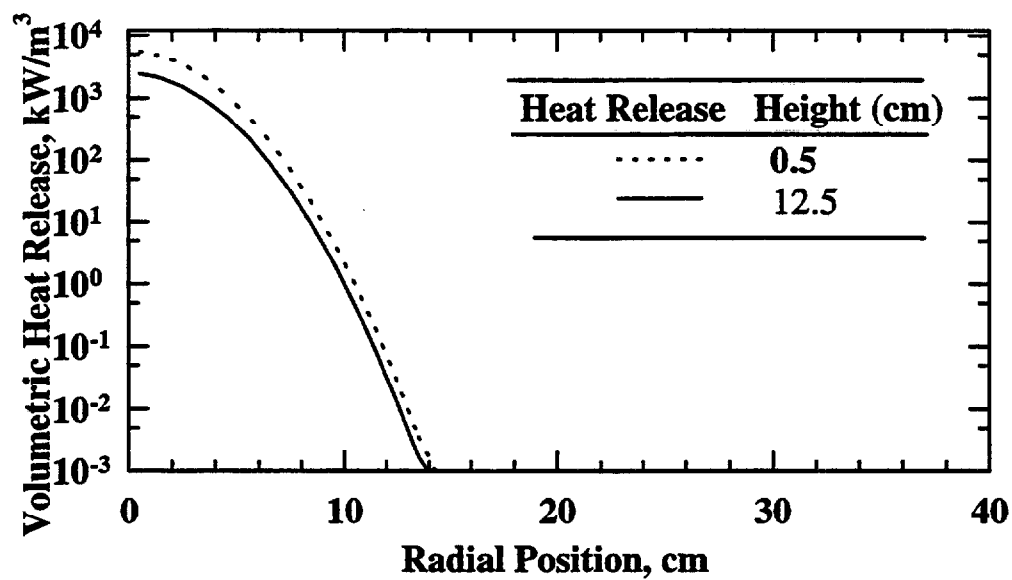


Figure 3.4 The volumetric heat release rate distribution at $z = 0.5$ cm and 12.5 cm estimated according to McCaffrey's flame structure correlations.

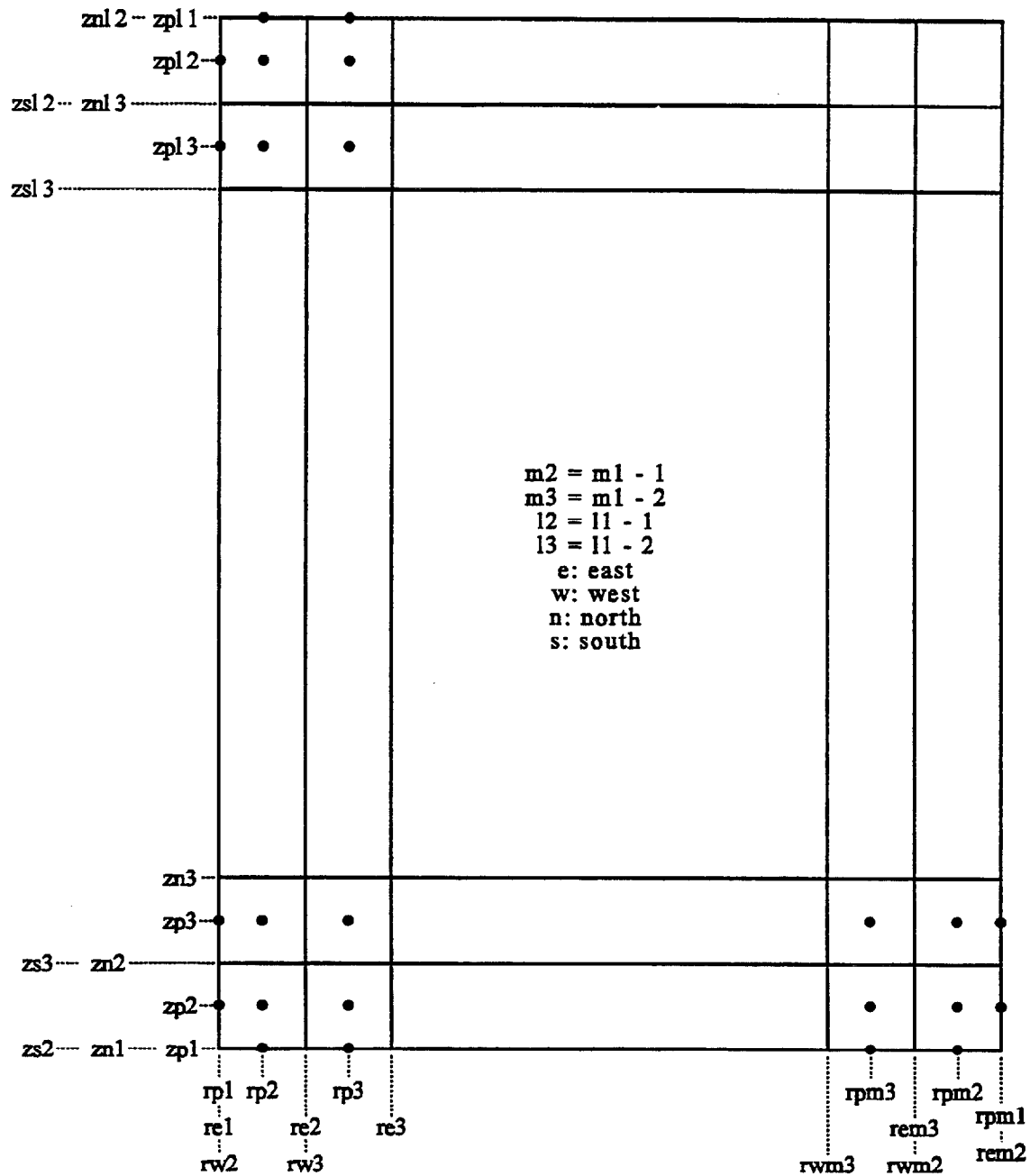


Figure 3.5 Discretization of the computational domain and designation of the control volume surfaces and grid points.

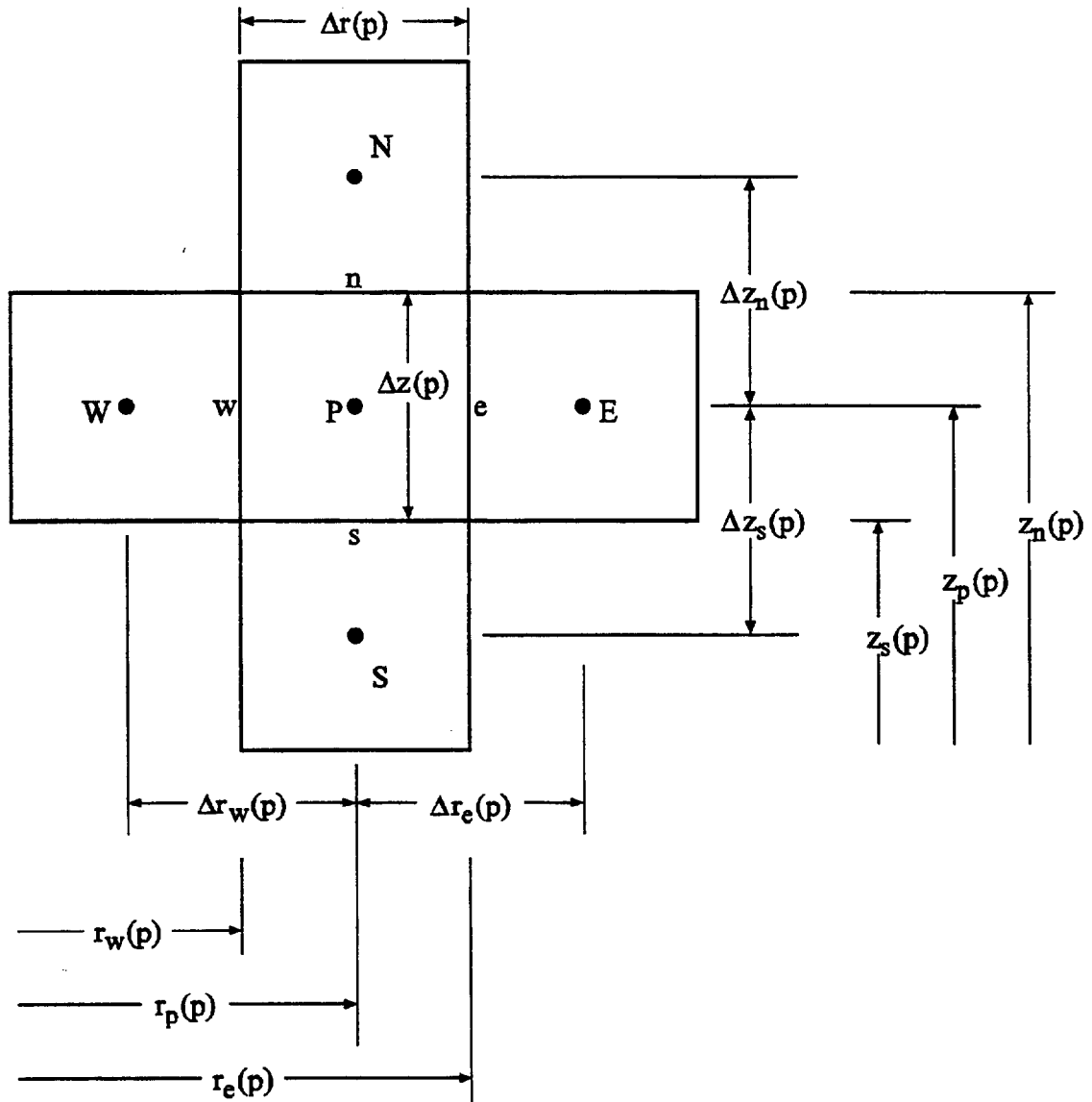


Figure 3.6 A typical element in the discretized computational domain.

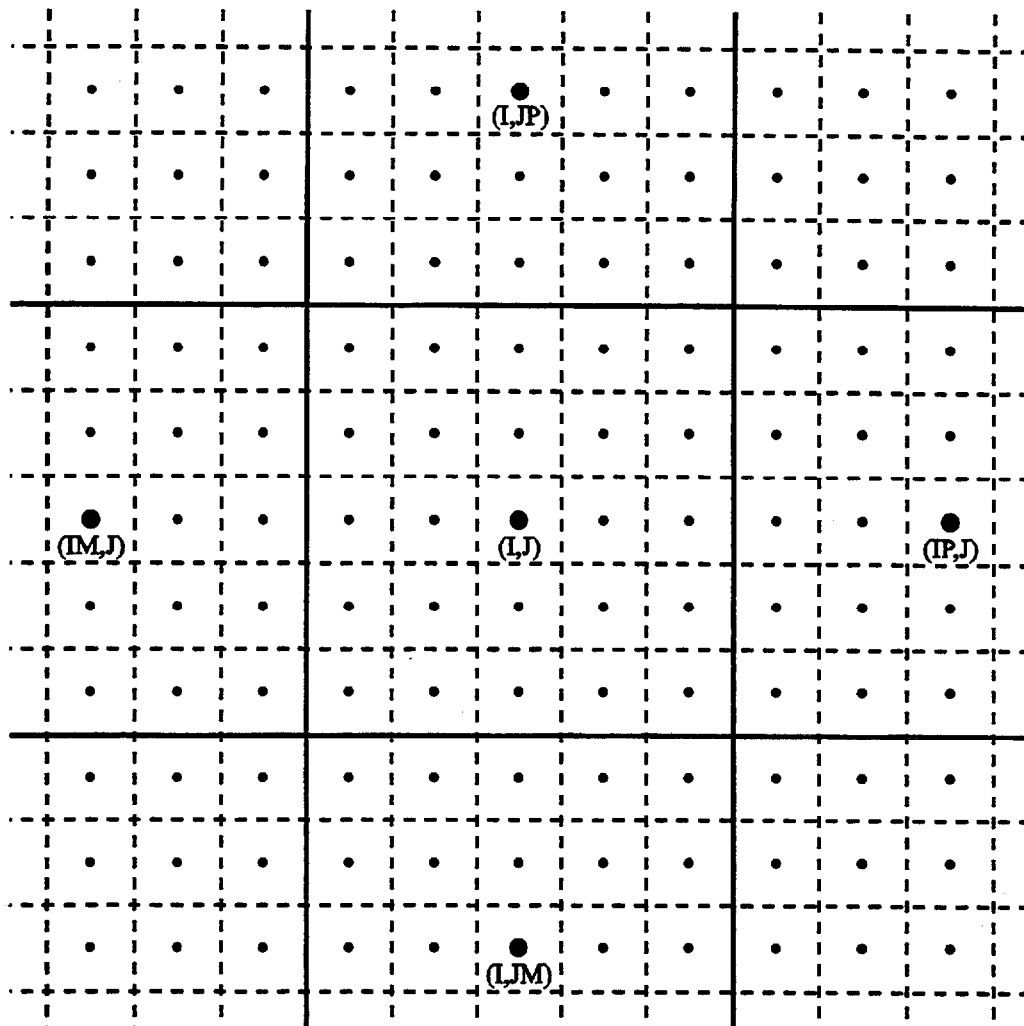


Figure 3.7 The pattern of coarse control volume block encompassing fine control volume grid cells.

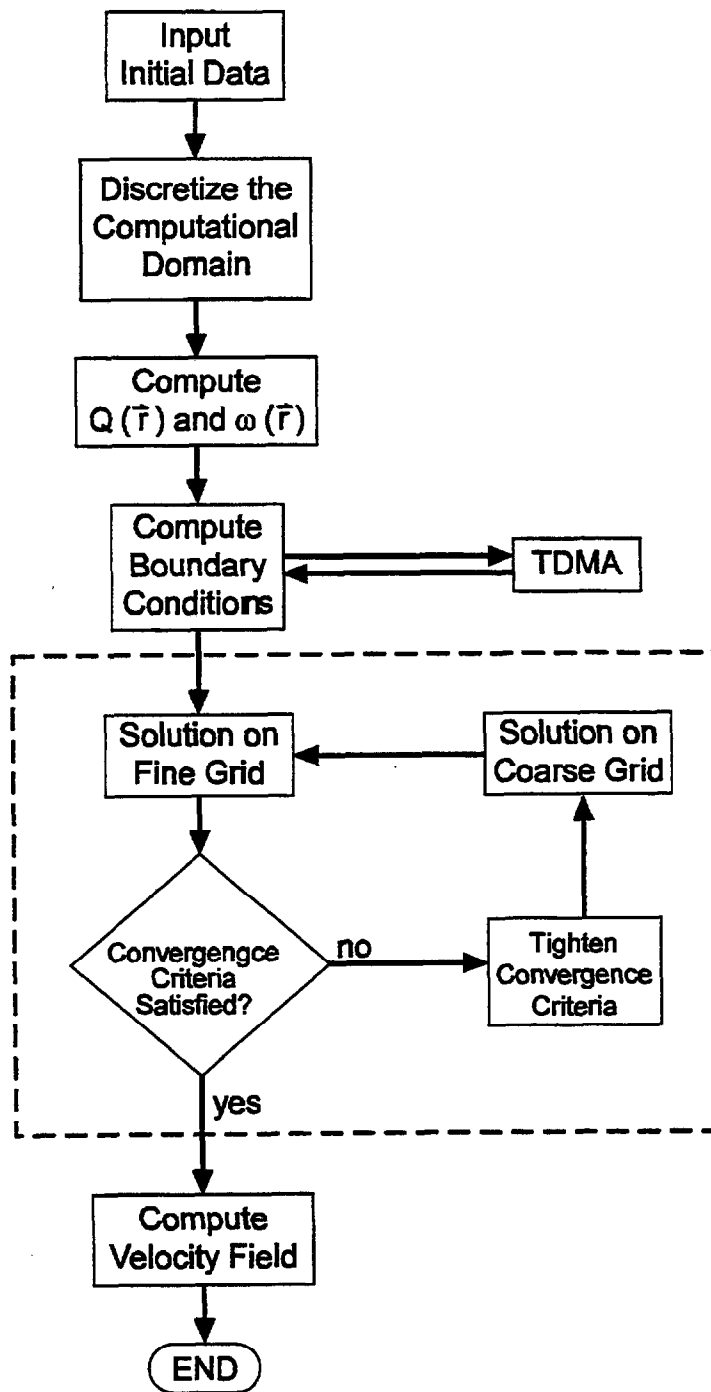


Figure 3.8 Flow chart of the computer code.

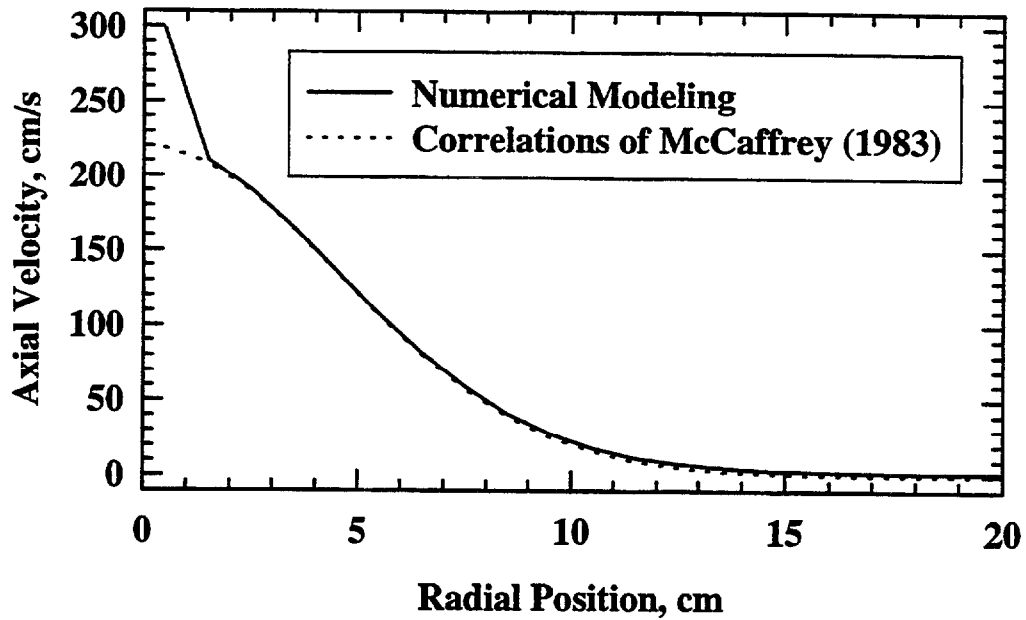


Figure 3.9a The predicted axial velocity at $z = 42.5$ cm by using Eqs. 3.46 and 3.47.

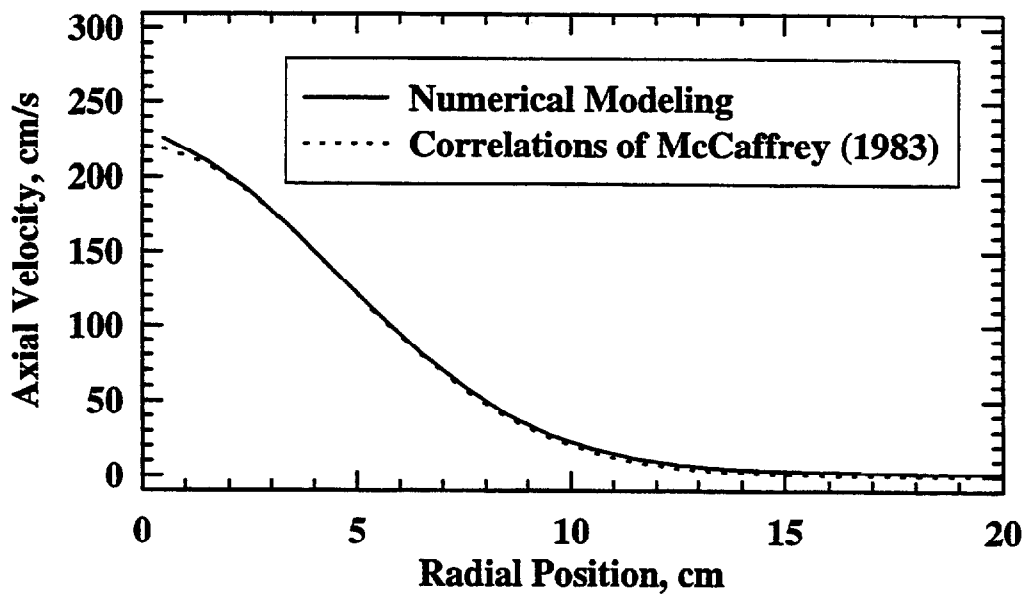


Figure 3.9b The predicted axial velocity at $z = 42.5$ cm by using Eqs. 3.48 and 3.49 for boundary nodes.

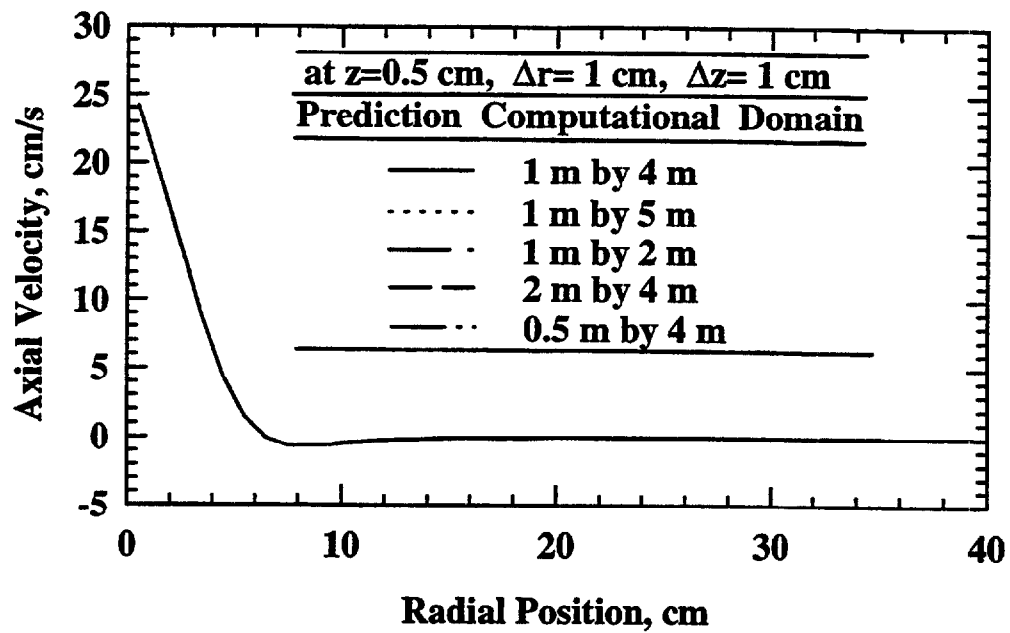


Figure 3.10a Comparison of the predicted axial velocities at $z = 0.5$ cm using computational domains of different sizes.

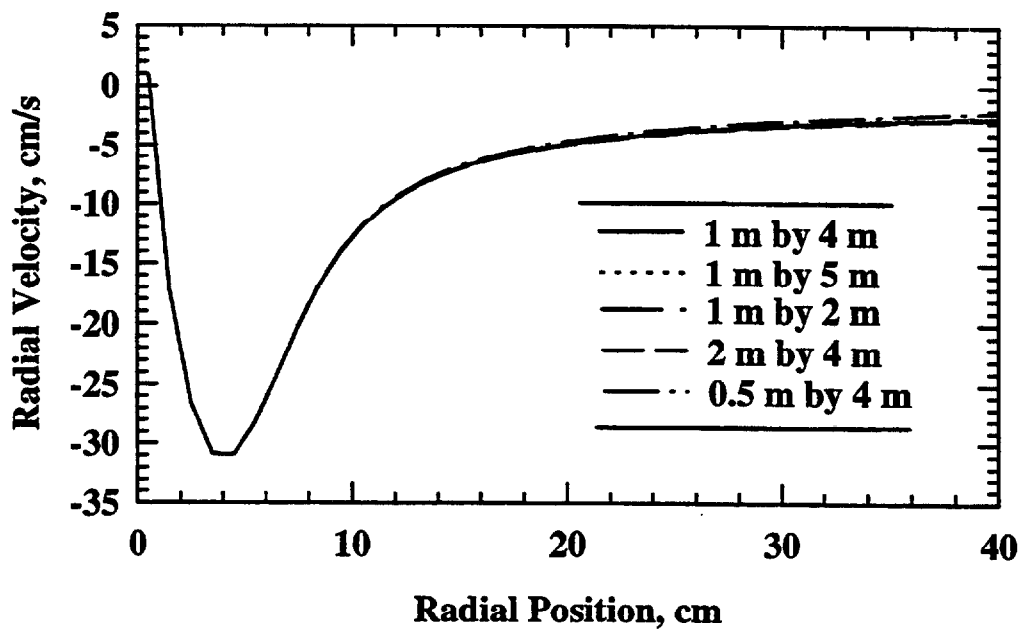


Figure 3.10b Comparison of the predicted radial velocities at $z = 0.5$ cm using computational domains of different sizes.

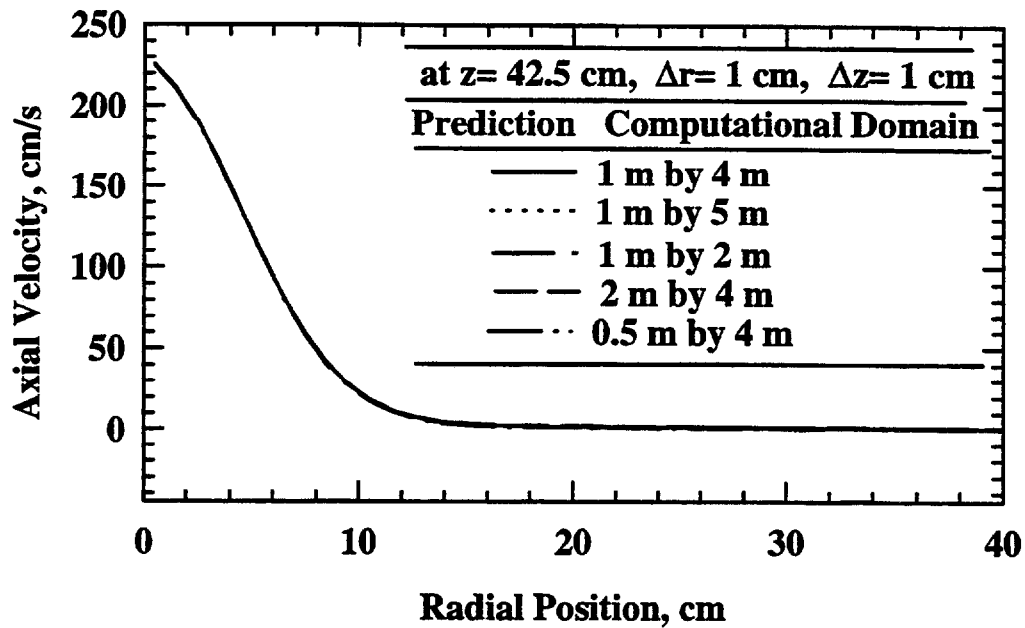


Figure 3.11a Comparison of the predicted axial velocities at $z = 42.5$ cm using computational domains of different sizes.

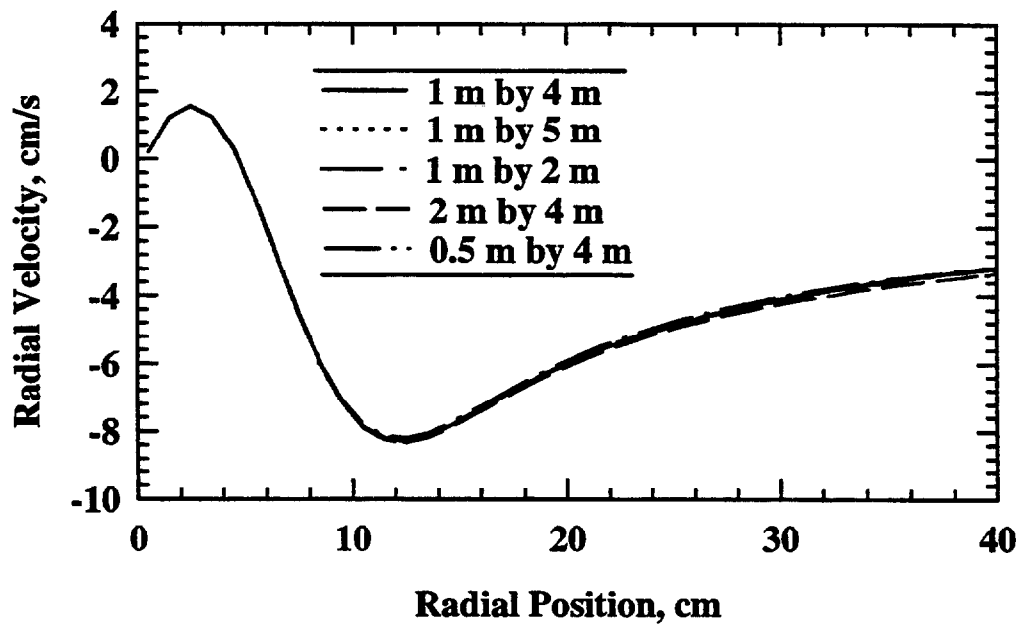


Figure 3.11b Comparison of the predicted radial velocities at $z = 42.5$ cm using computational domains of different sizes.

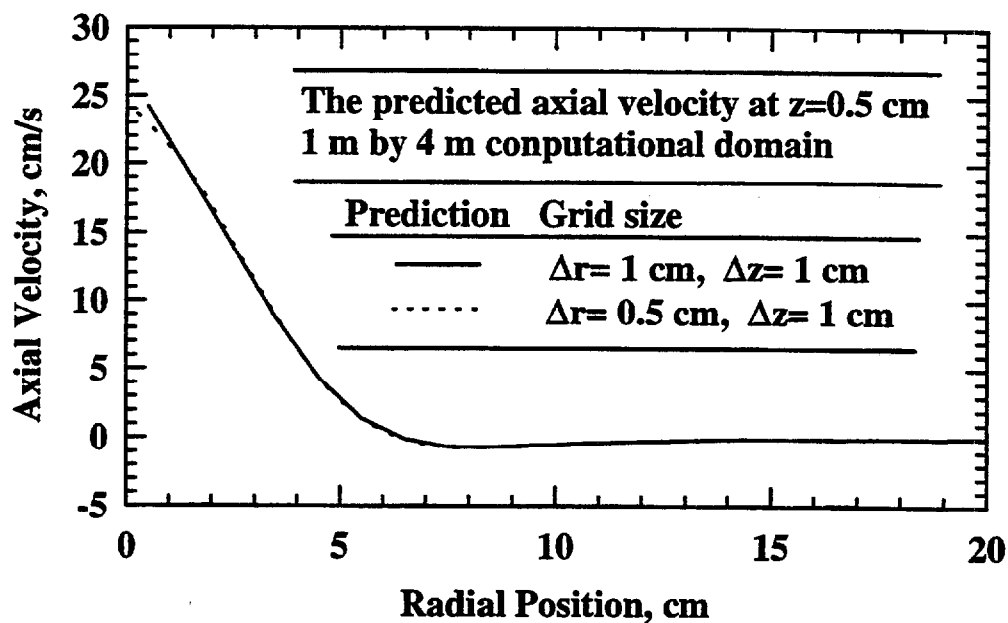


Figure 3.12a Comparison of the predicted axial velocities at $z = 0.5$ cm using different radial grid spacings.

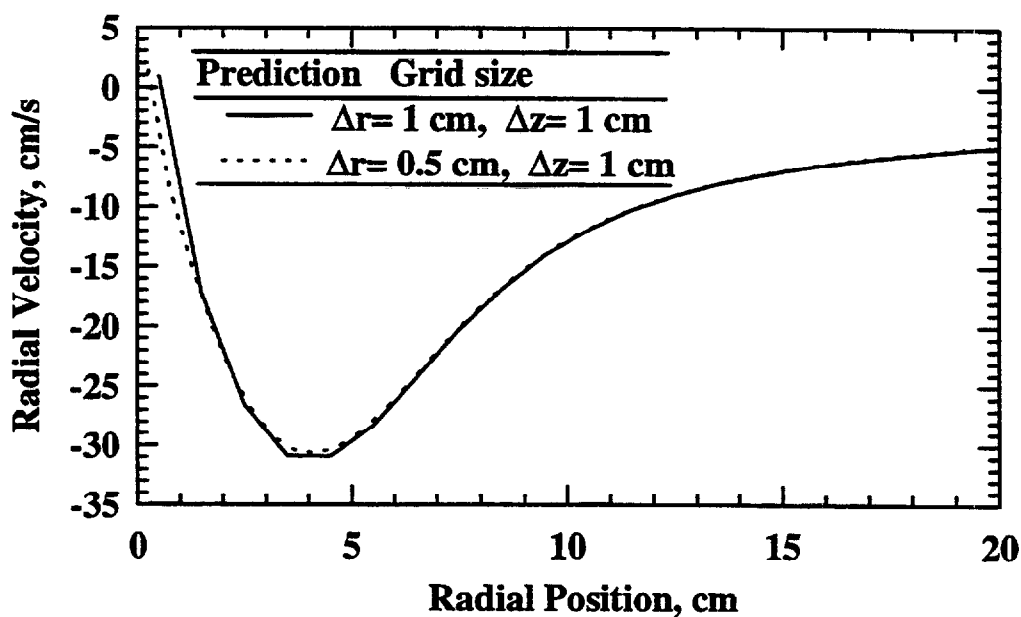


Figure 3.12b Comparison of the predicted radial velocities at $z = 0.5$ cm using different radial grid spacings.

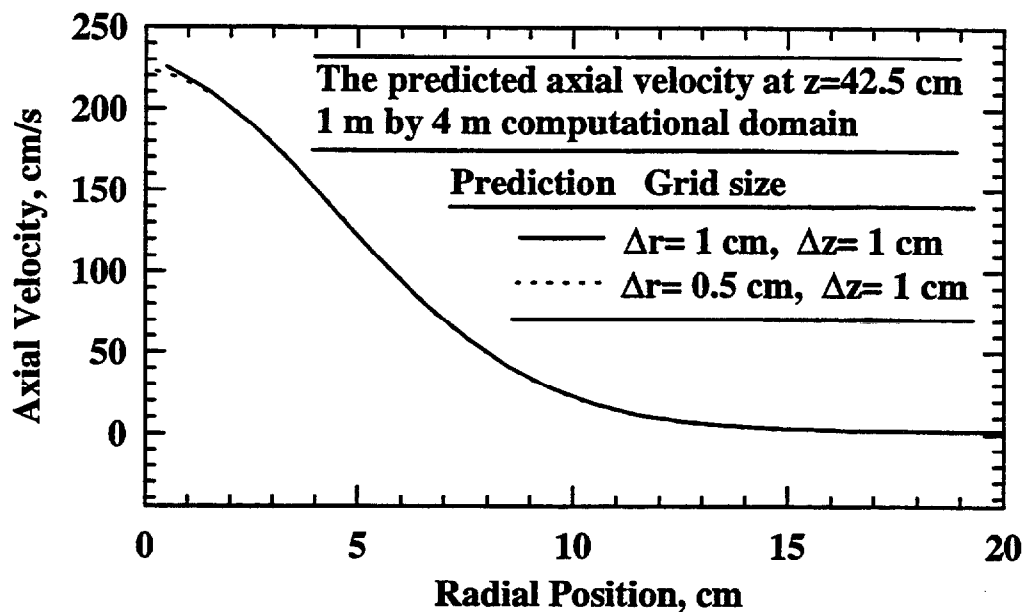


Figure 3.13a Comparison of the predicted axial velocities at $z = 42.5$ cm using different radial grid spacings.

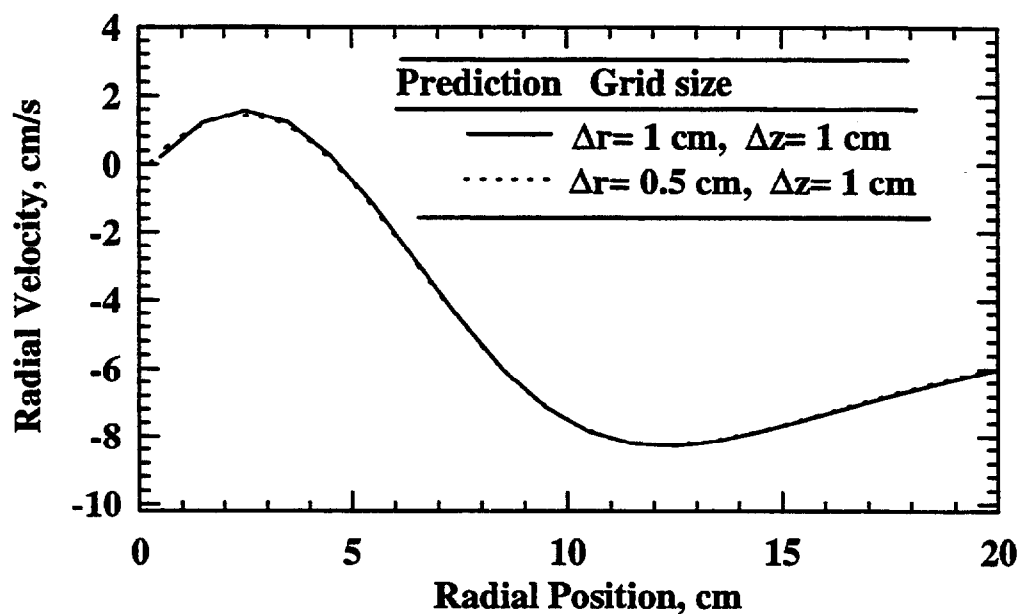


Figure 3.13b Comparison of the predicted radial velocities at $z = 42.5$ cm using different radial grid spacings.

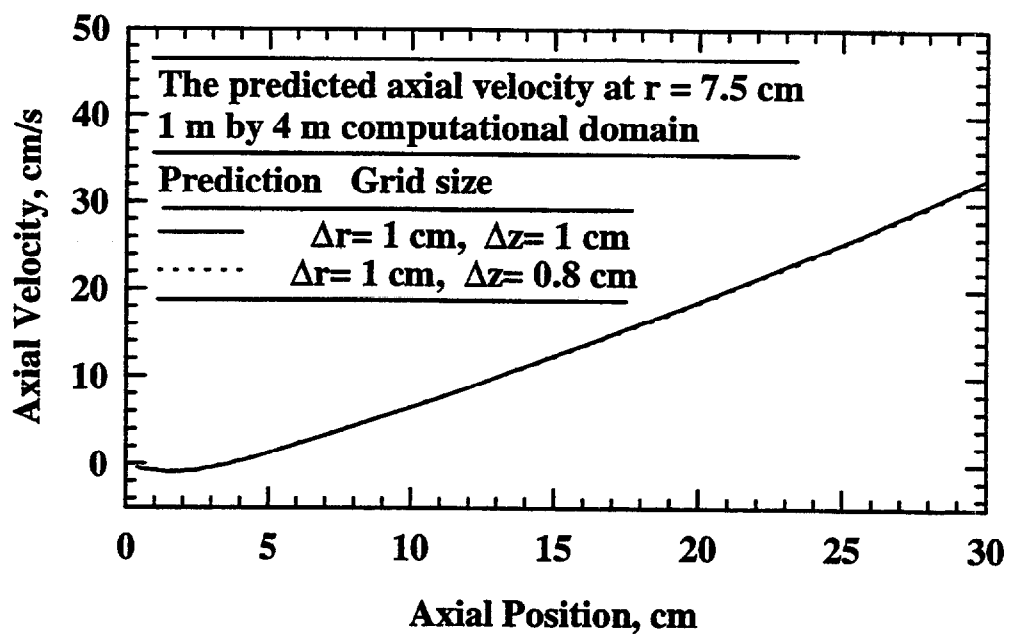


Figure 3.14a Comparison of the predicted axial velocities at $r = 7.5$ cm using different axial grid spacings.

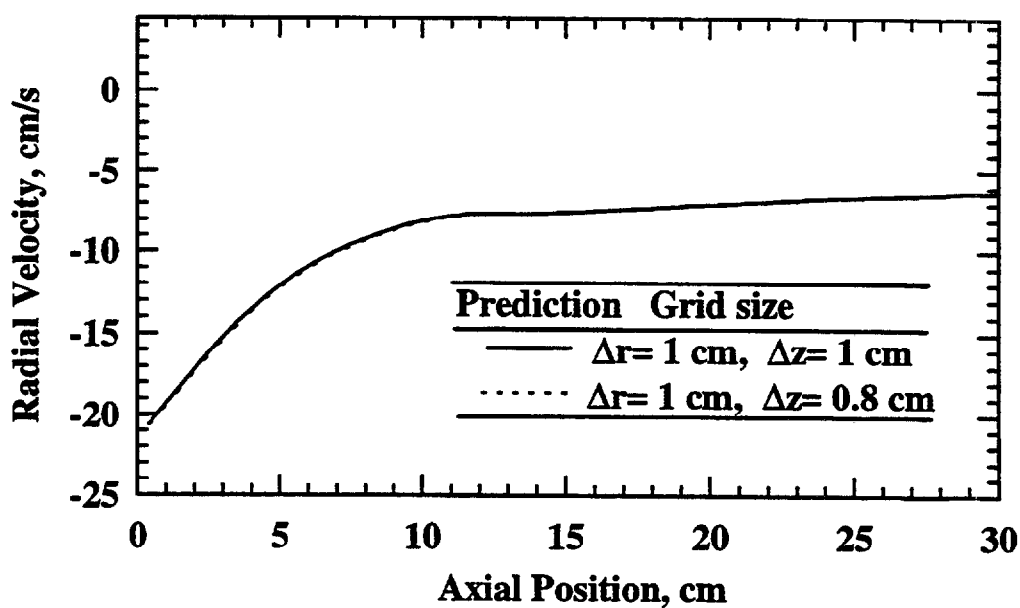


Figure 3.14b Comparison of the predicted radial velocities at $r = 7.5$ cm using different axial grid spacings.

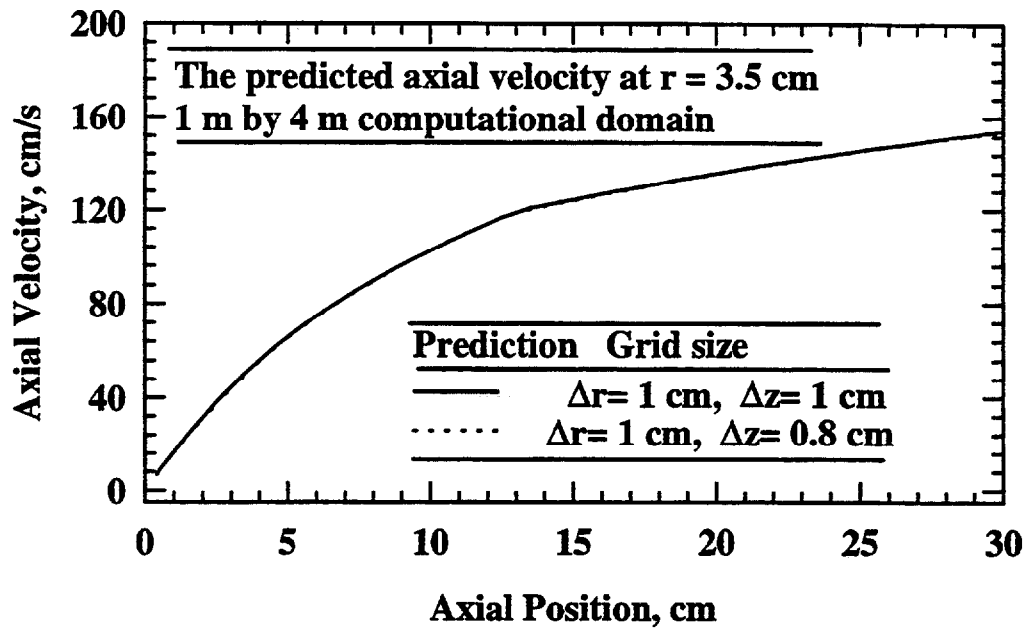


Figure 3.15a Comparison of the predicted axial velocities at $r = 3.5$ cm using different axial grid spacings.

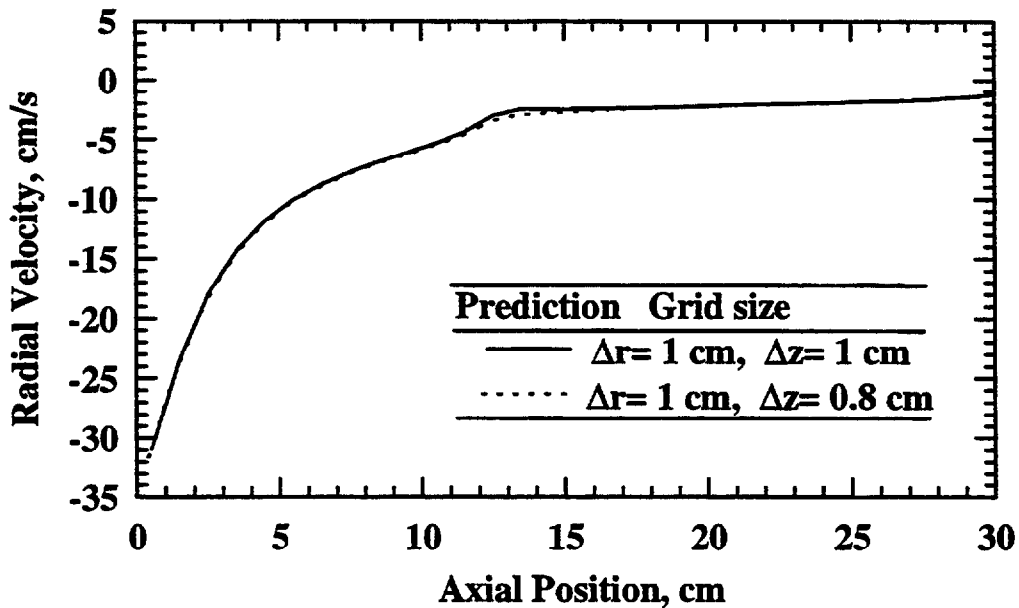


Figure 3.15b Comparison of the predicted radial velocities at $r = 3.5$ cm using different axial grid spacings.

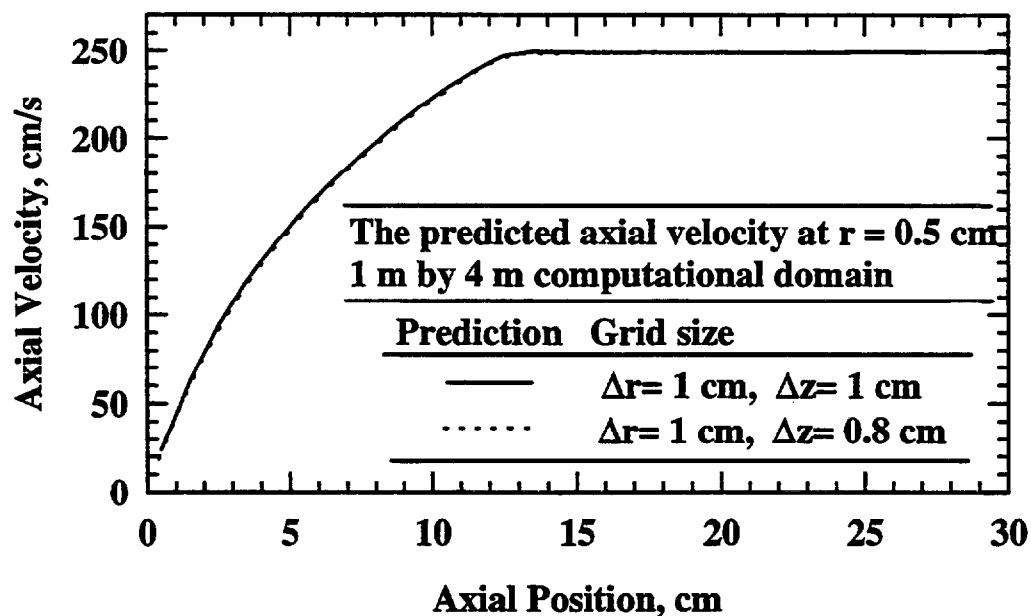


Figure 3.16a Comparison of the predicted axial velocities at $r = 0.5$ cm using different axial grid spacings.

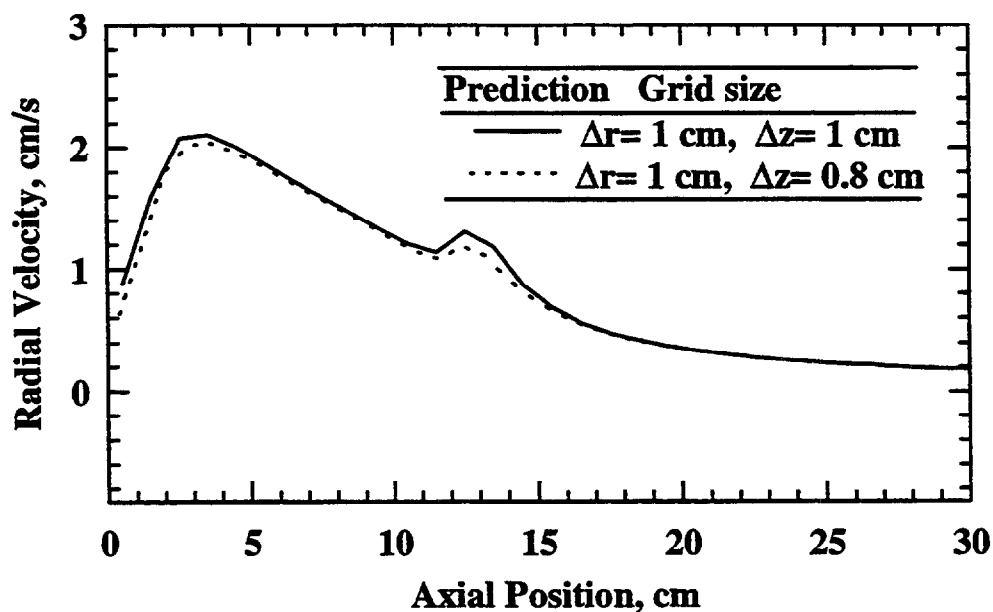


Figure 3.16b Comparison of the predicted radial velocities at $r = 0.5$ cm using different axial grid spacings.

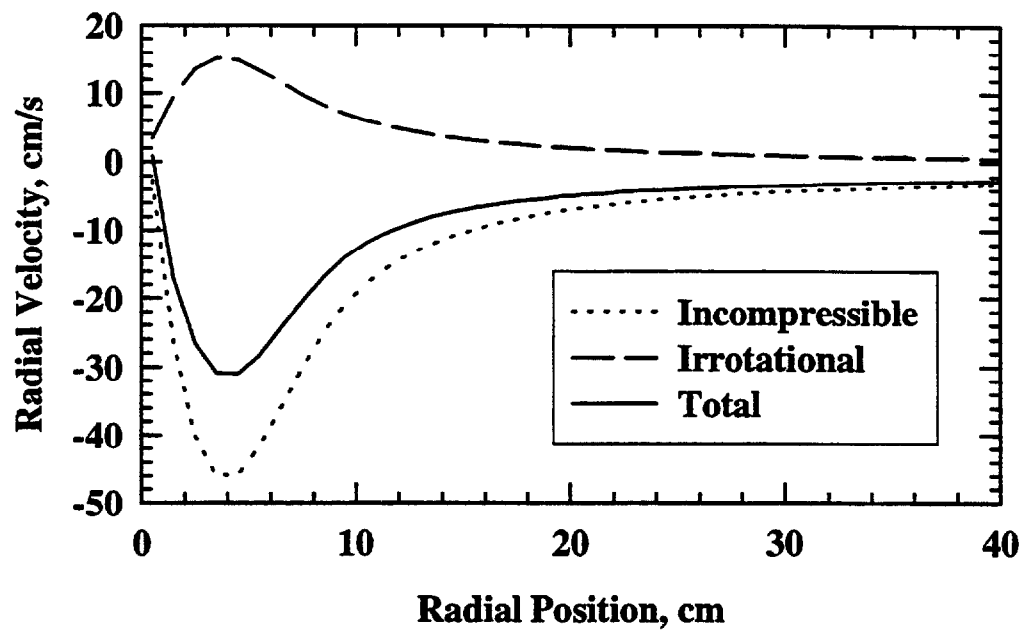


Figure 3.17a Decomposition of the radial velocities at $z = 0.5$ cm into irrotational velocity due to heat release and incompressible velocity caused by vorticity.

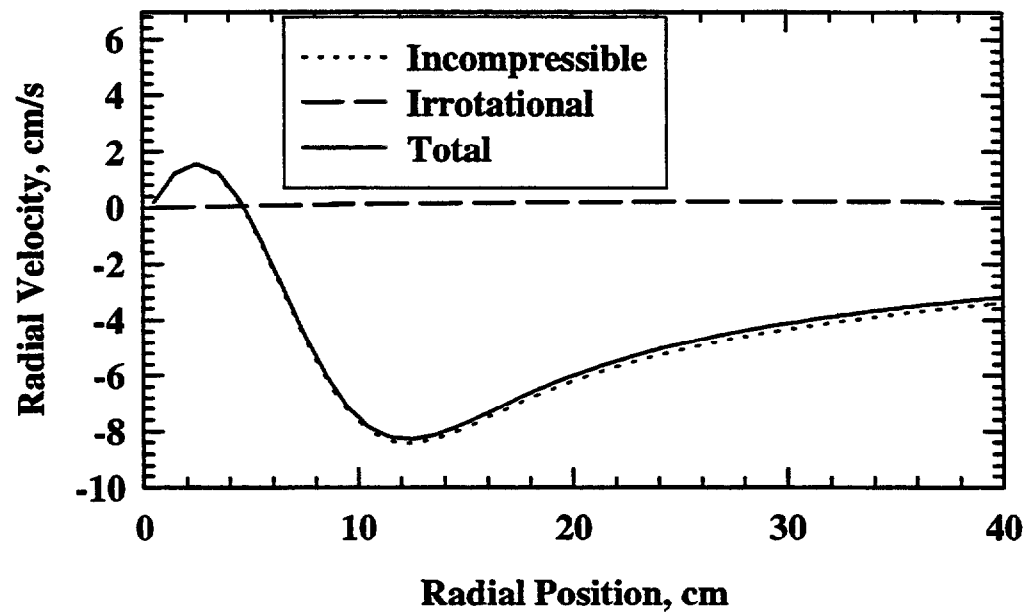


Figure 3.17b Decomposition of the radial velocities at $z = 42.5$ cm into irrotational velocity due to heat release and incompressible velocity caused by vorticity.

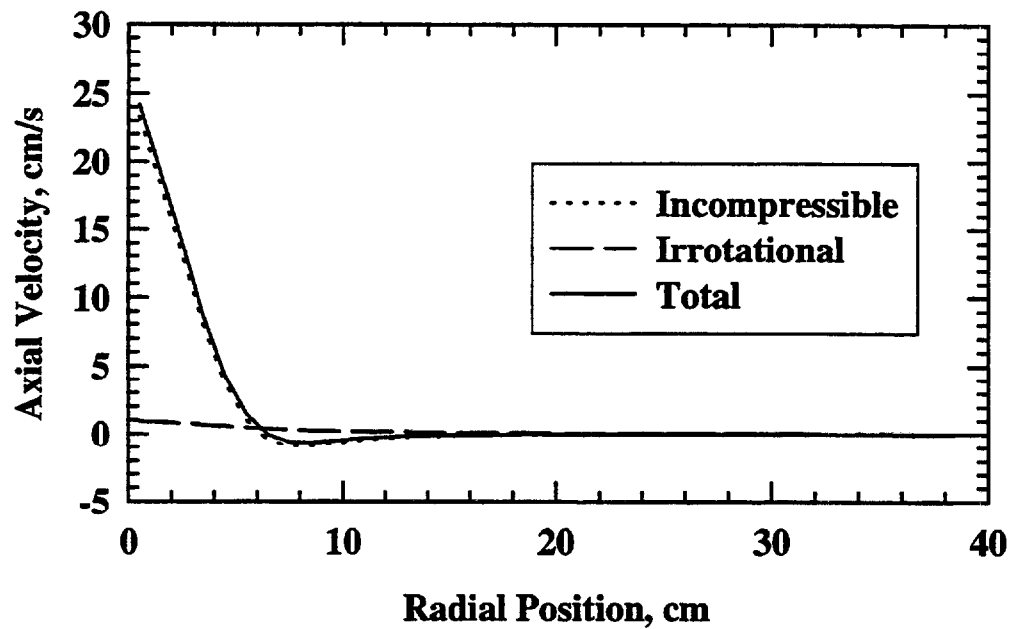


Figure 3.18a Decomposition of the axial velocities at $z = 0.5$ cm into irrotational velocity due to heat release and incompressible velocity caused by vorticity.

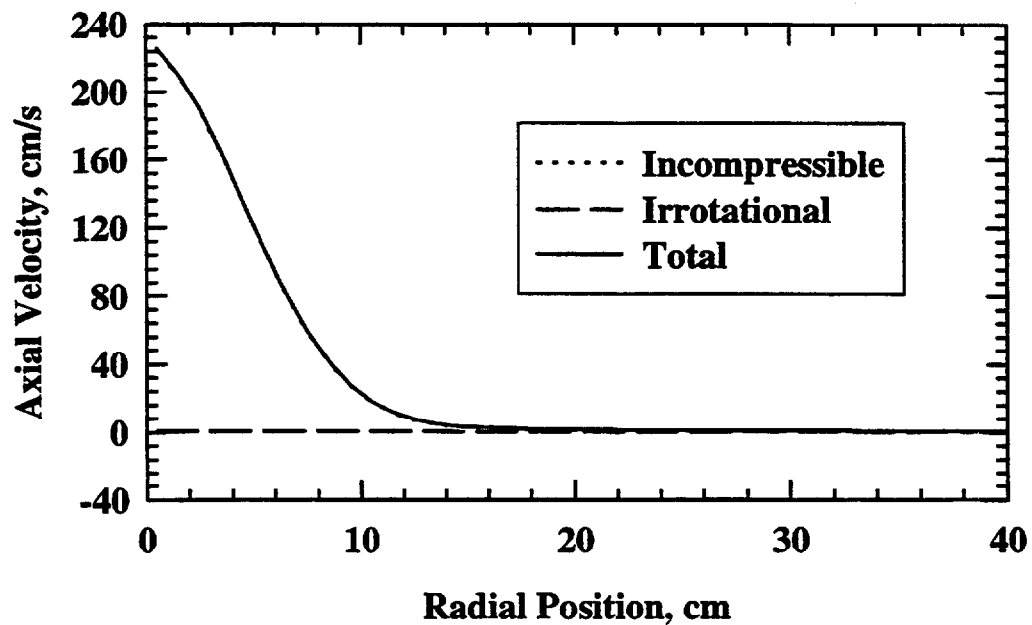


Figure 3.18b Decomposition of the axial velocities at $z = 42.5$ cm into irrotational velocity due to heat release and incompressible velocity caused by vorticity.

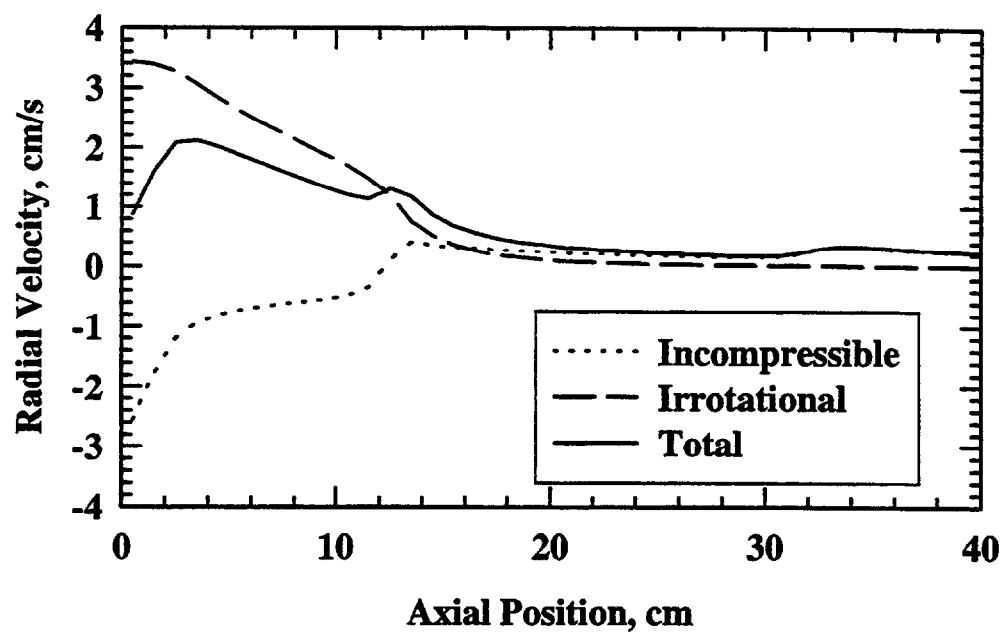


Figure 3.19 Decomposition of the radial velocities at $r = 0.5$ cm into irrotational velocity due to heat release and incompressible velocity caused by vorticity.

CHAPTER 4 LDV RESULTS AND DISCUSSION

The mean entrainment flow field obtained from the LDV measurement of vertical and horizontal velocity components of the flow field induced by the 7.1 cm toluene pool fire with a 51 cm sheet metal floor is discussed first. The vorticity distribution computed from the mean velocity field is also discussed. The transient properties of the velocity field including Probability Density Functions (PDFs) and Power Spectral Densities (PSDs) are discussed next. Entrainment rates deduced from the mean velocity field are reported and compared with available data and a correlation. Fire-induced flow velocities predicted by the numerical model are compared with the experimental data. Some improvements in these predictions are obtained by using the actual visible flame shapes for the present fires.

4.1 The Mean Entrainment Flow Field and the Vorticity Distribution

Figure 4.1 shows a two-dimensional vector plot of the measurements of mean velocities around the fire. The numerical values of the data are provided in Table F.1 in Appendix F. Although data on only one side of the fire are collected, velocity vectors have been plotted on both sides in Fig. 4.1 to emphasize the assumed mean axisymmetry of the fire. The mean visible flame interface is plotted as a solid curve and the farthest position of the visible flame interface is plotted as a dashed curve. Values of the radii of the mean and the farthest visible flame boundary are documented in Table 4.1. Near the liquid surface, these curves are close to each other but vary by up to 0.25 pool diameters near the height of one diameter. The measurements show that a radial inflow is established even at a radial distance of 13.5 cm (almost 2 diameters) from the fire

centerline. Part of the inflow at large radii turns and flows in a vertical direction as it gets towards the fire due to the effect of flame buoyancy while the radial inflow velocity remains almost unchanged despite the reduction in area. As the visible flame interface is approached the flow accelerates and turns upward to become predominantly vertical due to the combined action of the density gradient and the expansion generated by the heat release. The experimentally observed flow field in Fig. 4.1 is qualitatively similar to that discussed in detail by Baum and McCaffrey (1988).

Table 4.1 Radii of the visible flame boundary

Height (cm)	Mean Flame (cm)	Maximum Flame (cm)
1	2.5	2.6
2	1.8	2.0
3	1.6	2.0
4	1.5	2.5
5	1.4	3.2
6	1.5	3.5
7	1.5	3.6
8	1.5	3.7
9	1.5	3.7
10	1.5	3.8
11	1.8	4.0
12	2.0	4.5

A consequence of the velocity field shown in Fig. 4.1 is that the choice of R in eq. (1.1) for estimating the mass of air set in motion by the fire has to be relatively large. A second observation from Fig. 4.1 is that out of the air mass set in motion only a small part crosses the visible flame interface. The definition of entrainment based on mass flow entering the visible flame implied in the combustion literature is therefore not identical to

the definition in the fluid mechanics literature given in eq. (1.1). The measurements shown in Fig. 4.1 are useful in revealing these facts.

A single component (in the azimuthal direction) of the mean vorticity is computed from the mean velocity data. Since the grid spacing in the mapping of the velocity field around the pool fire is 2 cm in the radial direction and 1 cm in the vertical direction, a discussion about the validity of the resulting vorticity becomes necessary. Vorticity can not be measured directly, instead it has to be obtained from a spatial derivative of velocities using a suitable finite differencing scheme. The uncertainties in the velocity measurements are amplified by the process of taking a derivative and cause up to an order of magnitude higher uncertainties in the vorticity estimates. For this reason, vorticity measurement remains a challenge in experimental fluid dynamics. According to Lourenco and Krothapalli (1995), the error in vorticity measurement stems from two sources of different nature, one is the truncation error associated with the finite differencing scheme, and the other is the uncertainty in the velocity measurement. While the truncation error decreases with a finer grid, the uncertainty from the velocity measurements increases with a smaller grid spacing. One method to increase the accuracy of vorticity measurement is to adjust the grid size to minimize the composite error. Another method to attenuate these errors in differentiating the velocity to obtain vorticity is to refine the measured velocity field by convolving it with an axisymmetric Gaussian kernel (Reuss et al., 1989). In the present LDV measurements, no effort is made to increase the quantitative accuracy of the estimated vorticity. It is believed, however, that the grid sizes are large enough to diminish the effect of uncertainty in velocity measurements.

For a complete view of the qualitative vorticity distribution, a three-dimensional representation of the vorticity in the near region of the pool fire is given in Fig. 4.2. While the radial velocity field induced by the buoyant diffusion flame does not have any sharp cutoff or change in character at the flame boundary, the vorticity field has a feature very similar to that of the temperature field in that it has a sharp drop-off at the flame surface. Away from the pool fire, the flow is almost irrotational as shown by the negligible vorticity. These data are consistent with the theory proposed by Baum and McCaffrey

(1988) that in a buoyant diffusion flame, vorticity is generated solely by the density gradient near the flame boundary. The vorticity distributions at three different heights are plotted in Fig. 4.3. The data show that the vorticity increases with height at a given radial location near the flame. This coincides with the trend of vertical velocity which also increases with height at a certain radial location, as shown by Fig. 4.4. However, unlike the vorticity, the vertical velocity increases with height even at radial locations away from the flame surface. It is noted that the contribution of the radial velocity component to the vorticity is much smaller when compared with that of the vertical velocity component. Thus it can be concluded that the vorticity is mainly generated by the change in vertical velocity along the radial direction. This proves the validity of the neglect of vorticity component originating from the radial velocity change in the axial direction in the numerical model discussed in Chapter 3.

As the vertical velocity increases with height in the flame region, its capability to generate vorticity also increases as the flow has larger momentum to break away from the surrounding air and to accelerate the spinning of fluid elements. In Fig. 4.3, the positions of the average and farthest visible flame boundaries are shown for reference. It is noted that the radius of the maximum visible flame boundary and the radial extent of fluid containing vorticity are comparable. To define a flow area for the calculation of the entrainment rate, Taylor (1956) proposed two ways to delineate the entrainment surface, one is the visible flame interface, and the other is the vortex sheet. Although, theoretically a vortex sheet can be used to define the boundary for the calculation of entrainment, it is much more difficult to measure than the visible flame boundary. In this study, the air entrainment rate into the maximum visible flame boundary is calculated using the normal component of velocity and ambient density. At locations very close to the flame, the mean temperature of the air is expected to be higher since there is some heat transfer between the air and the flame by diffusion and mixing. The choice of ambient density provides an upper bound on the mass flux of material entering the visible flame.

4.2 The Transient Characteristics of the Entrainment Phenomena

Baum and McCaffrey (1988) discussed that the fire-induced flow field is inherently transient but transient measurements were not available for inclusion in their analysis. The data resulting from the present LDV measurements are transient and reveal some interesting features of the flow field. The findings and the data can also be of use in the evaluation of current and future transient field models of pool fires. The Probability Density Functions (PDFs) of radial velocity, U_r , and axial velocity, U_z , at three different heights at $r = 3.5$ cm, 4.5 cm, and 11.5 cm are shown in Fig. 4.5 through Fig. 4.14. The PDFs are plotted as a function of the velocity values. The mean and RMS values of the velocity at each location are noted in the figures.

Fig. 4.5 shows the PDFs of the radial velocities at $z = 1, 5$, and 9 cm at $r = 3.5$ cm. At $z = 1$ cm, the mean velocity is 12.2 cm/s with negligible portion of velocities being negative. Sometimes the velocity can be as high as 30 cm/s, which is more than twice the mean value, indicating that there are considerable fluctuations even near the base of the fire. At $z = 5$ cm, the mean radial velocity becomes smaller, decreases to 6.3 cm/s, but the shape of the PDF does not differ very much from that at $z = 1$ cm, with a much larger RMS velocity of 5.6 cm/s in comparison to the mean value of 6.3 cm/s. At $z = 9$ cm location, a significant portion of the probability of radial velocities is associated with negative values. Thus material from the flame flows outward for some realizations of the flow at this location.

Figure 4.6 shows the PDFs of vertical velocities at the same locations as those in Fig. 4.5. At $z = 1$ cm, there is a considerable portion of negative velocities although the mean velocity in the axial direction is 6.44 cm/s. At $z = 5$ cm, the weighted central point of the major portion of the PDF is around 16 cm/s, but the mean velocity is in fact 22.7 cm/s due to the occasional intrusion of the high velocity flame into the measuring volume. As a result, the RMS of the velocity also increases to 28.18 cm/s. At $z = 9$ cm, the effect of flame intrusions becomes even stronger. The mean velocity increases to 42.72 cm/s, and the RMS increases to 42.04 cm/s. To discuss the presence of the flame in the measuring volume further, the PDF of the vertical velocity at $z = 9$ cm is plotted in Fig.

4.7 with a larger range for the velocity coordinate. The PDF has a finite small value until the velocity increases to 130 cm/s. Small numbers of realizations up to 200 cm/s are also observed. Figure 4.1 also shows that $z = 9$ cm at $r = 3.5$ cm is inside the maximum visible flame boundary. At $z = 5$ and 9 cm, the vertical velocity is rarely negative as seen in Fig. 4.6. There is fluctuation of velocities even when the intrusion of flame is not taken into account as shown by the shape of the PDFs.

Figure 4.8 is the PDF of the measured radial velocities at $z = 1, 5$, and 9 cm at $r = 4.5$ cm. As with the values at $r = 3.5$ cm, the mean velocity becomes smaller and the shape of the PDF becomes flatter with height. The negative tail of the PDF becomes larger and longer with height because the flame becomes more unsteady. The PDFs of the vertical velocities at the same locations are presented in Fig. 4.9. At $z = 1$ cm, the mean vertical velocity is rather small and can be overcome by the fluctuations, resulting in finite probabilities of negative velocities. Both the mean and the RMS of the vertical velocities increase with height. At $z = 9$ cm, although the fluctuation becomes stronger as shown by the flatter shape of the PDF and the larger RMS, the velocity is seldom negative because of the much larger mean. The PDFs of the radial velocity at $z = 3, 9$, and 22 cm at $r = 11.5$ cm are displayed in Fig. 4.10. The shape of the PDFs does not change significantly with height. The RMS of the velocities at the three locations, 4.6 cm/s, 4.8 cm/s, and 4.2 cm/s, respectively, are close to each other because the $r = 11.5$ cm location is always outside the flame boundary at all three heights. It is noted that the mean velocities decrease from 8.8 cm/s at $z = 3$ to 5.8 cm/s at $z = 9$ cm and to 4.2 cm/s at $z = 22$ cm. This reduction in mean radial velocity with height is probably caused by an increase in flame radius. Figure 4.11 shows the PDFs of the vertical velocity at the same locations. The mean values of vertical velocities increase with height, but the RMS remain almost the same, although the shapes of the PDF of the velocities change considerably with height. The absence of the flame in the measuring volume at $z = 22$ cm and $r = 11.5$ cm is also demonstrated by the fact that the vertical velocity at this point never increases beyond 50 cm/s, as shown in Fig. 4.12.

To examine the frequency content of the transient velocity data, Power Spectral Densities (PSDs) are calculated from the time-series of the velocity measurement. A standard 512-point fast Fourier transform is applied to every 512 data points in the time-dependent record of velocity. Individual FFTs are averaged over many realizations to obtain PSDs.

Fig. 4.13 shows the normalized PSDs of the radial velocity measurements at three different heights at $r = 4.5$ cm. There are no marked peaks in any of the plots, showing that the velocity field is not changing at some specific frequency. The PSDs of the vertical velocities at $r = 4.5$ cm are plotted in Fig. 4.14. The PSDs of the radial velocities and the vertical velocities at $r = 11.5$ cm are plotted in Fig. 4.15 and Fig. 4.16, respectively. All these plots have the same characteristics as Fig. 4.13 and show that the characteristic pulsation frequencies of the pool fire are not transferred to the entrainment velocity field.

4.3 Entrainment Rates Based on the Mean Entrainment Flow Field

Only a part of the oxygen that flows into the visible flame interface with the air is involved in the combustion reactions. Therefore, even a smaller fraction of the oxygen set in motion by the fire is consumed by it. The remaining oxygen together with the nitrogen set in motion mixes with the combustion products and reduces their relative concentrations and temperature in the upper layer and in the exhaust flow.

Present entrainment rate measurements based on the mean velocity data obtained at three different radial positions ($R = 4.5, 6.5, 11.5$ cm) as well as estimates of entrainment into the visible flame boundary are shown in Fig. 4.17. The entrainment up to a height z based on the cylindrical surfaces $R = 4.5, 6.5, 11.5$ cm is calculated as:

$$\dot{m}_{\text{ent}}(z) = 2\pi\rho_{\infty}R\int_0^z \overline{U}_r(z)dz \quad (4.1)$$

Since the velocity vector has both a \overline{U}_z component and a \overline{U}_r component at the radial locations under consideration, the above estimates are always lower than the entrainment

rate given by eq. (1.1). In some fire size calculations, mass flow rate across the visible flame boundary is desired. In order to calculate the entrainment into the visible flame surface, the shape of the maximum extent of flame is determined from a video record of 30 frames as shown in Fig. 4.1. The entrainment into this surface up to a height z was calculated as:

$$\dot{m}_{\text{ent}}(z) = \int_0^z \frac{2\pi R(z)}{\cos \theta} \rho_{\infty} (\bar{\mathbf{U}} \cdot \bar{\mathbf{n}}) dz \quad (4.2)$$

where $R(z)$ is the maximum visible extent of the flame boundary, θ is the angle between the local flame surface and the vertical, $\bar{\mathbf{U}}$ is the local velocity vector, and $\bar{\mathbf{n}}$ is the unit vector in the direction $-\theta$ to the horizontal. The integration was completed numerically.

The data based on the 11.5 cm position show that the mass-flow rate of air set in motion by the fire is a factor of up to 6 higher than the estimates based on the correlation of Delichatsios (1987). As discussed in Chapter 1 and in Appendix A, the correlation by Delichatsios (1987) uses the fundamentally correct nondimensional parameter Fr_f . Hence, only this correlation is plotted in Fig. 4.17. The estimates of mass flow rates based on the two smaller radial positions are lower and the data based on $r = 4.5$ cm are close to the entrainment into the visible flame boundary shown by dark circles. Several measurements from past work are also shown in Fig. 4.17. The correlation of Delichatsios (1987) was developed using the data of Cetegen et al. (1984), Beyler (1983), and Delichatsios and Orloff (1983). The correlation shows satisfactory agreement with these data although there is considerable scatter amongst the data. The data of Weckman (1989) are based on measurements of axial velocity in the fire and appear to be in reasonable agreement with, although consistently lower than, the correlation. The data of Thomas et al. (1965) were obtained from velocity measurements very near the edge of the pool. Thomas' data are a little higher than the correlation. The present $r = 4.5$ cm measurements are similar to Thomas's data, probably because both are entrainment rate of air into a cylindrical surface around the pool.

It is noted that the correlation shows slope changes near $z/D = 1$ and $z/D = 6$. At both points, the slope becomes larger, indicating a stronger local entrainment rate. A single set of experimental data from the literature is not available to confirm these slope changes. The experimental data from the literature in different z/D regimes are obtained either from different pool fires or from different measurement techniques such as a smaller sampling hood in the case of Toner et al. (1987). In the present investigation, the local entrainment rates of air into an imaginary cylinder at $r = 6.5$ and 11.5 cm (circle with center dot and open circle in Fig. 4.17) becomes less as shown by the flatter trend in the nondimensionalized entrainment rates. However, the present experimental data for entrainment into the maximum visible flame boundary (black circles) show a trend of increase of entrainment rates with height after $z/D = 1$. This is mainly caused by an increase of entrainment area with larger maximum visible flame boundary at higher locations. This shows that different choices of the definition of air entrainment lead to qualitative as well as quantitative differences.

4.4 The Predicted Entrainment Velocity Field

Using the numerical model developed in Chapter 3, the flow field induced by the 7.1 cm toluene pool fire with the floor is computed. The predicted velocity vector field is shown in Fig. 4.18. It is in qualitative agreement with the measured mean flow field shown in Fig. 4.1. Air is entrained starting at very large radii. Near the floor, the flow is almost horizontal. At smaller radii, the magnitude of the velocity increases because of reduced flow area. In the region very near the fire, the velocity turns upward and increases significantly in magnitude by the buoyancy effect of the flame. Spread of the flame with axial distance can be observed from the dependence on height of the radial position where the velocity turns upward. The predicted velocity component due to expansion solely caused by the heat release rate is shown in Fig. 4.19. According to the model, the volumetric heat release rate is the largest at the bottom of the flame resulting in

the largest expansion velocity near the flame base. The velocity decreases with radial distance due to the increase in flow area. At $r = 3.5$ cm, the velocity becomes smaller with height because of the decrease in volumetric heat release rate. The predominantly horizontal flow pattern clearly shows the effect of the floor. The component of the flow field caused by vorticity generated by the density gradient in the flame is shown in Fig. 4.20. The velocity magnitude is much larger than that of the expansion flow field, and it is clear that the total entrainment flow field is dominated by the incompressible flow field generated due to vorticity. In the lower region very close to the flame boundary, the velocity is a little downward, and there are some negative vertical velocities remaining in the total velocity field shown in Fig. 4.18. Although there are instantaneous downward velocities in the vertical velocity measurements as shown by flow visualization and the PDF of the vertical velocities in Figs. 4.6, 4.9 and 4.11, the vertical component of the mean velocities is not expected to be negative. It is speculated that the vorticity is overestimated, which in turn results in an overprediction of the entrainment.

Measurements and predictions of vertical velocity profiles at $z = 1$ cm, 6 cm, and 12 cm are plotted in Fig. 4.21. The predicted velocities are obtained by interpolation on the original computation grids. At $z = 1$ cm, both the predicted and the measured velocities are near zero at locations away from the flame, while in the region very near the flame, the predicted velocity increases more rapidly than the measurements. At $z = 6$ cm and $z = 12$ cm, the predictions are smaller than the measurement in the far region, but are much larger than the measurement in the region near the flame boundary.

Comparisons of the radial velocity predictions and the measurements at the same heights are plotted in Fig. 4.22. At $z = 6$ cm and $z = 12$ cm, both the predictions and the measurements are small, and the agreement between them is relatively good. At $z = 1$ cm, although the discrepancy between the prediction and the measurement is small at $r > 9.5$, the agreement worsens very quickly at smaller radial locations. The predicted entrainment velocity is much larger than the measurement in the region near the flame.

The discrepancies between the measurements and predictions of the fire-induced flow field are primarily caused by errors in the prescription of the vorticity generation rate

and the heat release rate within the fire. Measurements of the visible flame shape, documented in Table 4.1 and shown in Fig. 4.1, show that the flame shape contracts quickly before remaining approximately constant for some distance. The measured flame shape and the predicted flame shape (McCaffrey's correlation for $R(z)$) are plotted in Fig. 4.23. Above $z = 12$ cm, the measured visible flame shape is assumed to expand at an angle of 8.5 degrees to the centerline of the burner. As a first step toward improving the predictions of the entrainment flow field, the $R(z)$ specification in the model was changed to the visible flame shape shown in Fig. 4.23.

Fig. 4.24 shows a comparison between the radial velocity measurements and the new predictions obtained using the visible flame shape. Although at $z = 1$ cm, the agreement becomes better in the region near the flame when compared with Fig. 4.22, the predictions become smaller than the measurements at larger radial positions. The predicted radial velocities at $z = 6$ cm and 12 cm also become smaller. Hence the vorticity becomes smaller with smaller flame radii. Figure 4.25 shows a comparison between the vertical velocity measurements and the predictions obtained with the mean visible flame shape. The overall agreement between the predictions and the measurements is better when compared with Fig. 4.21, apart from the fact that at $z = 1$ cm the vertical velocity becomes negative at $r = 3.5$ cm. Figure 4.26 shows the velocity vectors predicted using the visible flame boundary. These look similar to the measured mean velocity vectors in Fig. 4.1, except in the region near the flame base. An examination of the irrotational flow field component and the incompressible flow field component shows that the vertical velocities are negative in both fields in this region. Although the negative incompressible vertical velocities become smaller, they remain downward because the vorticity is still overpredicted.

In the numerical model the driving force of the entrainment flow field, namely the vorticity distribution and the volumetric heat release rate field, are estimated based on the flame structure correlations which were obtained by curve fitting the velocity and temperature data measured in a large gas fueled buoyant flame, since correlations for a purely buoyant liquid fueled pool fire are not available. Assumptions made in the analysis

such as Gaussian radial profile for the volumetric heat release distribution are also expected to affect the accuracy of the velocity predictions. To further refine the numerical model, the flame structure and velocity distributions of the purely buoyant diffusion flames have to be investigated further to provide a more realistic estimation of the vorticity distribution and the volumetric heat release rate distribution.

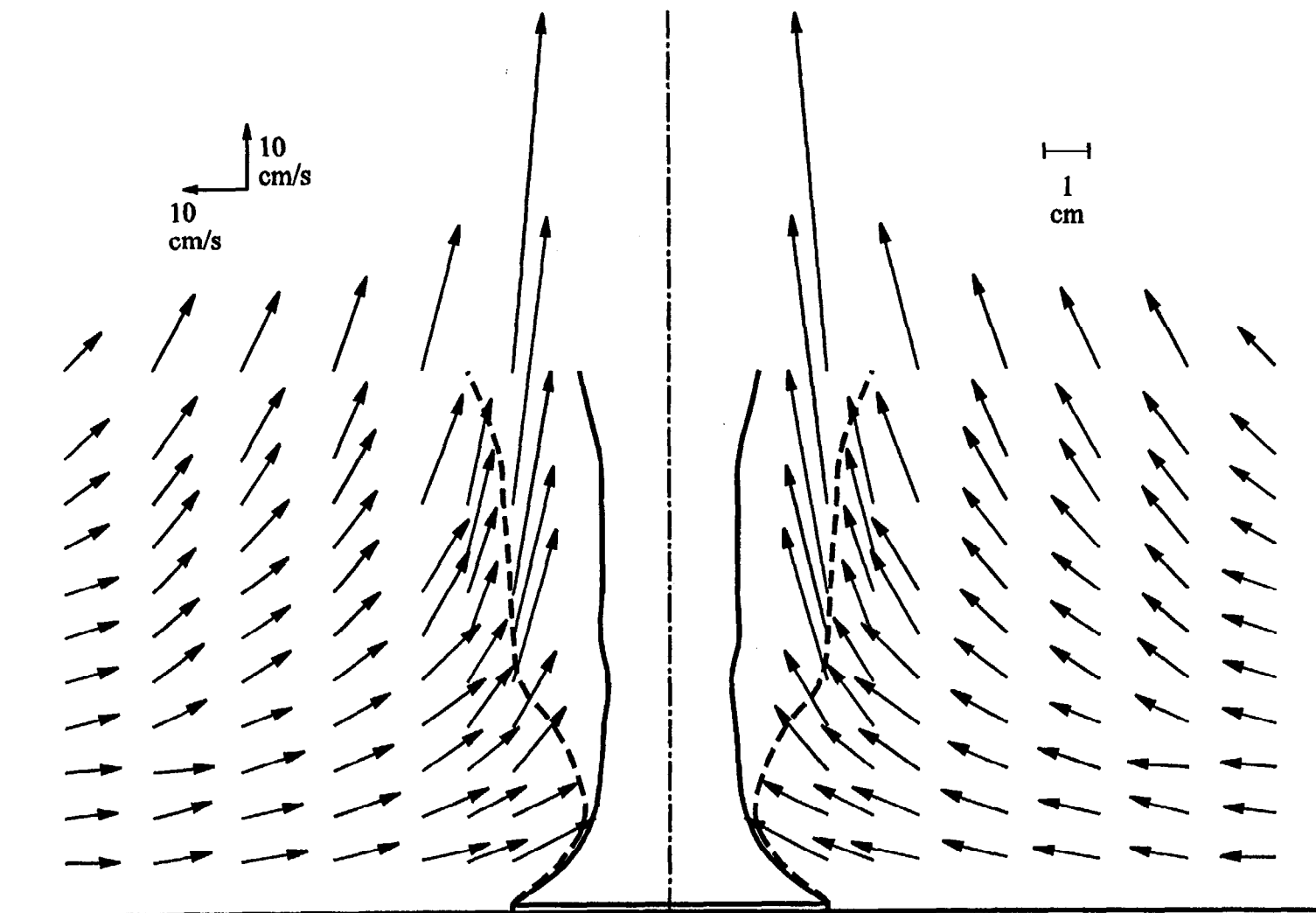


Figure 4.1 The mean velocity vectors around a 7.1 cm toluene pool fire obtained using LDV.

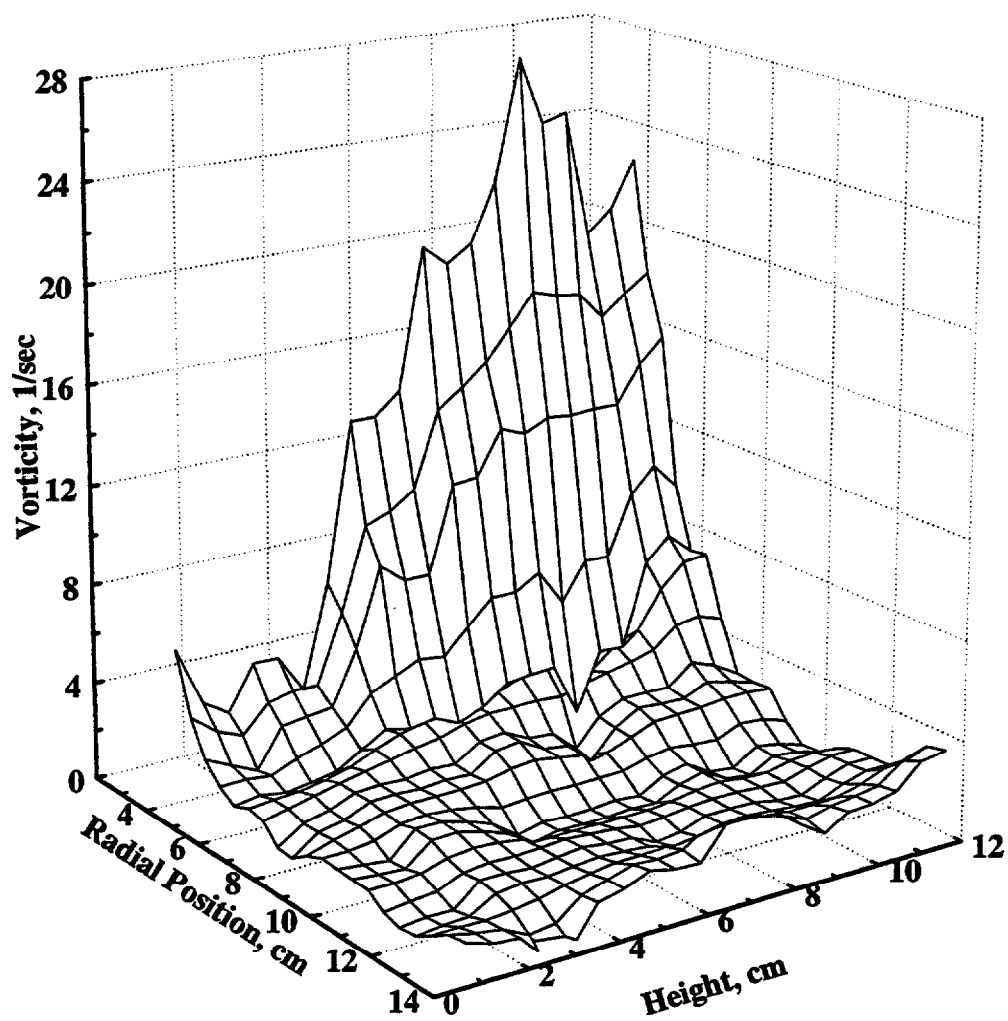


Figure 4.2 Azimuthal vorticity distribution in the near region of the flame evaluated based on mean velocity measurements.

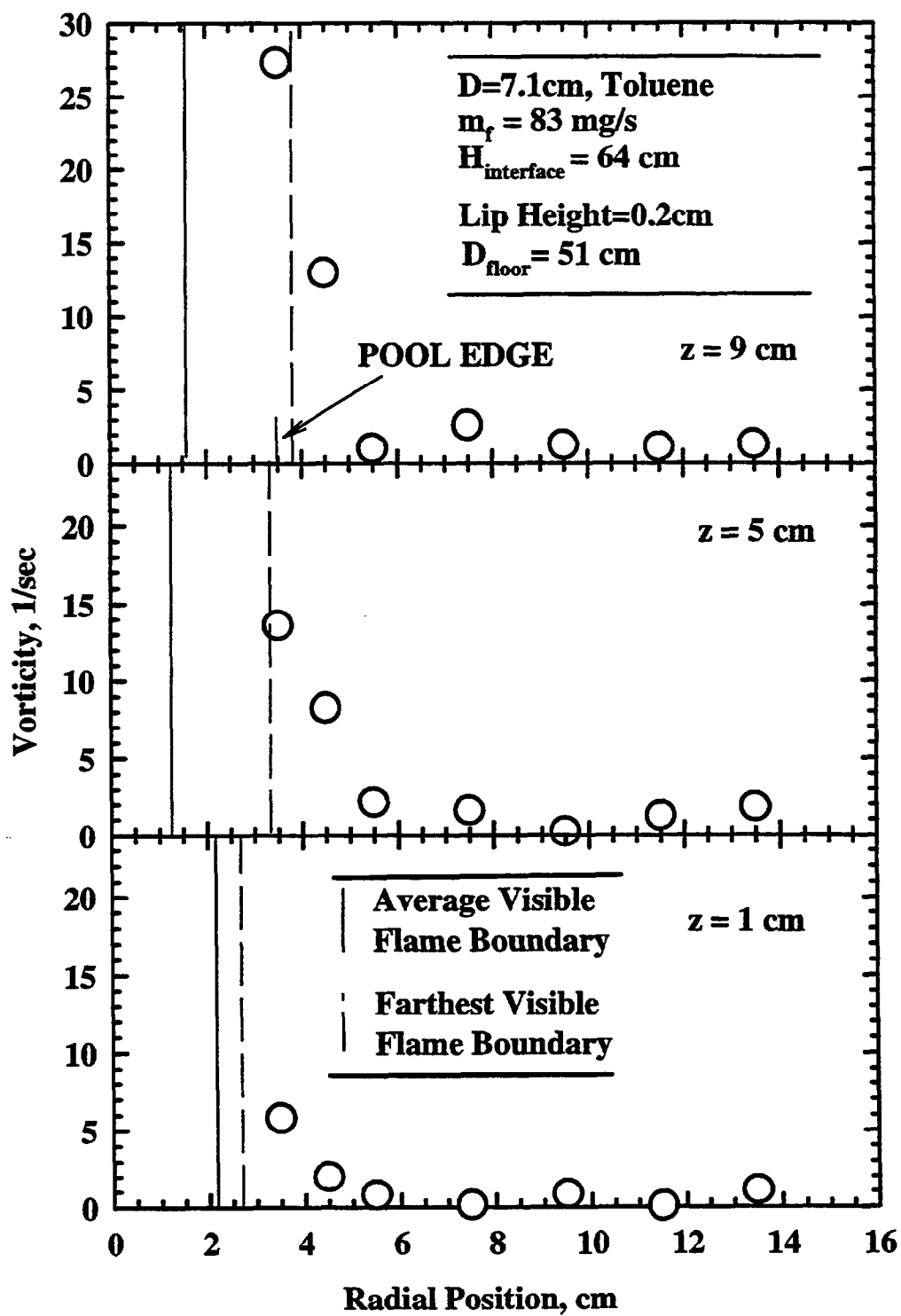


Figure 4.3 Vorticity distribution as a function of radial position at three different heights.

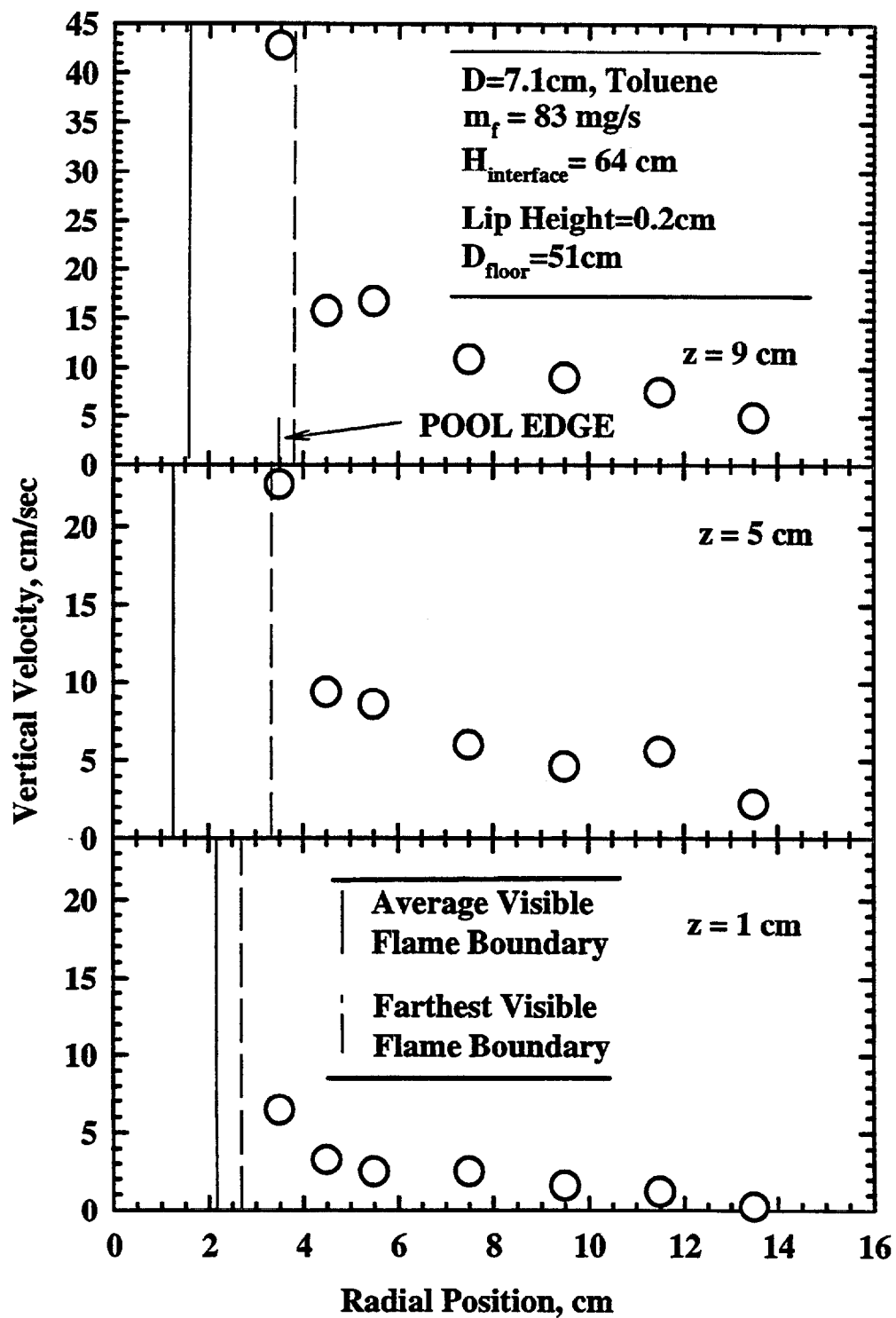


Figure 4.4 Vertical velocity distribution as a function a radial position at three different heights.

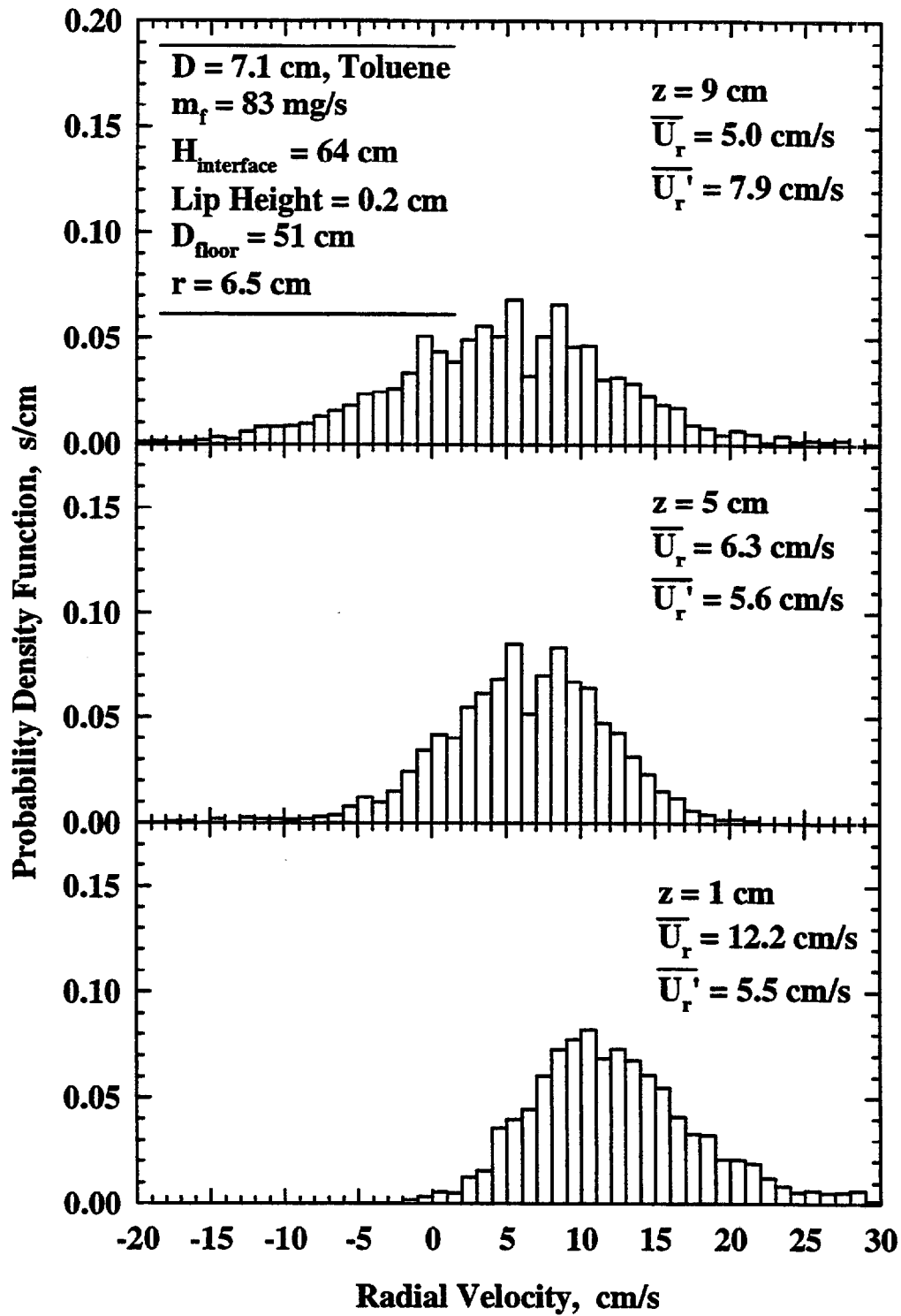


Figure 4.5 Discrete PDF of radial entrainment velocity at three different heights at $r = 3.5$ cm.

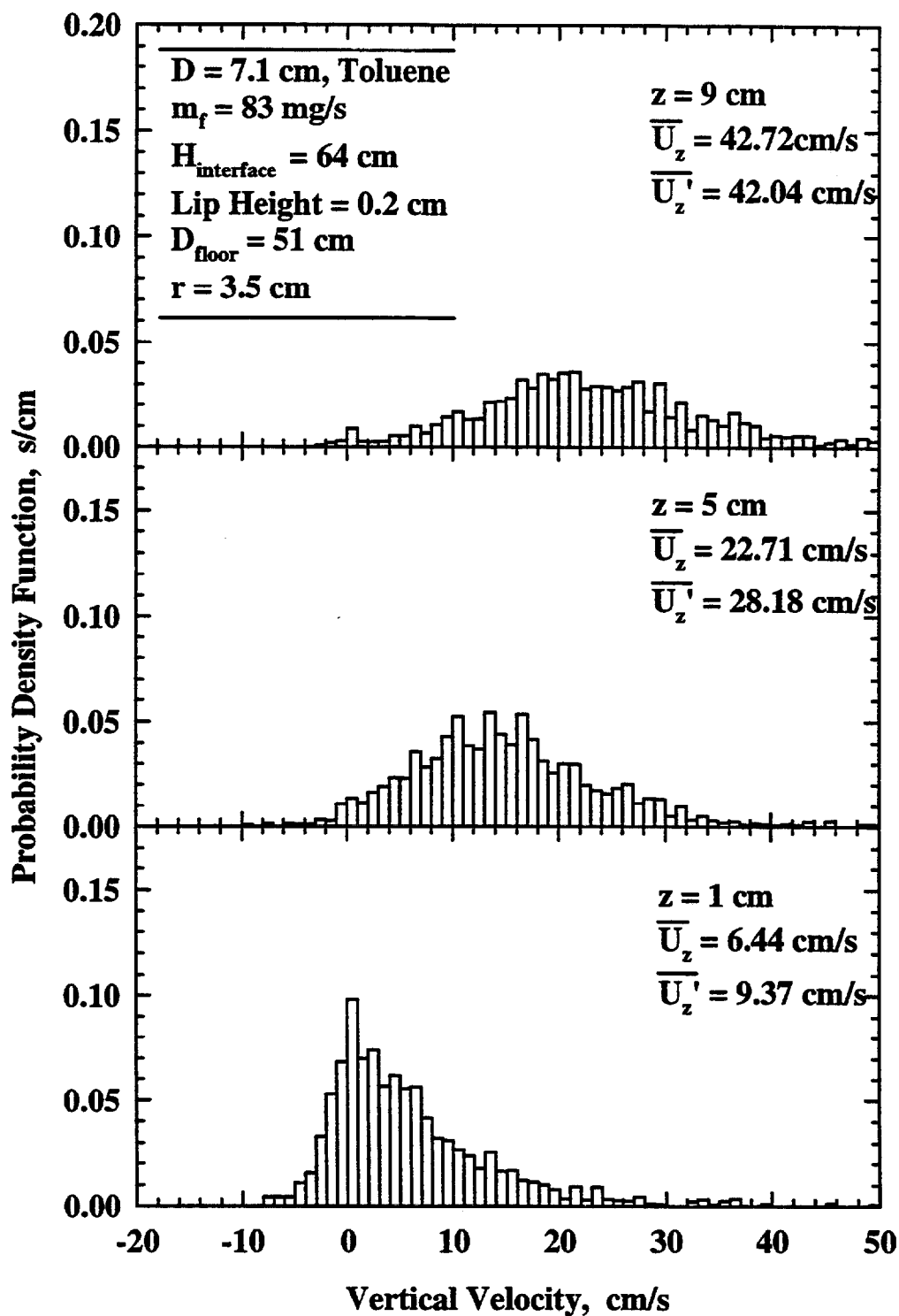


Figure 4.6 Discrete PDF of vertical entrainment velocity at three different heights at $r = 3.5$ cm.

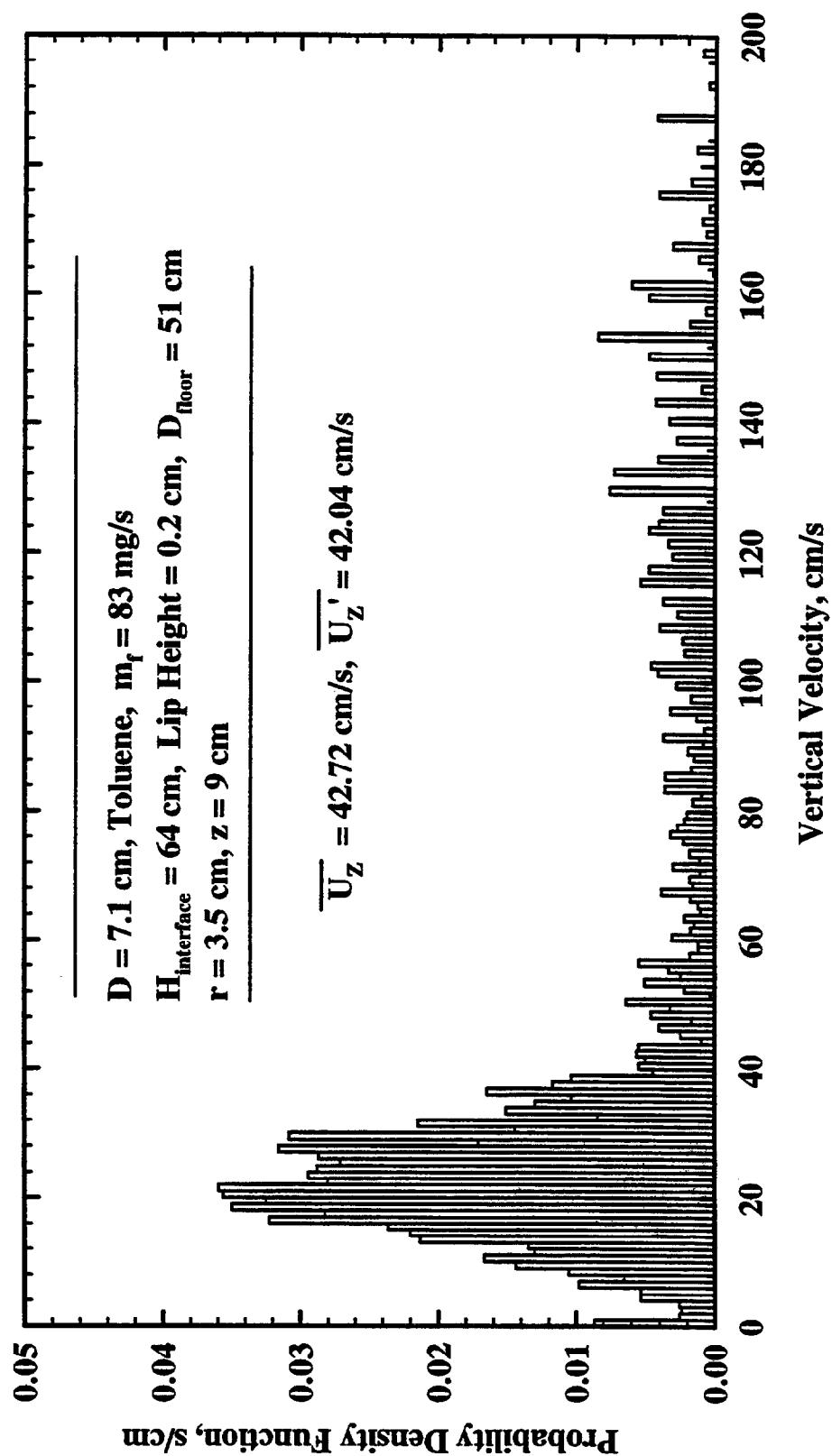


Figure 4.7 Discrete PDF of the vertical velocity at $z = 9 \text{ cm}$, $r = 3.5 \text{ cm}$.

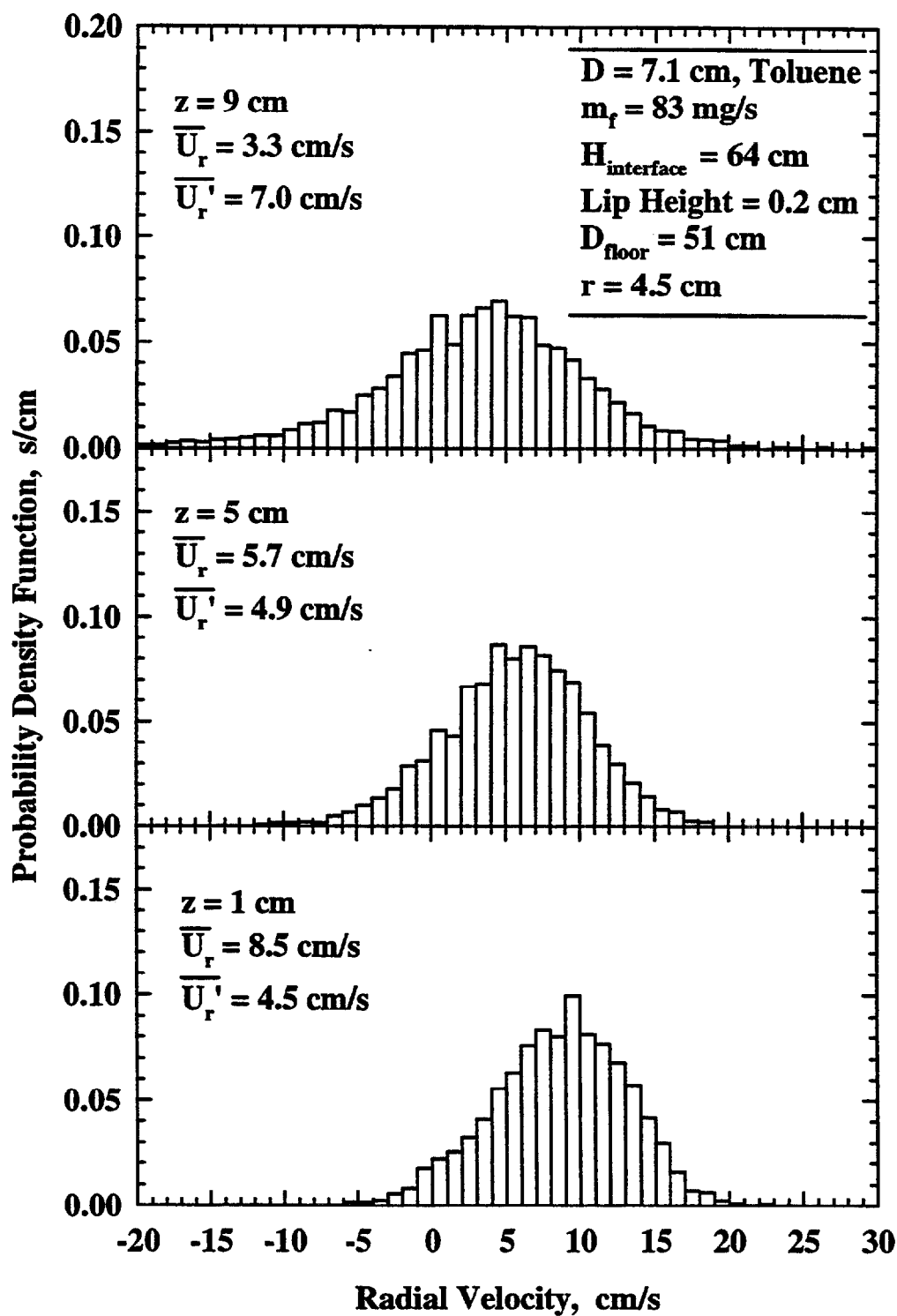


Figure 4.8 Discrete PDF of radial entrainment velocity at three different heights at $r = 4.5$ cm.

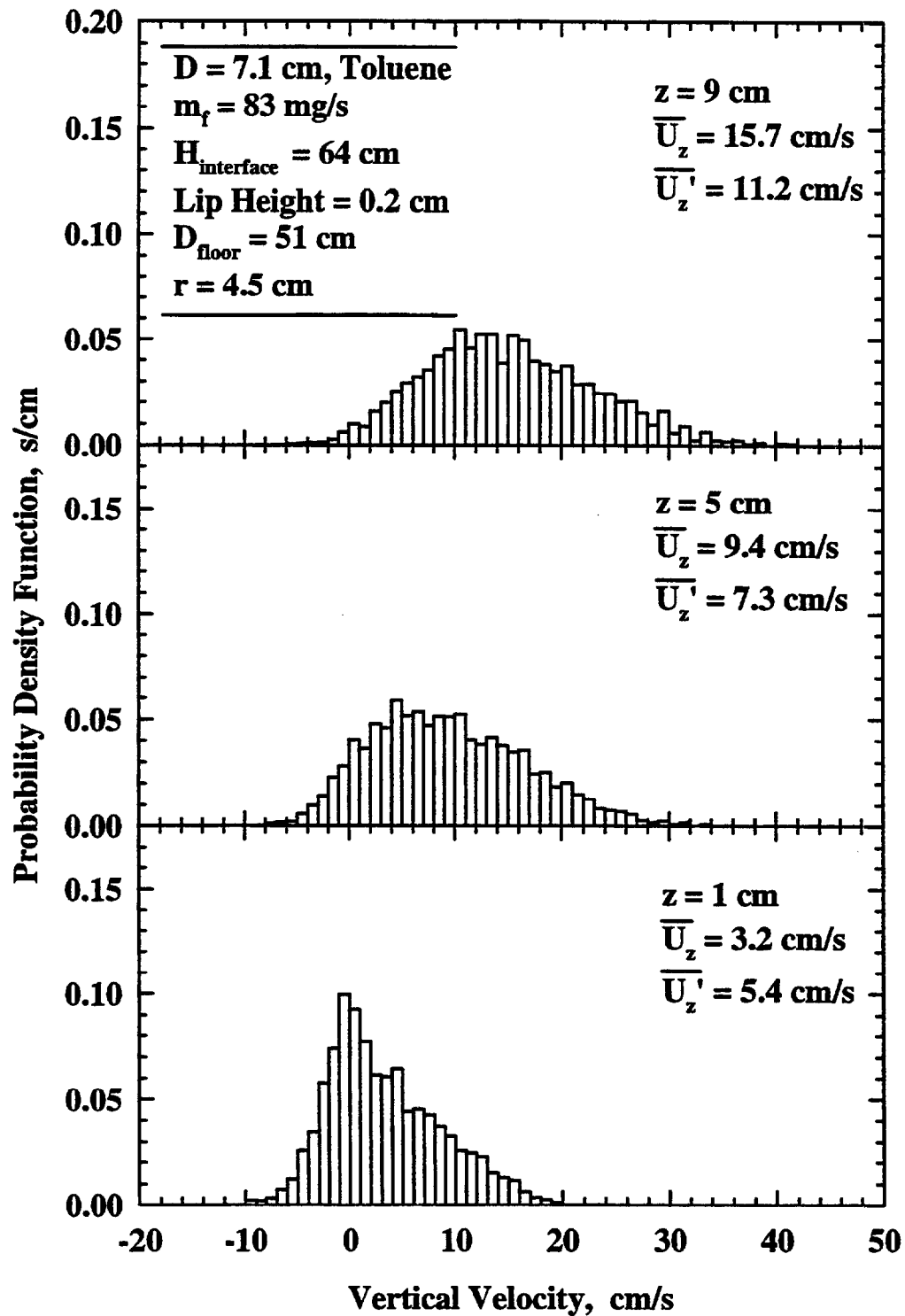


Figure 4.9 Discrete PDF of vertical entrainment velocity at three different heights at $r = 4.5$ cm.

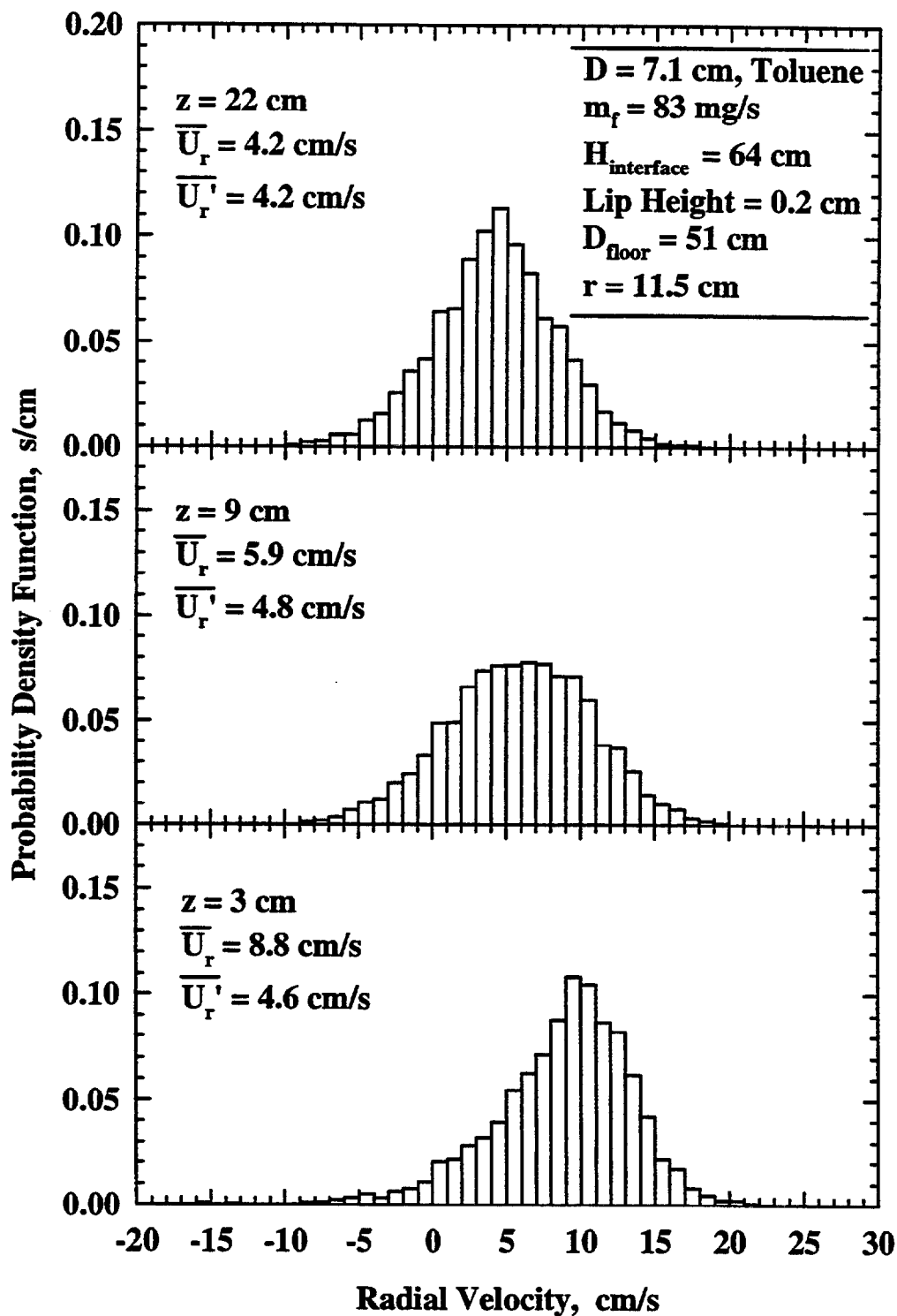


Figure 4.10 Discrete PDF of radial entrainment velocity at three different heights at $r = 11.5$ cm.

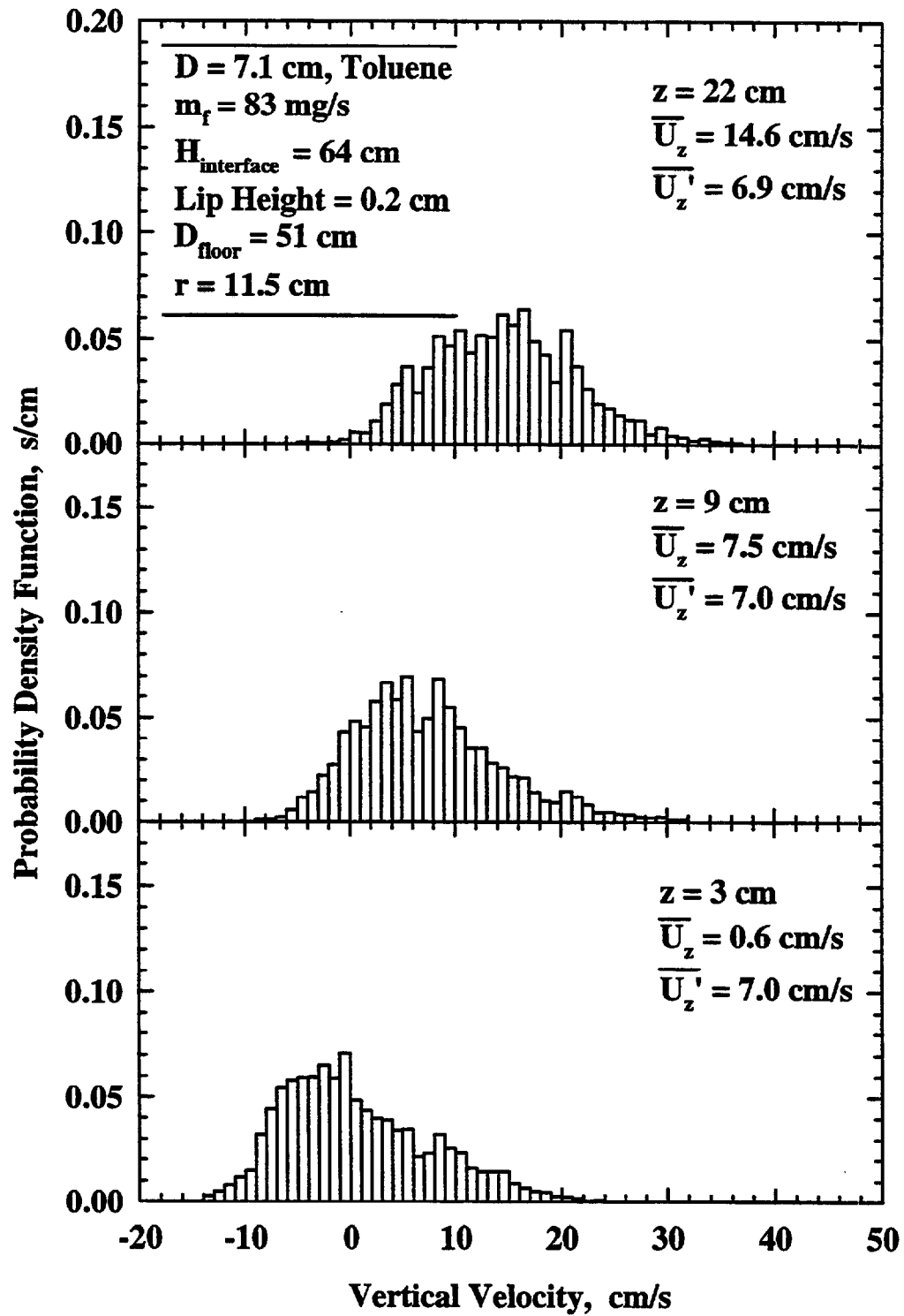


Figure 4.11 Discrete PDF of vertical entrainment velocity at three different heights at $r = 11.5 \text{ cm}$.

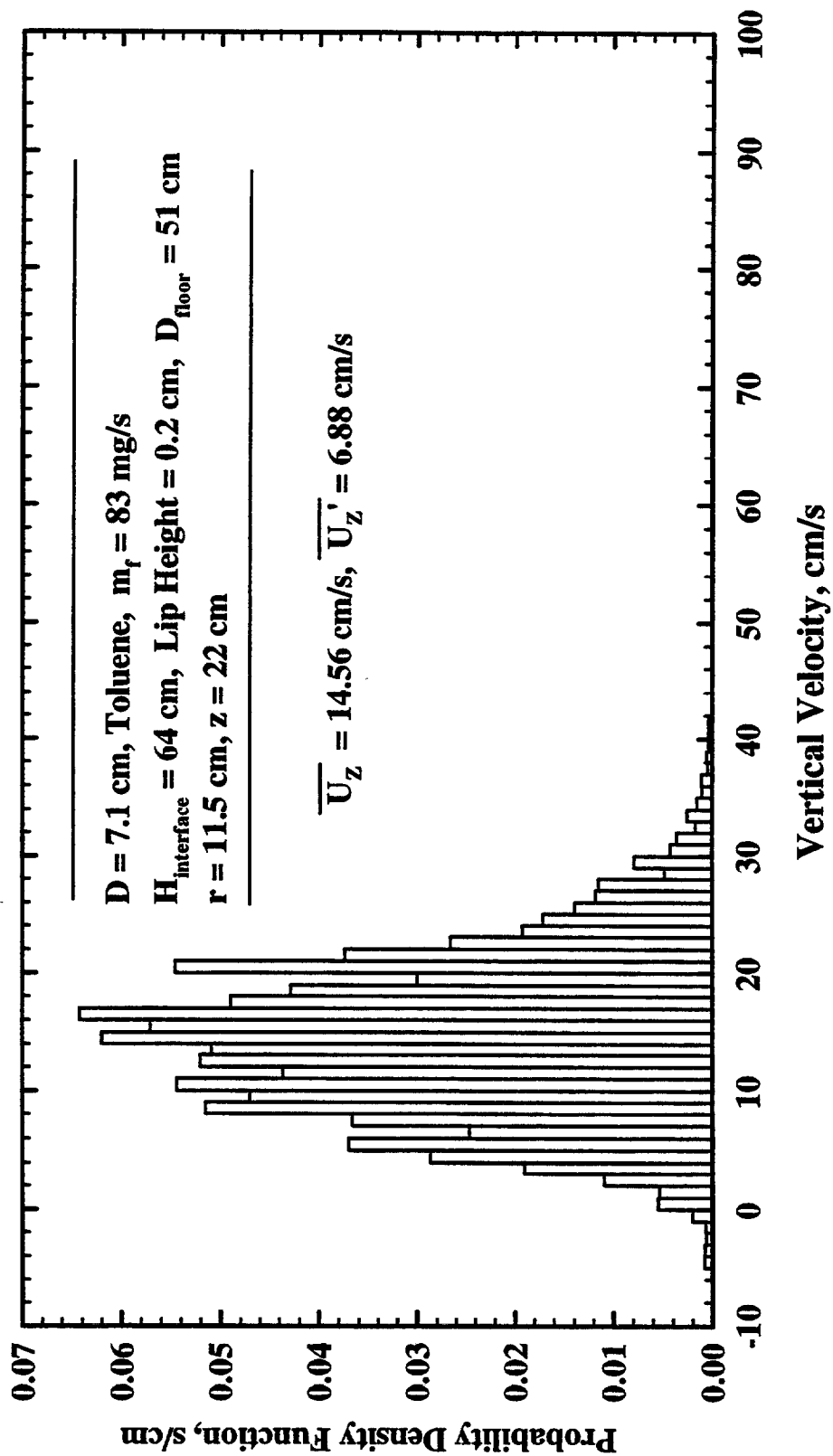


Figure 4.12 Discrete PDF of vertical entrainment velocity at $z = 22 \text{ cm}$ at $r = 11.5 \text{ cm}$.

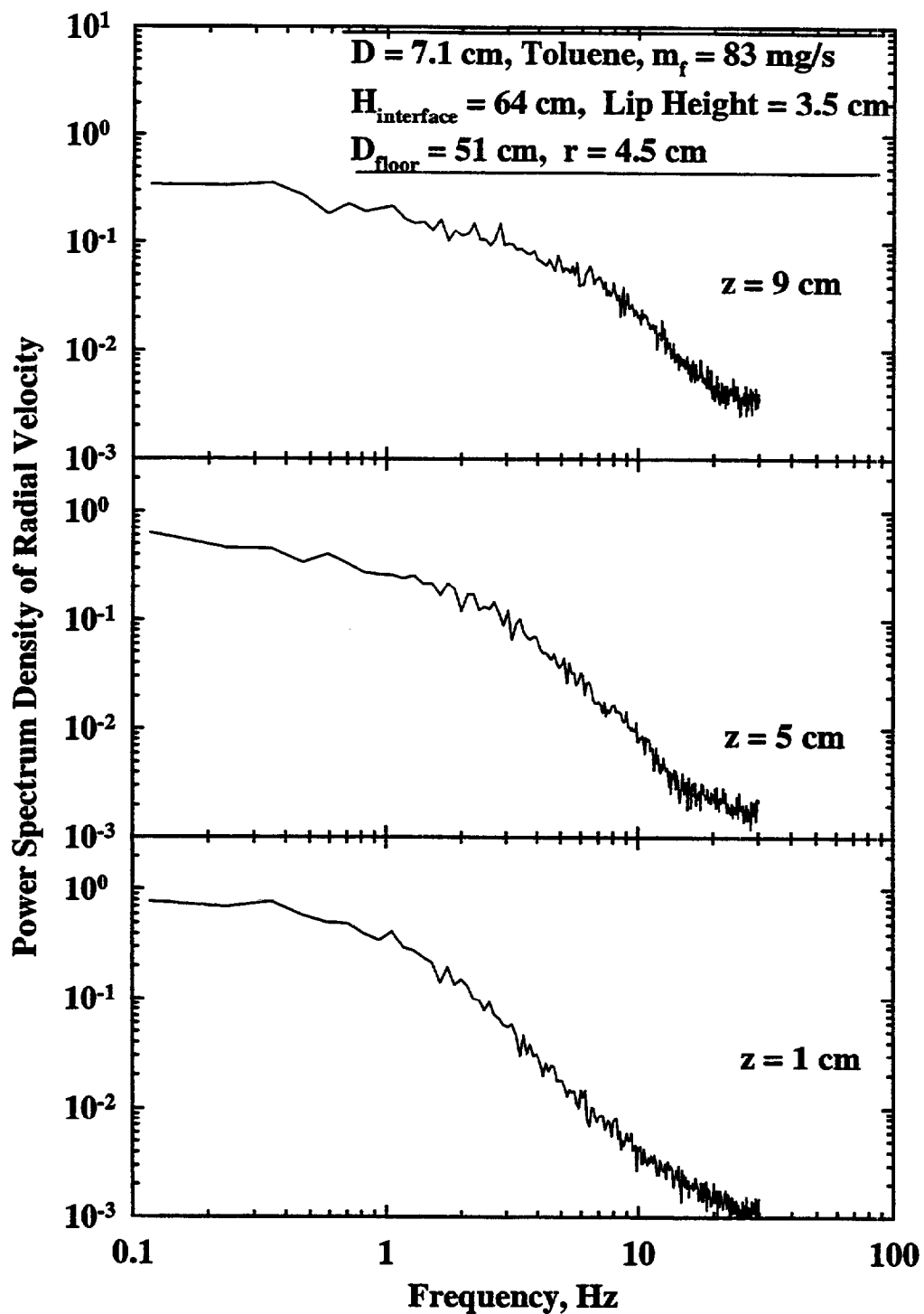


Figure 4.13 Power Spectrum Density of radial velocities at three different heights at $r = 4.5 \text{ cm}$.

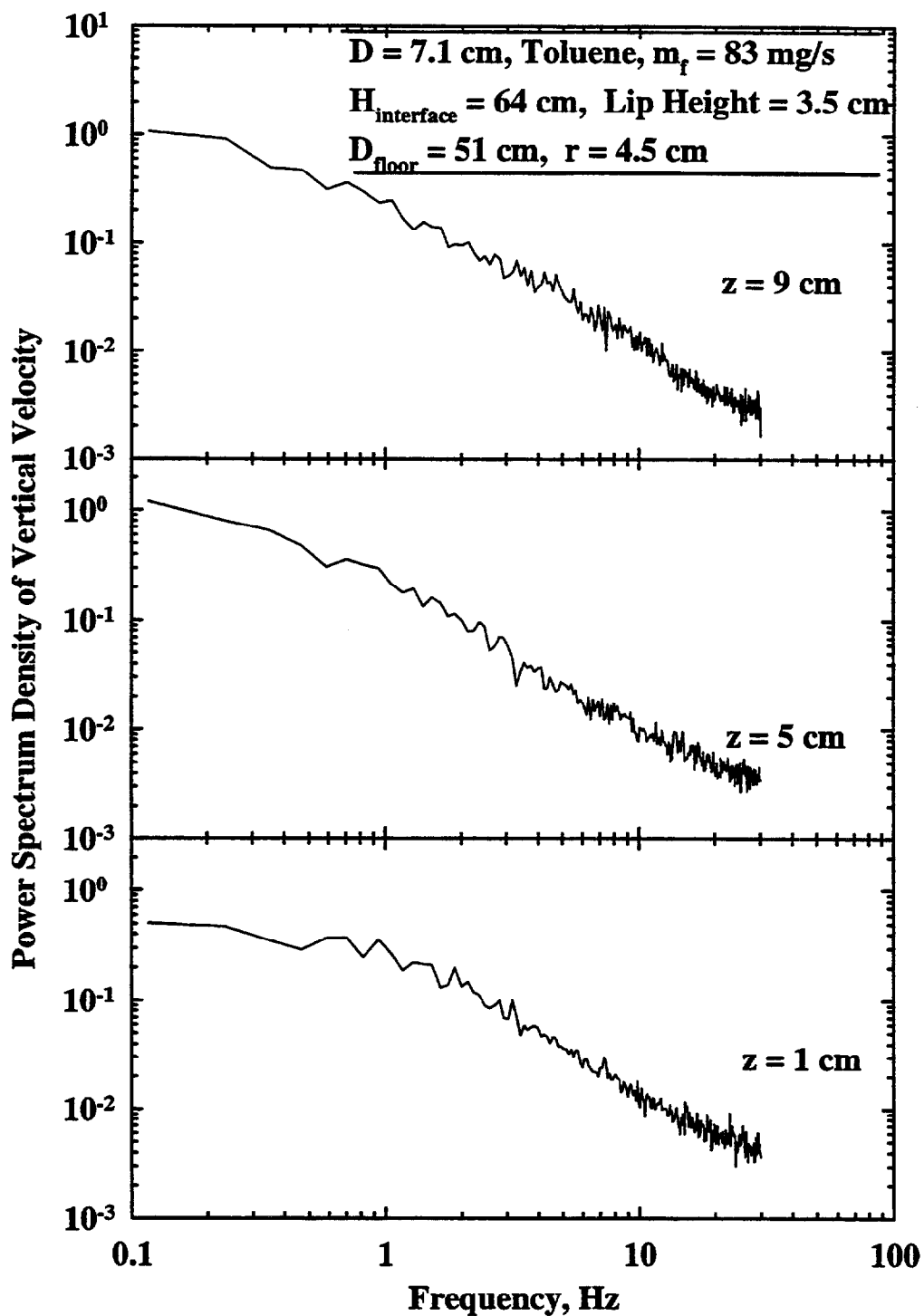


Figure 4.14 Power Spectrum Density of vertical velocities at three different heights at $r = 4.5 \text{ cm}$.

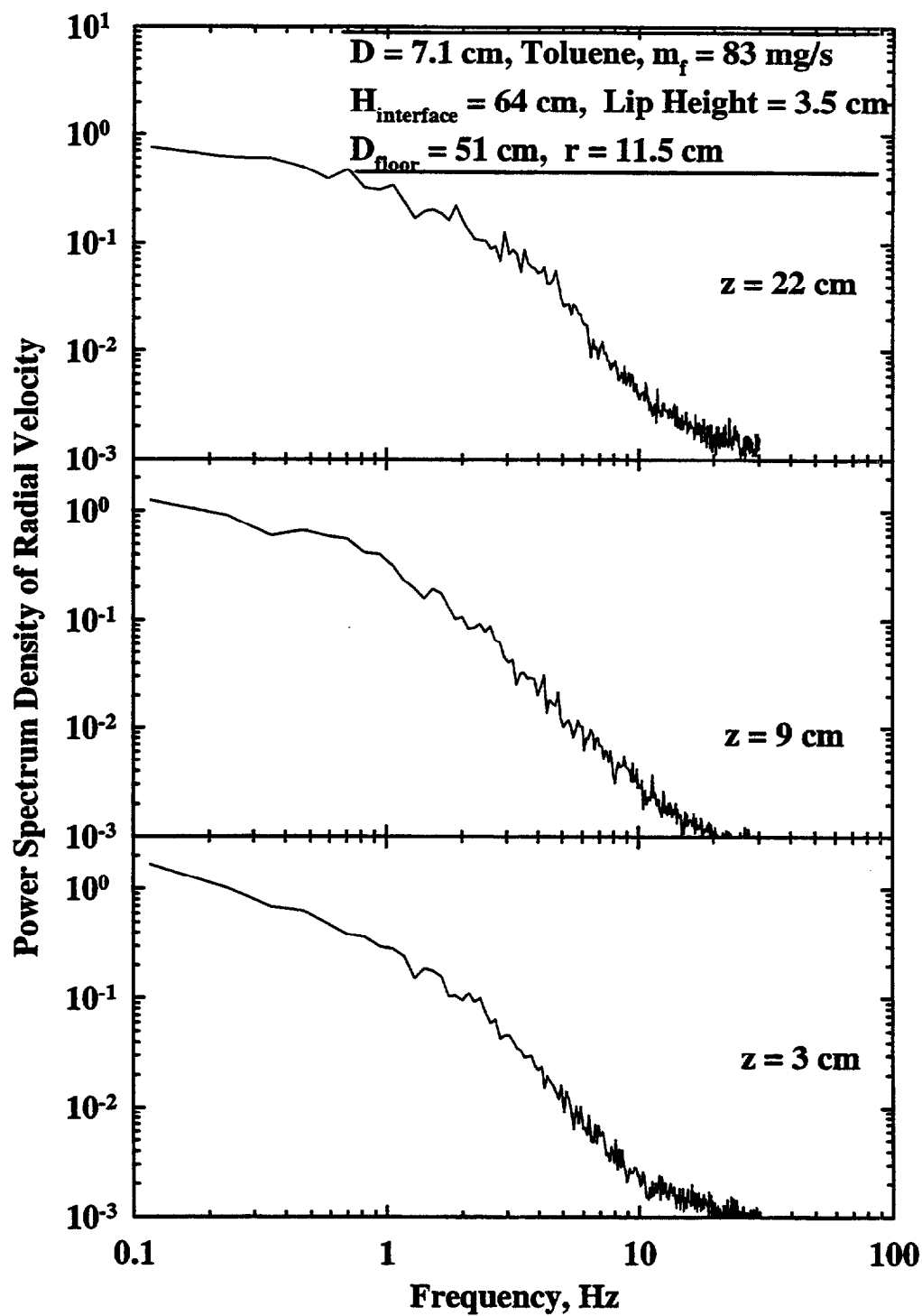


Figure 4.15 Power Spectrum Density of radial velocities at three different heights at $r = 11.5 \text{ cm}$.

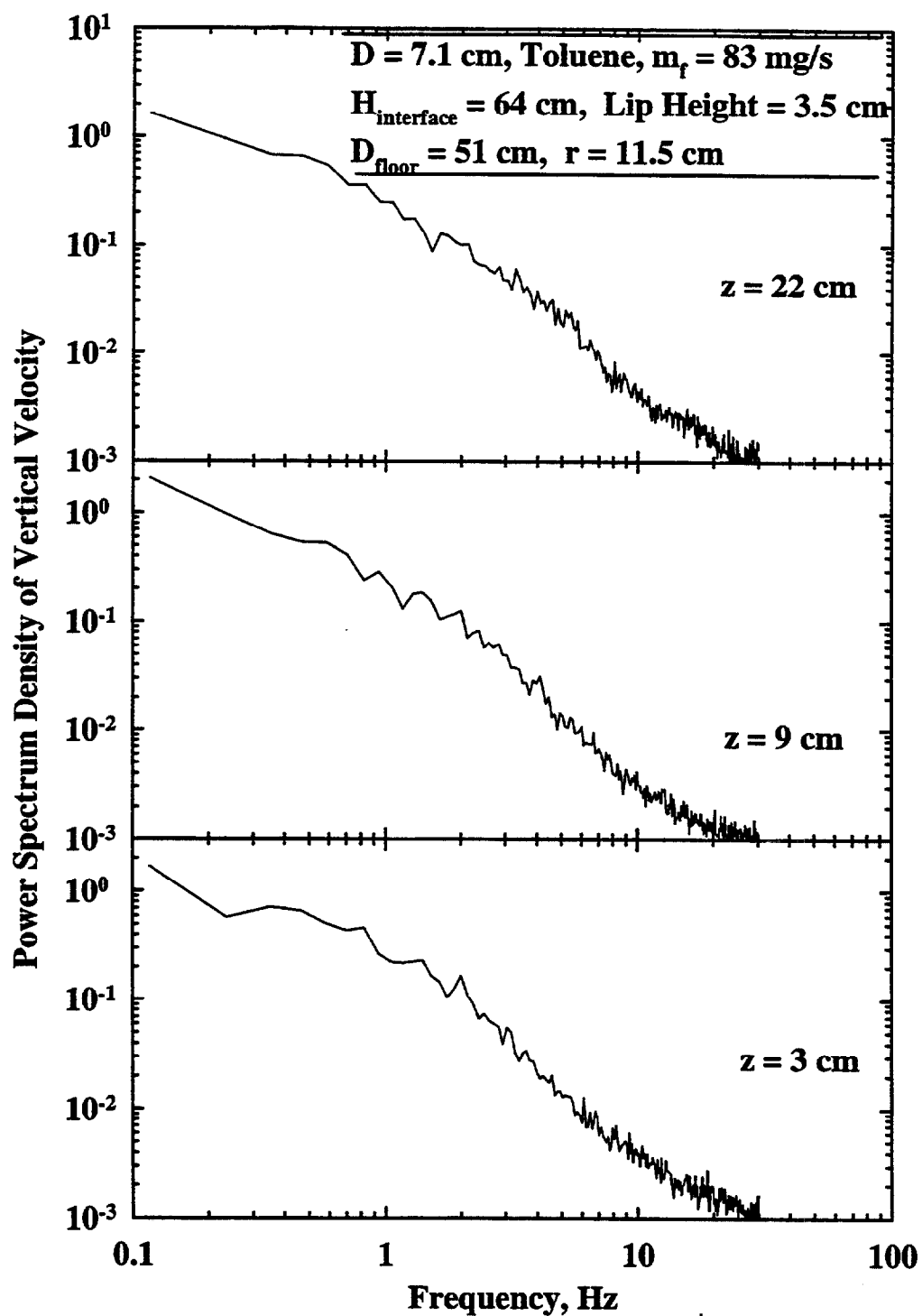


Figure 4.16 Power Spectrum Density of vertical velocities at three different heights at $r = 11.5 \text{ cm}$.

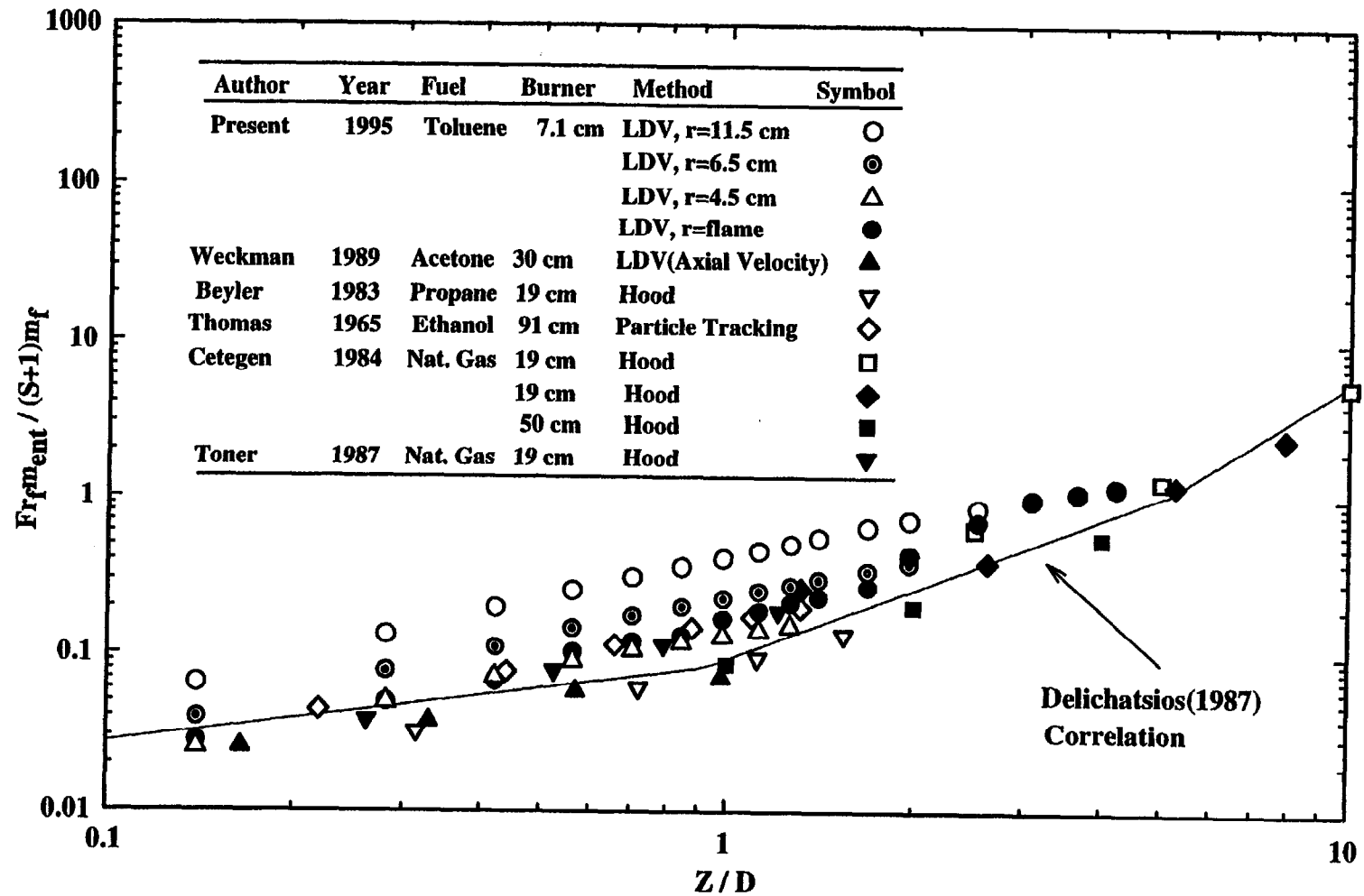


Figure 4.17 Comparison of present experimental data concerning entrainment mass-flow rates with past measurements and a correlation from the literature.

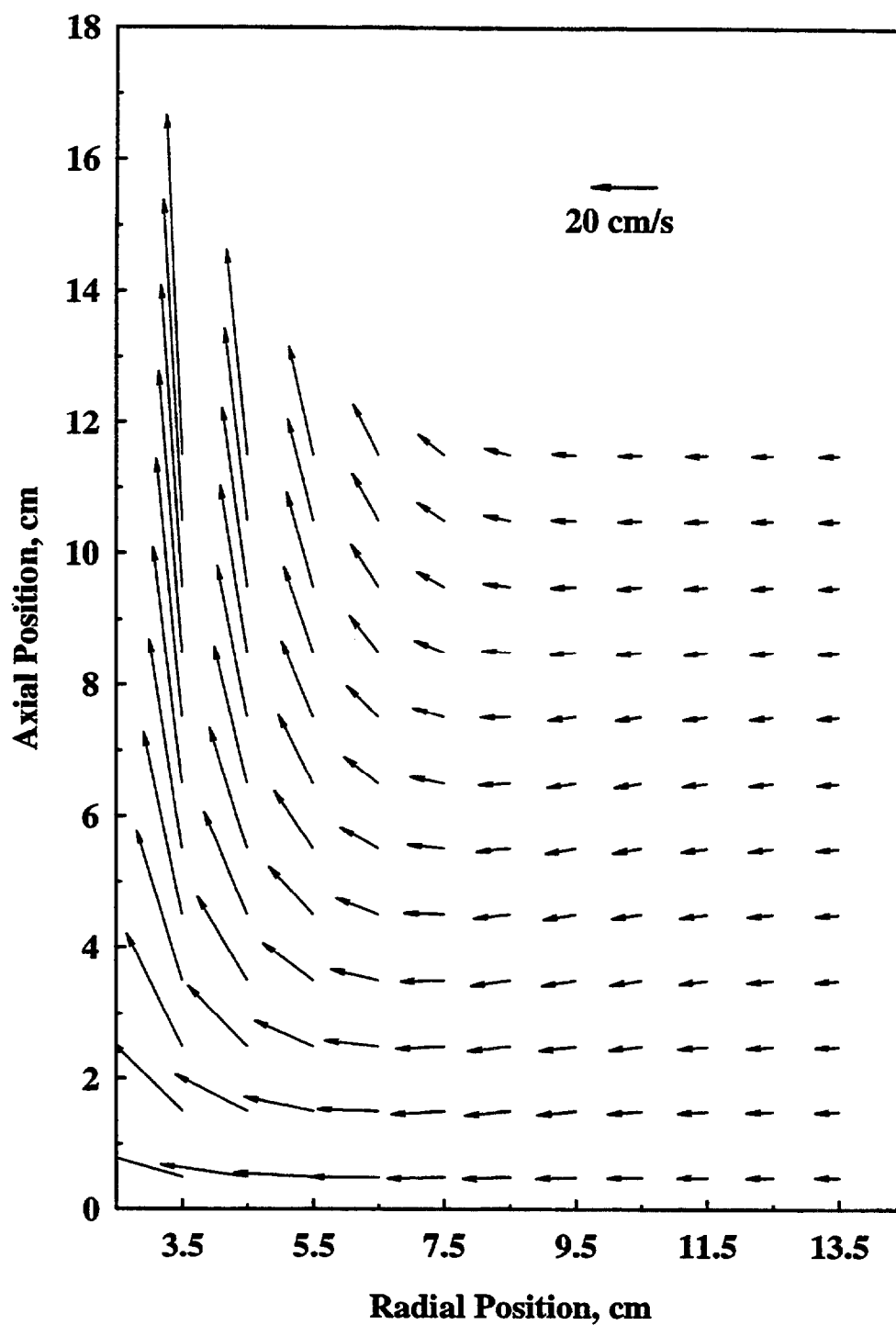


Figure 4.18 The predicted velocity field in the near region of a pool fire at heat release rate of 3.04 kW and radiative loss fraction of 30%.

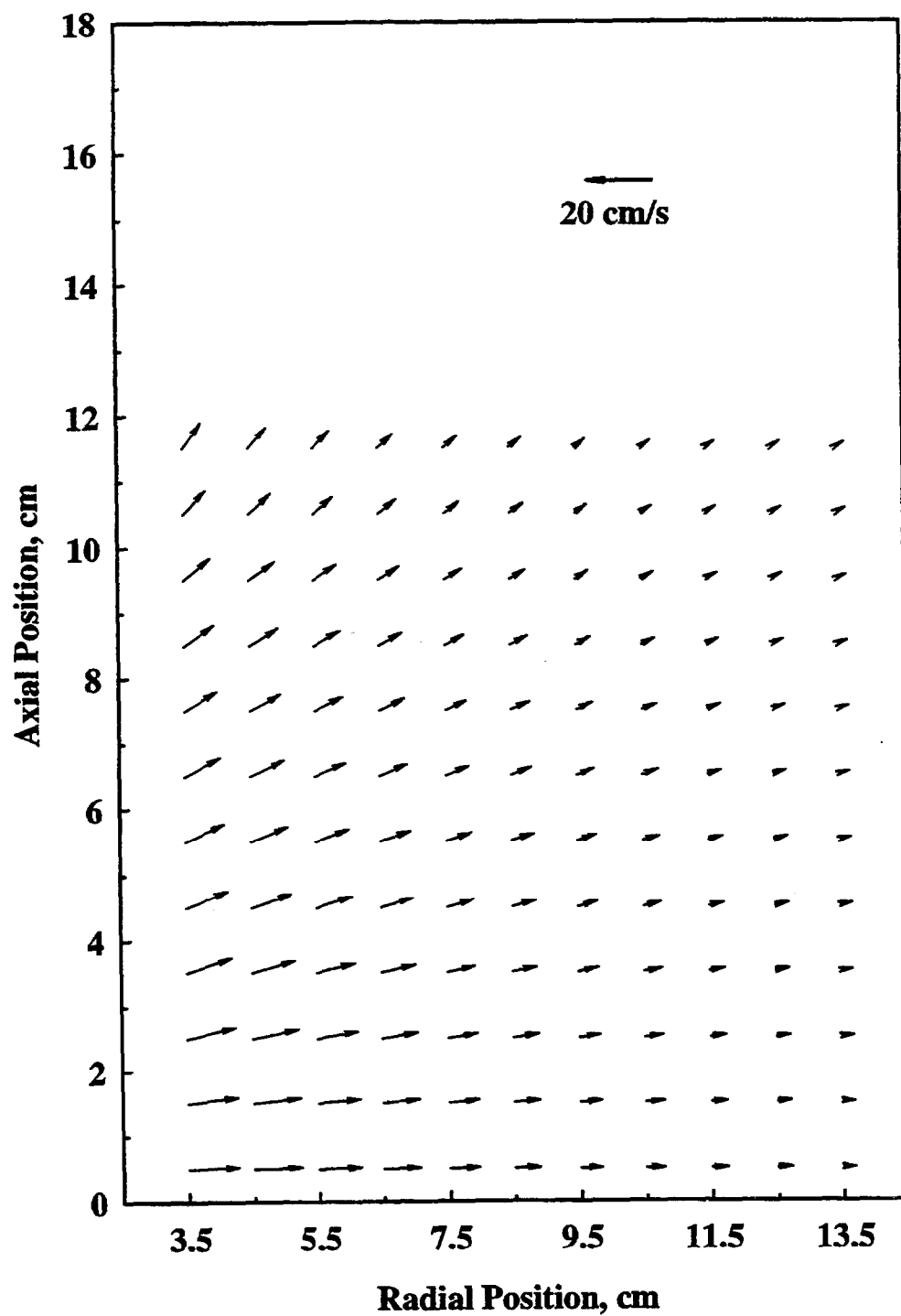


Figure 4.19 The predicted expansion velocity field in the near region of a pool fire at heat release rate of 3.04 kW and radiative loss fraction of 30%.

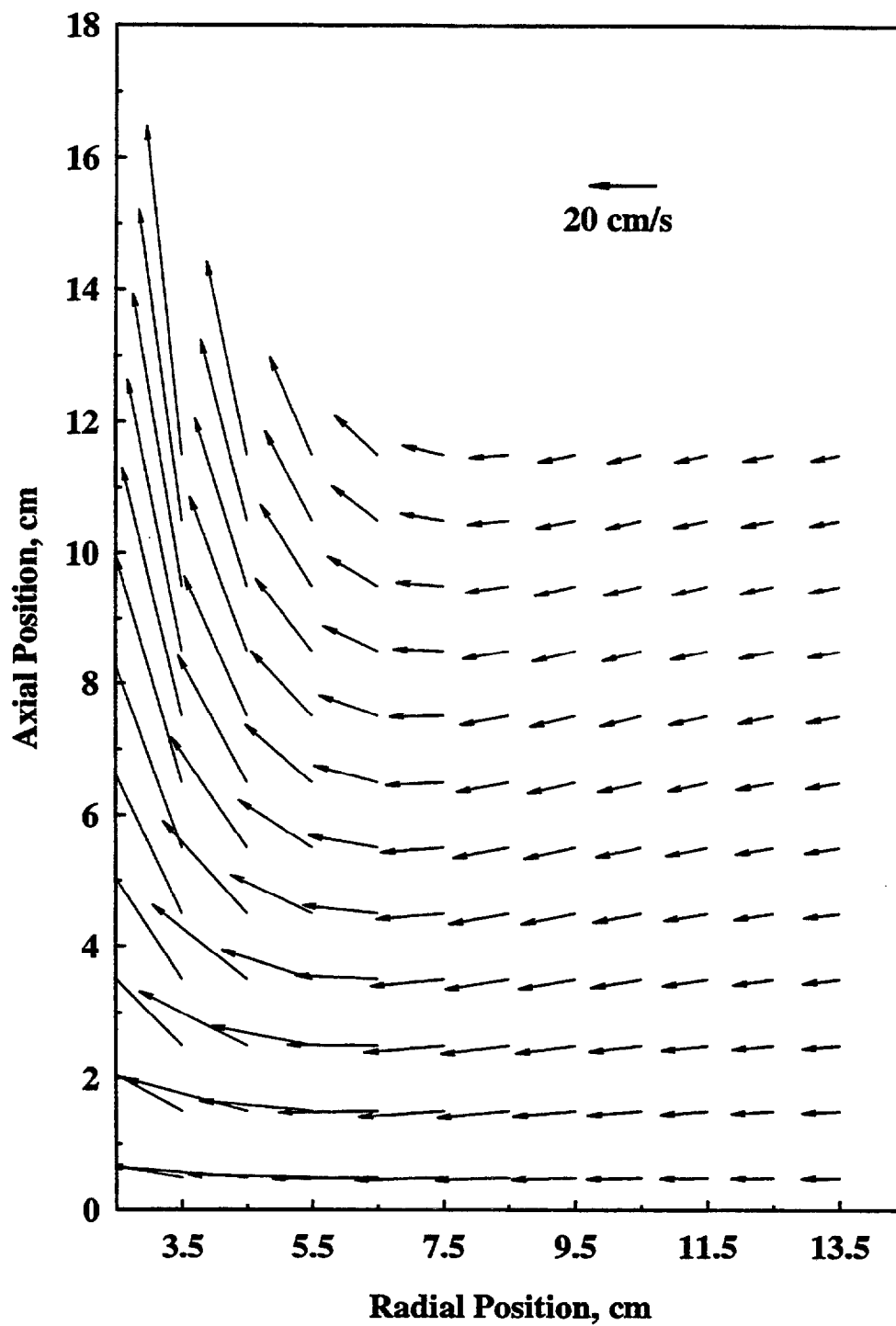


Figure 4.20 The predicted incompressible velocity field in the near region of a pool fire at heat release rate of 3.04 kW and radiative loss fraction of 30%.

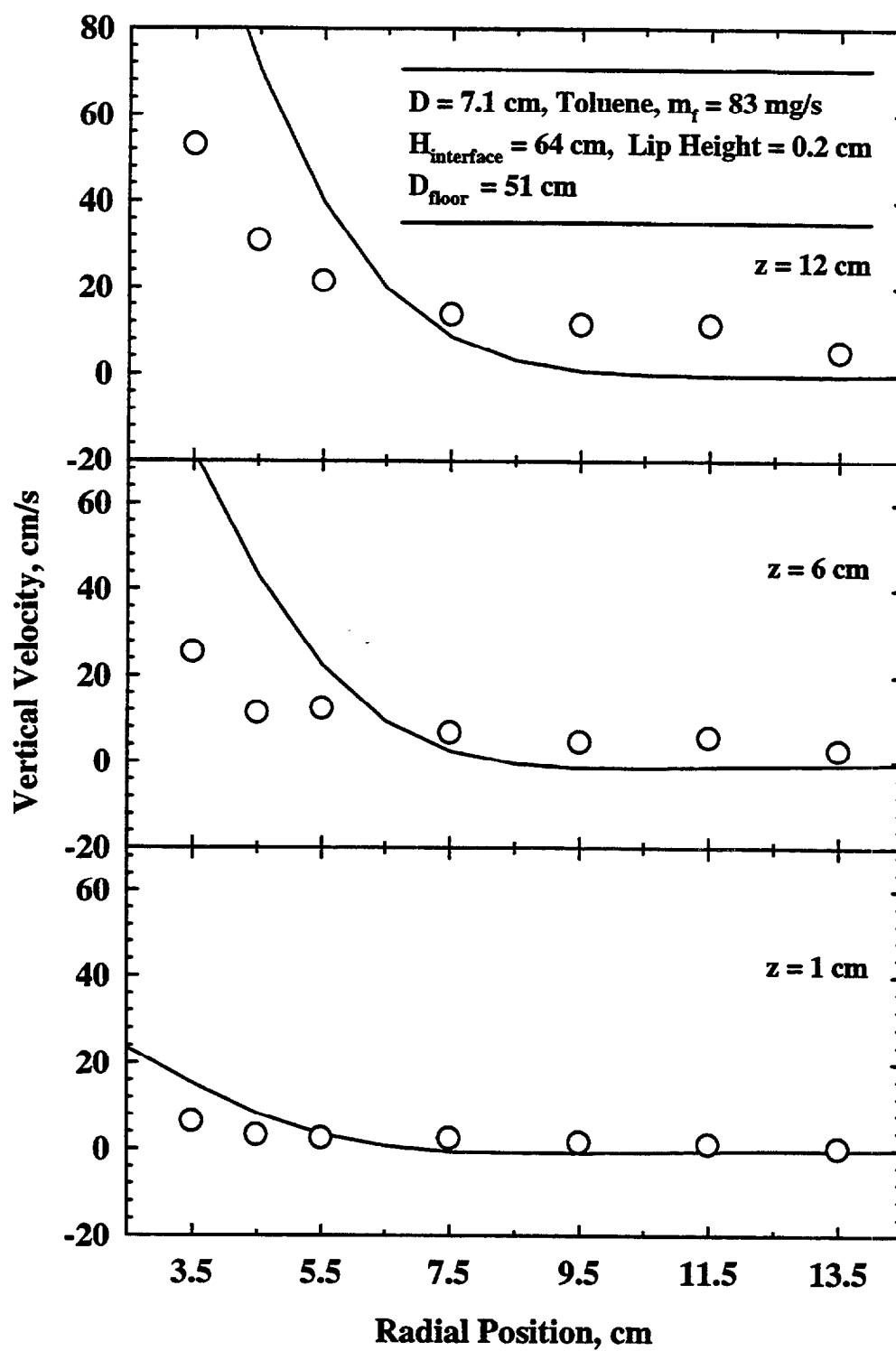


Figure 4.21 Comparison of predicted vertical velocities with measurements at three different heights.

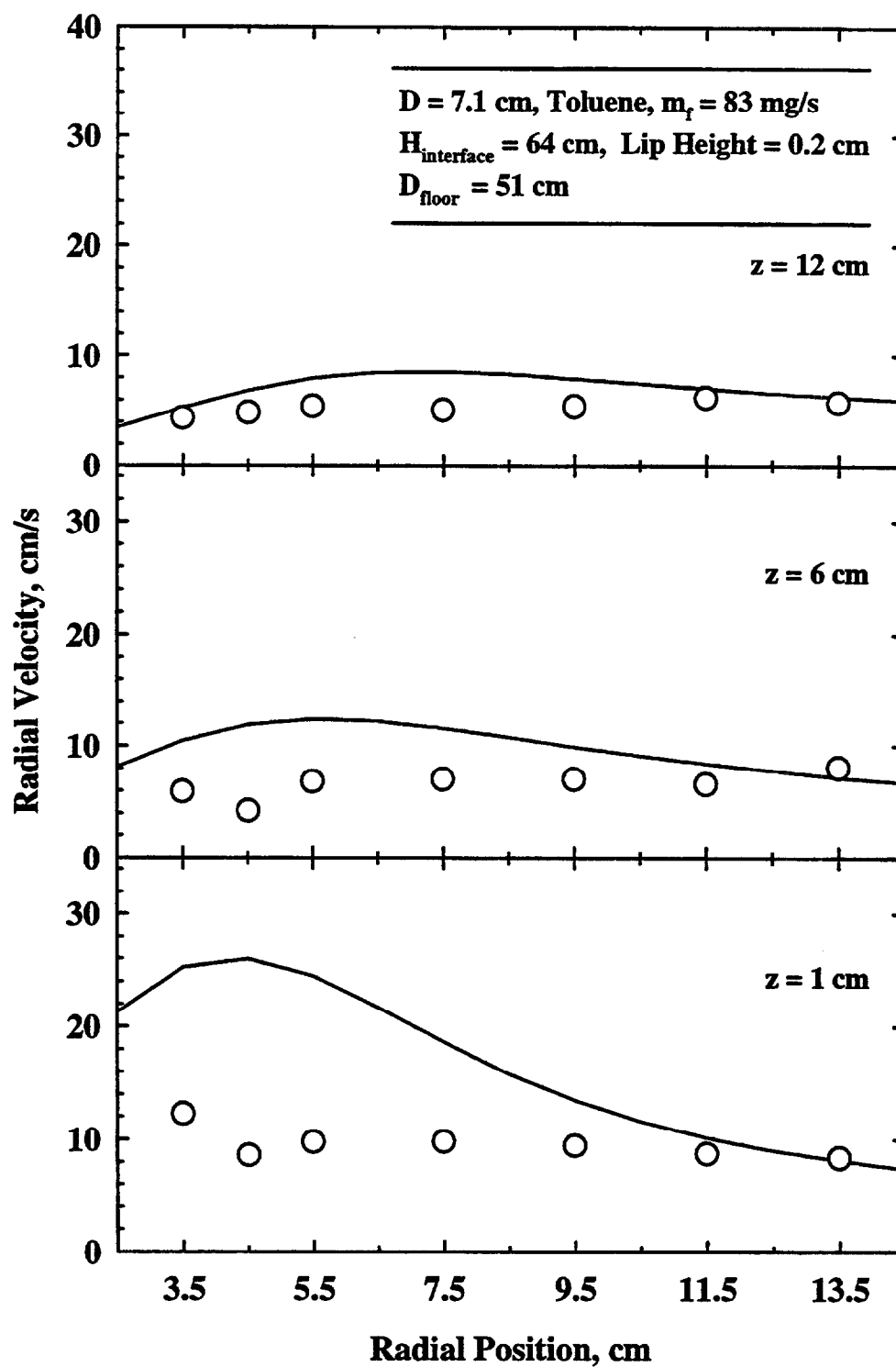


Figure 4.22 Comparison of predicted radial velocities with measurements at three different heights.

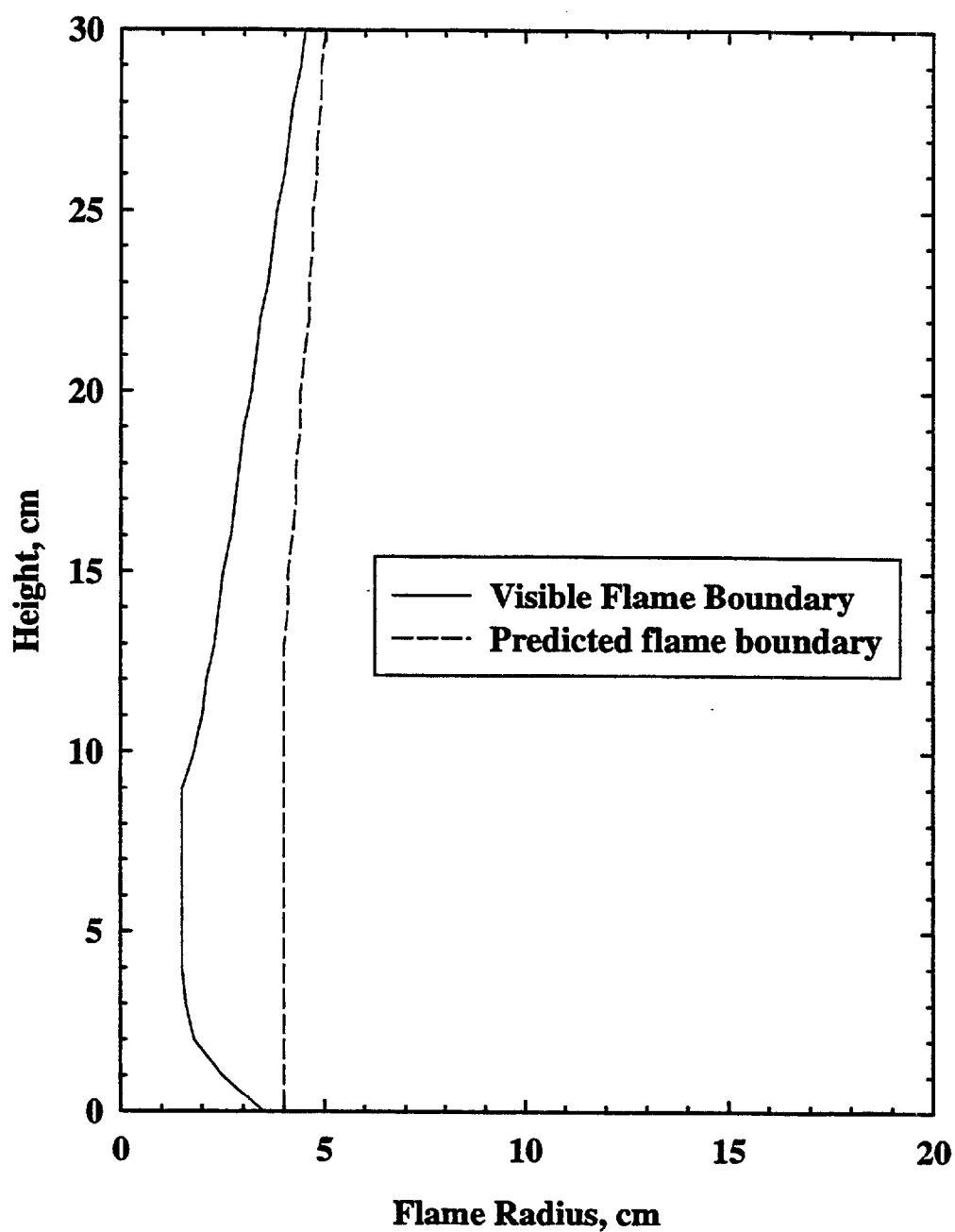


Figure 4.23 Comparison of measured visible flame boundary with the predicted flame radius as a function of height.

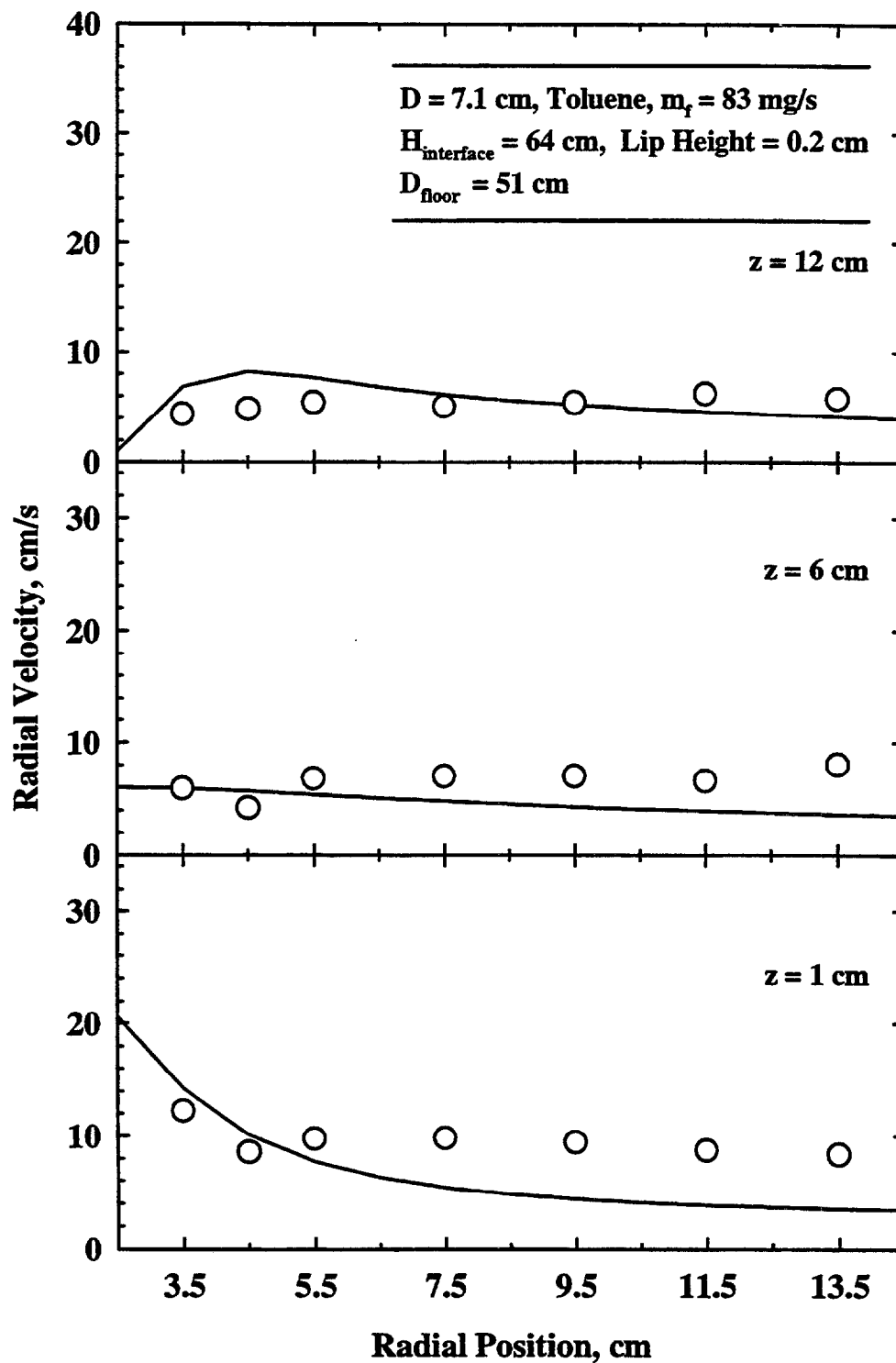


Figure 4.24 Comparison of measurements with the predictions of radial velocities computed with measured visible flame boundary at three different heights.

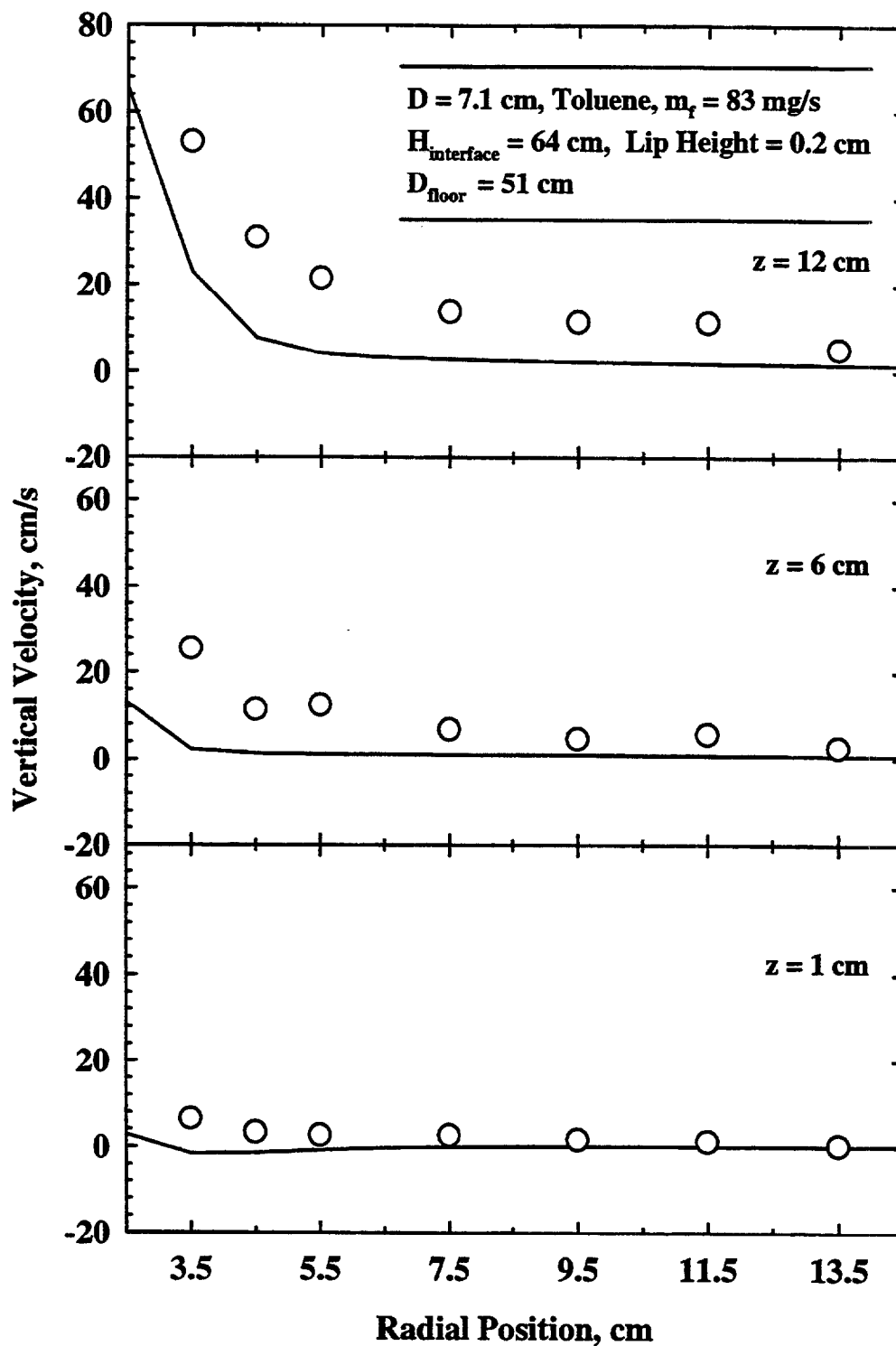


Figure 4.25 Comparison of measurements with the predictions of axial velocities computed with measured visible flame boundary at three different heights.

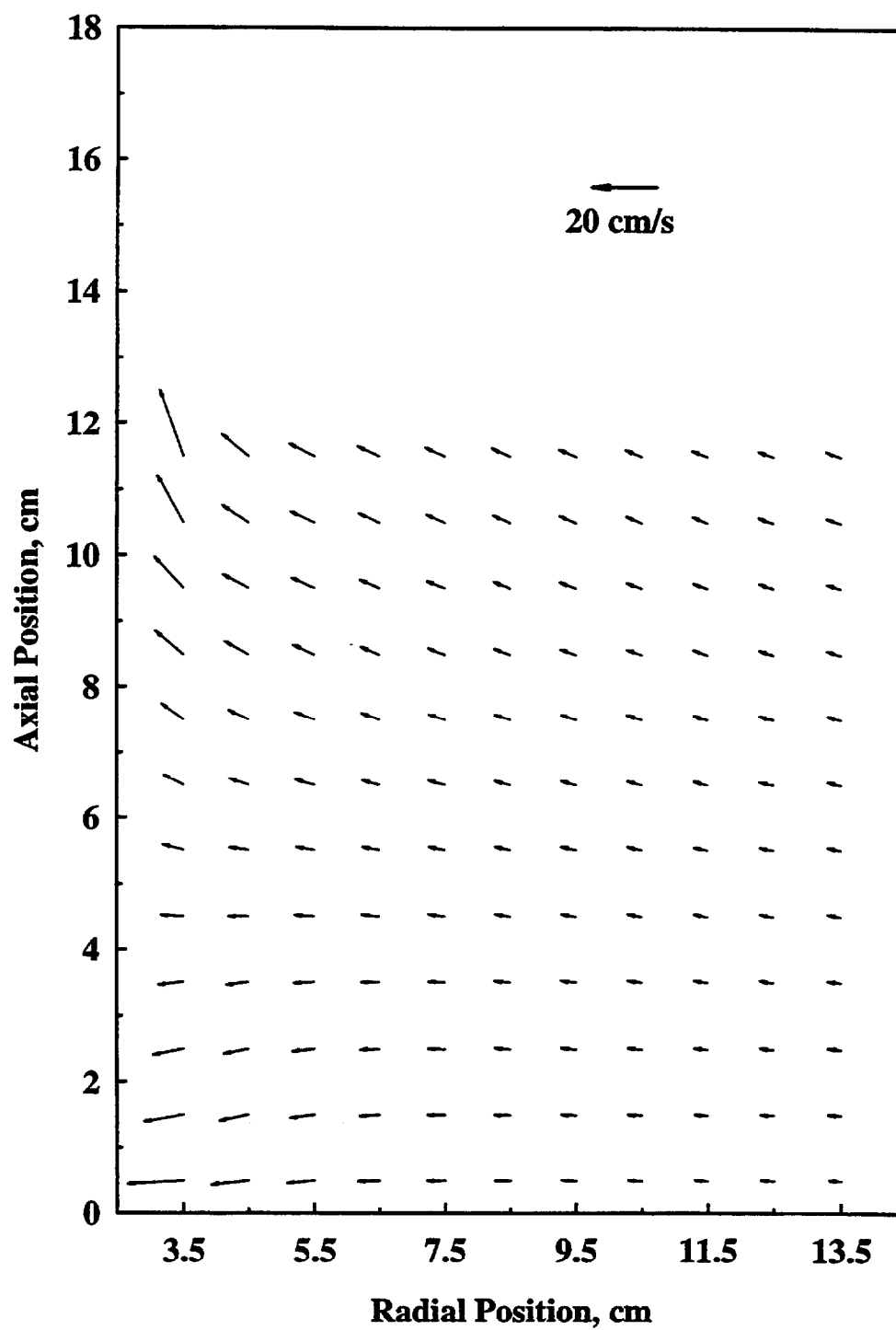


Figure 4.26 The predicted velocity field computed with measured visible flame boundary.

CHAPTER 5 PIV RESULTS AND DISCUSSION

Laser Doppler Velocimetry (LDV) measurements of the entrainment flow field show highly transient behavior. In order to capture the instantaneous flow structures, Particle Imaging Velocimetry (PIV) technique is applied to measure two-dimensional velocity field. The instantaneous entrainment flow patterns of various pool fires are discussed first. Mean entrainment velocity fields are obtained by averaging one hundred instantaneous velocity vector plots. The effect of a floor around pool fires is discussed in terms of the differences caused by the floor in both the instantaneous and the mean velocity fields. Air entrainment rates by pool fires of different diameters and burning different fuels are calculated based on the mean velocity fields. Measurements and predictions of the mean entrainment velocity field of a 30 cm toluene pool fire without a floor are compared as an application of the numerical method proposed in Chapter 3.

5.1 Instantaneous Entrainment Flow Structure

The entrainment flow patterns of fifteen pool fires are studied applying PIV. The test conditions are summarized in Table 5.1. For 30 cm pool fires, the entrainment flow field with a floor is not studied using PIV because a fire of definite size cannot be established. In the presence of a floor, fire creeps over the floor and moves randomly around. When the floor is cooled with water running through copper coil welded to the back of the sheet metal floor, fuel vapor condenses into liquid on the floor at colder locations but the random propagation of the fire along the floor continues at hotter locations. This is an interesting phenomenon which occurs routinely in natural pool fires but is not studied here in order to focus on simpler fires.

Table 5.1 Test conditions for pool fires.

Diameter (cm)	Fuel	Floor (cm)	\dot{m}_f (mg/s)	H_f (cm)	X_A (%)	X_R (%)
7.1	methanol	51	50	14	100	20
	heptane	51	70	31	90	30
	toluene	51	83	34	90	30
	methanol	none	50	16	100	20
	heptane	none	70	34	90	30
	toluene	none	83	33	90	30
15	methanol	51	245	30	100	20
	heptane	51	360	59	90	30
	toluene	51	350	56	90	30
	methanol	none	245	32	100	20
	heptane	none	385	62	90	30
	toluene	none	370	58	90	30
30	methanol	none	980	36	100	20
	heptane	none	2660	134	90	30
	toluene	none	2850	119	90	30

The entrainment flow field induced by a 7.1 cm toluene pool fire with a 51 cm sheet metal floor is studied first. Figure 5.1 shows the instantaneous velocity vectors in a vertical plane starting at a radial location of $r = 3.5$ cm (pool edge) up to a radial location of $r = 12.5$ cm. The positions marked in the figures are relative to the center of the burner. The velocity scales are also shown in the figures. In order to avoid interference caused by reflection of the laser sheet by the floor, the image begins at $z = 0.4$ cm above the floor. The image covers a vertical distance of over one pool diameter ($z = 8.4$ cm). The blank region in the right hand part is caused by interference from the luminous flame and data drop-off caused by high velocities across the laser sheet. A large bulge in the

instantaneous luminous surface is observed near the middle of the image. It is seen that over majority of the luminous surface, entrainment of surrounding material is occurring at the instant this image was captured. However, local radially outward velocity is observed near the farthest luminous point marked by "A" in the figure. Both upstream and downstream of the farthest luminous surface, strong entrainment flows denoted by "B" and "C" are observed. The structure denoted by "D" starts at the lowest left corner and meanders along the diagonal of the image before being entrained in the radial direction above the farthest visible flame extension. A local vortex structure denoted "E" in the region near the luminous flame surface is observed. A stagnation surface that indicates outflow in the circumferential direction from the plane of the image denoted by "F" is also observed. Thus, the flow field induced by the fire involves instantaneous entrainment upstream and downstream of the farthest visible flame bulge in the phase shown in the figure. Because the flow is highly transient with low mean value of velocities, sometimes the vertical entrainment might be negative even though the mean vertical velocity is larger than zero. The upper right corner of the field of view is such a region with negative vertical velocities. This is in agreement with the Probability Density Function (PDF) of the LDV measurement data of the vertical velocities as shown in Fig. 4.11, where there is a finite probability of negative vertical velocities at $r = 11.5$ cm at different heights.

At another instance, the luminous flame boundary moves closer to the pool edge as shown in Fig. 5.2. This vector plot shows the two dimensional velocity data for an area identical to that shown in Fig. 5.1. Strong vertical entrainment flow into the visible surface is observed near the upstream end of the visible flame structure departing the view region (highlighted by "A" in the figure). Local region denoted by "B" in which a stagnation plane showing inflow of air in the azimuthal direction into the plane of the image is observed. Over most of the luminous interface shown in the image, the flow of the material surrounding the fire is predominantly vertical. Thus locally, during this phase, very low radial inflow of air into the visible interface occurs. A large quantity of air is in motion in a vertically upward and radially outward (shown in the figure by "C") direction during this phase of the fire. This feature is also corroborated by the finite

probability of negative radial velocities at large radial locations in the LDV measurements as shown in Fig. 4.10.

During a third phase of the fire, shown in Fig. 5.3, the luminous interface moves almost completely out of the view of the camera. At the radius of the pool edge, there is strong "extrainment" as shown by the predominantly radially outward flow, marked by "A" in the figure. In the lower right corner of the view region near the pool edge, a vortex marked by "B" is observed. Further away from the flame interface, air is set in motion in the vertically upward direction. Local structures such as the vortex denoted by "C" are occasionally observed.

About 10% of the instantaneous velocity vector plots show vortex structures. Most of the vortices (about 90%), such as "C" in Fig. 5.1, "B" and "C" in Fig. 5.3, are in the positive direction in a cylindrical coordinate system with its origin at the center of the burner. Very rarely the vortices are in the negative direction. Figure 5.4 shows an example of a vortex in the negative direction, denoted by "A".

When the floor is removed, the pool fire contracts towards the centerline quickly and becomes much more stable. The flow induced by the fire becomes very stable too. Figure 5.5 is a typical velocity vector plot of the entrainment flow field induced by a 7.1 cm toluene pool fire without a floor. The instantaneous flow pattern is quite different from that for the fire with a floor as shown in Figs. 5.1 through 5.4. The surrounding air is moving irregularly at negligible velocity while enveloping the flame is a layer with a very large convection velocity. Figure 5.6 is another realization of the instantaneous two-dimensional entrainment flow field. Basically it shows the same features as Fig. 5.5 except that the flow is a little more irregular. All the instantaneous velocity vector plots of the entrainment flow induced by 7.1 cm toluene pool fire without a floor show the same features.

Figures 5.7 - 5.11 are the instantaneous velocity vector plot in a planar section around a 15 cm toluene pool fire with a 51 cm sheet metal floor. The floor is at zero axial position. The burning rate of the flame is 350 mg/s, and the heat release rate is 14.6 kW. The mean visible flame height measured by averaging 512 randomly chosen images of the video record is 56 cm.

Figure 5.7 is a typical instantaneous velocity vector plot of the entrainment flow field in the near region of the 15 cm toluene pool fire with a floor. The velocities are predominantly horizontal at all points with only a little variation. Seventy-five percent of the images show this pattern. In the region marked by letter "A", the velocities also show considerable upward, vertical component. In the regions designated with letters "B", "C", and "D", the vertical velocity components are even negative.

Figure 5.8 is another instantaneous velocity vector plot with features very similar to that of Fig. 5.7. However, the velocities are inward and at 45 degrees to the horizontal plane in the region designated with letter "A".

Entrainment is a transient, laminar flow. Sometimes the flow field can display very interesting patterns. At the radius of the burner edge in Fig. 5.9 horizontal velocities along the entire height of the view region shows that air is entrained. At the upper right corner of the view region, an azimuthal vortex structure denoted by "A" in the positive direction is captured. Three percent of the images have a vortex structure in the velocity field.

Instantaneous "extrainment" is observed in some images too. In Fig. 5.10, the vertical velocity components are always positive at the radial location of the burner edge. In the lower half region "A", the radial velocity components are inward, showing that air is entrained by the flame. However, in the upper half region "B", the radial velocity components are outward, showing that air is pushed away by the flame.

Figure 5.11 is similar except in the region "A" where the vertical velocity components are negative. Since the flame is not shown in the image, the relationship between the downward flow and the development of large scale flame structure in this figure is uncertain.

To study the effect of floor on the entrainment flow field of the 15 cm toluene pool fire, some of the instantaneous velocity vector plots of the flow field around a 15 cm toluene pool fire without a floor are plotted in Fig. 5.12 - 5.17. The burning rate of the fire is 370 mg/s, and the heat release rate is 15.4 kW. The average flame height is 58 cm.

Figure 5.12 is a typical velocity vector plot of the entrainment flow field of 15 cm toluene pool fire without a floor. The velocity vectors are mainly entrained towards the flame at 45 degree from the horizontal plane. Forty percent of the images show this feature. One major change in the entrainment flow field in the absence of a floor is that the flow becomes more "vertical". When there is a floor, the velocities are mostly horizontal at heights close the fuel surface as shown in Figs. 5.7 - 5.11. However, without the floor, the vertical velocity components are usually larger than corresponding radial velocity components at the fuel surface level. Several data points are missing close to the burner edge due to interference from flame luminosity.

In Fig. 5.13, the velocity vectors in region "A" have inward radial velocity components. However, in the middle region "B", the velocities are almost perfectly vertical. In the region designated with letter "C", the radial velocities are outward, showing a moment of "extrainment".

Sometimes the velocities at the radial location of the burner edge are almost horizontal as shown in Fig. 5.14. Twenty-five percent of the images have this feature.

The entrainment velocities along part of the axial distance at the radial location of the burner edge can also be vertical, as demonstrated by the velocities in region "A" in Fig. 5.15. Twenty-seven percent of the images have this feature.

Compared with the pool fires with a floor, the entrainment flow patterns of pool fires without a floor are more regular. However, there are still occasions (about eight percent of the images) when the velocities are outward or downward. In Fig. 5.16, the velocities in the bottom two third region at the radial location of the burner edge are typical of the entrainment flow of a 15 cm toluene pool fire without a floor. In the top one third region designated with letter "A", the entrainment velocities are negative. Another unusual feature of the plot is that in the bottom right corner of the view region "B", the radial velocity components are much larger than the vertical velocity components. Figure 5.17 is another normal entrainment velocity vector plot except in regions "A" and "B" where the velocities are outward.

To study the effect of different fuel types on the entrainment flow fields, the instantaneous flow fields of a 15 cm heptane pool fires, both with and without a floor, are

plotted. With a 51 cm sheet metal floor around the fire, the burning rate is 360 mg/s, and the heat release rate is 17.3 kW. The mean flame height is 59 cm.

Like the entrainment flow patterns of the 15 cm toluene pool fire with a 51 cm sheet metal floor, the entrainment flow velocities at the radial location of the burner edge are predominantly horizontal. Fig. 5.18 is an instantaneous entrainment velocity vector plot, where the vertical velocity components of the velocities at all points are negligibly small. It is noted that the entrainment flow patterns are usually not as regular as that shown in this figure.

Figure 5.19 is another realization of the instantaneous entrainment flow field. In region "A" close to the burner edge, the velocities are horizontal. At higher locations in region "B", the velocities are almost vertical. At the top region "C", the velocities are inward and at 45 degrees to the horizontal plane. In about twenty percent of the images the velocities at the radial location of the burner edge are mainly at 45 degrees to the horizontal plane. Figure 5.20 is one of such images.

Although the entrainment flow patterns of the 15 cm heptane pool fire are more regular than those of 15 cm toluene pool fires, outward and downward flows are observed around the heptane fires as well.

In Fig. 5.21, the velocities in region "A" are at 45 degrees to the horizontal plane. In region "B", the velocities are almost horizontal. In region "C", the vertical velocity components are negative.

In Fig. 5.22, air is radially entrained towards the flame in region "A". But in region "B", air is pushed away from the flame as shown by the outward radial velocity components.

The instantaneous entrainment flow patterns of a 15 cm heptane pool fire without a floor are also more regular than the entrainment flow patterns of the 15 cm toluene pool fires. Figure 5.23 is a typical realization of the entrainment flow field of 15 cm heptane pool fires without a floor. Most of the velocity vectors are radially inward and at 45 degrees to the horizontal plane. Nearly sixty percent of the image show this pattern. However, sometimes there are dramatic variations in the flow pattern. In region "A" in

Fig. 5.24, the velocities have outward radial components and downward vertical components.

For 30 cm pool fires, the entrainment flow is even more unstable. Figures 5.25 - 5.28 are four realizations of the instantaneous entrainment flow in the near field of a toluene pool fire established over a 30 cm pool burner. The visible flame boundary is shown by dropping-off of velocity vectors in the left-hand side region. One of the most apparent feature of these instantaneous entrainment flow fields is that the flow is very unsteady and the instantaneous flow fields are dramatically different from one frame to another. In Figure 5.25, the velocities at the radial locations of the burner edge are almost horizontal and inward, showing that air is drawn in by pool fire. At the level of the burner edge, there are also finite vertical velocity components, showing that air is being drawn from underneath. In the middle of the view region, the velocities are predominantly vertical. The velocities at locations farther away from the fire are much smaller than the velocities in the immediate vicinity of the fire.

Figure 5.26 shows a quite different pattern. The velocities become vertically upward in the whole region except in the upper left corner, where horizontal velocity components are larger than the vertical velocity components. On the left-hand edge near the top of the view region, the horizontal velocity components are outward, showing that air is flowing away from the fire. This phenomenon, termed “extrainment”, was also identified by Probability Density Function of the radial velocity measured using LDV and the instantaneous flow patterns obtained using PIV of the entrainment field of a 7.1 cm toluene pool fire with a floor. As discussed in Chapter 3, decomposition of the entrainment flow field into irrotational flow caused by heat release and incompressible flow caused by vorticity generated due to density gradient inside flame shows that vorticity is the largest in the region of the visible flame interface, and it entrains combustion material from the interior region as well as entrains air from surrounding. However, the radially outward velocity caused by vorticity exist only within the flame. Only instantaneous rupture of large scale structure can push air away from the fire.

The instantaneous two-dimensional velocity plot shown in Fig. 5.27 is the most peculiar, in which the velocity vectors under a flame bulge are even downward. In a

study of water jet entrainment applying PIV system (Liepmann and Gharib, 1992), it was observed that local entrainment rate was maximum immediately after the vortex ring near the jet exit, while at the location of the vortex ring, radial velocity is outward. Corresponding to vortex rings in a cold jet, buoyant non-premixed flames have a regular sequence of large-scale structure emanating from the fuel surface, moving along the flame, erupting and disappearing, resulting in periodic pulsation of the flame. This phenomenon is termed "puffing" in the literature (Hamins et al., 1992; Weckman and Sobiesiak, 1988; Cetegen and Ahmed, 1993). It is speculated that the radial velocity is outward at the outer edge of such large-scale structures, and the local entrainment rate also reaches a maximum value immediately after the large-scale structure, corresponding to the relationship between a vortex ring and the local entrainment velocity in a cold jet. The entrainment rate is so large that air is entrained from both downward and upward, causing air near the large-scale structure to flow downward. The velocity field in a cross-section across the jet axis was not measured by Liepmann and Gharib (1992). However, in another study of entrainment of transient turbulent reaction jets (Tomita et al., 1992), backflow of air in the vicinity of the flame sheet was also identified using pathline method. The PDFs of LDV measurement data of the vertical velocities at locations close to the burner edge also demonstrated some portion of negative vertical velocities, but since LDV is a point velocity measurement technique, it could not determine the relationship between the velocity distribution and the phase of the flame structure. Five percent instantaneous velocity vector plots of the entrainment flow have this feature. These new findings about the entrainment flow pattern is helpful in direct numerical simulation of buoyant diffusion flames. In Figure 5.10, air flows towards the flame under the bulge but the material flows away from the flame above the bulge. Three percent instantaneous velocity vector plots of the entrainment flow show this pattern. A vortex denoted by letter "C" is also captured in Fig. 5.28. It is in the positive direction in a cylindrical coordinate system.

Figures 5.29 - 5.31 are the instantaneous two-dimensional flow patterns of the entrainment flow fields of a 30 cm heptane pool fire without a floor. In Fig. 5.29, the velocity vectors are mainly at 45 degrees to the horizontal plane. In Fig. 5.30, the

velocity vectors are almost horizontal. In Fig. 5.31, the velocities are almost vertical. These three patterns identify the three phases of the fire induced flow field.

5.2 The Mean Entrainment Flow Fields

Despite the seemingly random change of velocities in direction and magnitude in the instantaneous velocity vector plots, the mean velocity fields show a regular pattern. Figure 5.32 is the mean flow field induced by the 7.1 cm toluene pool fire with a floor, obtained by averaging over one hundred instantaneous vector plots. In order to compare PIV measurements with the LDV data, only data at the locations having LDV measurements are plotted. The figure shows that the radial inward flow starts at the farthest side of the view region of the camera. Just like the LDV measured two-dimensional vector plots of the mean velocity field shown in Fig. 4.1, the radial velocity components remain almost constant with decreasing radial location in spite of the reduction in the flow area. Continuity equation is preserved by a significant increase in vertical velocity component with height and with decreasing radius, due to the buoyancy effect of the fire and a reduction in the flow area. The mean vertical and radial velocity profiles at four different heights from the two measurement methods are plotted in Figs. 5.33 and 5.34 to assess the validity of PIV system. Figure 5.33 is the comparison of radial velocities obtained using the two different measurement techniques. At a given height, the radial velocity component remain almost constant over the radial distance in the measuring range. Comparison of radial velocities in different plots shows that the radial velocity decreases slightly with axial distance at a given radial location. At all positions, the two sets of data are comparable within experimental uncertainty. Comparison of the vertical velocities from LDV and PIV measurements are plotted in Fig. 5.34. At a given height, the vertical velocity increases with decreasing radial distance from the flame. Comparison of the plots in the figure shows that the vertical velocity increases with height at a given radial location. The two sets of data are also comparable within experimental uncertainty at all positions.

Figure 5.35 is the mean velocity vector plot of the flow field induced by a 7.1 cm toluene pool fire in the absence of a floor. It is quite different from the velocity vector plots of mean entrainment flow induced by the same fire but in the presence of a 51 cm sheet metal floor, as shown in Fig. 5.32. It is noted that the mean velocity vector plot looks very similar to the instantaneous velocity vector plots as shown in Figs. 5.5 and 5.6. Away from the pool burner, the mean velocity of the air is insignificant in either the axial or the radial direction. Very close to the pool fire is a layer of entrained air following the shape of the flame, moving at comparatively very high speed. The vertical velocities at a given height increase as it gets near the flame surface. Air entrained by the pool fire mostly comes from beneath the pool burner instead of from radially far away locations. Comparison of this figure with Fig. 5.32 proves the speculation of Thomas (1965) and the theoretical analyses of Taylor (1958). Because a floor prevented air coming from below, Thomas speculated that entrainment flow fields would be very different depending upon whether there is a floor around the fire. Theoretically, governing equations of the entrainment flow are elliptic in nature and are very sensitive to change in boundary conditions. Since the presence of a floor changes the boundary conditions, it is expected that the floor changes the entrainment flow pattern dramatically. In his theoretical analyses, Taylor (1958) showed that the air entrained by a thermal jet in a semi-infinite environment came from far away region, while the entrainment velocity of a thermal jet in an infinite environment became almost vertical within a short range of radial distance.

However, when the pool fire is large, air will be set in motion starting at locations far away from the pool fire even in the absence of a floor. Figure 5.36 is the velocity vector plot of the entrainment flow field around a 15 cm toluene pool fire without a floor. Even at $r = 20.5$ cm, the magnitude of the entrainment velocities are obviously larger than zero. Over all the view region, the radial velocity and the vertical velocity components are comparable in magnitude. Figure 5.37 is the mean velocity vector plot of the flow induced by a 15 cm heptane pool fire. It has the same characteristics as Fig. 5.36.

Figure 5.38 is the velocity vector plot of the mean two-dimensional entrainment flow field around a 15 cm toluene pool fire with a 51 cm sheet metal floor. The entrainment velocities are almost horizontal. Figure 5.39 is the velocity vector plot of the mean entrainment flow field around a 15 cm heptane pool fire with a 51 cm sheet metal floor. The flow pattern is very similar to that of Fig. 5.38.

Figure 5.40 is the mean velocity vector plot of the flow induced by a 30 cm toluene pool fire without a floor. At a given height, both axial and radial velocities increase with smaller distance to the flame, and at a given radial location, the velocity only change slightly over the axial distance. Even at $r = 27$ cm, which is 12 cm away from the pool burner edge, there is still considerable magnitude of velocity. At this location, the radial and axial velocity components are close to each other in magnitude. The entrainment flow pattern of the 30 cm heptane pool fire shown in Fig. 5.41 is very similar to the entrainment flow pattern of the 30 cm toluene pool fire.

5.3 Air Entrainment Rates

Air entrainment rates are calculated based on the mean velocity field of the flow induced by pool fires. For simplicity it is calculated as the total air entering a cylindrical surface enclosing the pool fire. Figure 5.42 is the air mass flow rate into a cylindrical surface of radius 4 cm, normalized using the parameters proposed by Delichatsios (1987), plotted against the height normalized by the pool diameter for the 7.1 cm pool fires without a floor. Error bars, the standard deviation of different times of measurements, are also plotted in the figure as estimate of the experimental uncertainty. The dimensionless entrainment rates for the pool fires burning three different kinds of fuels do not follow exactly the same trend. The methanol pool fire has the smallest dimensionless air entrainment rates. The dimensionless entrainment rate of the toluene pool fire is higher than those of the methanol and heptane pool fires in the lower region, but gradually falls below those of the heptane fire. The normalized entrainment rates of the heptane pool fire are the highest at elevated heights. However, they almost collapse

to one curve apart from the scatter in data. A curve fit for the entrainment rate data of the 7.1 cm pool fires without a floor is:

$$\frac{Fr_f m_{ent}}{(S+1)m_f} = 0.167(z/D)^{0.78} \quad (5.1)$$

where m_{ent} is the dimensional air entrainment rate as a function of height, Fr_f is the fire Froude number defined in Appendix A, S the mass stoichiometric ratio, m_f is the fuel consumption rate, z the axial distance above the fuel surface, and D is the pool diameter.

The dimensionless entrainment rates of the 15 cm pool fires without a floor are plotted against normalized height in Fig. 5.43. In the lower region, there is a good agreement between dimensionless entrainment rates of the pool fires burning different fuels. Above $z/D = 0.5$, the data from different pool fires begin to separate. The separation might be caused by the different flame shapes resulting from burning of different fuels. The methanol pool fire has a bump in dimensionless air entrainment rate about $z/D = 0.7$, rising above the dimensionless entrainment rates of the toluene and heptane pool fires. Above $z/D = 0.85$, the dimensionless entrainment rates of the pool fires are in the order of toluene, heptane and methanol. It is noted that the error bars increases with height. The flames are unstable at higher locations, resulting in larger uncertainties in the mean velocity and the air entrainment rates. A curve fit for the air entrainment rates of the 15 cm pool fires without a floor is

$$\frac{Fr_f m_{ent}}{(S+1)m_f} = 0.135(Z/D)^{0.78} \quad (5.2)$$

which is about 20% lower than the dimensionless air entrainment rates of the 7.1 cm pool fires. The effect of pool fire size on the entrainment rate is obvious.

The 30 cm pool fire entrainment rate data are normalized and plotted in Fig. 5.44. The dimensionless air entrainment rates for the toluene fire are always higher than those of the heptane and methanol pool fires. Equation 5.2 is a good curve fit for the 30 cm pool fire entrainment rate data too. Therefore 30 cm pool fires and 15 cm pool fires can be classified into the same regime in entrainment studies.

The dimensionless entrainment rates of 7.1 cm pool fires with a 51 cm sheet metal floor are plotted in Fig. 5.45. In the lower region, the data for the three fuels

collapse well, but the entrainment rates for the toluene pool fire gradually become larger than those of heptane pool fire at the same height, and the entrainment rates of the methanol pool fire gradually become smaller than those of the heptane pool fires. A curve fit for the entrainment data of all three fuels is

$$\frac{Fr_f m_{ent}}{(S+1)m_f} = 0.14(z/D)^{0.8} \quad (5.3)$$

Which is lower than the entrainment rate of the same fires but without a floor by about 20%.

When the 51 cm sheet metal floor is placed around the 15 cm pool fires, the flames become very unstable. However, the error bars representing experimental uncertainty do not increase significantly. The normalized air entrainment data are plotted in Fig. 5.46. No attempt is made to find a curve fit for the data because the differences between pool fires burning different fuels are too large.

5.4 Comparison of Prediction and Measurement of Entrainment Velocity

It is known from Chapter 4 that assuming a constant flame radius profile results in overprediction of entrainment velocities. In calculating the entrainment velocity field of the 30 cm toluene pool fire, the flame radius profile is adjusted as a single parameter to achieve best agreement between measured radial velocity and predicted radial velocity. The flame radius profile chosen is shown in Fig. 5.47, and comparison of the predicted radial velocity and the measured radial velocity is plotted in Fig. 5.48. Very good agreement at all heights is obtained as a result of the single adjustment in flame radius.

The predicted mean entrainment velocity field is shown in Fig. 5.49. Comparison of it with the measured mean entrainment velocity field shown in Fig. 5.40 shows that vertical entrainment velocities are still overpredicted. More accurate volumetric heat release rate and vorticity distribution inputs are needed for better accuracy of the predictions.

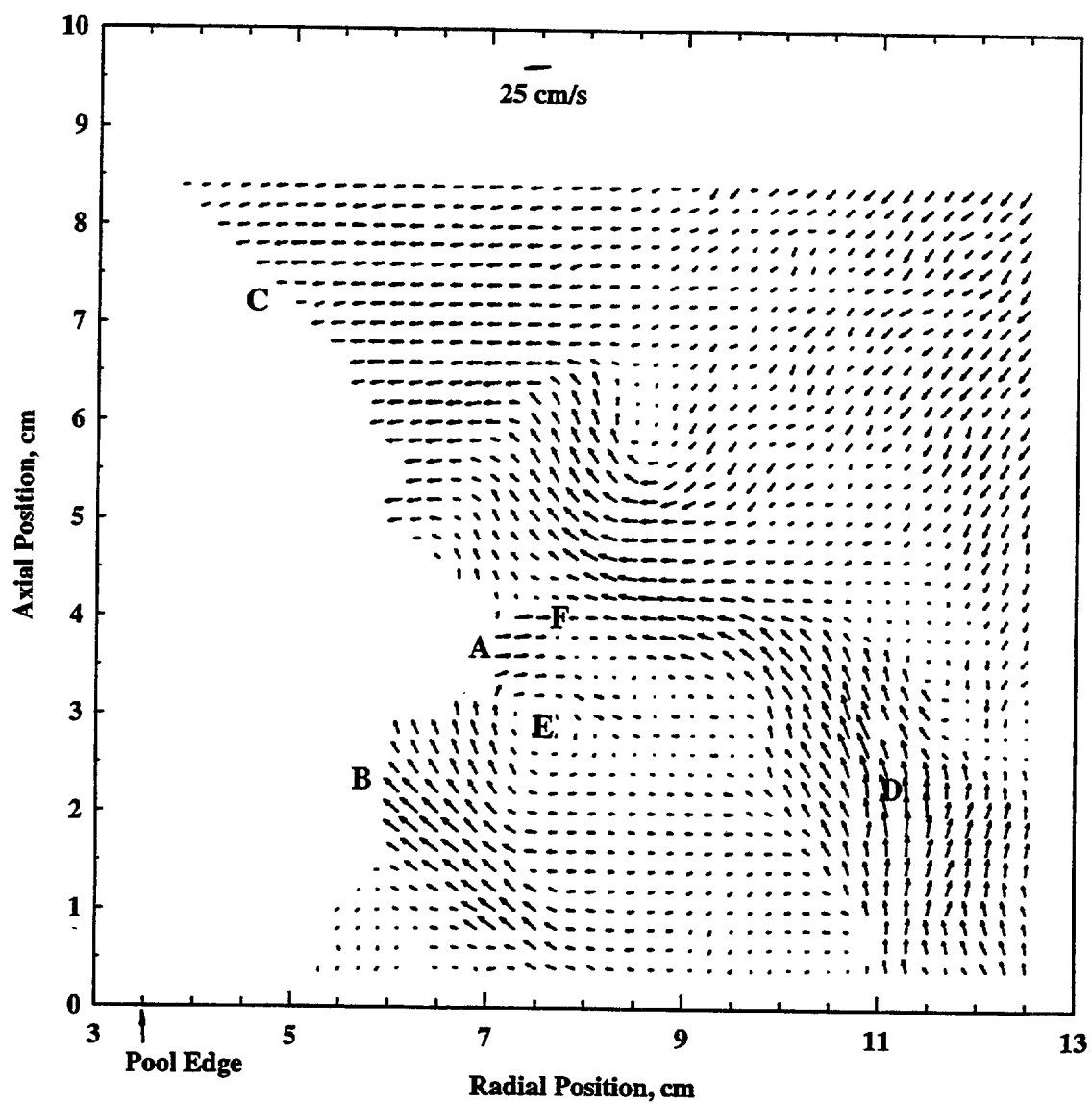


Figure 5.1 Instantaneous velocity vectors around a 7.1 cm toluene pool fire with a floor obtained using PIV showing the strong entrainment upstream and downstream of a flame bulge.

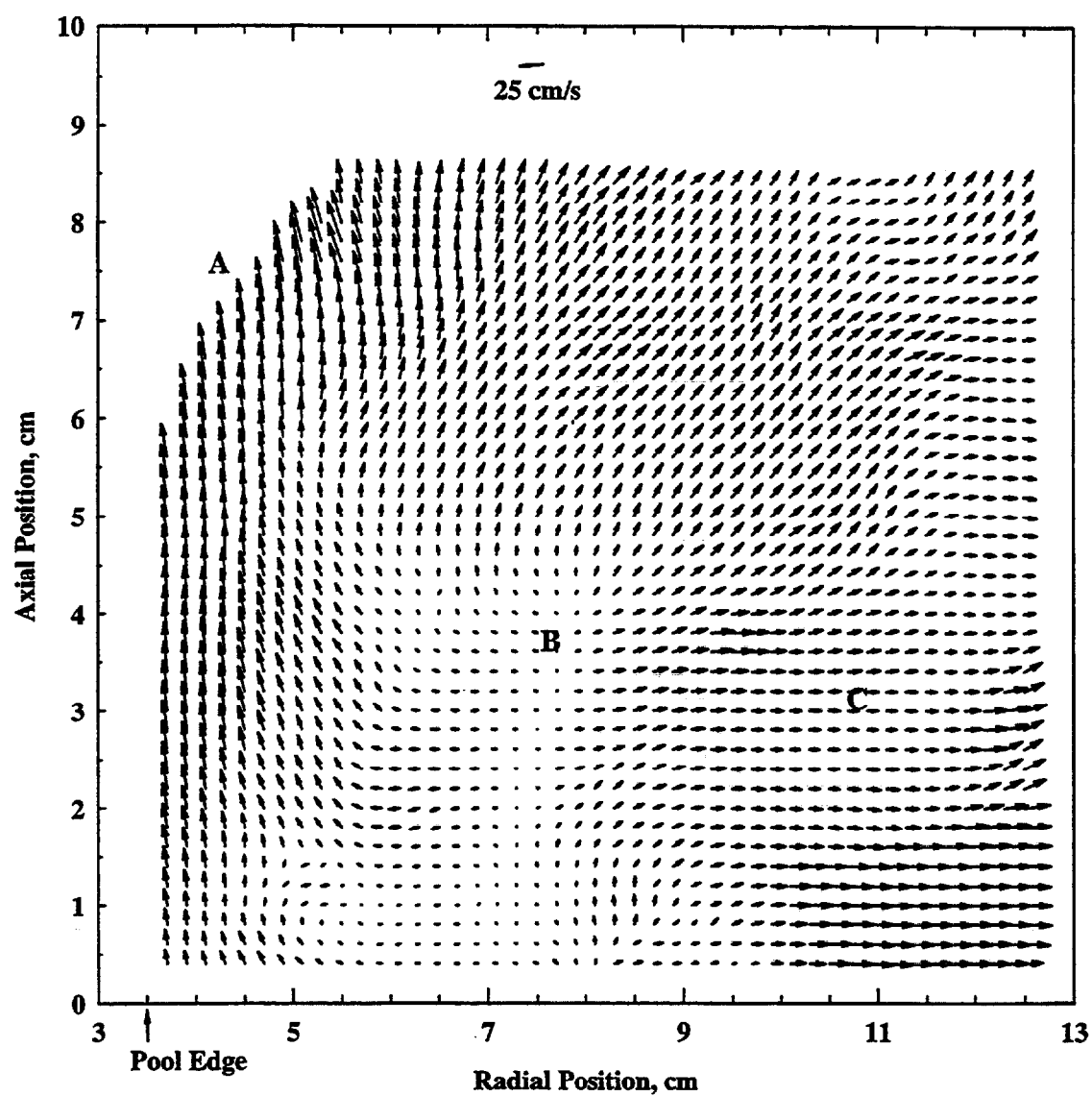


Figure 5.2 Instantaneous velocity vectors around a 7.1 cm toluene pool fire with a floor obtained using PIV showing the vertical phase of the transient flow.

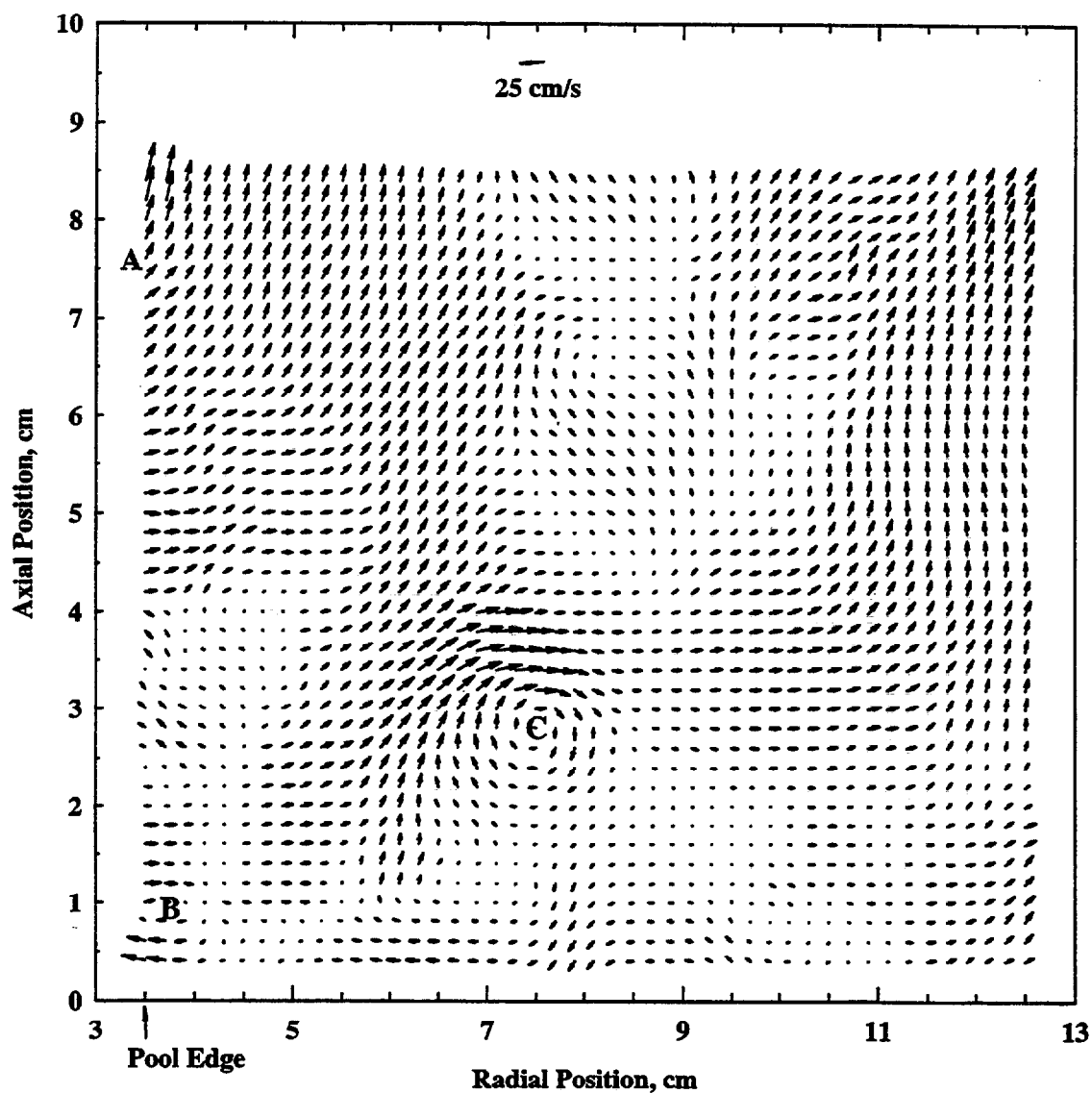


Figure 5.3 Instantaneous velocity vectors around a 7.1 cm toluene pool fire with a floor obtained using PIV showing the extrainment phase of the flow.

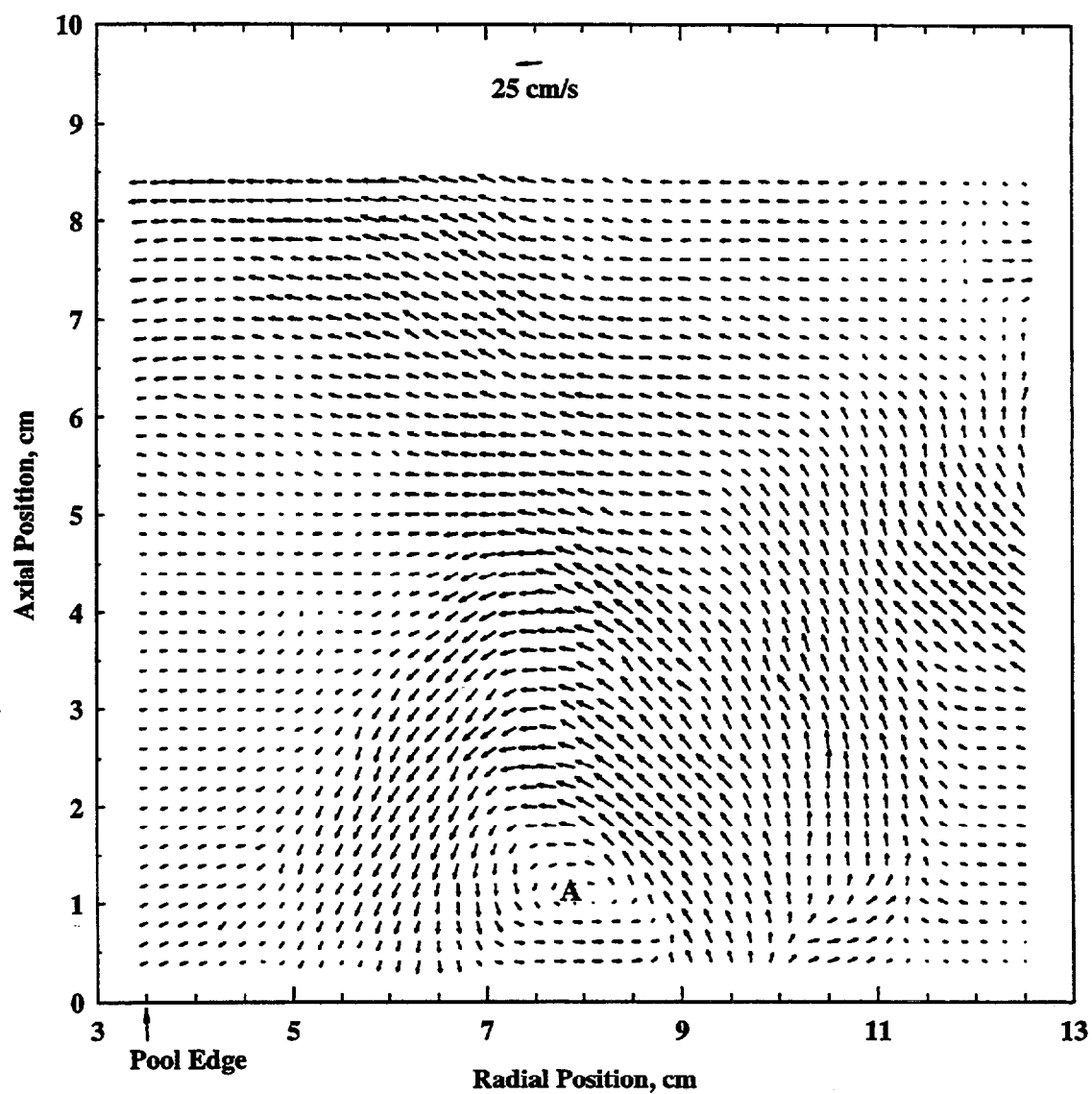


Figure 5.4 Instantaneous velocity vectors around a 7.1 cm toluene pool fire with a floor obtained using PIV showing vortex in the negative direction.

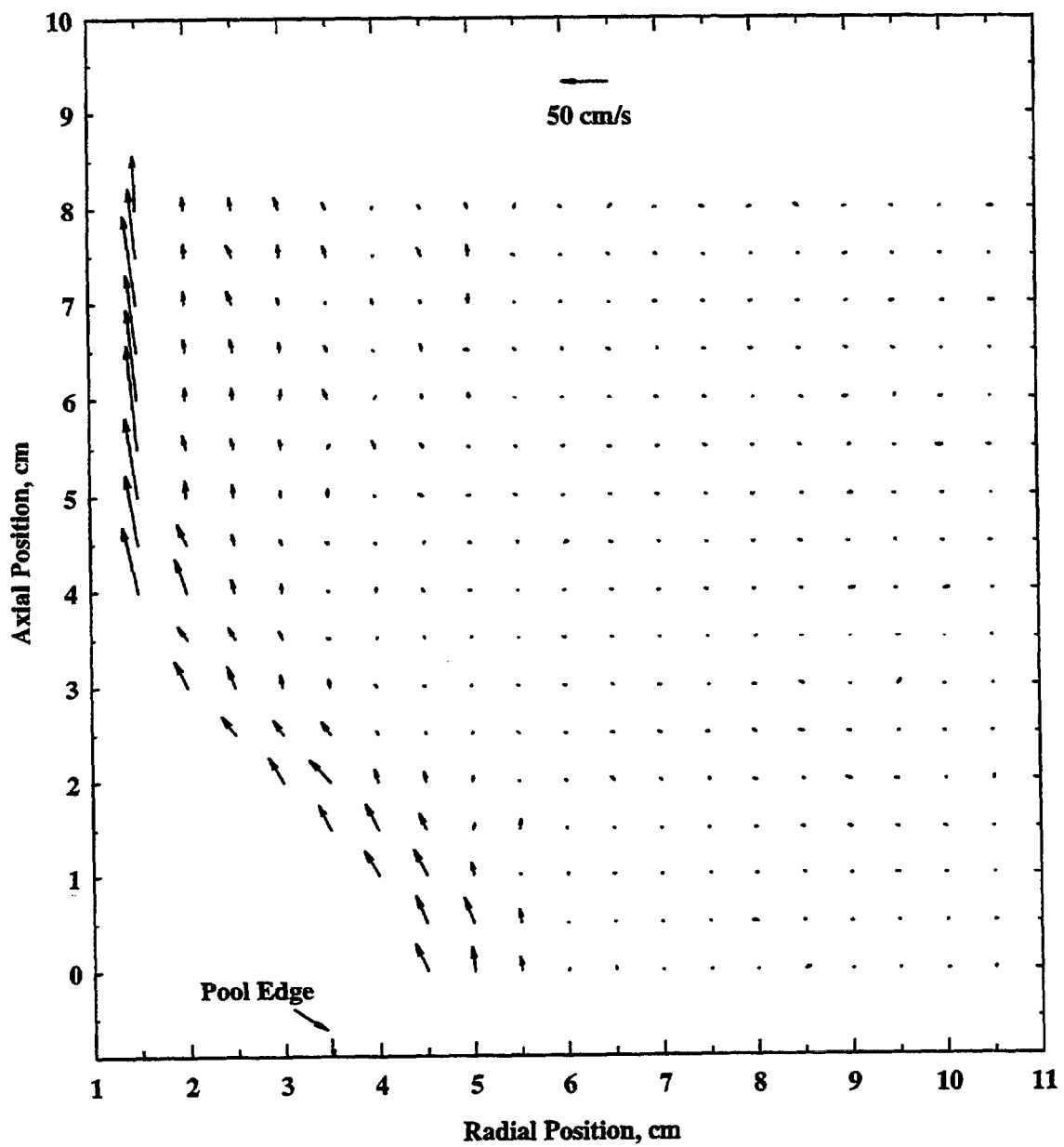


Figure 5.5 An instantaneous velocity field of the flow induced by a 7.1 cm toluene pool fire without a floor.

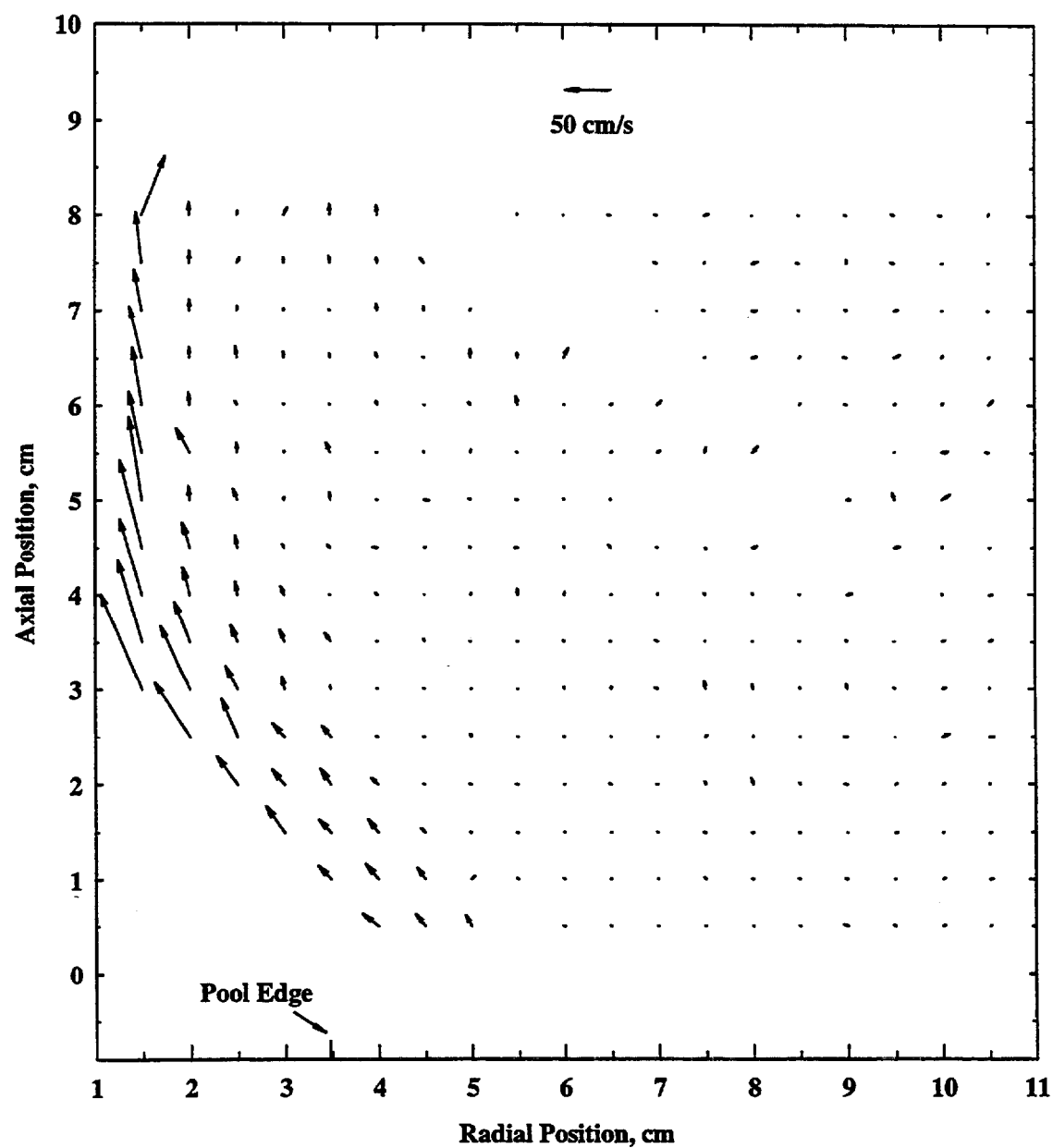


Figure 5.6 An instantaneous velocity field of the flow induced by a 7.1 cm toluene pool fire without a floor.

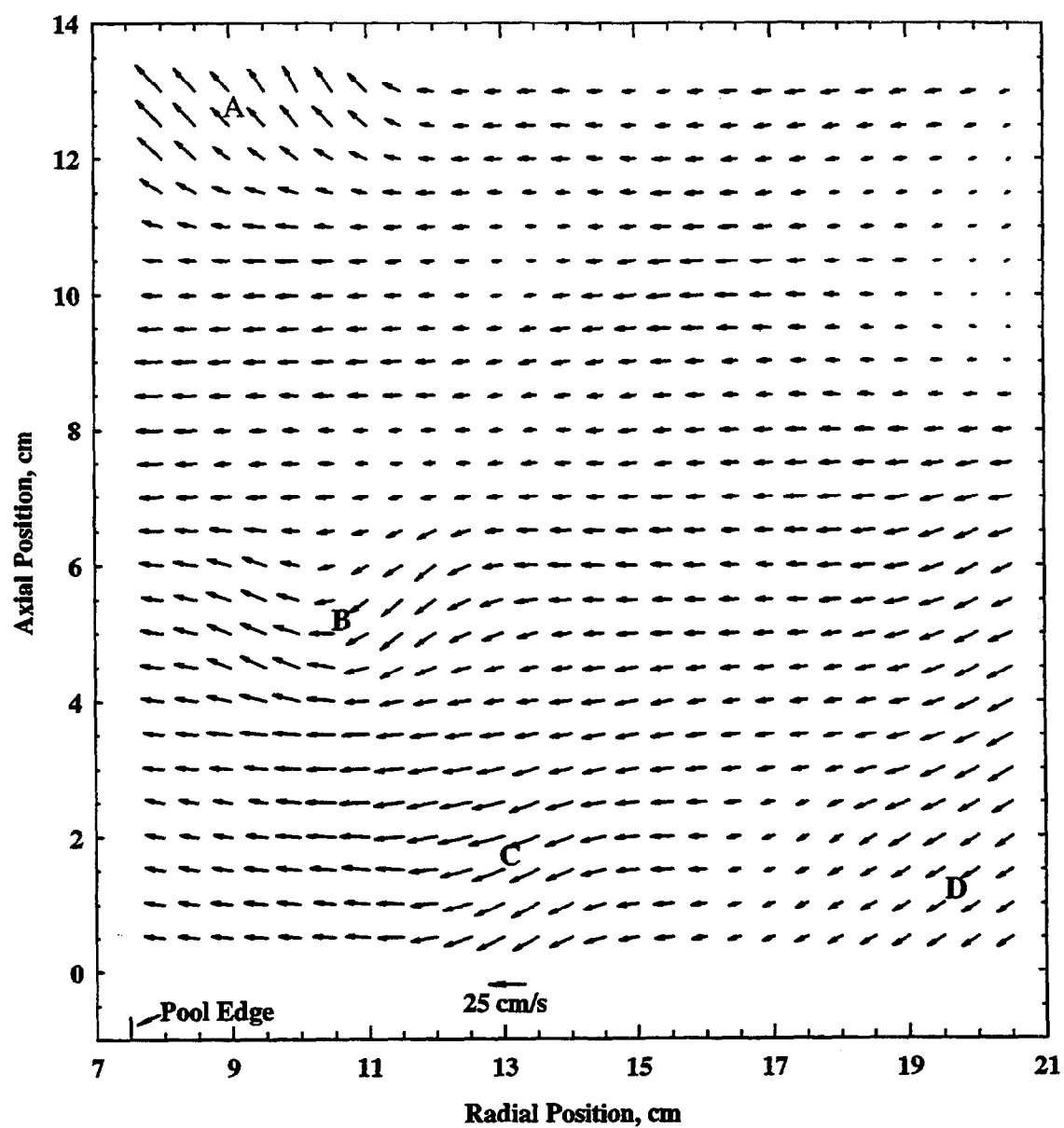


Figure 5.7 Instantaneous velocity vectors around a 15 cm toluene pool fire with a 51 cm sheet metal floor.

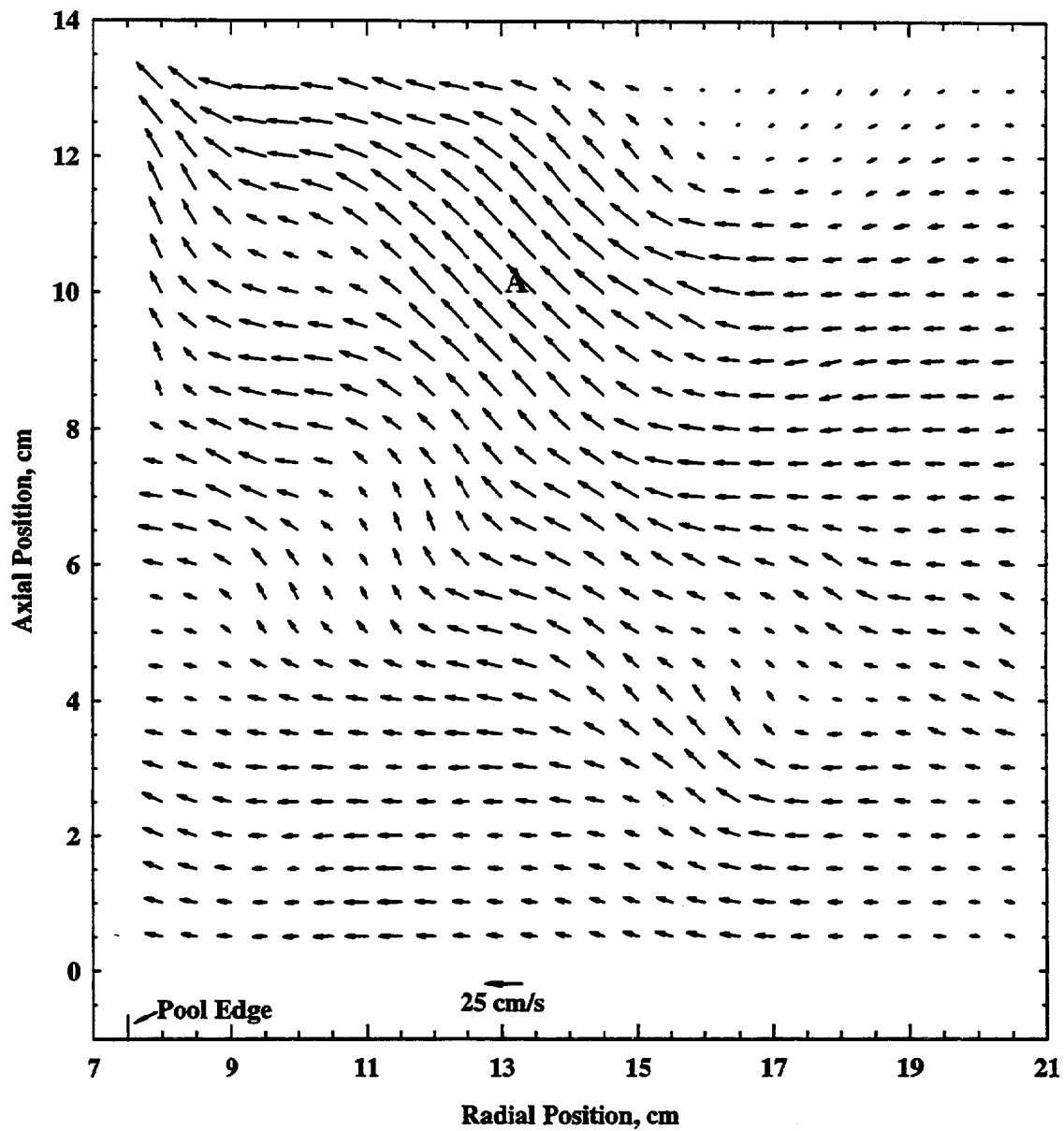


Figure 5.8 Instantaneous velocity vectors around a 15 cm toluene pool fire with a 51 cm sheet metal floor.

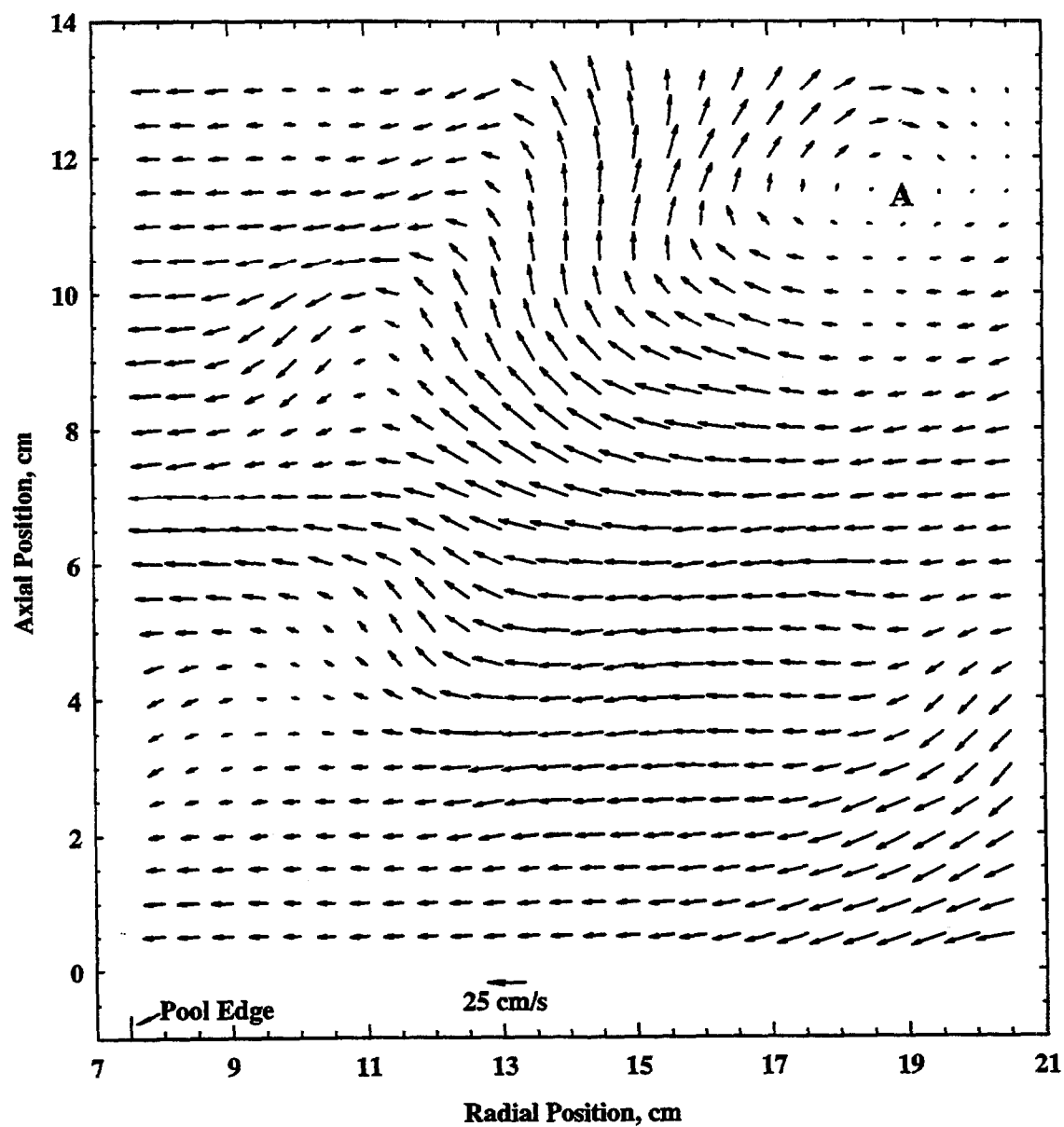


Figure 5.9 Instantaneous velocity vectors around a 15 cm toluene pool fire with a 51 cm sheet metal floor.

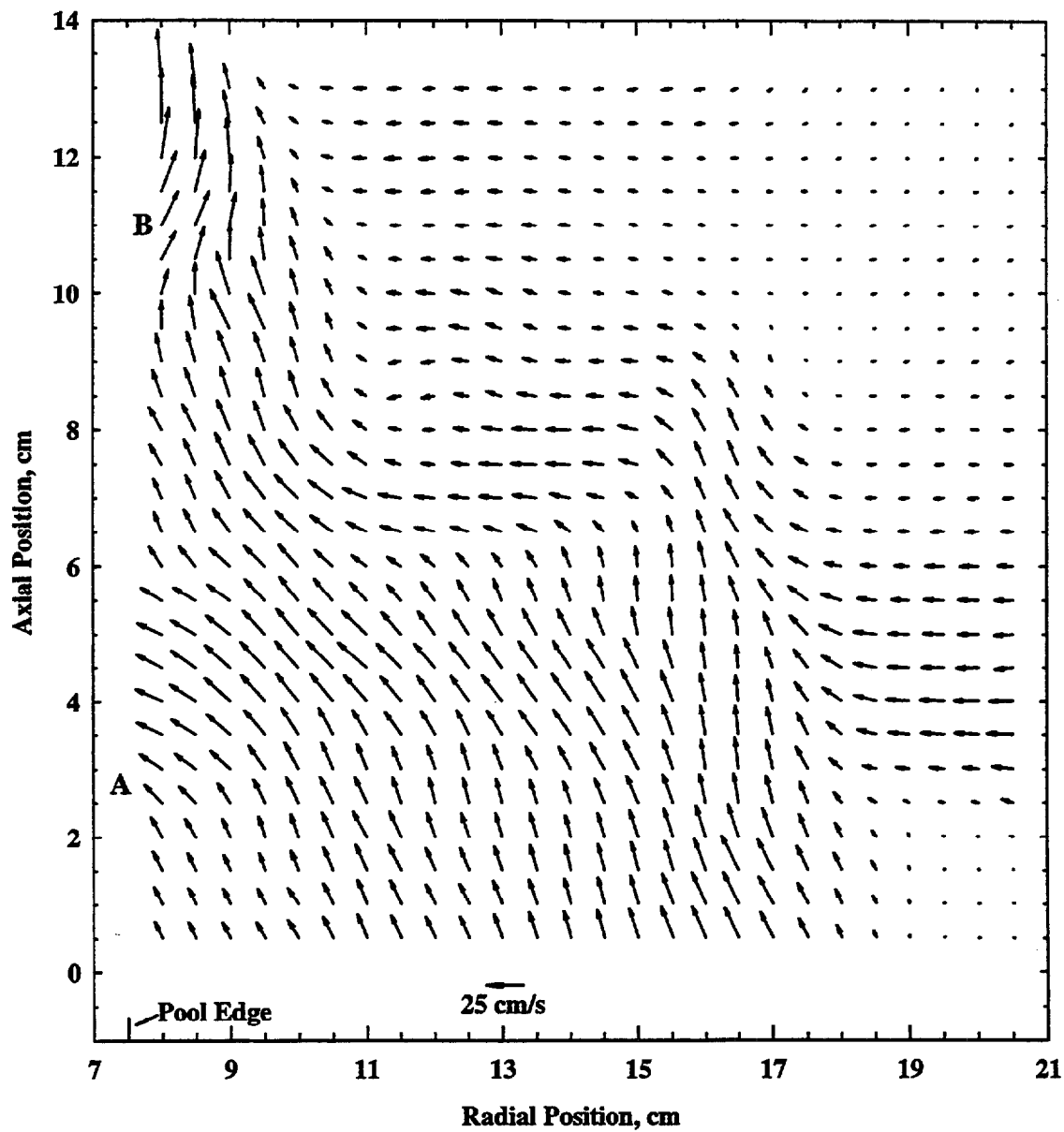


Figure 5.10 Instantaneous velocity vectors around a 15 cm toluene pool fire with a 51 cm sheet metal floor.

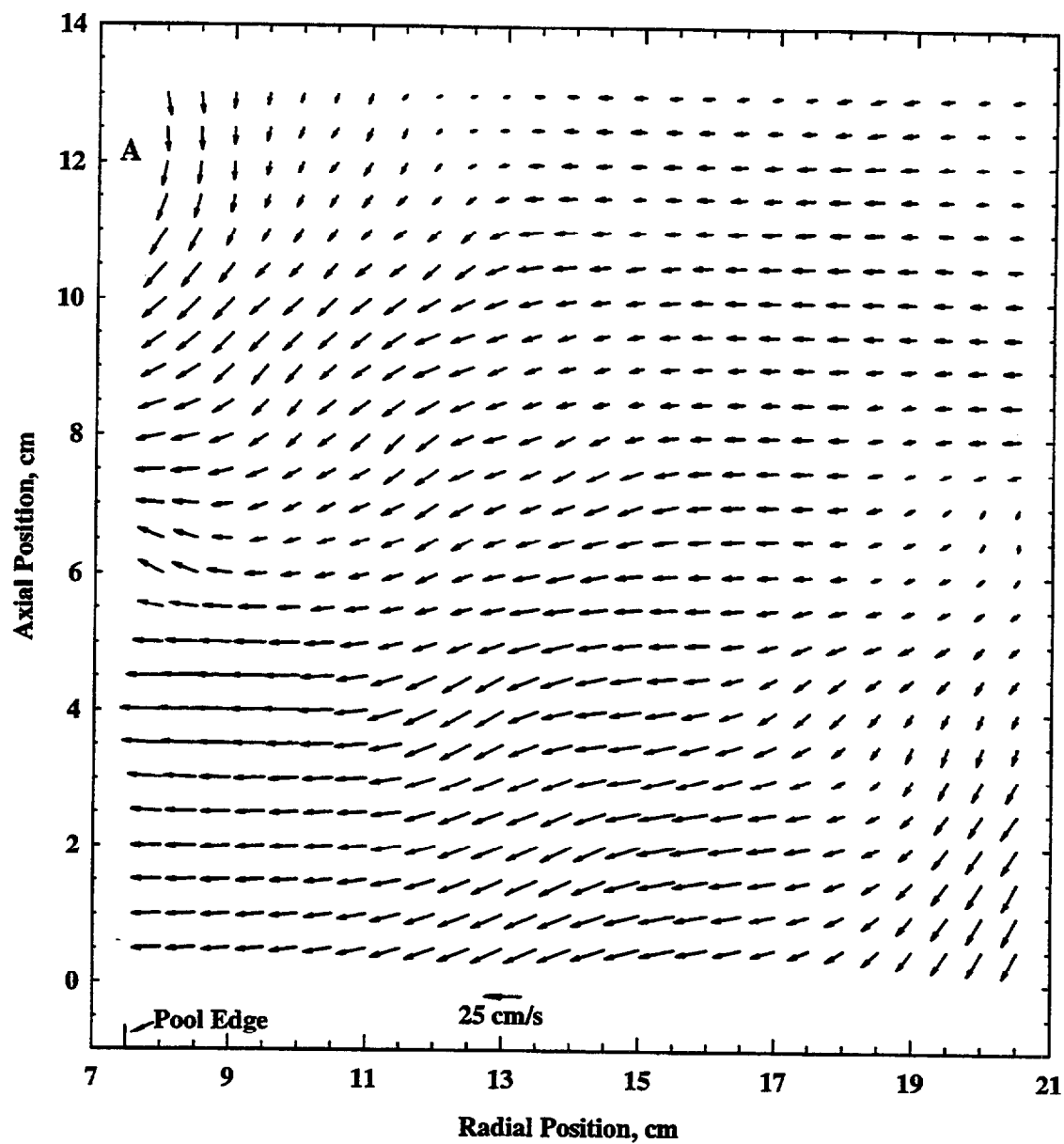


Figure 5.11 Instantaneous velocity vectors around a 15 cm toluene pool fire with a 51 cm sheet metal floor.

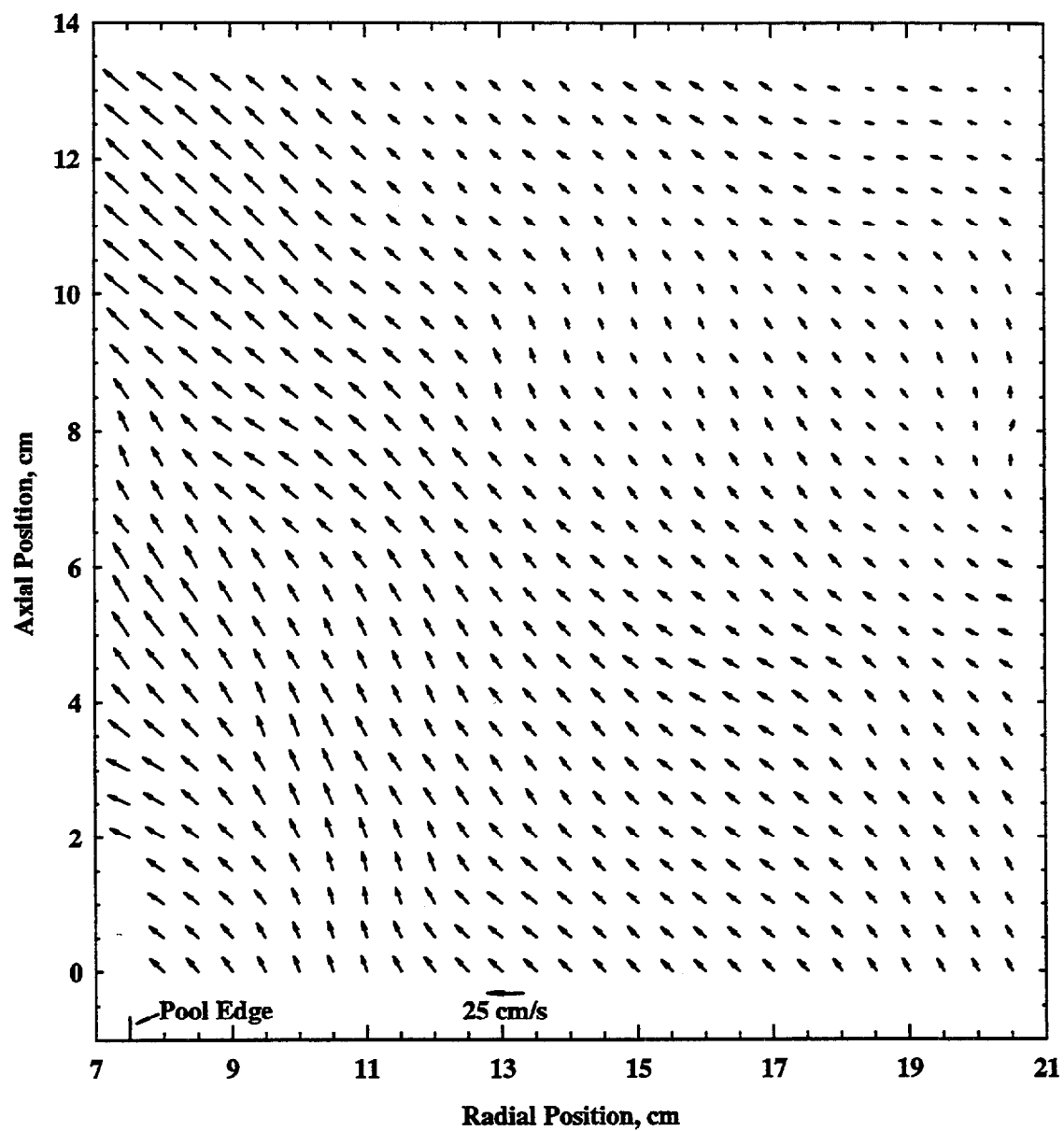


Figure 5.12 Instantaneous velocity vectors around a 15 cm toluene pool fire without a floor.

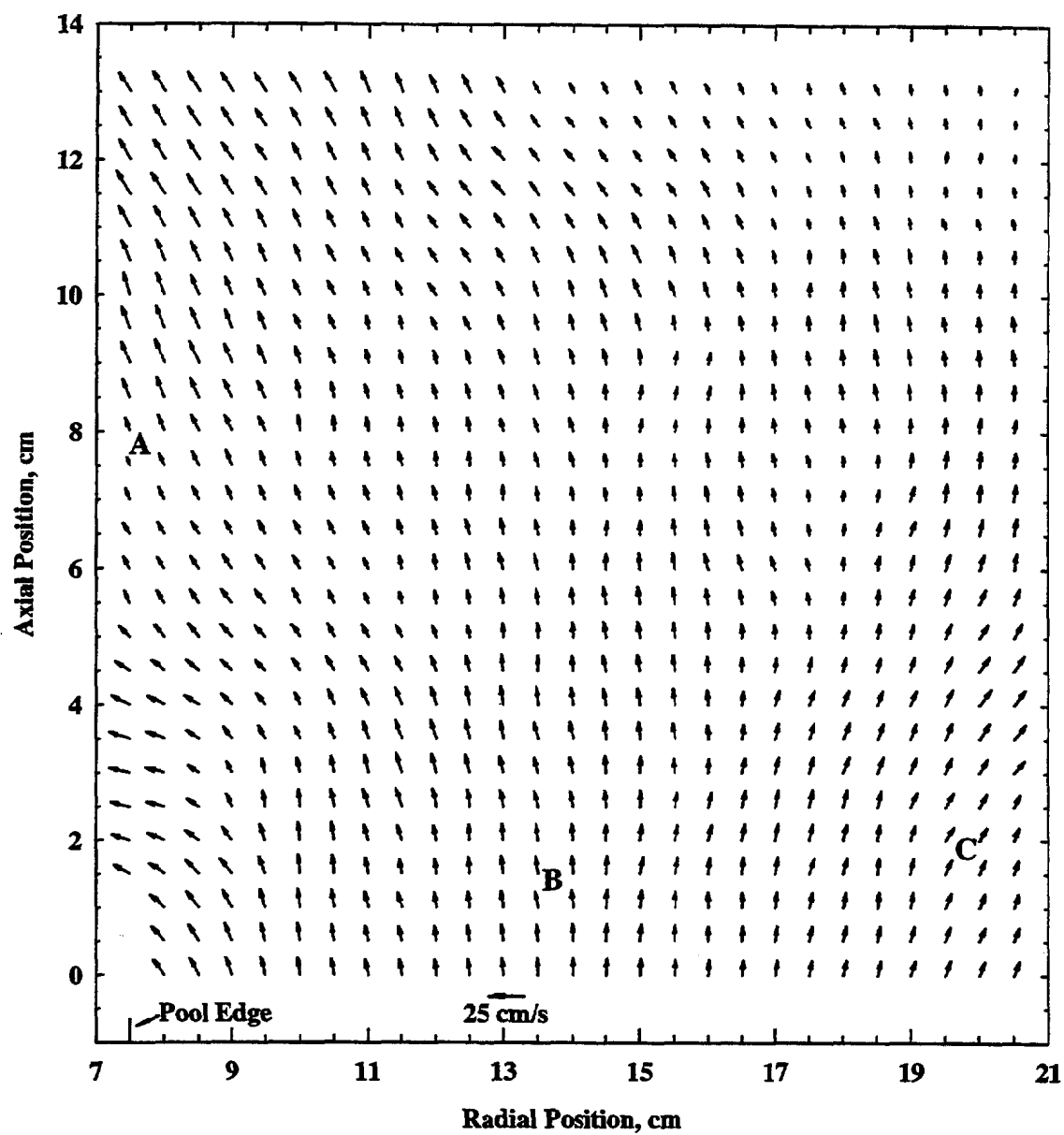


Figure 5.13 Instantaneous velocity vectors around a 15 cm toluene pool fire without a floor.

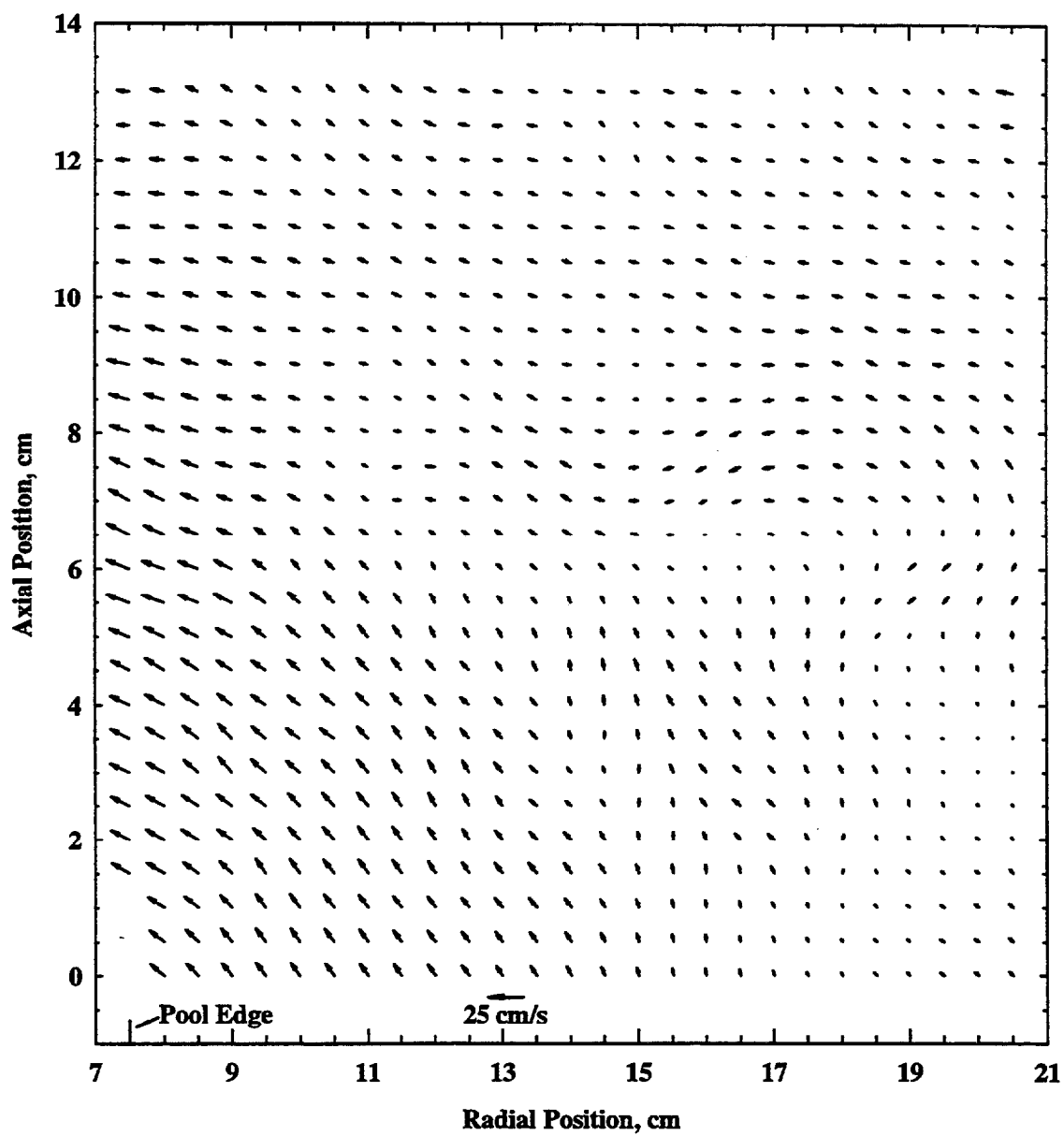


Figure 5.14 Instantaneous velocity vectors around a 15 cm toluene pool fire without a floor.

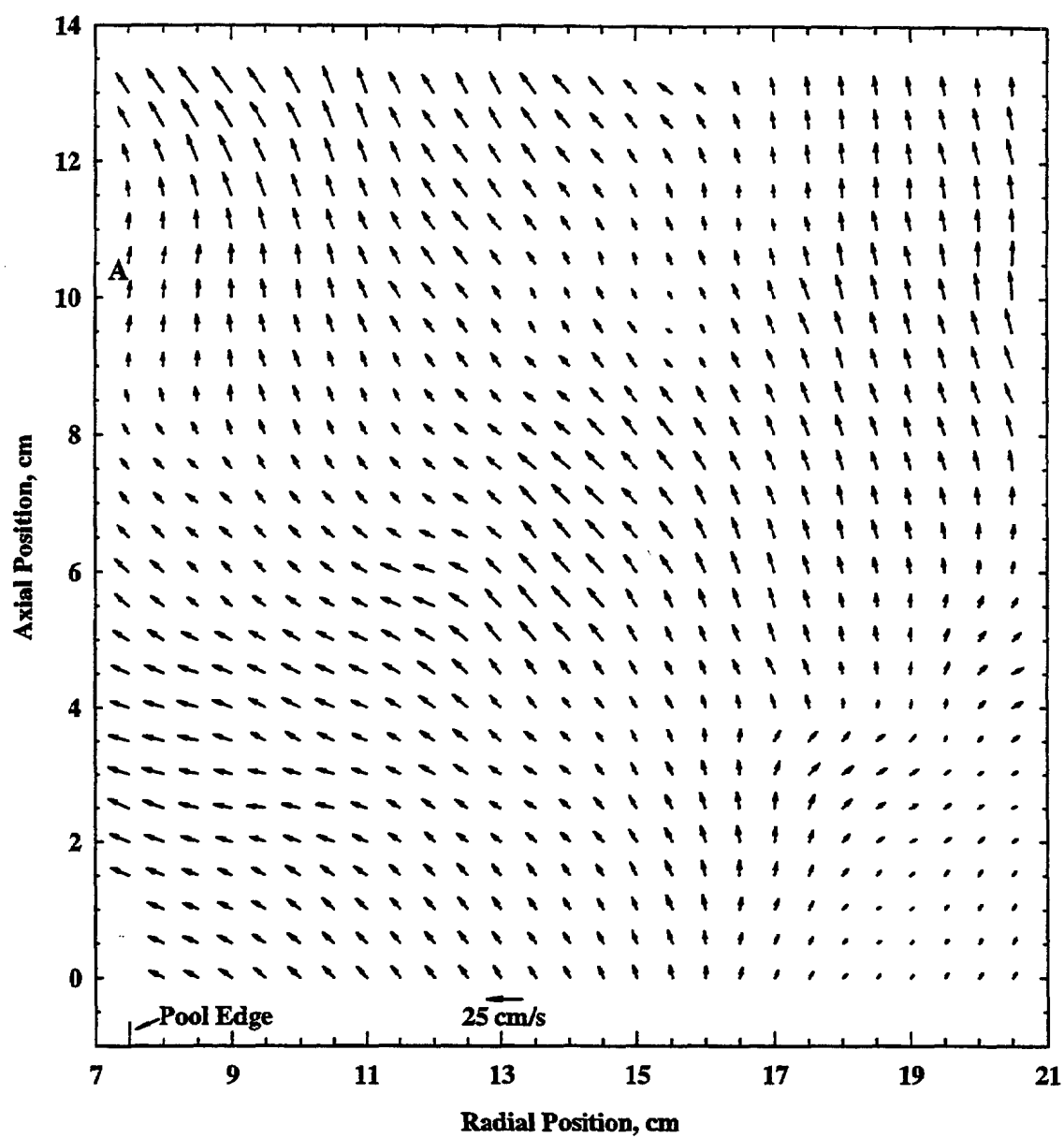


Figure 5.15 Instantaneous velocity vectors around a 15 cm toluene pool fire without a floor.

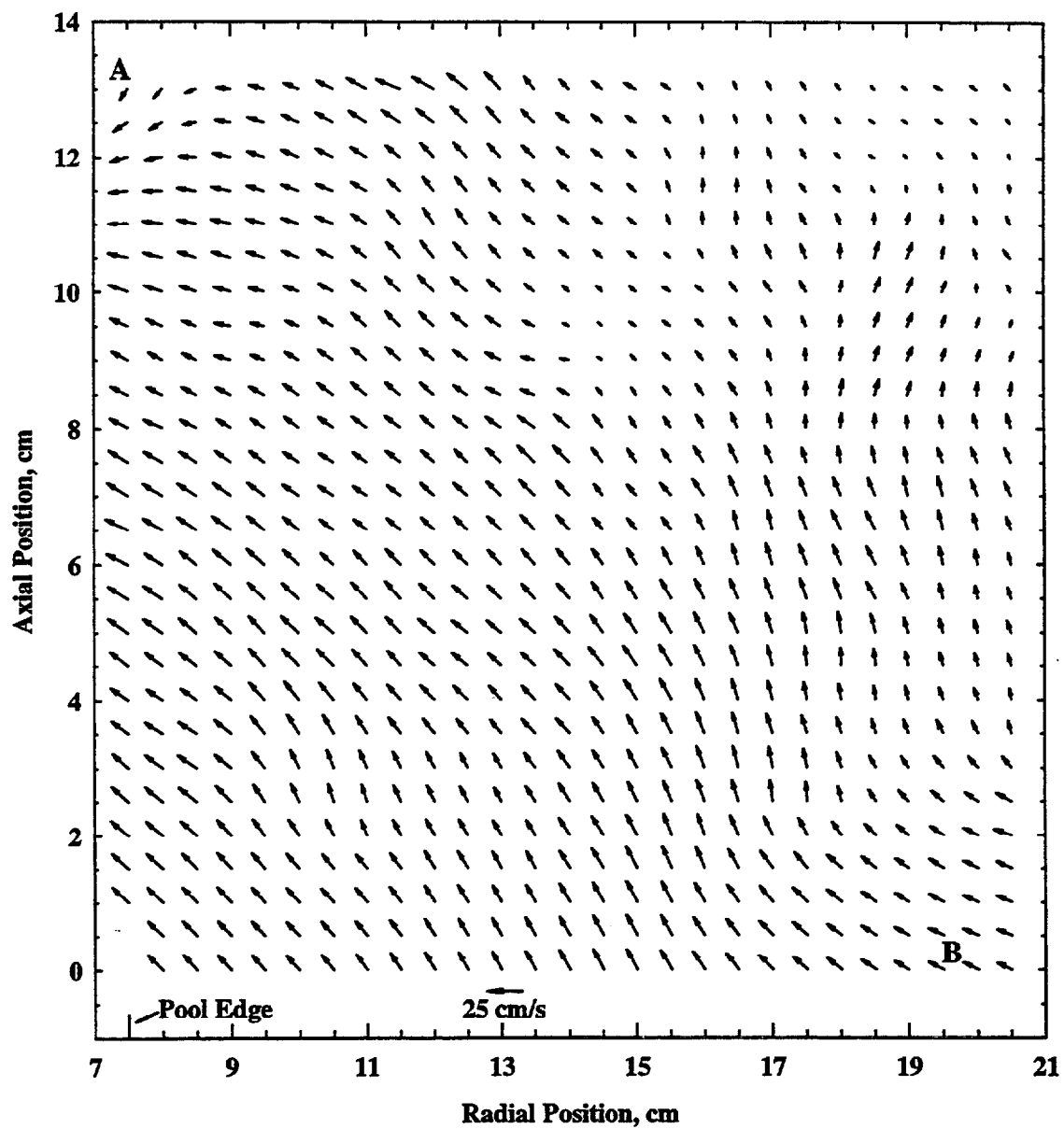


Figure 5.16 Instantaneous velocity vectors around a 15 cm toluene pool fire without a floor.

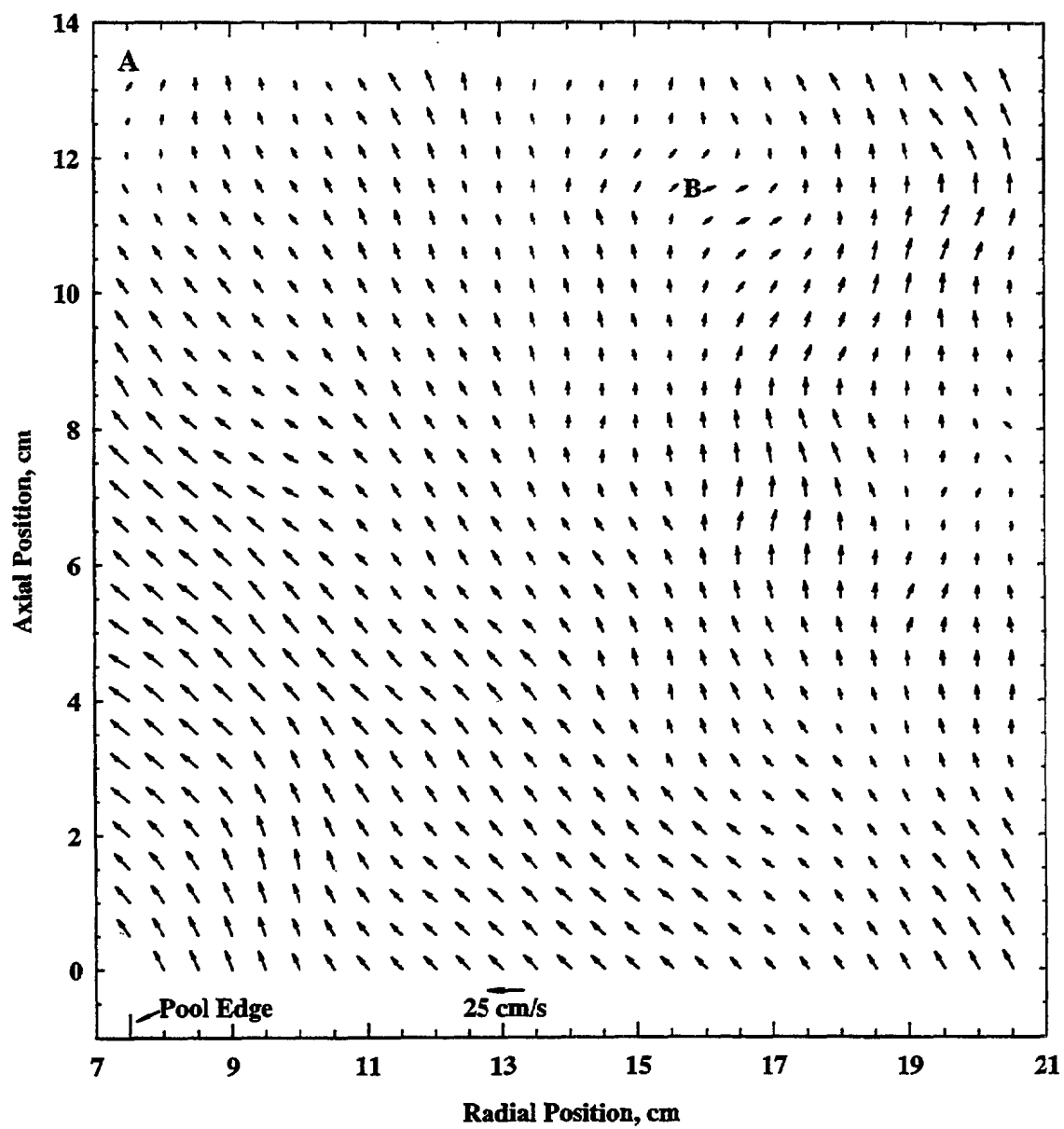


Figure 5.17 Instantaneous velocity vectors around a 15 cm toluene pool fire without a floor.

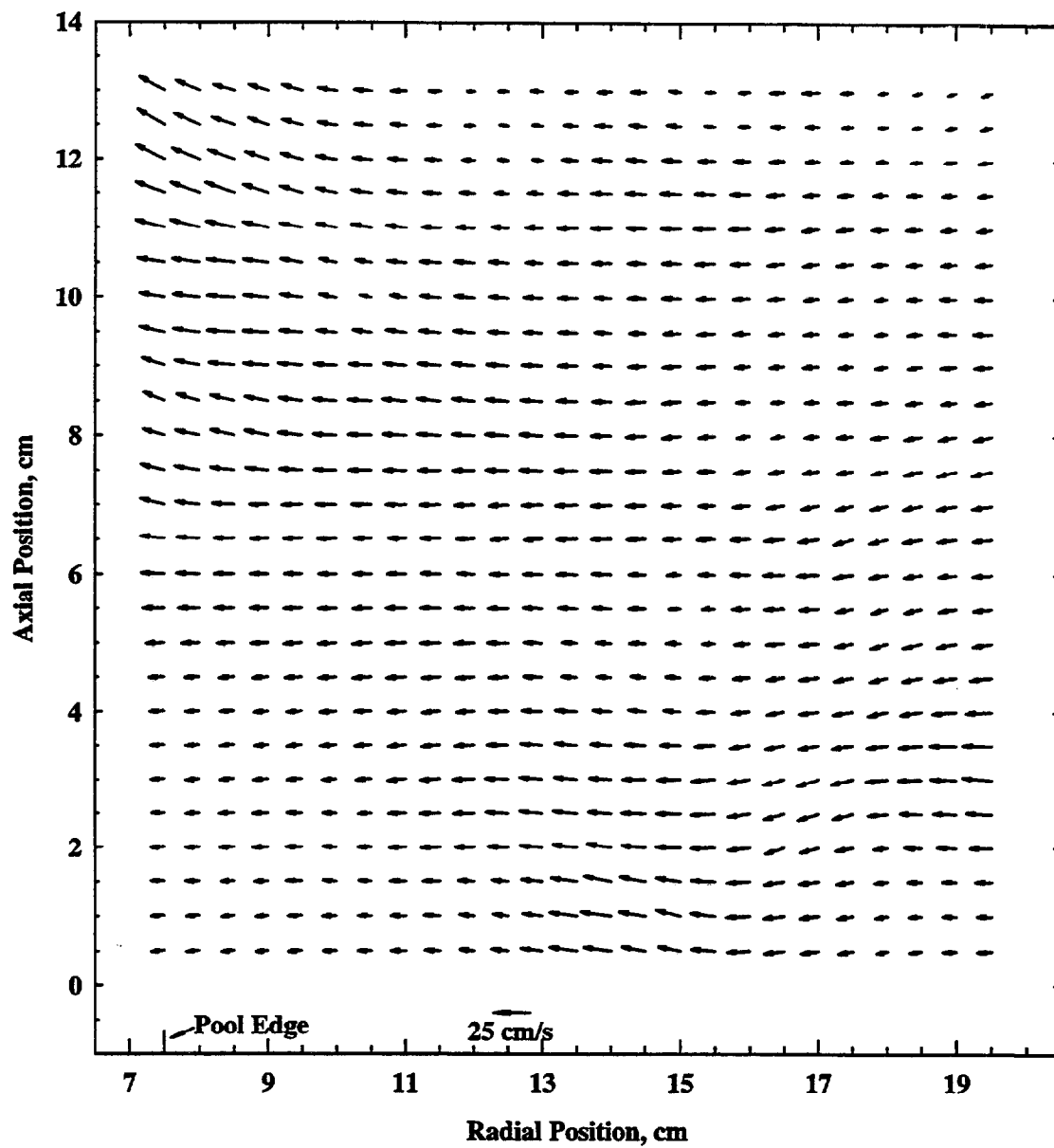


Figure 5.18 Instantaneous velocity vectors around a 15 cm heptane pool fire with a 51 cm sheet metal floor.

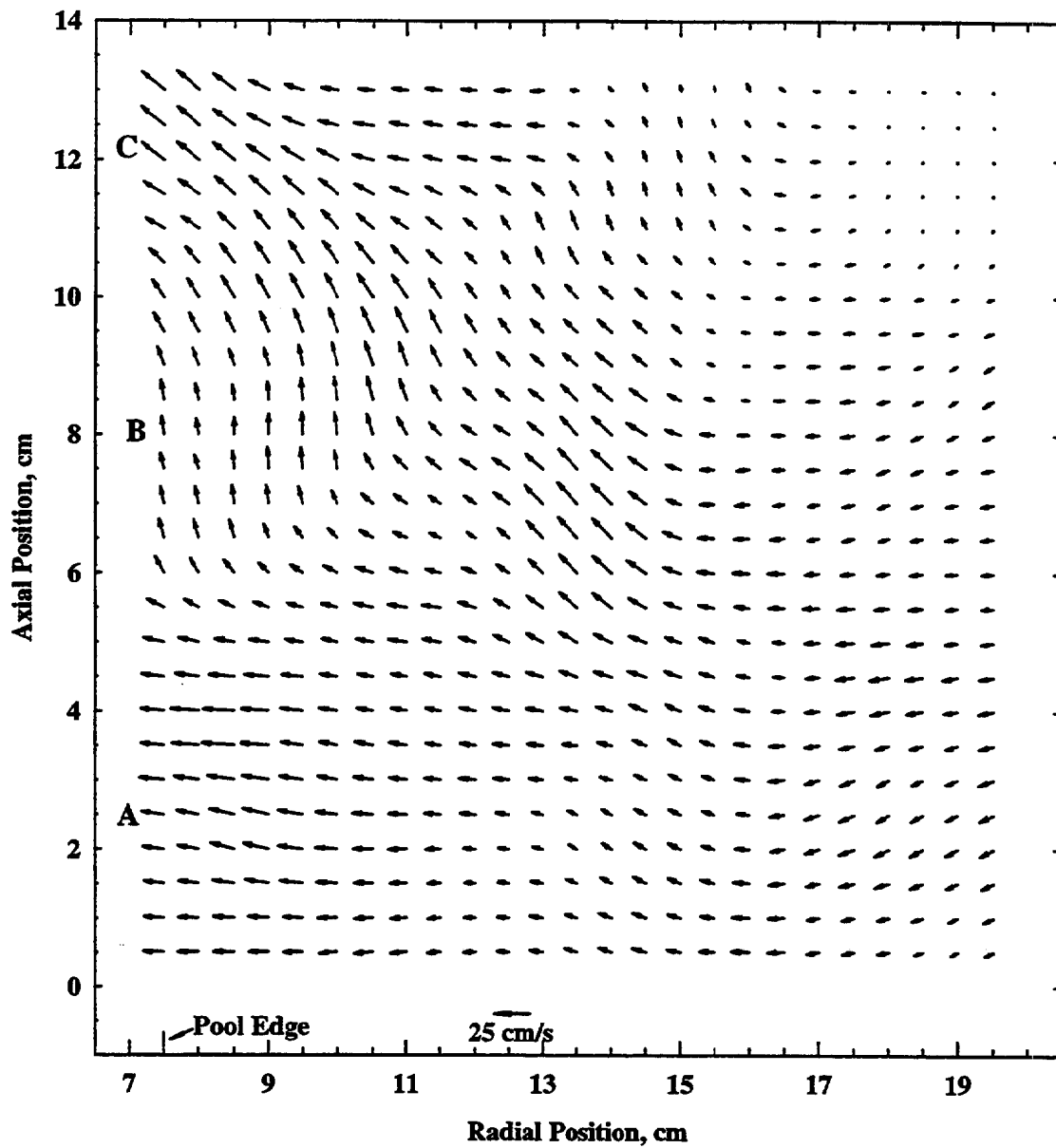


Figure 5.19 Instantaneous velocity vectors around a 15 cm heptane pool fire with a 51 cm sheet metal floor.

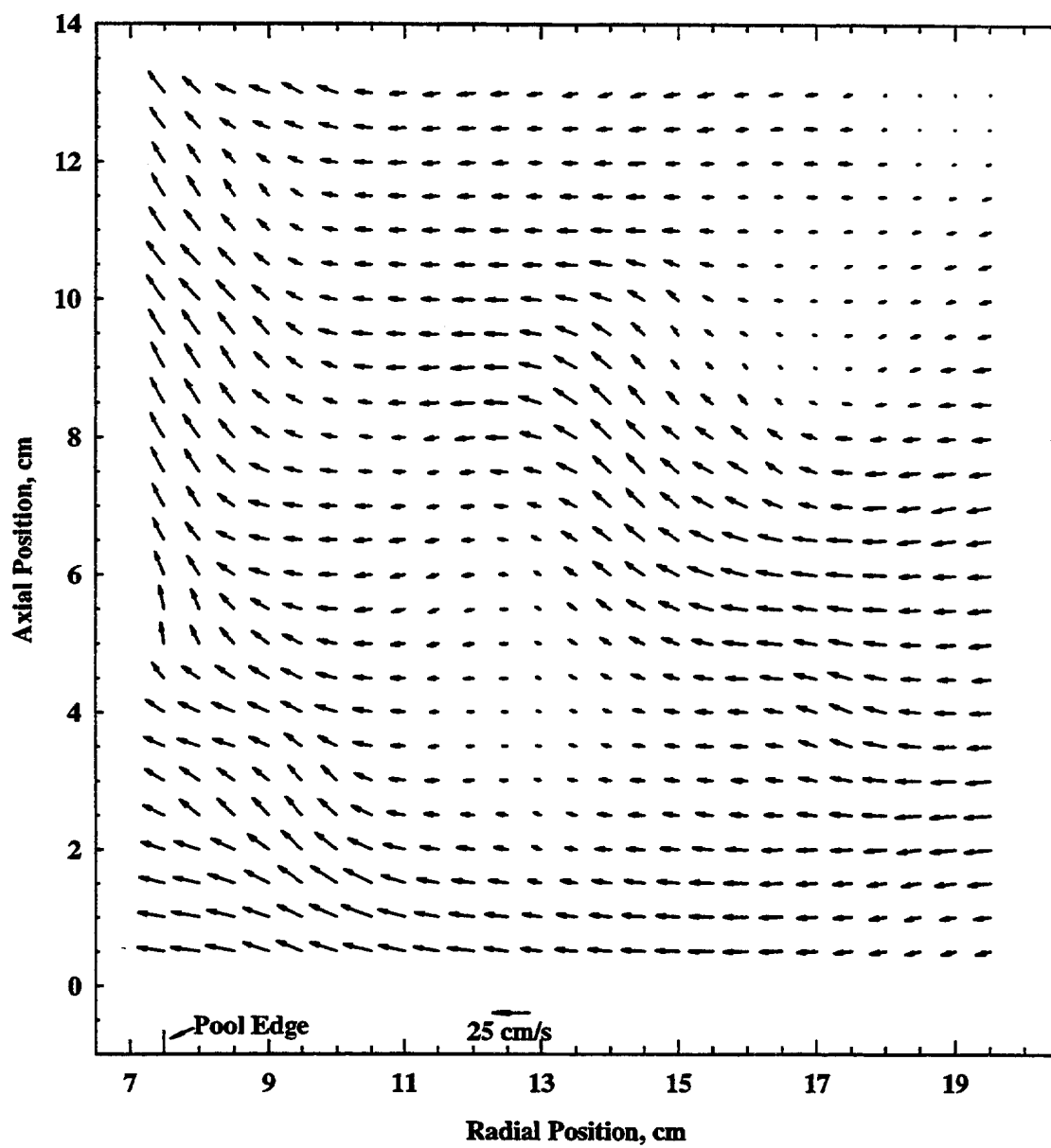


Figure 5.20 Instantaneous velocity vectors around a 15 cm heptane pool fire with a 51 cm sheet metal floor.

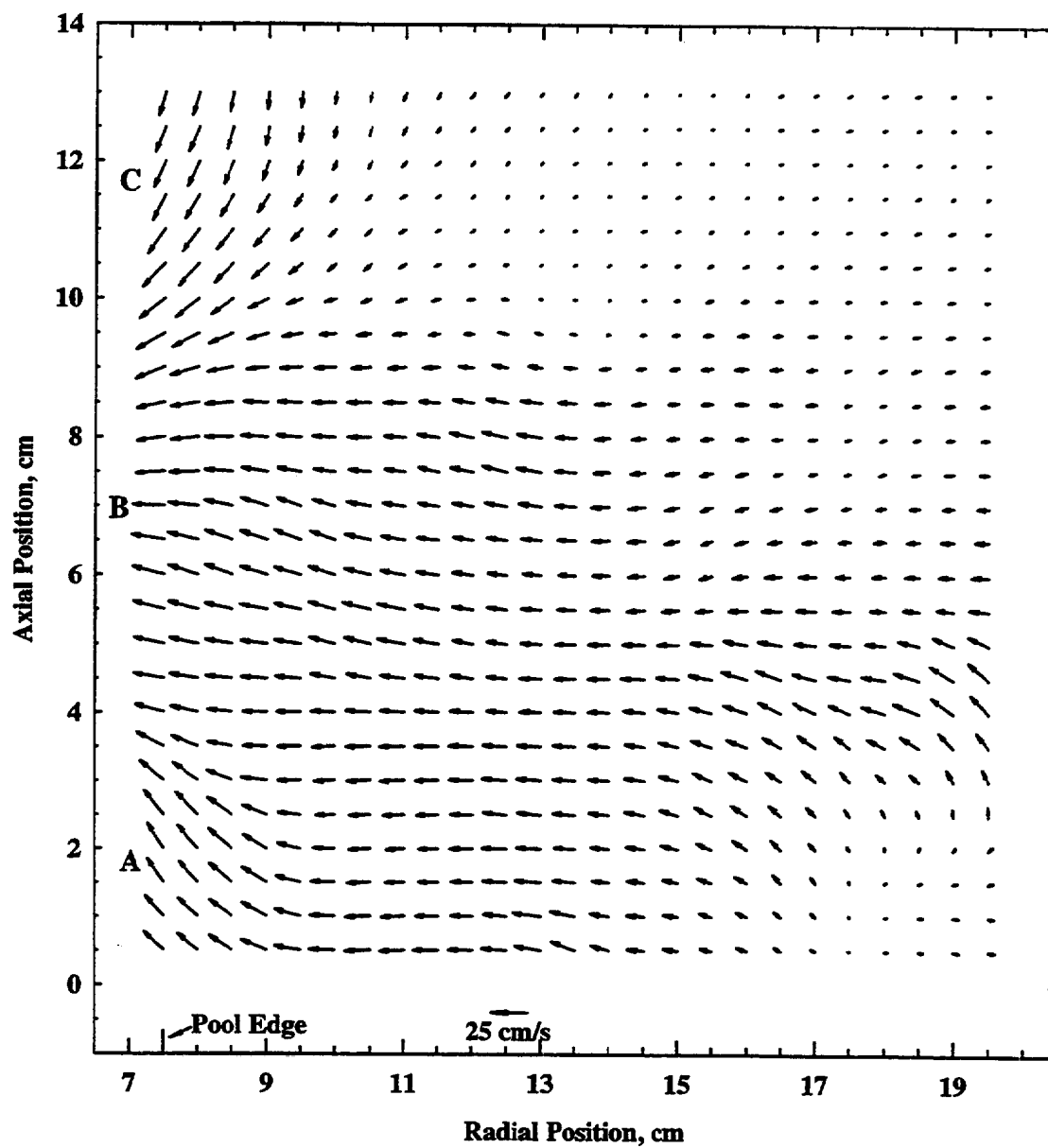


Figure 5.21 Instantaneous velocity vectors around a 15 cm heptane pool fire with a 51 cm sheet metal floor.

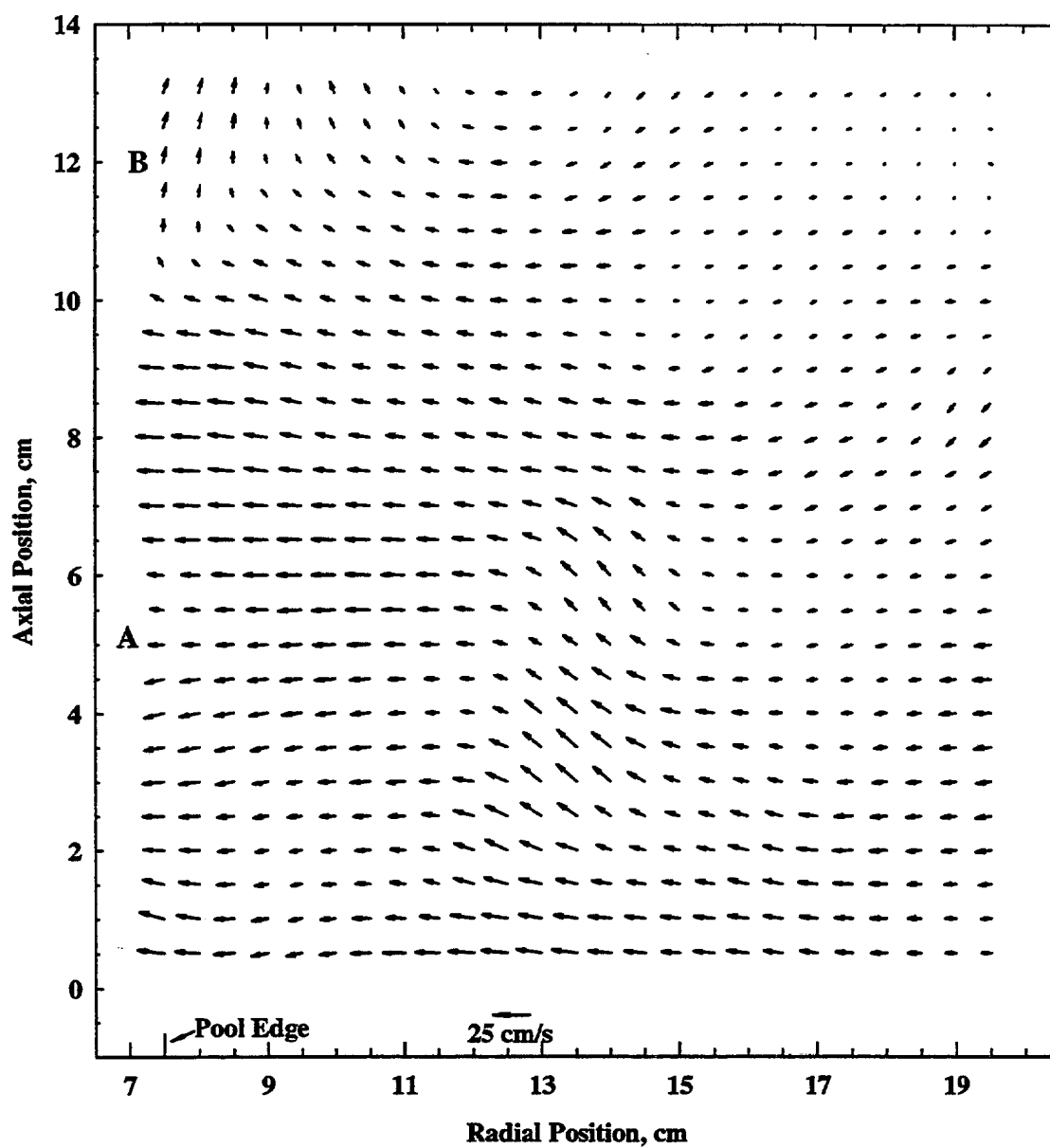


Figure 5.22 Instantaneous velocity vectors around a 15 cm heptane pool fire with a 51 cm sheet metal floor.

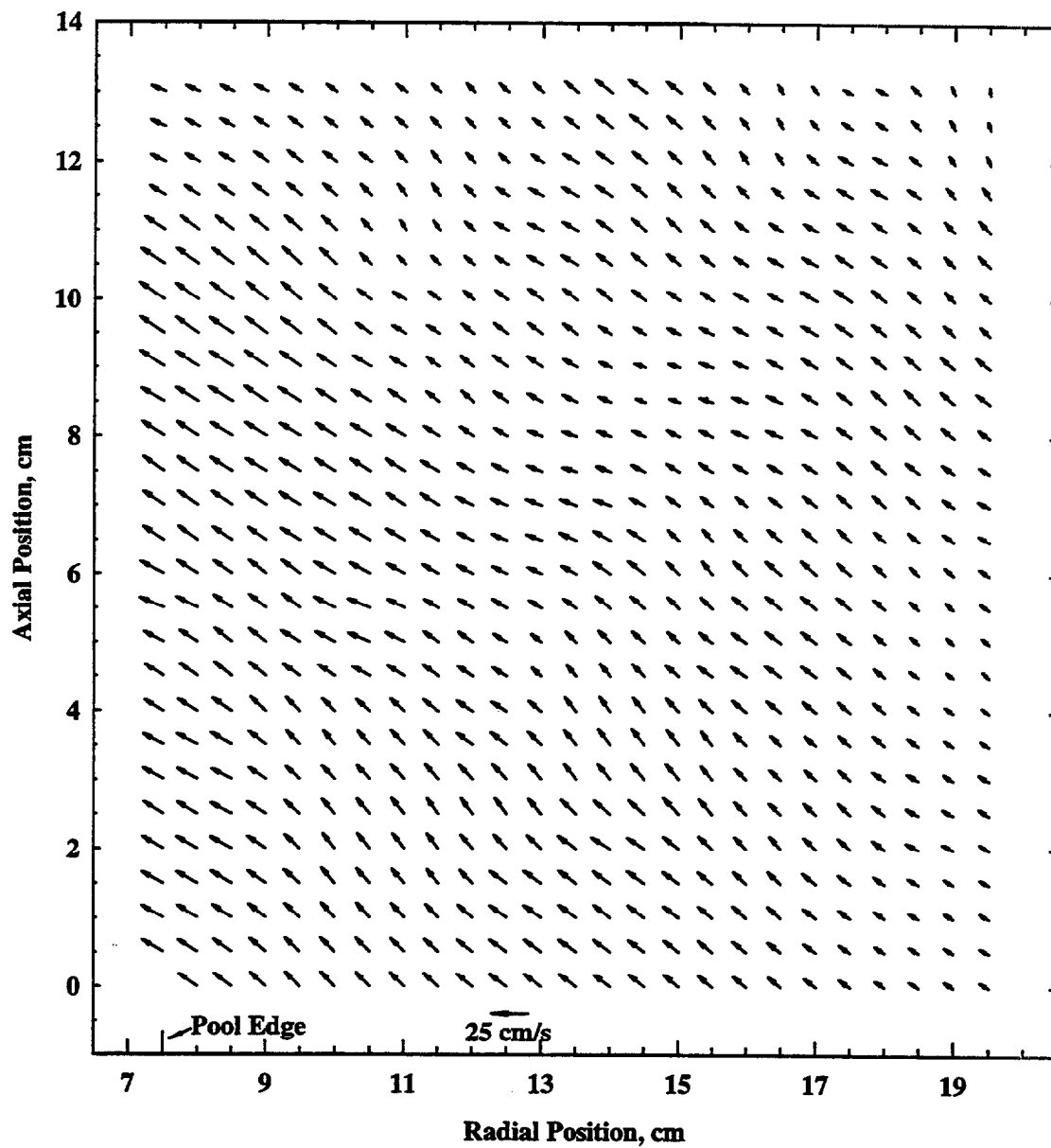


Figure 5.23 Instantaneous velocity vectors around a 15 cm heptane pool fire without a floor.

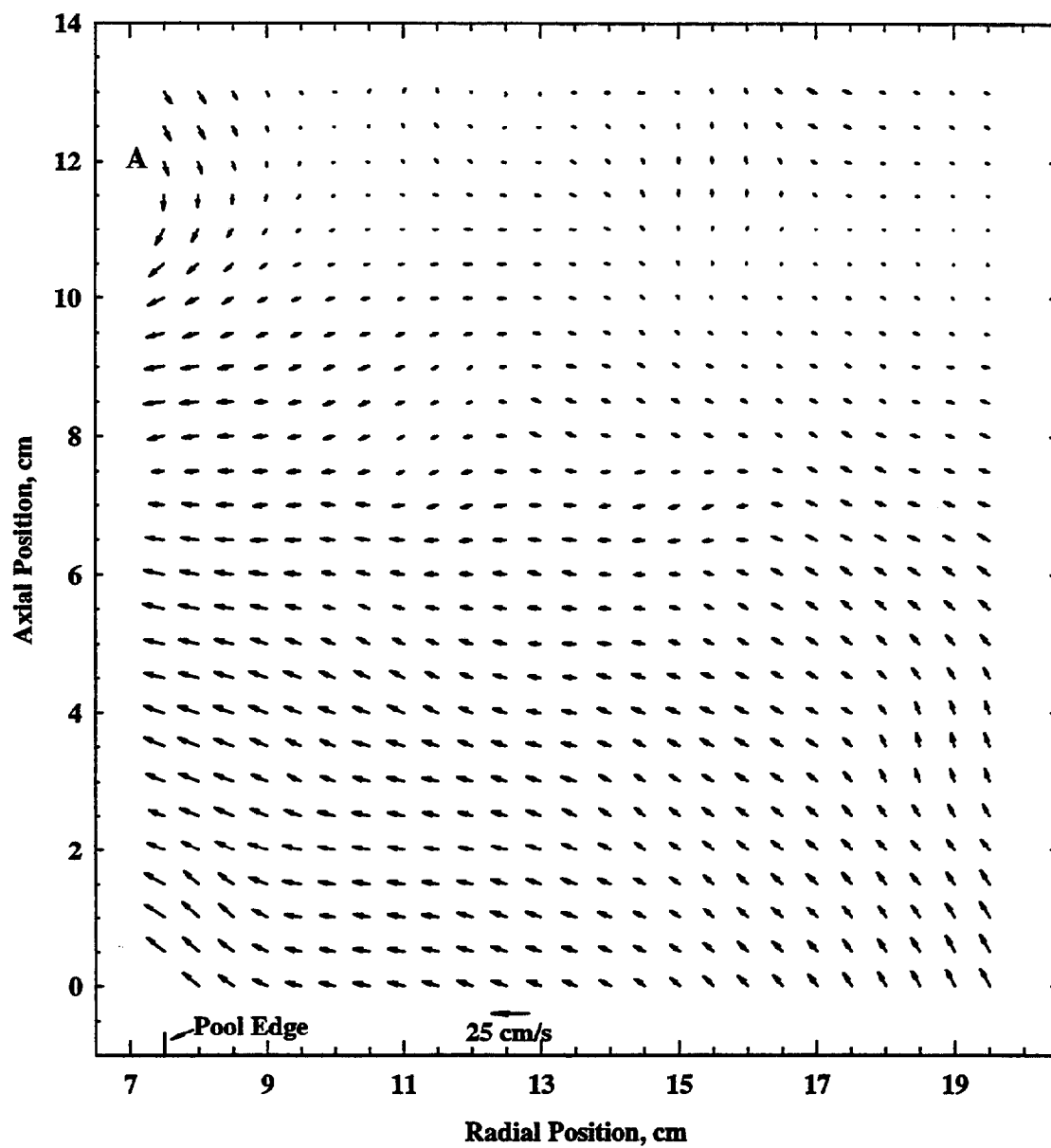


Figure 5.24 Instantaneous velocity vectors around a 15 cm heptane pool fire without a floor.

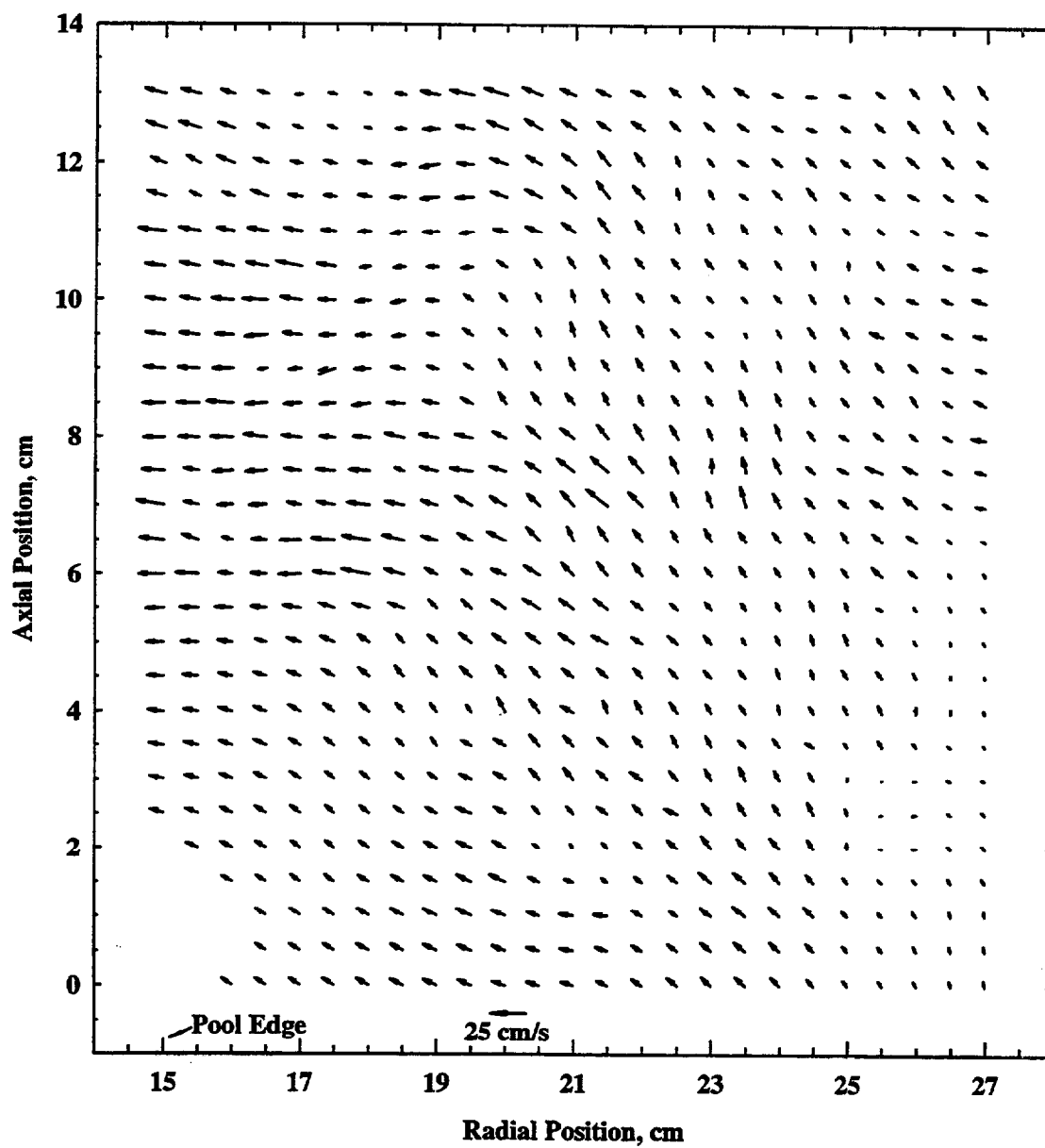


Figure 5.25 Instantaneous velocity vectors around a 30 cm toluene pool fire without a floor obtained using PIV showing the strong entrainment at the radial location of pool burner.

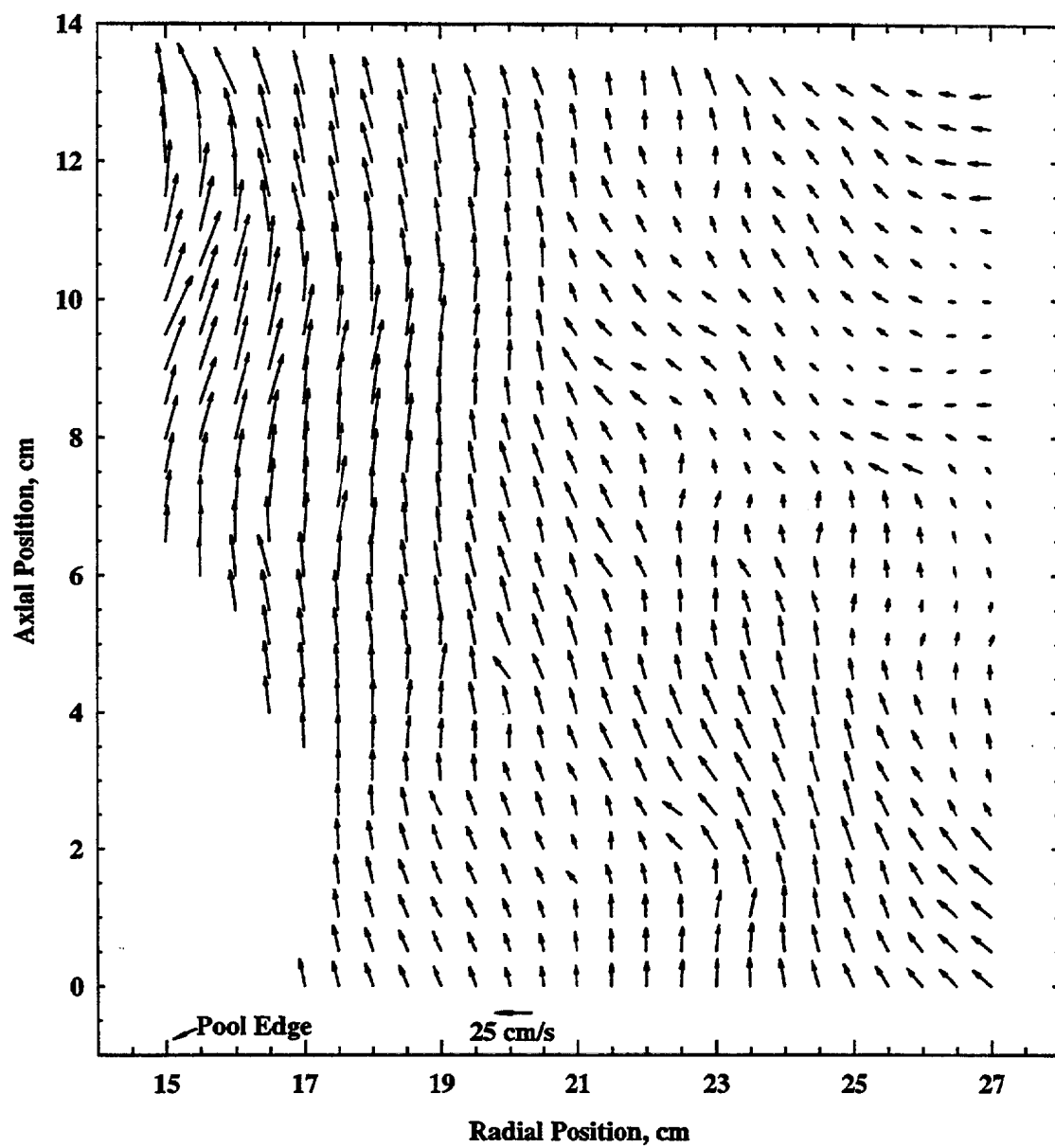


Figure 5.26 Instantaneous velocity vectors around a 30 cm toluene pool fire without a floor obtained using PIV showing the vertical and extrainment phase of the transient flow.

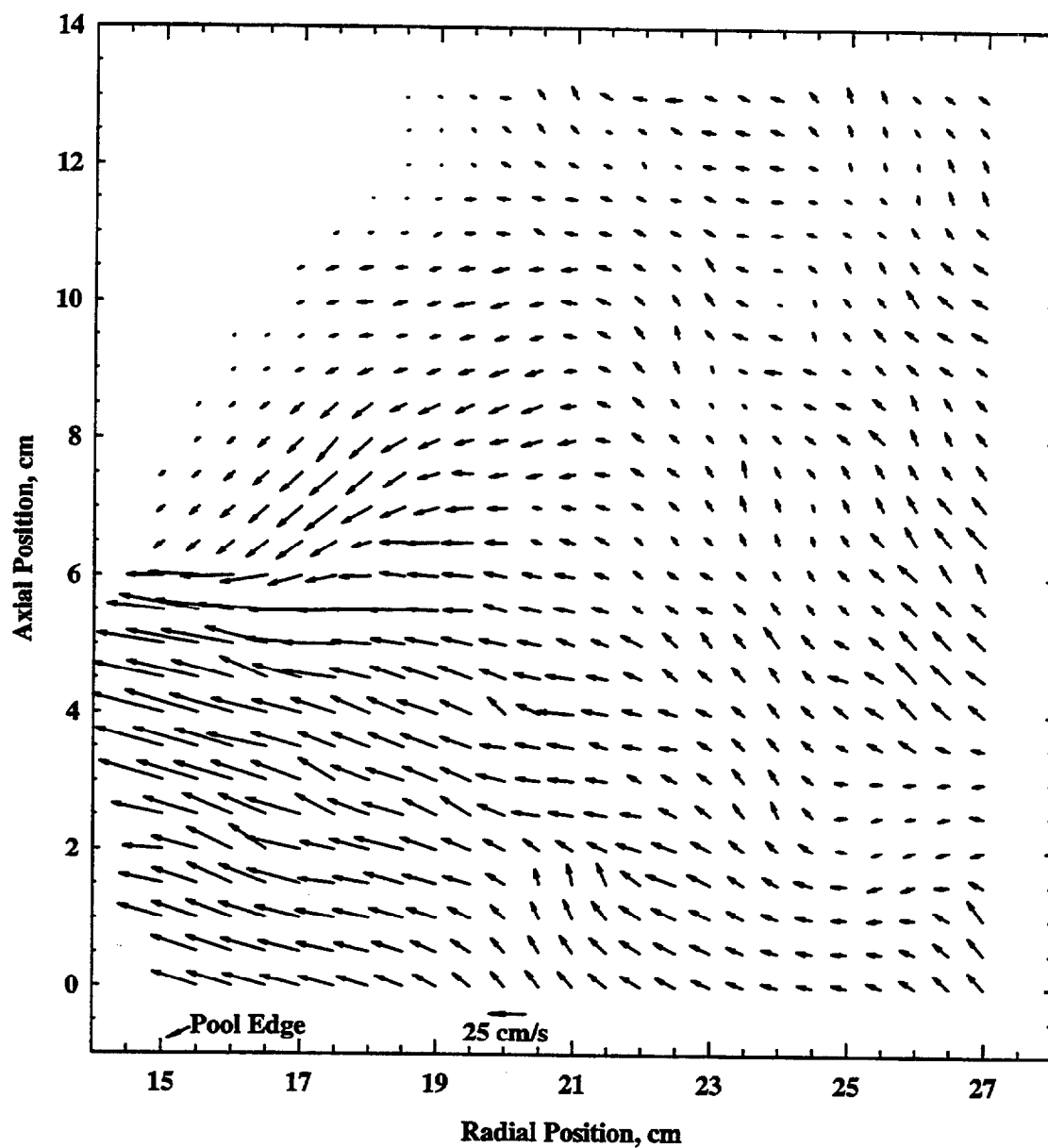


Figure 5.27 Instantaneous velocity vectors around a 30 cm toluene pool fire without a floor obtained using PIV showing the downward flow after a flame bulge.

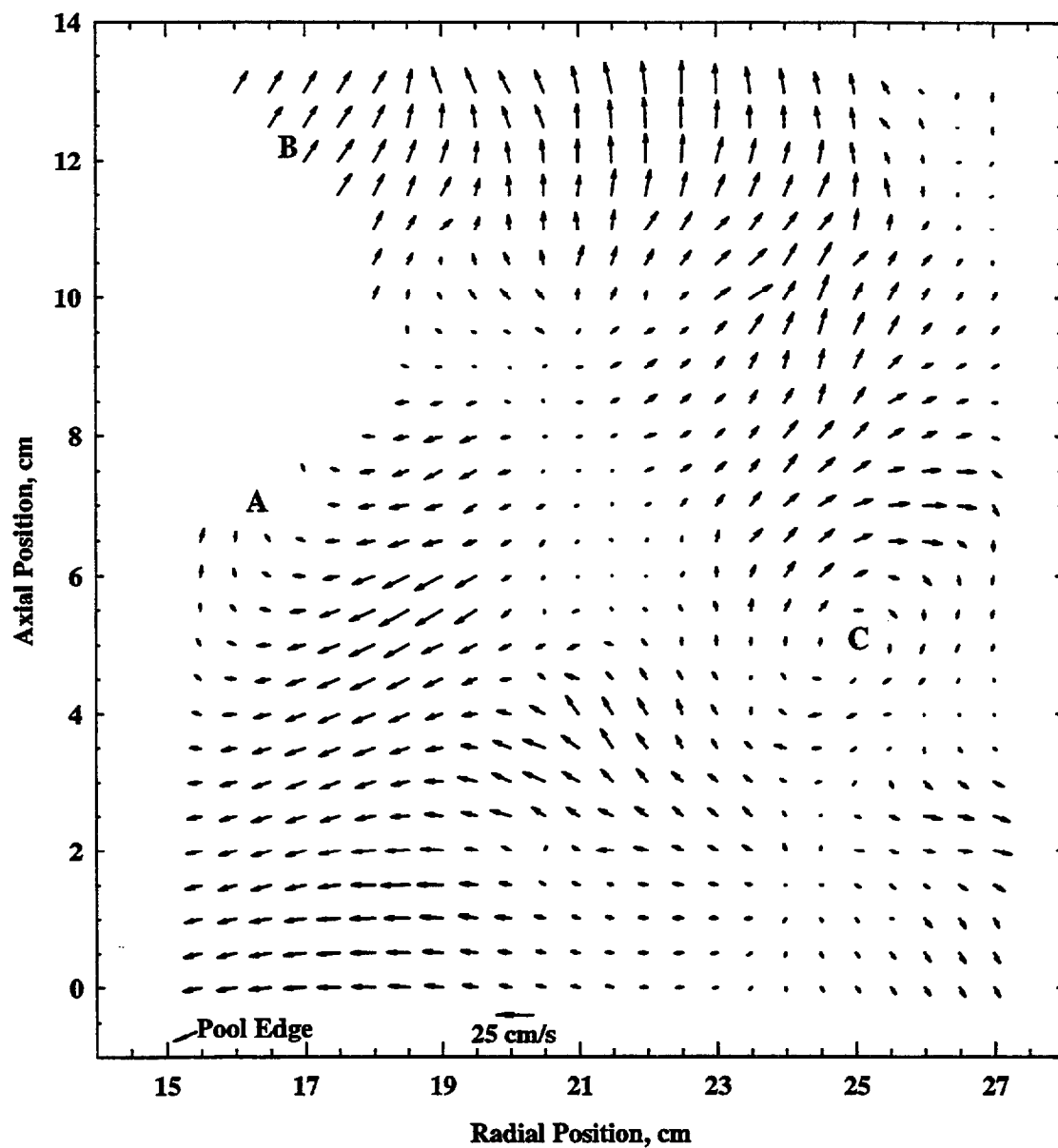


Figure 5.28 Instantaneous velocity vectors around a 30 cm toluene pool fire without a floor obtained using PIV showing the flow about a flame bulge.

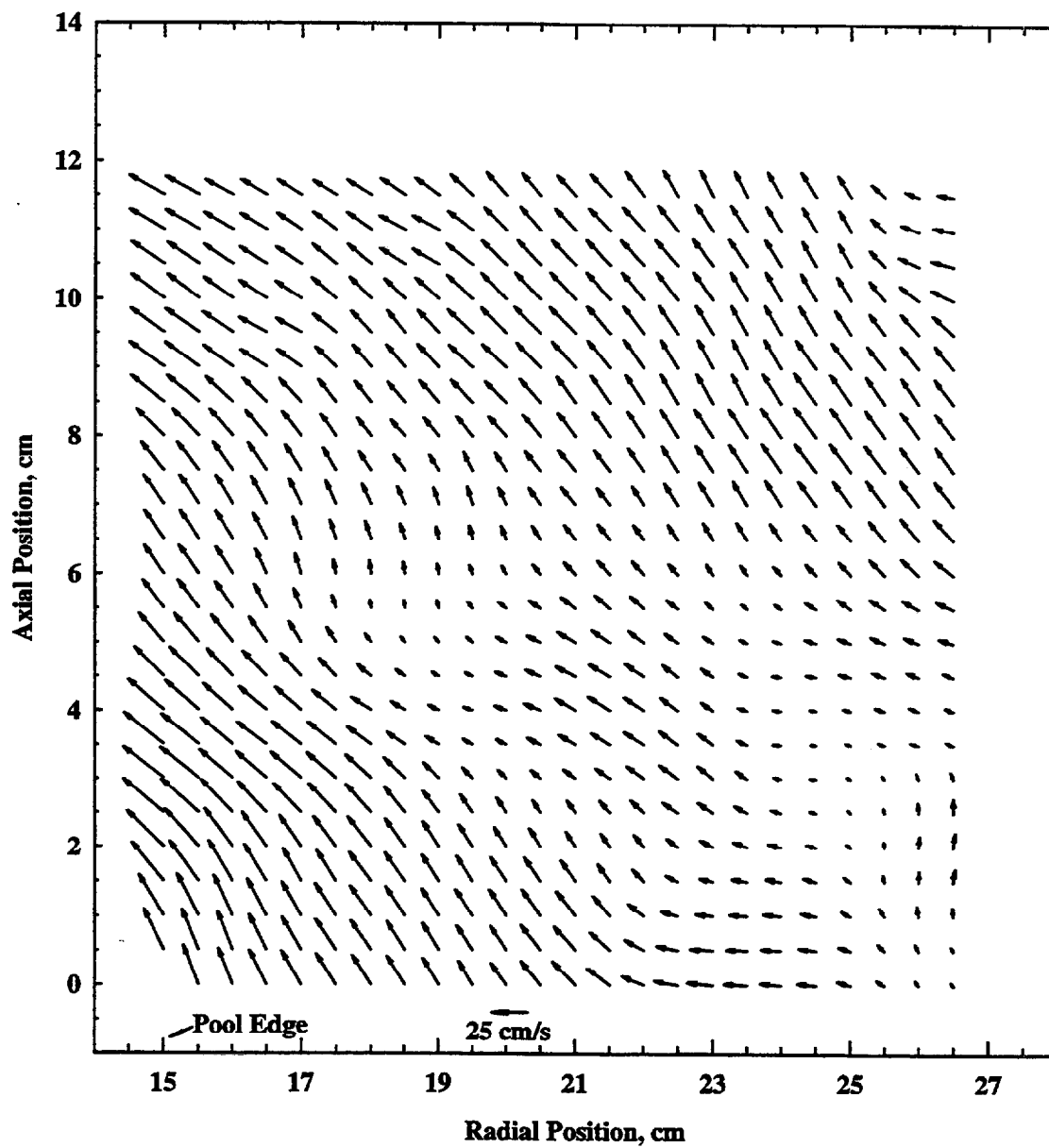


Figure 5.29 Instantaneous velocity vectors around a 30 cm heptane pool fire without a floor obtained using PIV showing the flow.

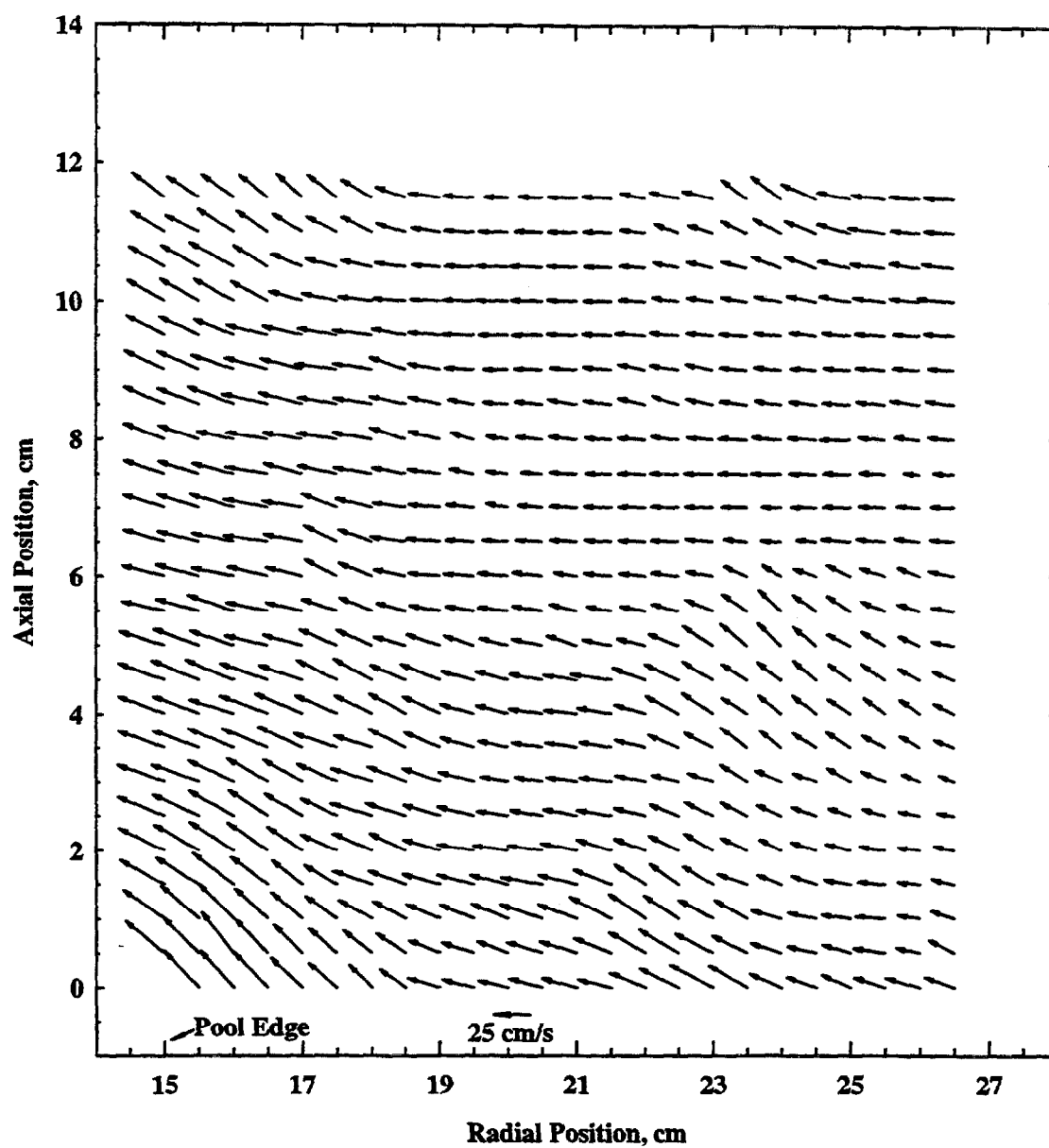


Figure 5.30 Instantaneous velocity vectors around a 30 cm heptane pool fire without a floor obtained using PIV showing the flow.

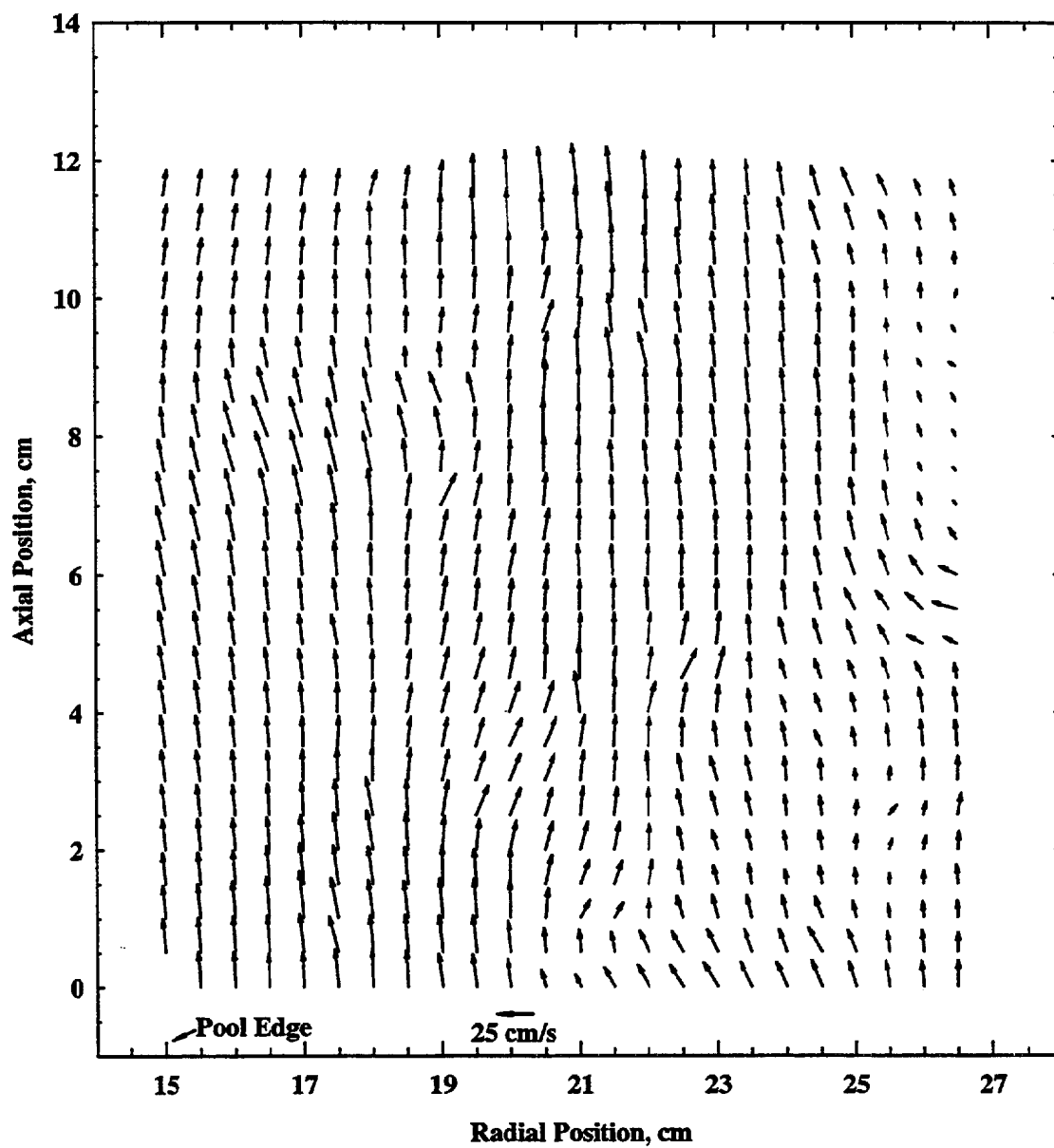


Figure 5.31 Instantaneous velocity vectors around a 30 cm heptane pool fire without a floor obtained using PIV showing the flow.

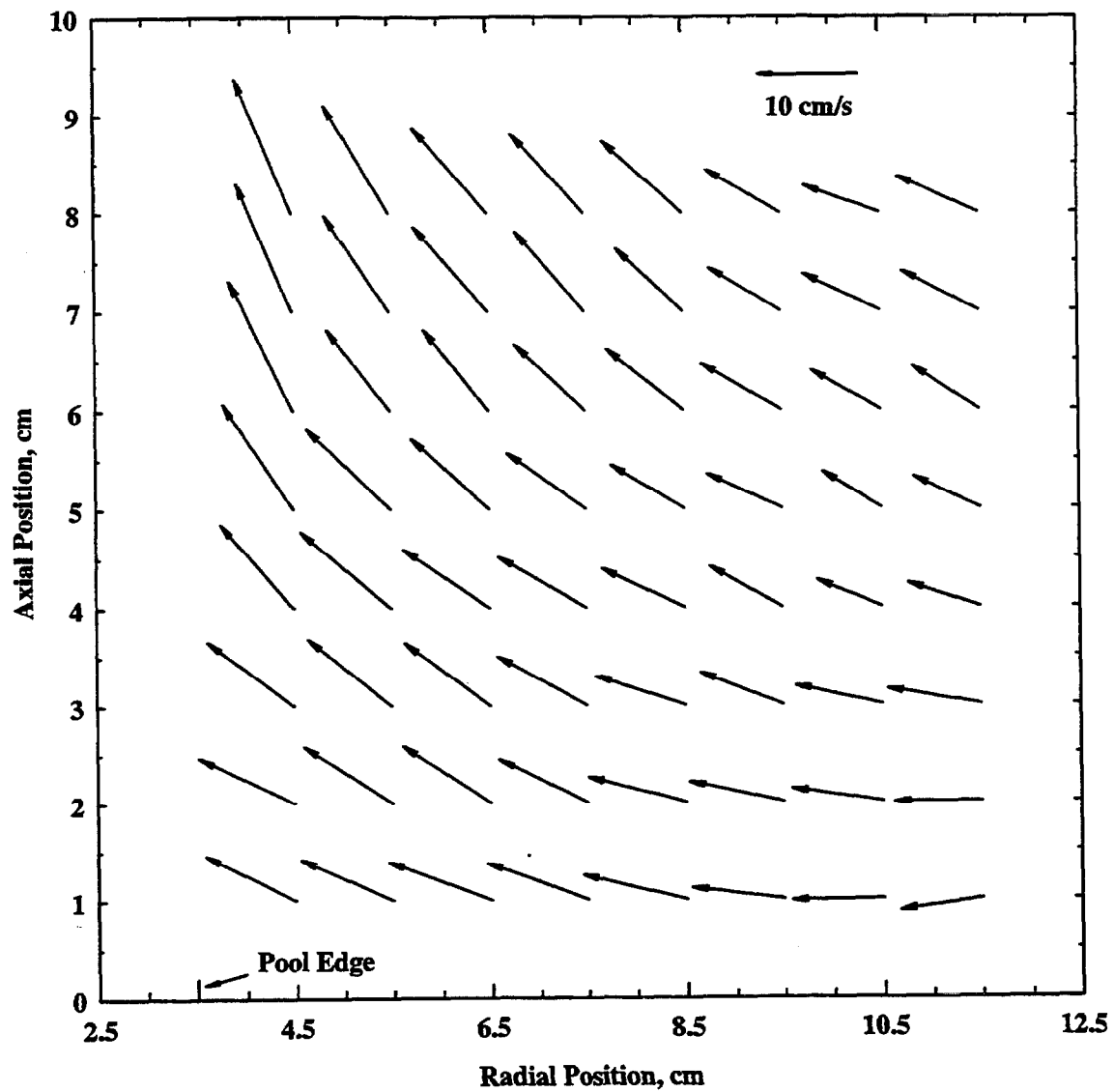


Figure 5.32 The mean entrainment flow field of a 7.1 cm toluene pool fire with a floor obtained using PIV.

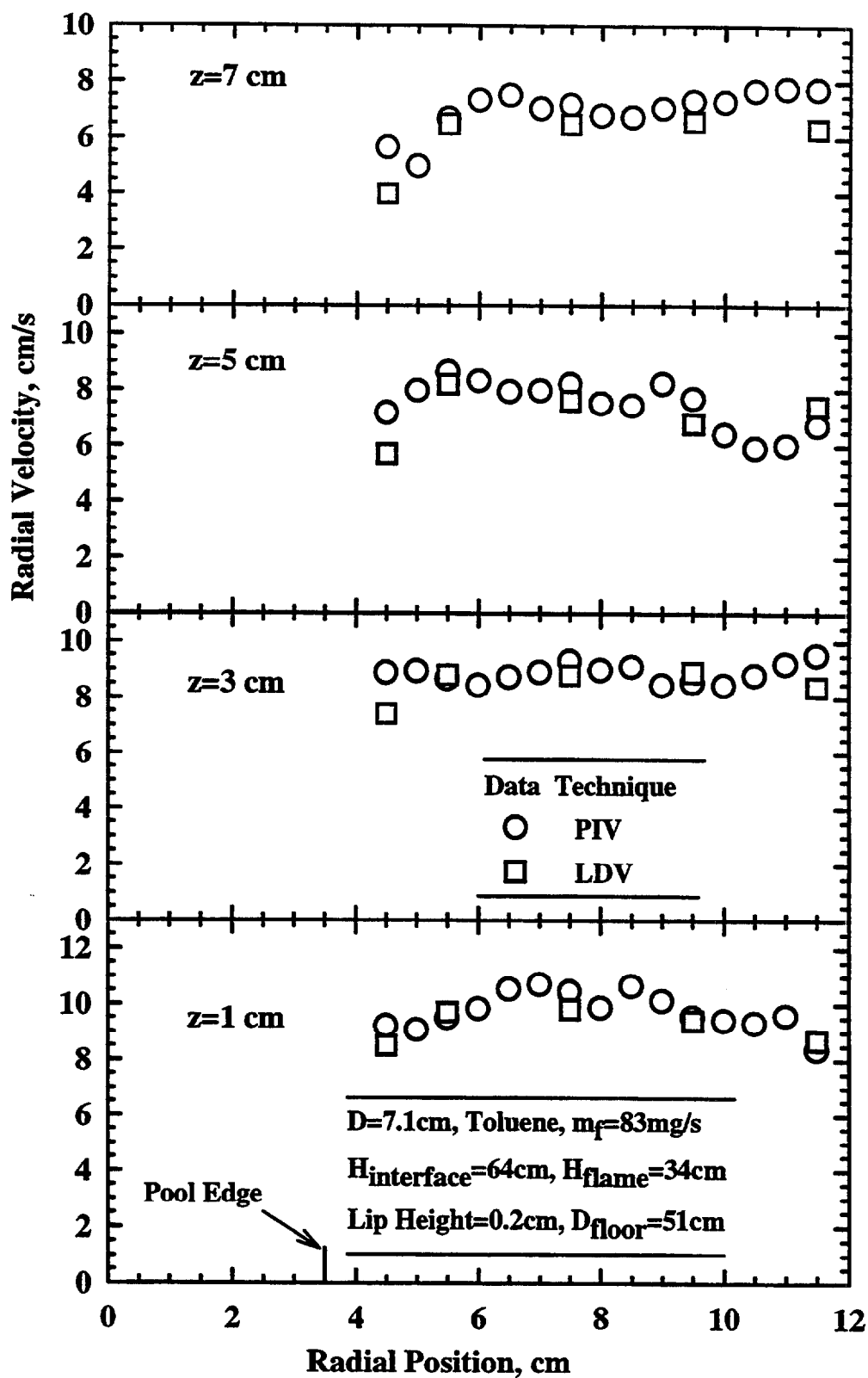


Figure 5.33 Radial velocity measurements near a 7.1 cm toluene pool fire with a floor using LDV and PIV instruments.

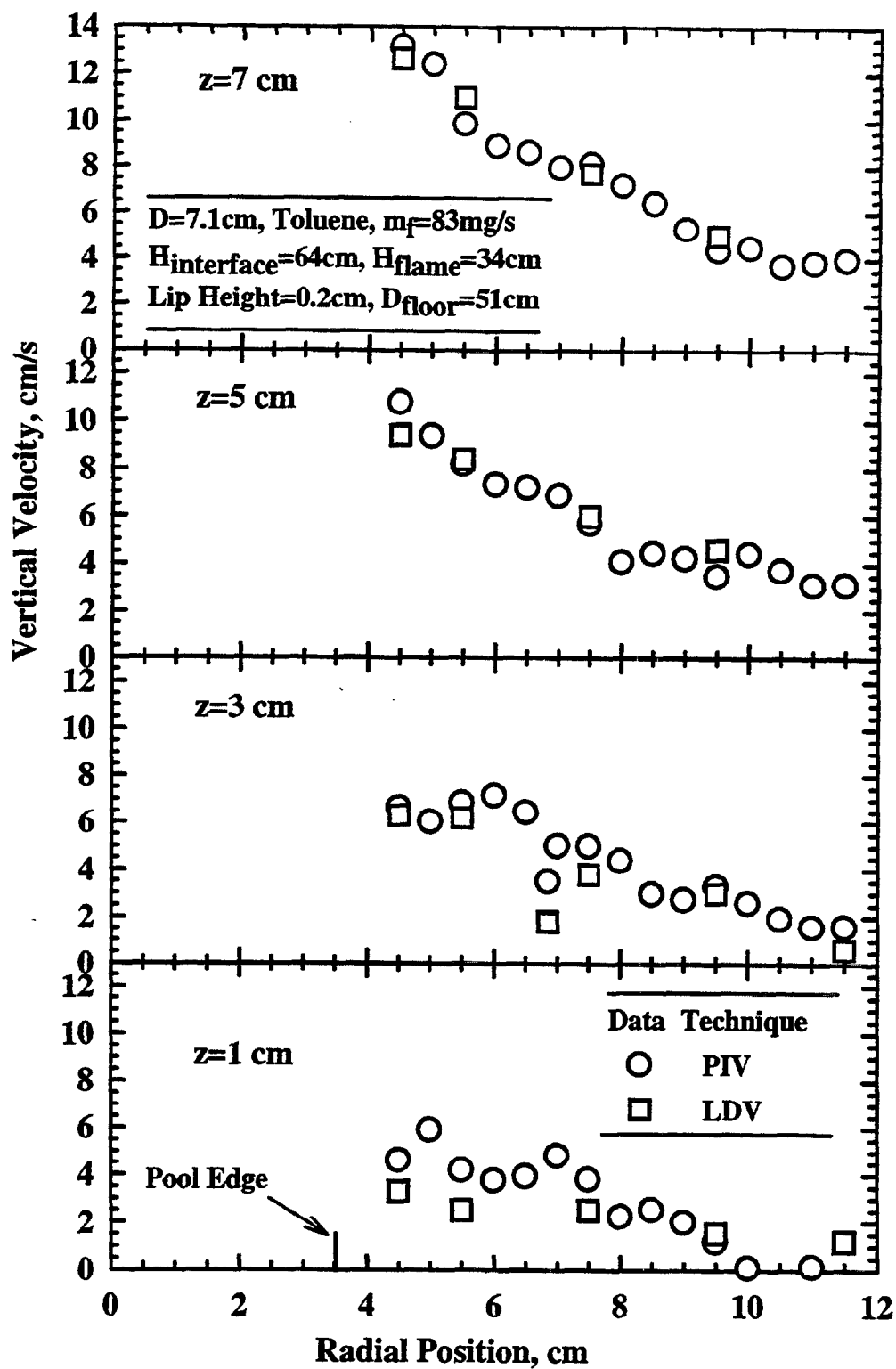


Figure 5.34 Vertical velocity measurements around a 7.1 cm toluene pool fire with a floor using LDV and PIV instruments.

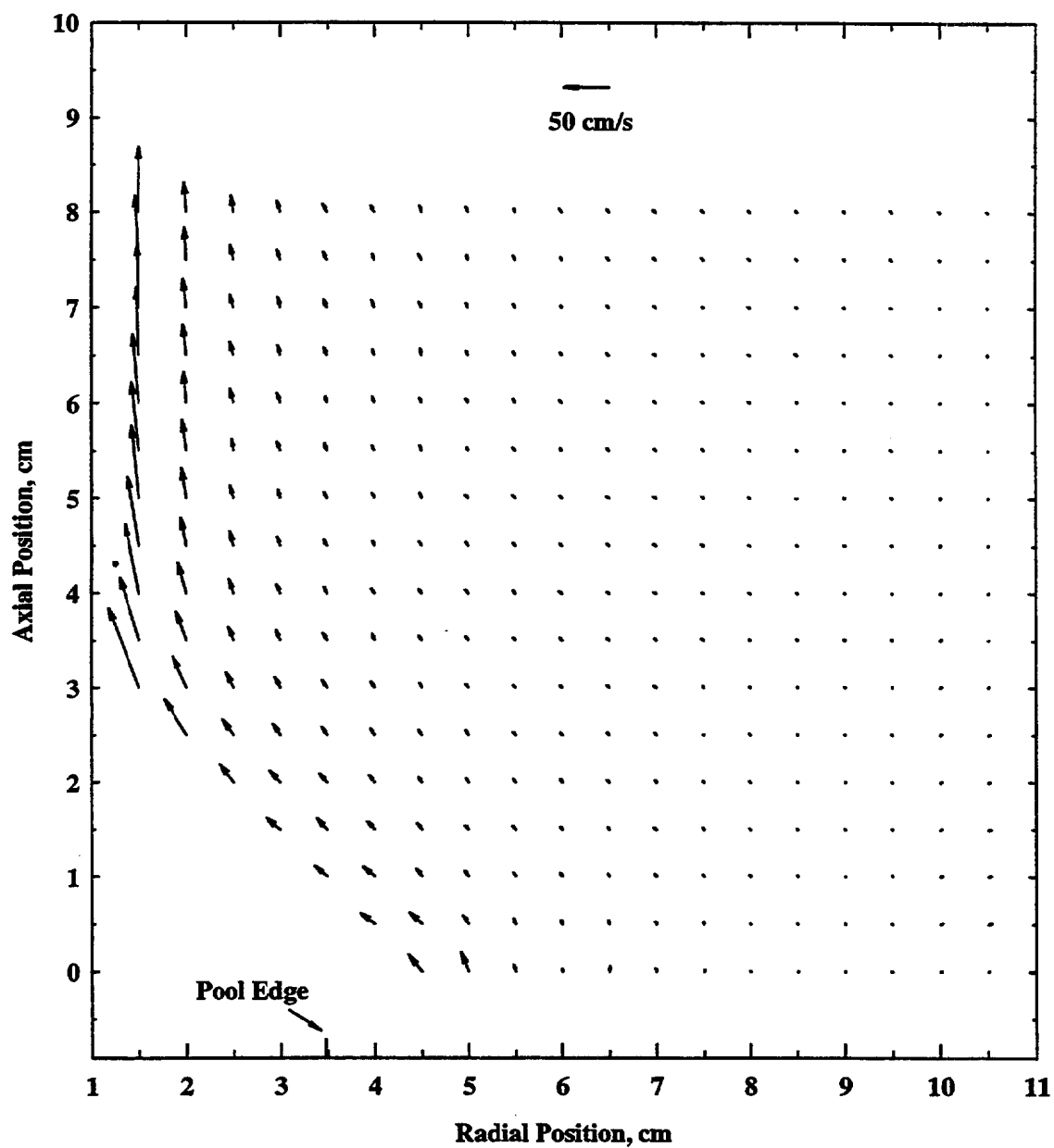


Figure 5.35 The mean velocity field around a 7.1 cm toluene pool fire without a floor obtained using PIV.

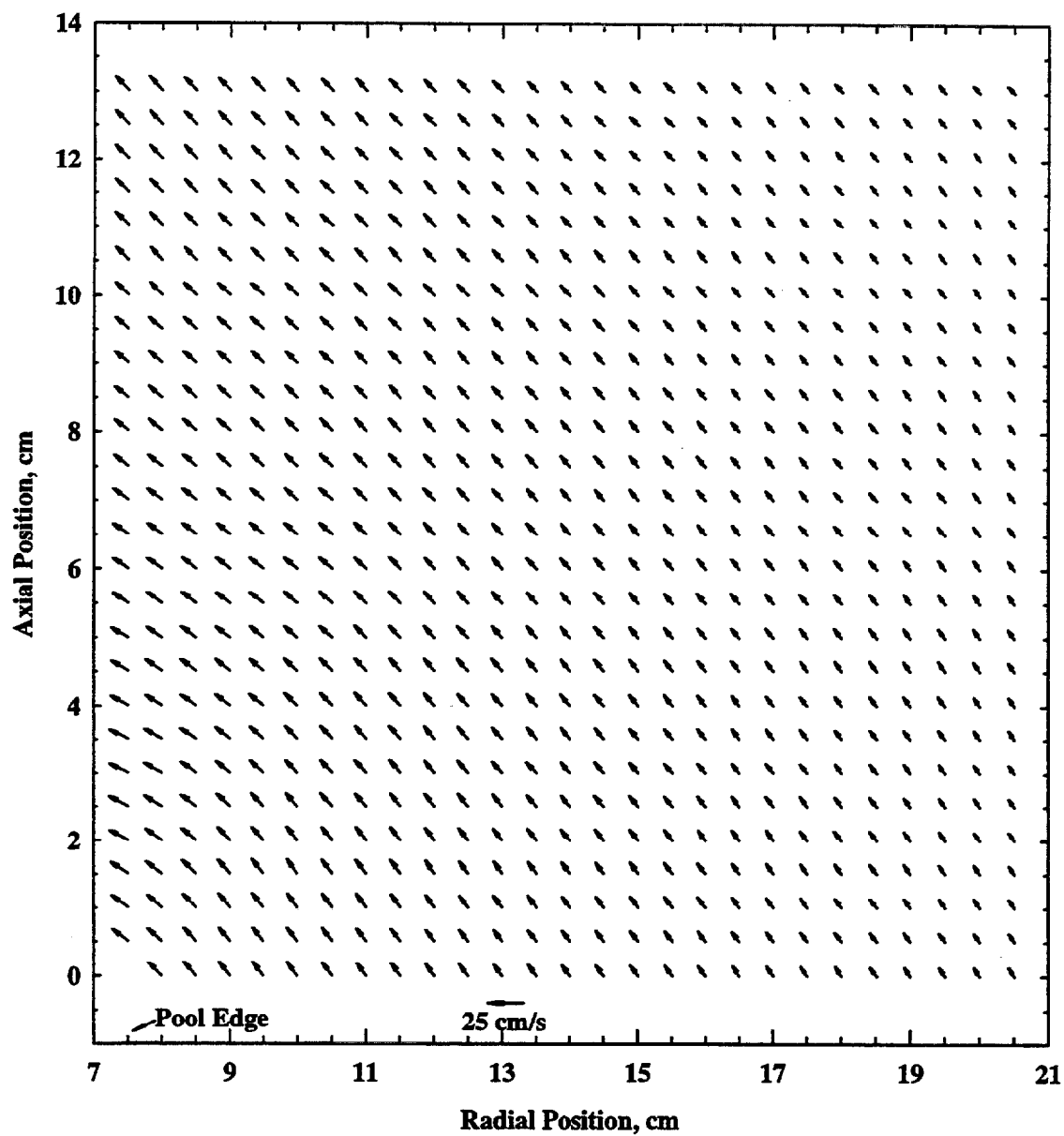


Figure 5.36 The mean velocity field around a 15 cm toluene pool fire without a floor obtained using PIV.

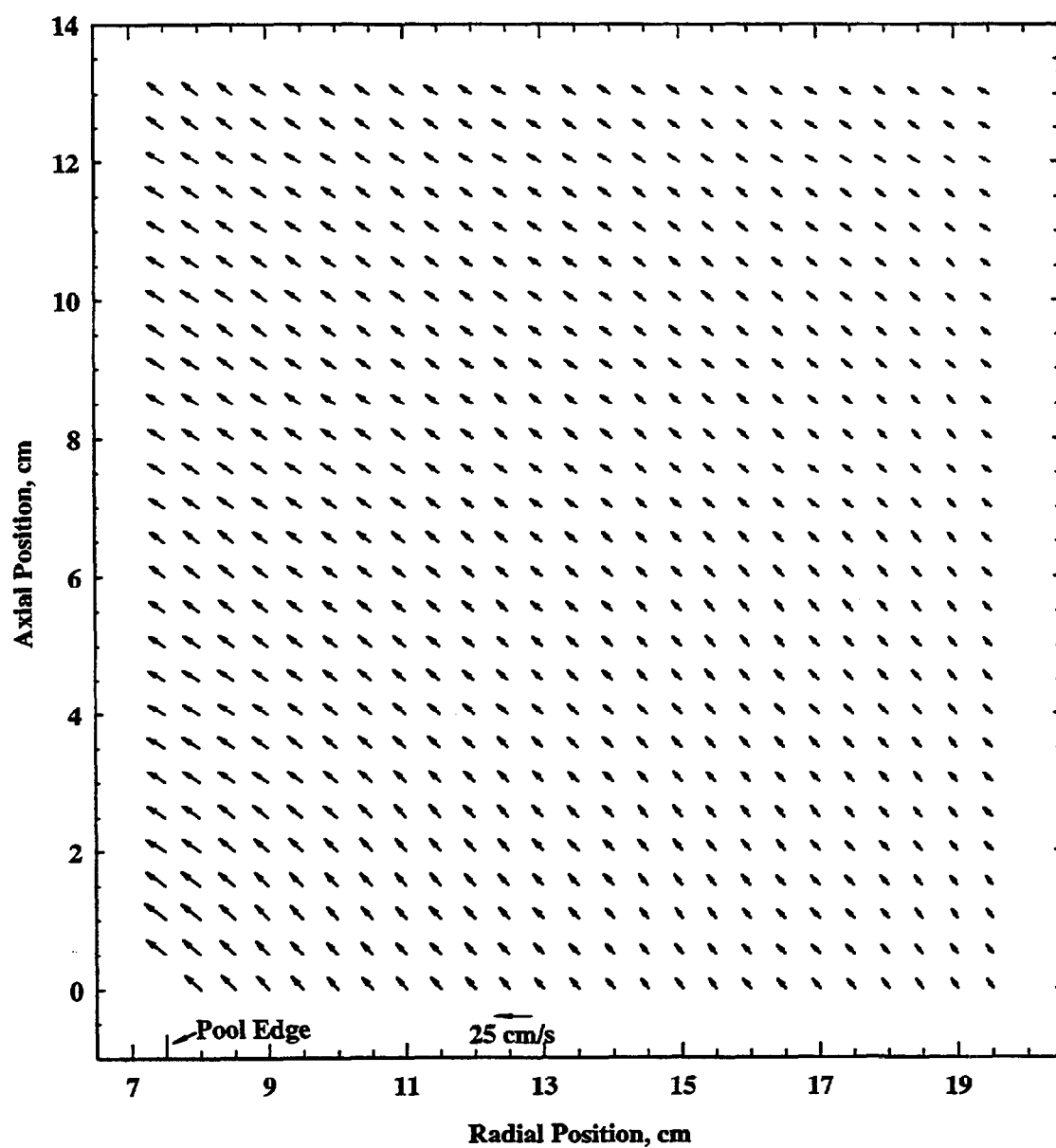


Figure 5.37 The mean velocity field around a 15 cm heptane pool fire without a floor obtained using PIV.

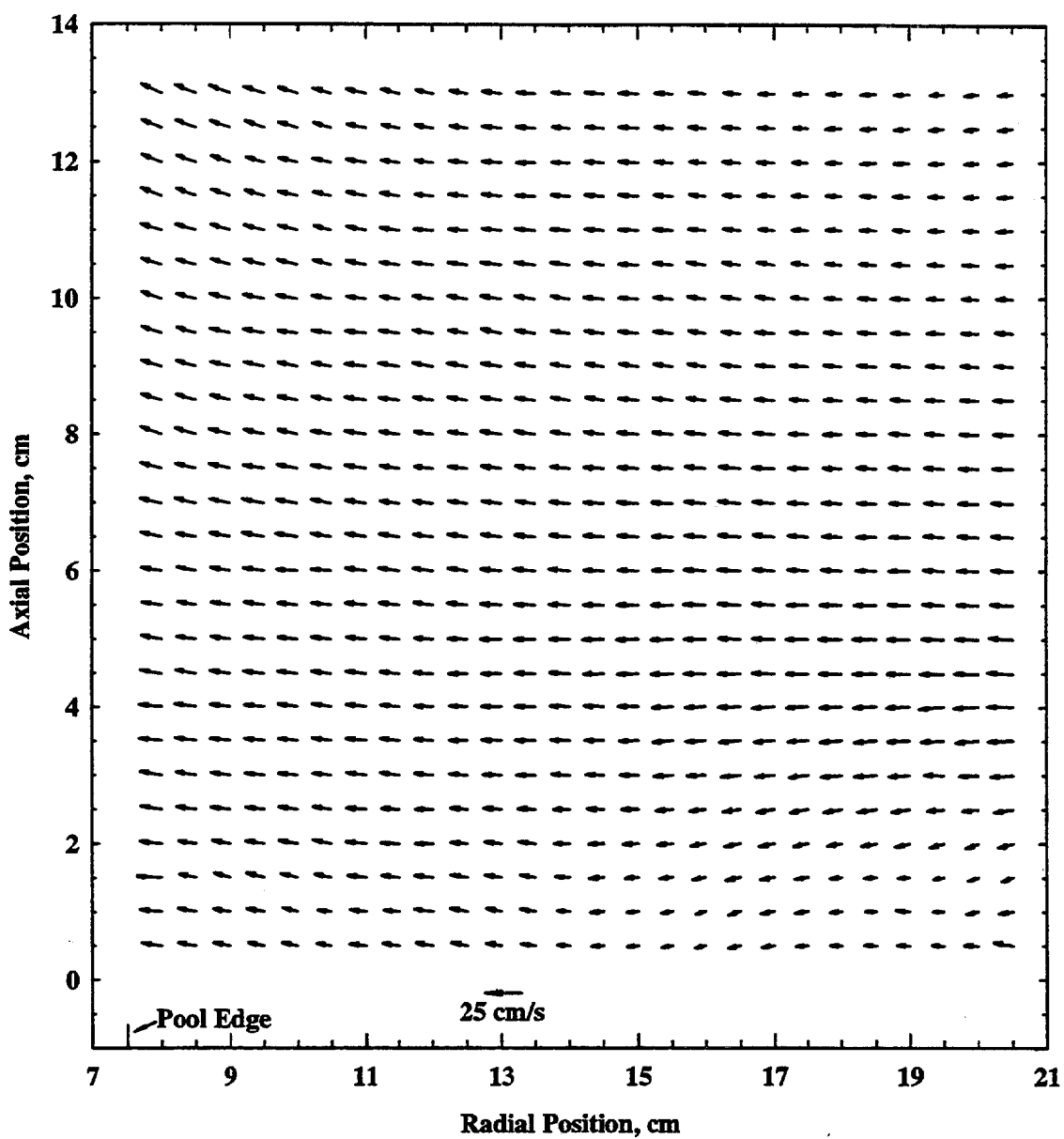


Figure 5.38 The mean velocity field around a 15 cm toluene pool fire with a floor obtained using PIV.

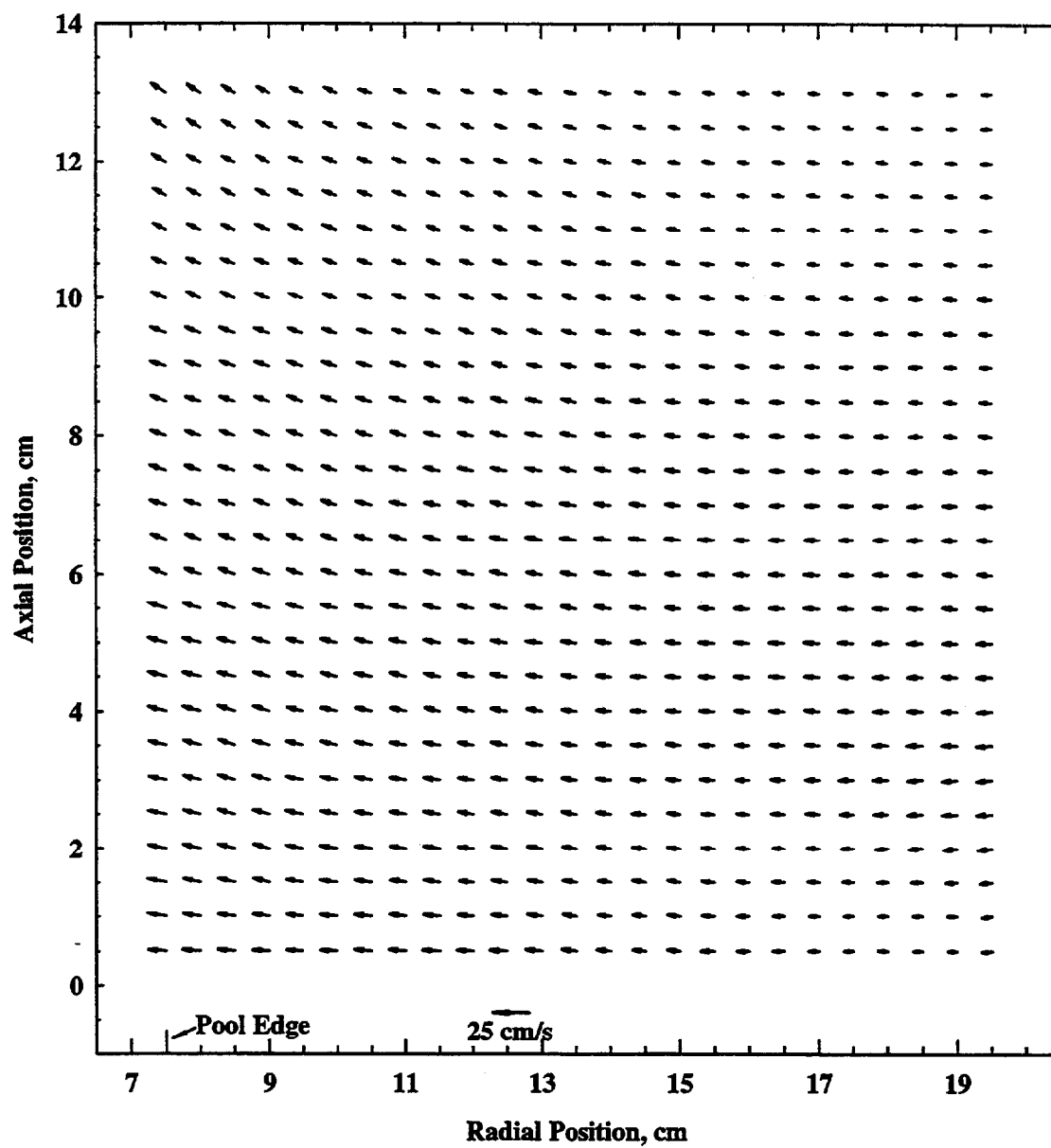


Figure 5.39 The mean velocity field around a 15 cm heptane pool fire with a floor obtained using PIV.

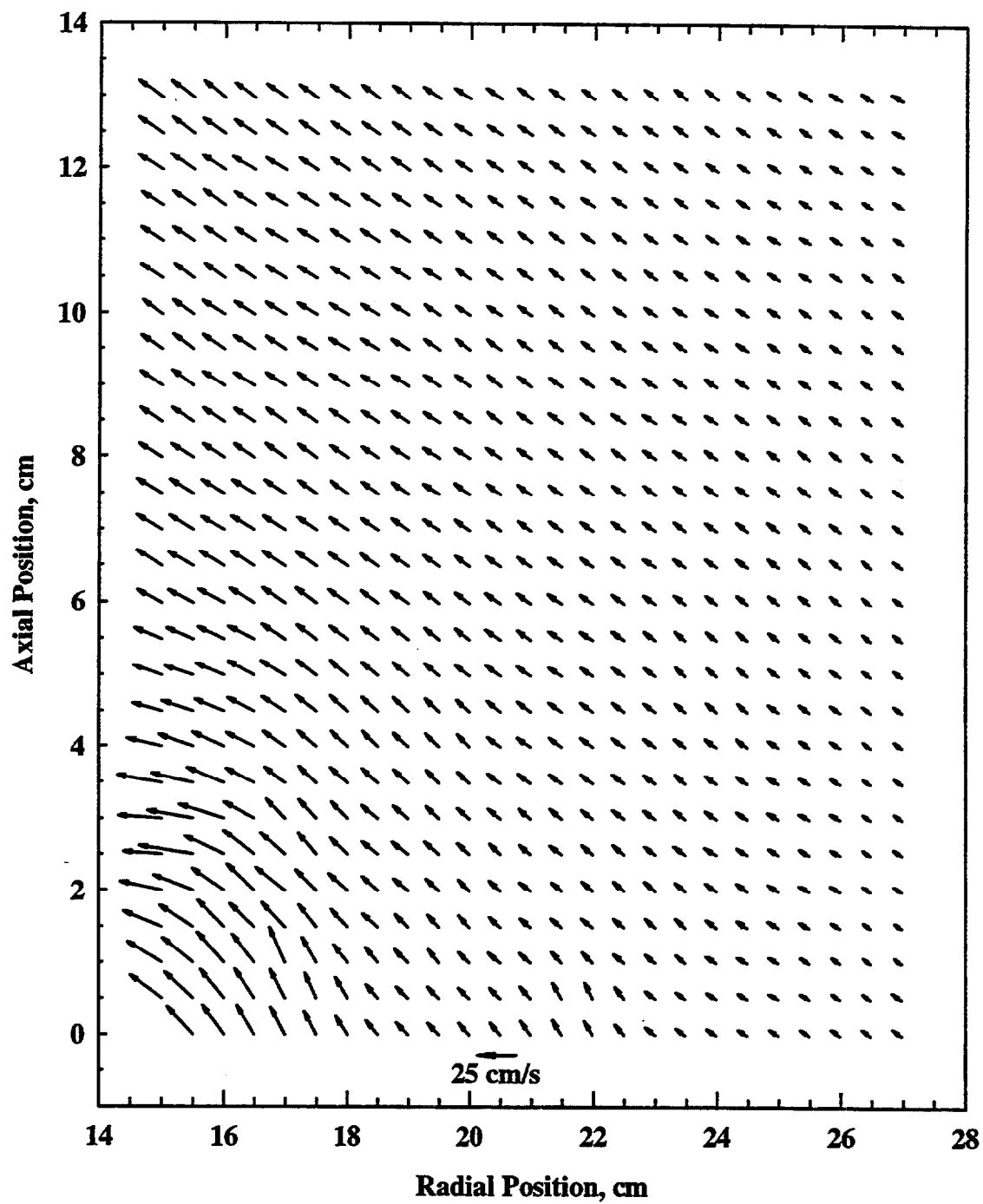


Figure 5.40 The mean entrainment flow field around a 30 cm toluene pool fire without a floor obtained using PIV.

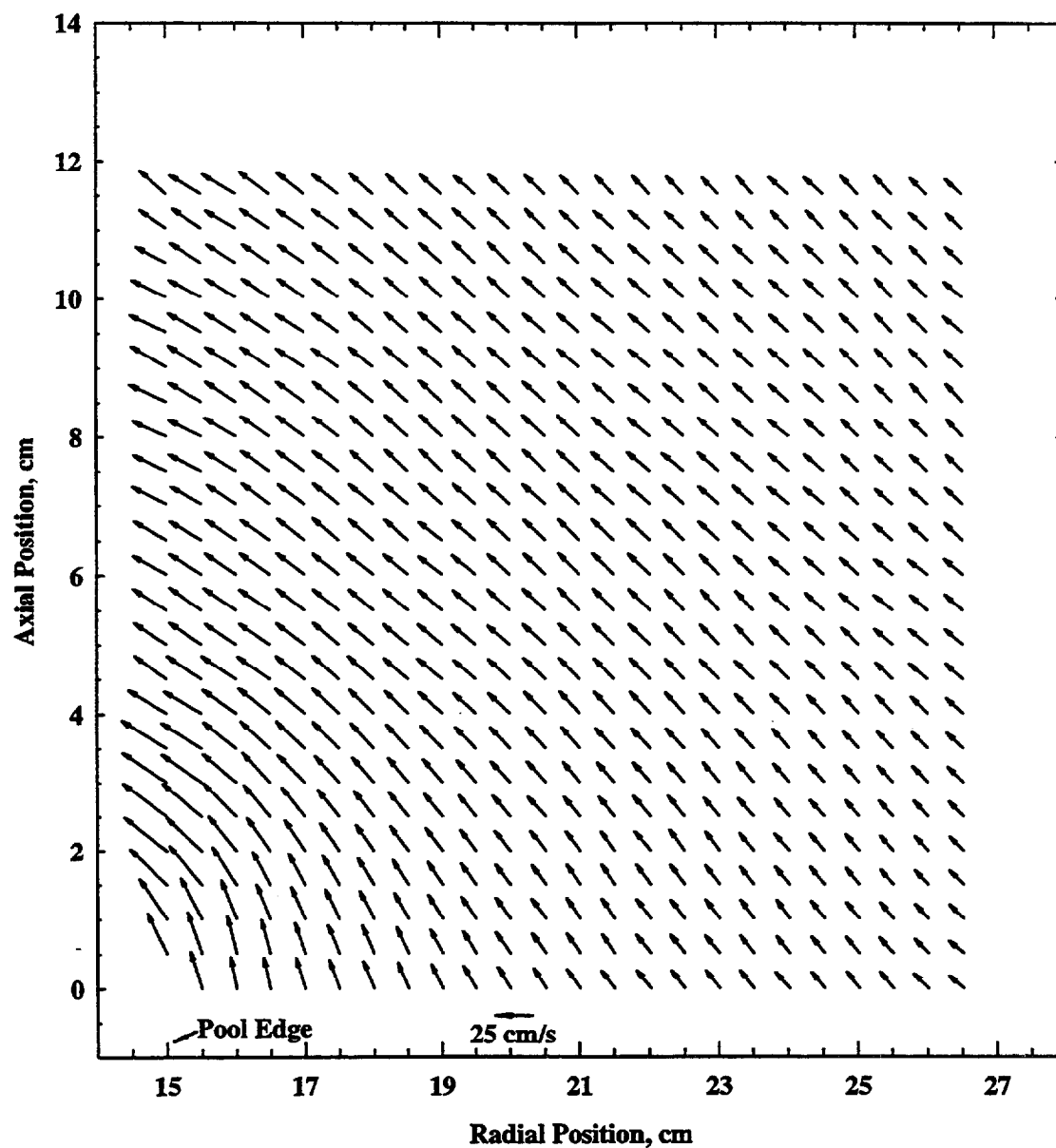


Figure 5.41 The mean entrainment flow field around a 30 cm heptane pool fire without a floor obtained using PIV.

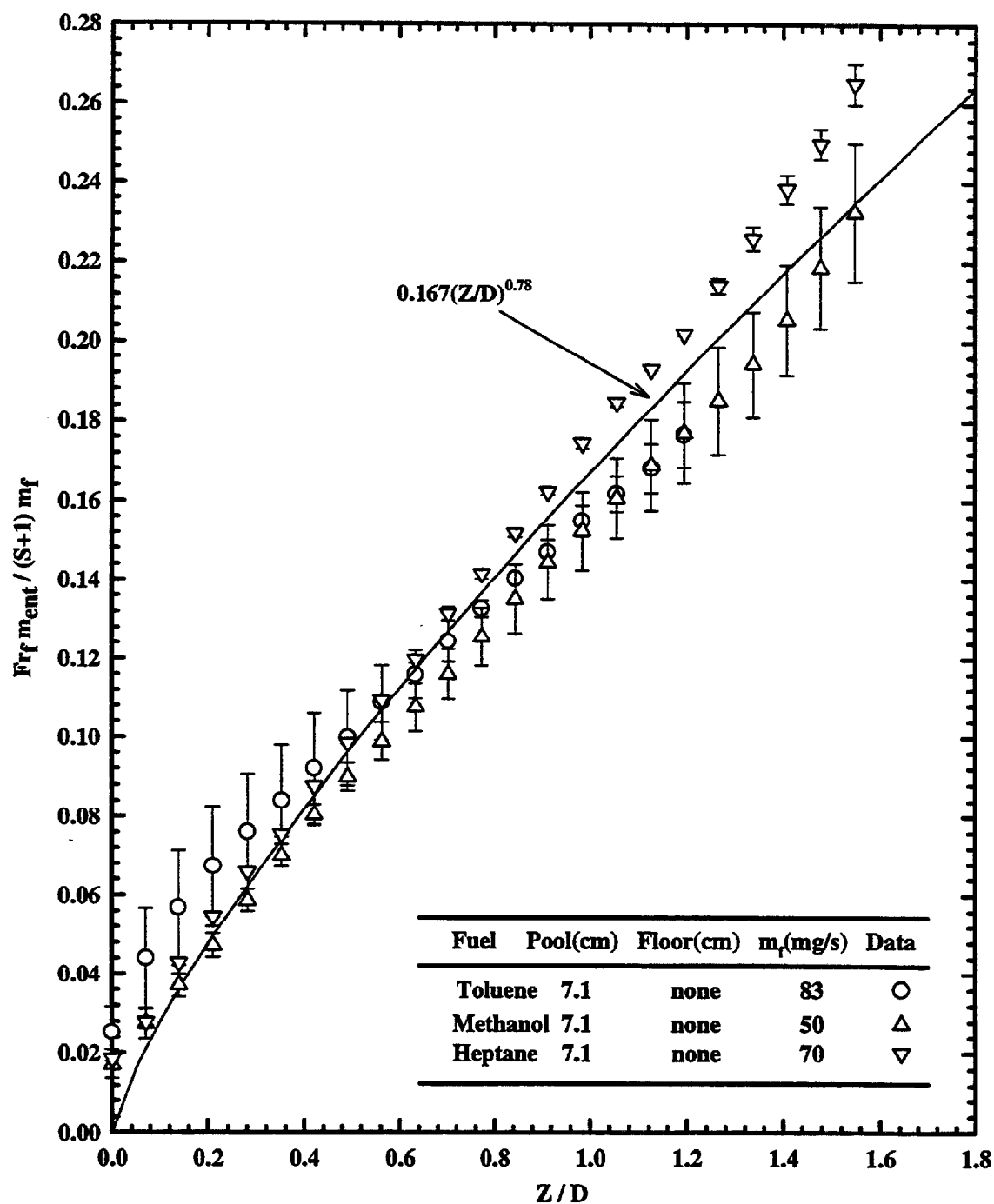


Figure 5.42 Normalized air entrainment rate for three 7.1 cm pool fires without a floor as a function of normalized distance above the fuel surface.

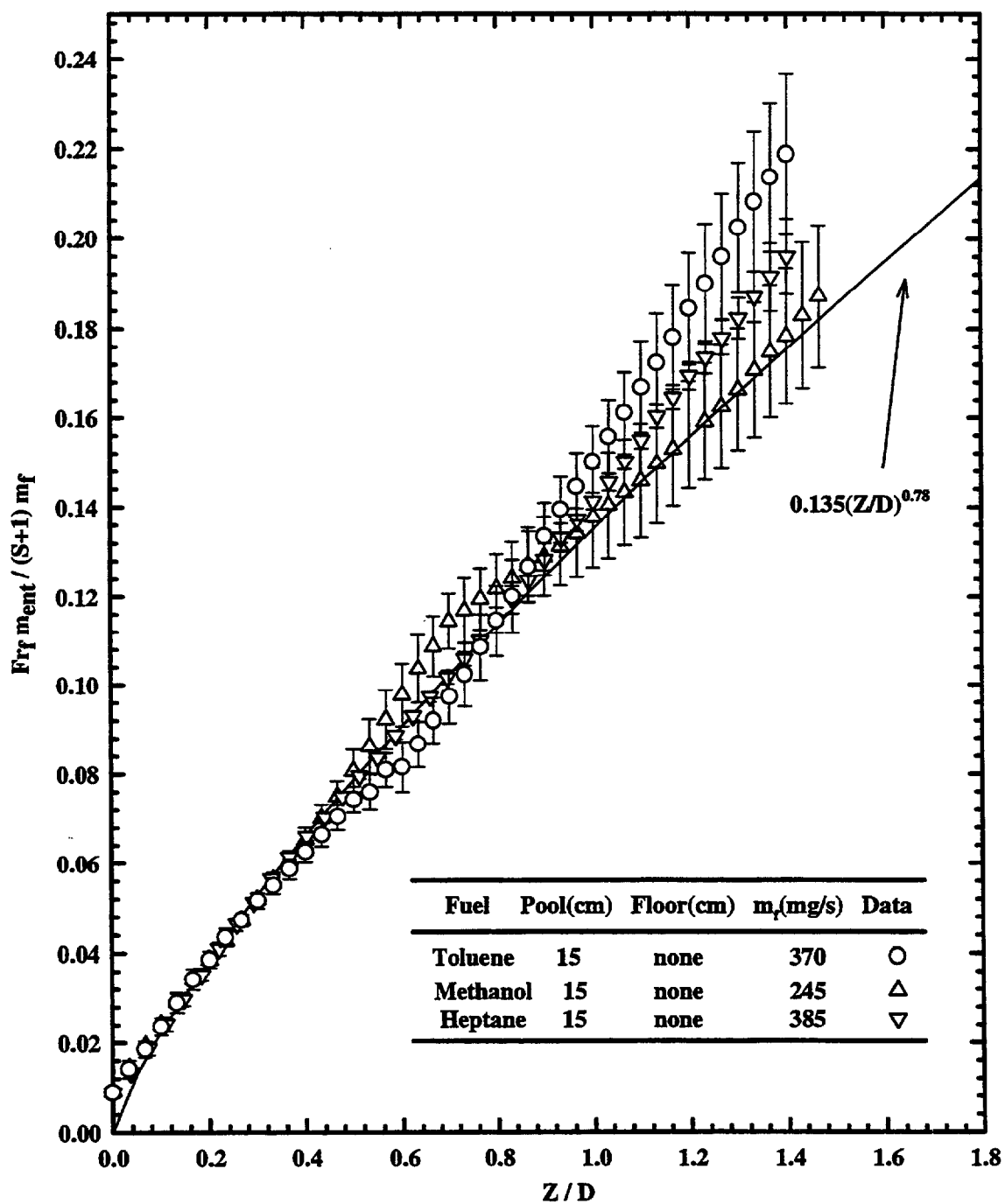


Figure 5.43 Normalized air entrainment rate for three 15 cm pool fires without a floor as a function of normalized distance above the fuel surface. Δ

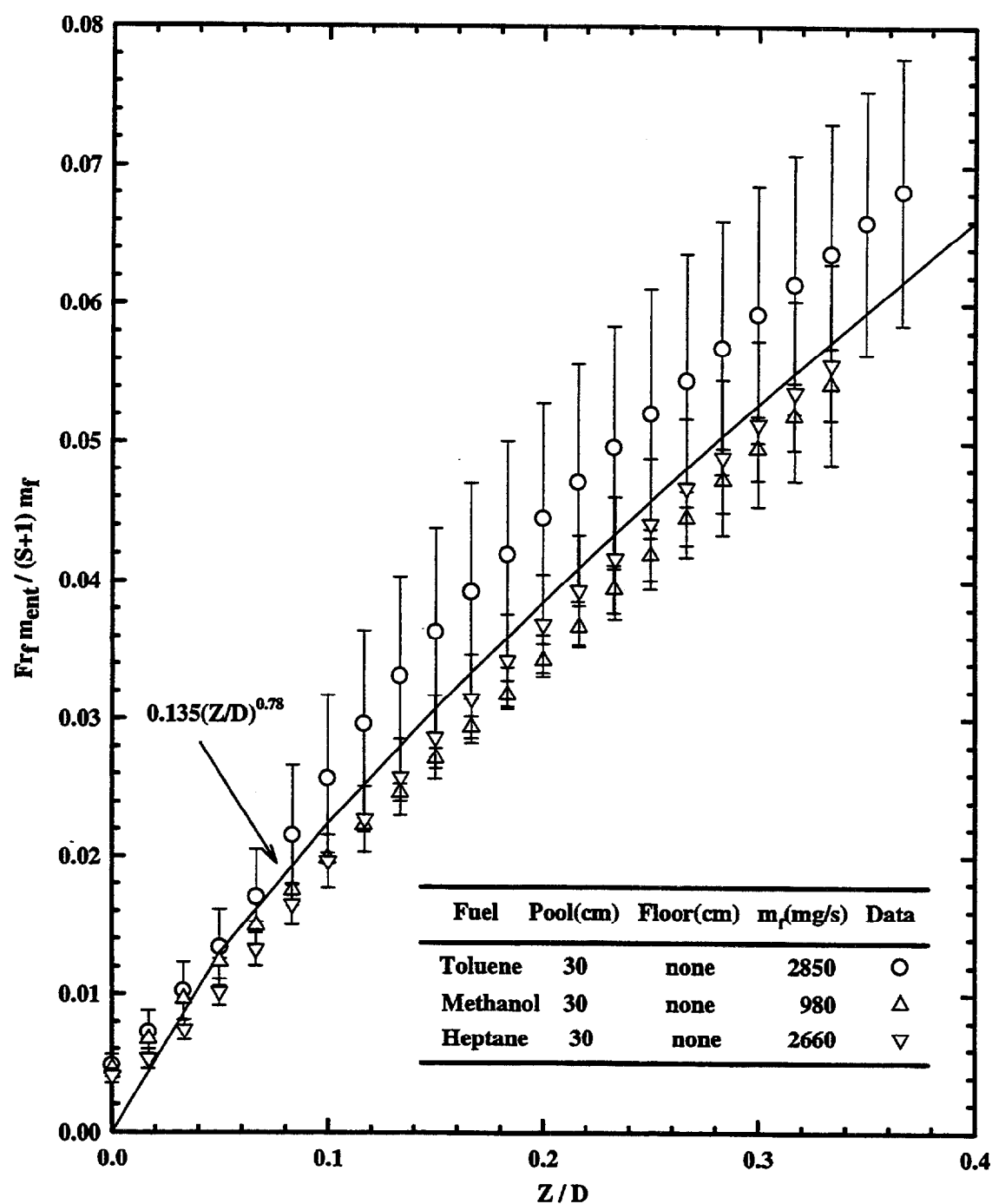


Figure 5.44 Normalized air entrainment rate for three 30 cm pool fires without a floor as a function of normalized distance above the fuel surface.

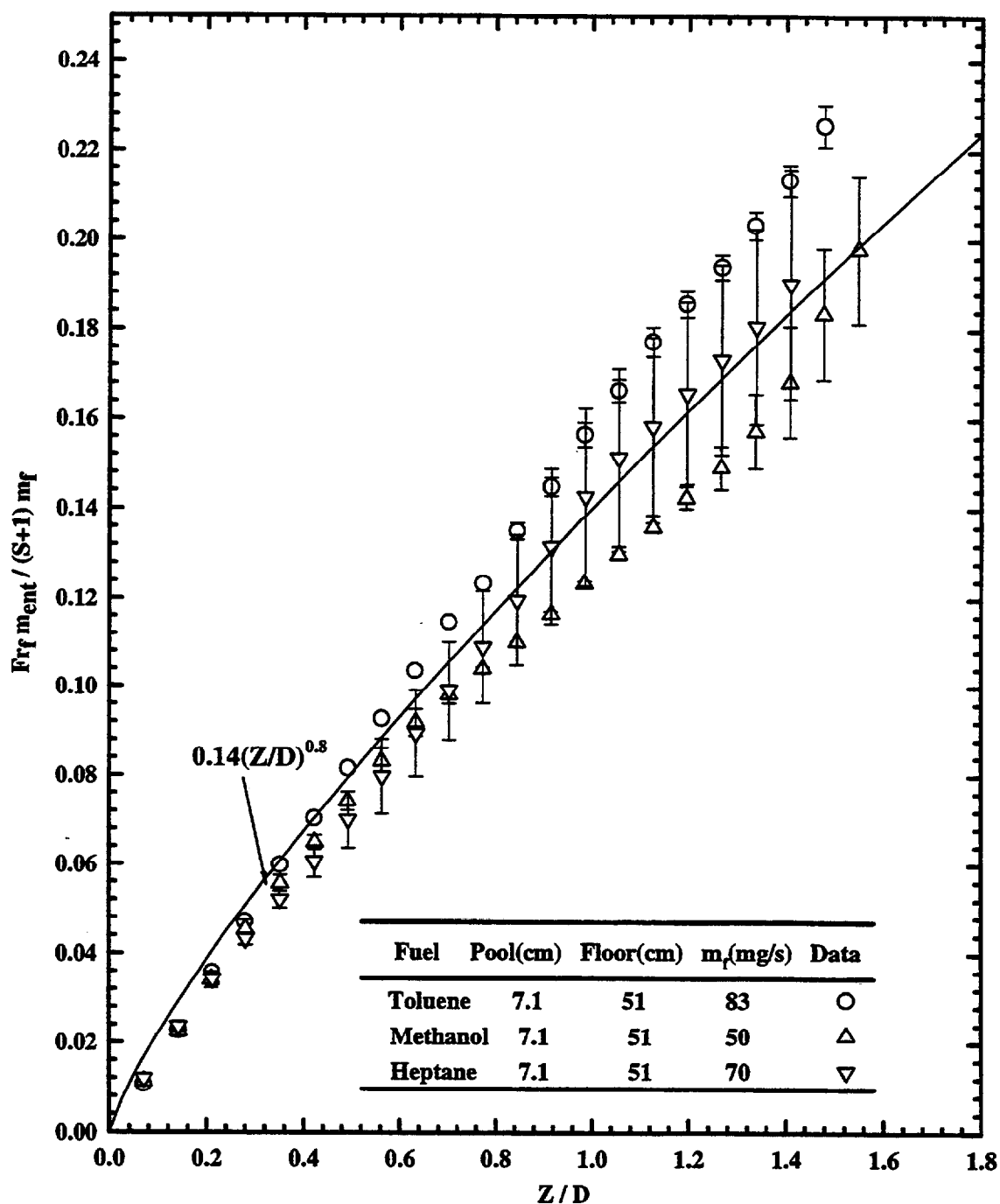


Figure 5.45 Normalized air entrainment rate for three 7.1 cm pool fires with a floor as a function of normalized distance above the fuel surface.

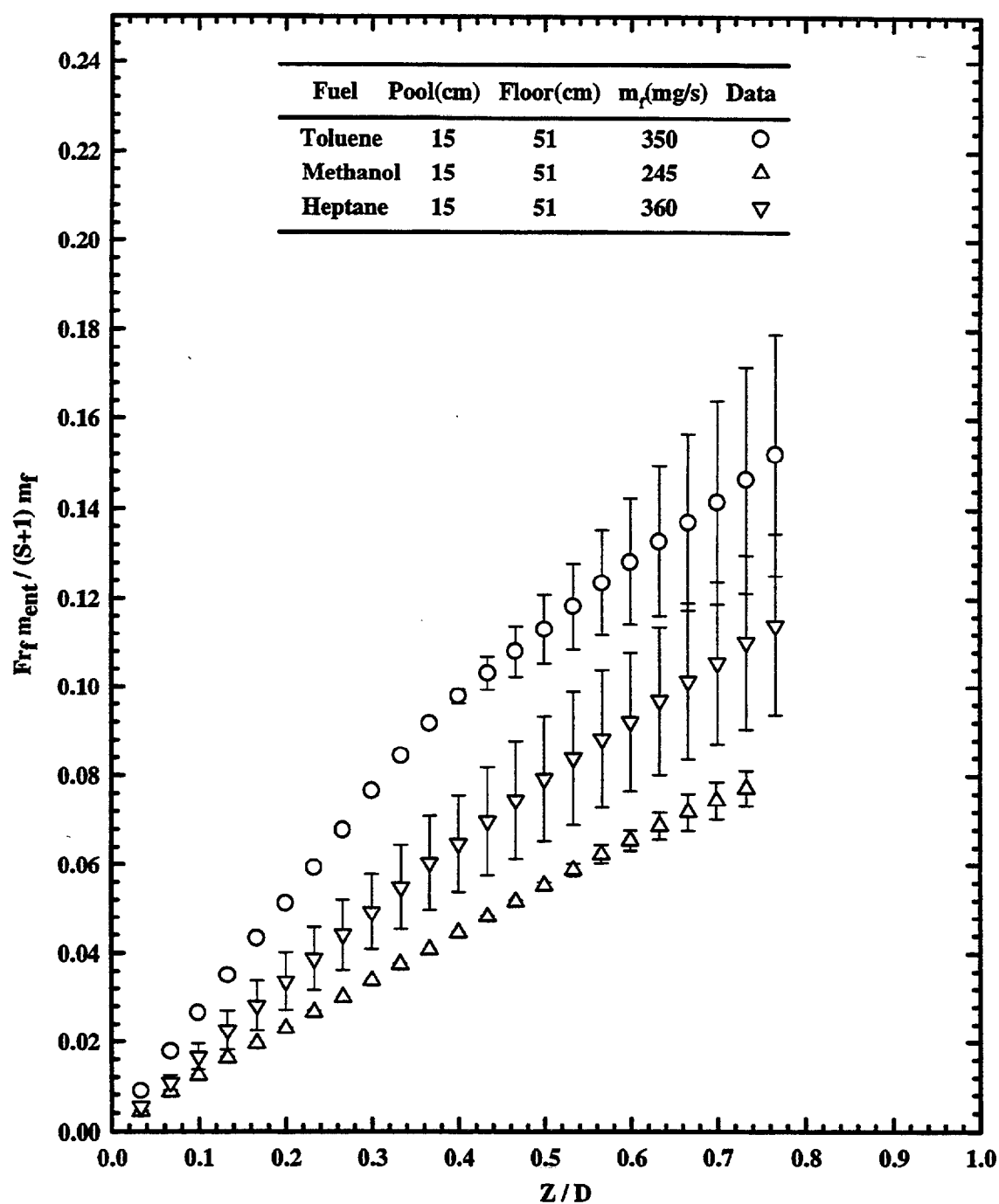


Figure 5.46 Normalized air entrainment rate for three 15 cm pool fires with a floor as a function of normalized distance above the fuel surface.

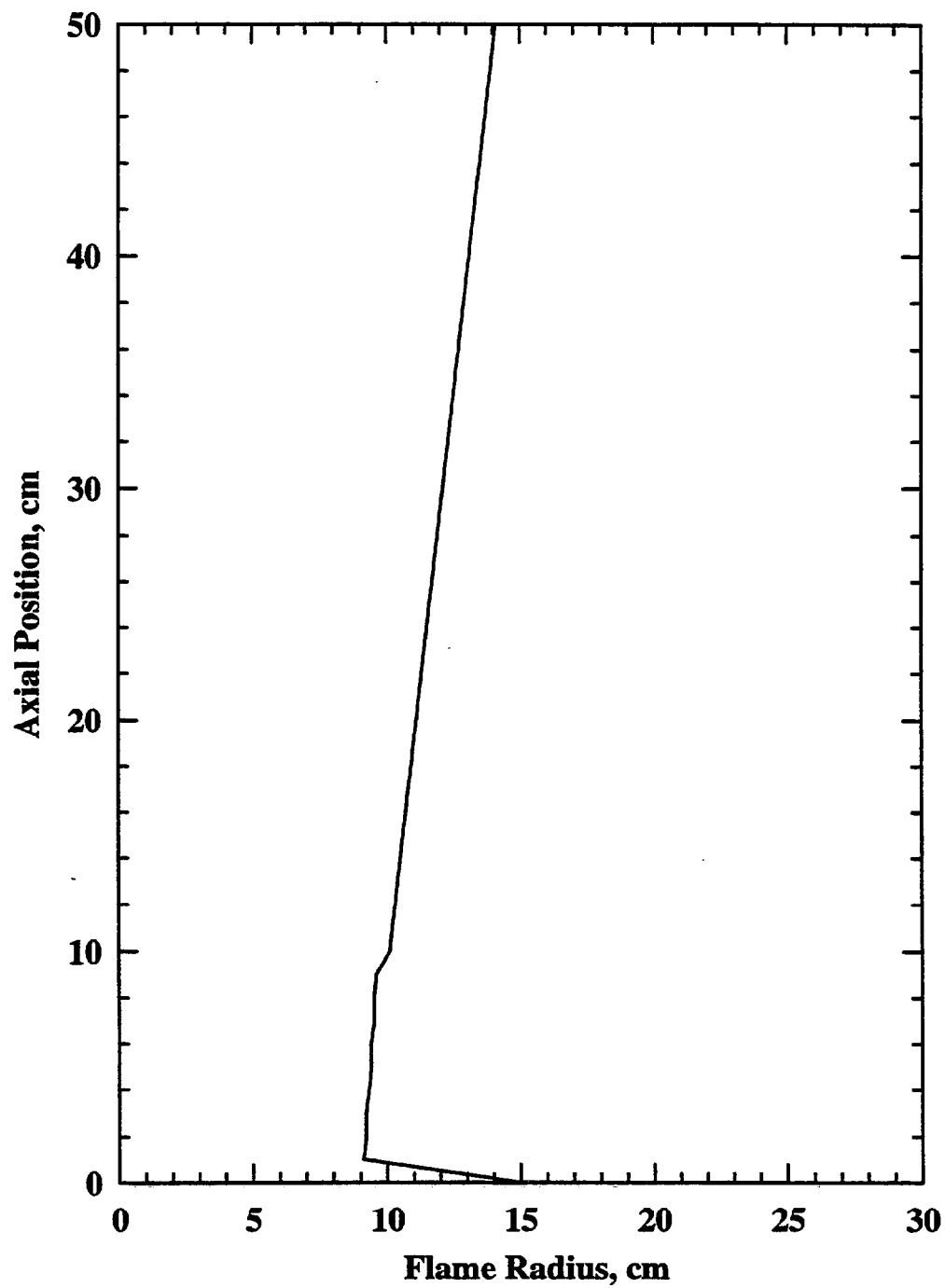


Figure 5.47 Flame radius profile used in predicting the entrainment flow field of a 30 cm toluene pool fire without a floor.

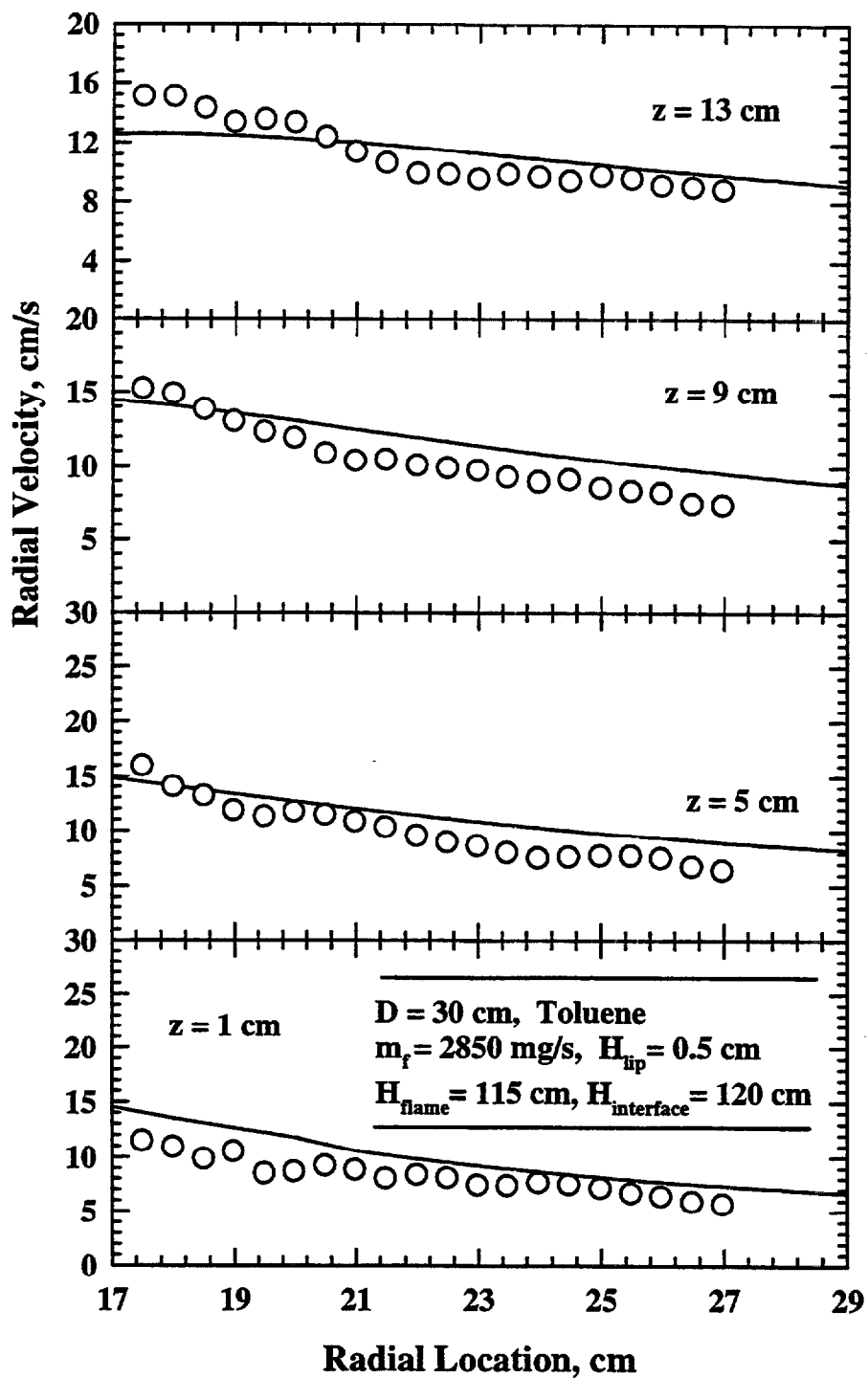


Figure 5.48 Measurements and prediction of radial velocity around a 30 cm toluene pool fire with adjusted flame radius profile in predictions.

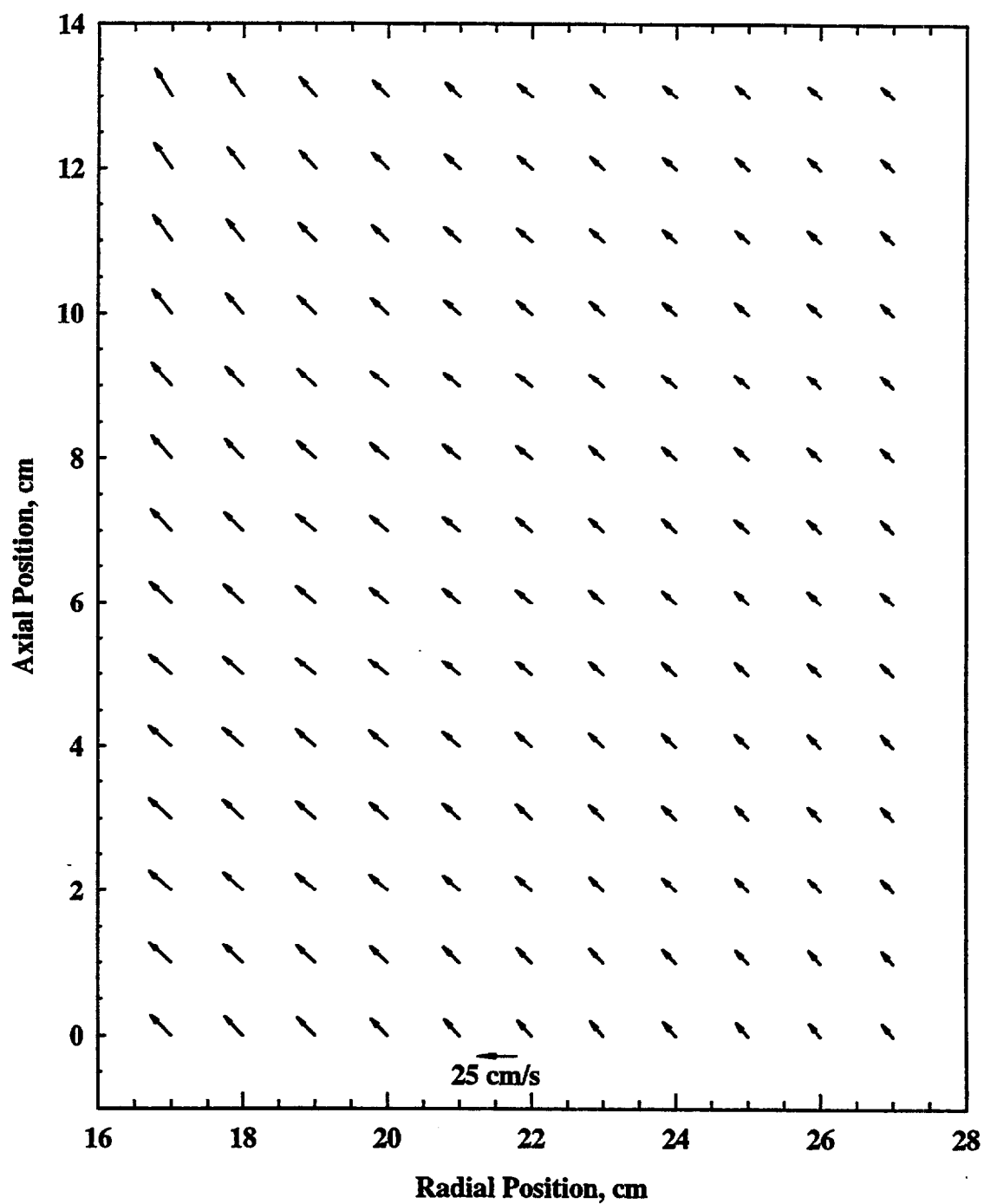


Figure 5.49 Predictions of velocity vectors around a 30 cm toluene pool fire with adjusted flame radius.

CHAPTER 6 SUMMARY, CONCLUSIONS AND RECOMMENDATIONS

6.1 Conclusions

An experimental and a numerical study were carried out of the flow fields induced by pool fires. Pool burner of three diameters, namely 7.1 cm, 15 cm and 30 cm, are used. For the two smaller pool burners, the effect of putting a 51 cm sheet metal floor around the pool fire is also studied. Three kinds of fuels, methanol, toluene and heptane, are burned. The velocity field of the flow induced by a 7.1 cm toluene pool fire with the metal floor is mapped with a Laser Doppler Velocimetry (LDV) system. The transient characteristics of the velocities are studied by analyzing their discrete Probability Density Functions (PDFs) and Power Spectral Densities (PSDs). Although air is always entrained into the flame on an average, instantaneous radially outward velocities were observed with a large probability, showing that air is sometimes pushed away from the flame. PDFs of the vertical velocities show that the vertical velocity of the ambient air is rarely over 50 cm/s, but the vertical velocity of the flame gas can be much higher. The PSDs of the velocities show that the entrainment flow field is not coherent with the periodic pulsation of the pool fire.

The flow patterns of the entrainment flow fields are studied using Particle Imaging Velocimetry (PIV). A floor around a 7.1 cm pool fire changes the mean entrainment patterns as well as salient features of the instantaneous entrainment flow. When there is a floor around the pool fire, the entrainment flow starts far away from the flame and is very irregular, with occasional vortices in the flow. In the absence of a floor, there is a layer of air at very high convection speed enveloping the flame while the ambient is rather quiescent. The mean velocity vector plots shows that in the presence of a floor the

entrained air originates from far away region. Without a floor, the air entrained comes from underneath in a region very close to the pool fire.

The effect of burner size on the entrainment is shown by the fact that even without a floor, the entrainment flow field of a 30 cm toluene pool fire starts far away from pool fire. The instantaneous flow patterns are highly transient compared to those of 7.1 cm toluene pool fire. Around the flame bulge, the flow can even be outward or downward. The mean velocity vector plot shows that at $r = 27$ cm, the radial velocity components are comparable to vertical velocity components.

As expected from fundamental fluid mechanical considerations, the mean vorticity field estimated using the velocity data showed an irrotational flow field surrounding the fire with an intense generation of vorticity concentrated near the flame sheet. This intense vorticity region causes an inflow of ambient air near the outer edge of the fire in the continuous, intermittent and plume regions. The layer containing vorticity also causes an outflow of fuel and other material near the fire centerline into the flame sheet. The volumetric expansion caused by the combustion process counteracts the inward vorticity-induced motion. However, at larger radial locations, the flow induced by vorticity dominates the field.

Air entrainment rates are evaluated based on the mean velocity field, and the results are compared with data and a correlation in the literature. Only one correlation from the literature is selected for comparison because it utilizes nondimensional groups that can be derived from fundamental equations as shown in Appendix A. Different choices of entrainment boundaries lead to qualitative as well as quantitative differences in the air entrainment rates. The large scatter in the existing entrainment correlations can be attributed to the differences in explicit or implicit definitions of entrainment implied by the different measurement techniques. Fuel types have little effect on the dimensionless air entrainment rates normalized by the fire Froude number, mass stoichiometric ratio and fuel consumption rate. Without floor, the normalized air entrainment rates of 15 cm and 30 cm pool fires collapse to one line, which is about 20% lower than the normalized air

entrainment rate correlation for the 7.1 cm pool fires. A floor around the 7.1 cm pool fires lowers the normalized air entrainment rates by about 20%.

A kinematic model for the pool fire induced flow field was adapted from Baum and McCaffrey (1988). The flow field is decomposed into an irrotational flow and an incompressible flow. The source terms in the governing equations are estimated by analyzing the velocity and temperature distribution correlations for buoyant diffusion flames. The boundary conditions on the outer edge of the computational domain are approximated with asymptotic values. The governing differential equations are discretized by a control volume method and the resulting system of algebraic equations is solved by the Gauss-Seidel iteration method. A multigrid scheme is used to accelerate convergence of iteration. The validity of the numerical model is tested by comparing the results computed on domains of different sizes and using different grid spacings. Vorticity generated by the density gradient inside the flame plays a dominant role in determining the flow pattern. Heat release from combustion causes an approximately hemispherical expansion pattern in the presence of a floor. The sheet of maximum vorticity lies close to the flame sheet, and it not only entrains air from the surrounding, but also entrains material from the interior region.

There is qualitative agreement between the mean velocity measurements and the predictions of the entrainment flow fields of both pool fires with floor and without floor. When the measured visible flame shape is used, the overall agreement between the predictions and the measurements is improved.

Finally, the extreme sensitivity of the fire induced flow field to the boundary conditions, and the differences in definitions of entrainment surfaces in different engineering models suggest that numerical computations of the fire induced flow field are significantly better than empirical correlations.

6.2 Recommendations for Future Work

To improve the accuracy of the entrainment flow field prediction, the driving forces for the flow field, i.e., the volumetric heat release rate distribution and the vorticity distribution, need to be evaluated more accurately. This can be accomplished by either measuring the velocity distribution and the species distribution inside the fires or by developing a detailed numerical model, coupled with the entrainment flow field model, to simulate the fire directly and provide the heat release rate and vorticity distributions for the entrainment flow field model. Measurements of the heat release rate and the vorticity distribution are needed for the evaluation of such a model. Measurements of heat release rate and vorticity distributions in fires have always been challenging since instruments for measuring these quantities directly are not available. Particle Imaging Velocimetry (PIV) in surrogate gaseous fires with a pulsed laser for obtaining accurate estimates of vorticity is being considered. Estimates of local heat release rate may have to be based on the mean gas species concentration data obtained by sampling and gas chromatography.

LIST OF REFERENCES

LIST OF REFERENCES

- Adams, J.S., Williams, D.W., and Tregellas-Williams, J., 1973, "Air Velocity, Temperature, and Radiant-Heat Measurements Within and Around a Large Free-Burning Fire," *Fourteenth Symposium (International) on Combustion*, The Combustion Institute, Pittsburgh, pp. 1045.
- Adrian, R.J., 1978, "Estimation of LDA Signal Strength and Signal-to-Noise Ratio," *TSI Quarterly*, Vol. IV, pp. 3-8.
- Adrian, R.J., 1984, "Scattering particle characteristics and their effect on pulsed laser measurements of fluid flow: speckle velocity vs particle image velocimetry," *Applied Optics*, Vol. 23, No. 11, pp. 1690-1691.
- Adrian, R.J., and Yao, C.S., 1985, "Pulsed laser technique application to liquid and gaseous flows and the scattering power of seed materials," *Applied Optics*, Vol. 24, No. 1, pp. 44-52.
- Adrian, R.J., 1986, "Multi-point optical measurements of simultaneous vectors in unsteady flow -- a review," *Int. J. Heat & Fluid Flow*, Jan., pp. 127-145.
- Adrian, R.J., 1991, "Particle-imaging techniques for experimental fluid mechanics," *Annu. Rev. Fluid Mech.*, Vol. 23, pp. 261-304.
- Batchelor, G.K., 1967, *An Introduction to Fluid Dynamics*, Cambridge University Press, Cambridge, U.K.
- Baum, H.R., and McCaffrey, B.J., 1988, "Fire Induced Flow Field--Theory and Experiment," *Fire Safety Science - Proceedings of 2nd International Symposium*, Tokyo, Japan.
- Baum, H.R., Rehm, R.G., Barnett, P.D., and Corley, D.M., 1983, "Finite Difference Calculations of Buoyant Convection in an Enclosure, I, the Basic Algorithm," *SIAM Journal of Scientific and Statistical Computation*, Vol. 4, No. 1, March, , pp. 117-135.

- Beyler, C.L., 1983, Development and Burning of a Layer of Products of Incomplete combustion Generated by a Buoyant Diffusion flames, Ph.D. Thesis, Harvard University, Cambridge, Massachusetts.
- Cetegen, B.M., Zukoski, E.E., and Kubota, T., 1982, "Entrainment and Flame Geometry of Fire Plumes," NBS-GCR-82-402, National Bureau of Standards, Washington, D.C.
- Cetegen, B.M., Zukoski, E.E., and Kubota, T., 1984, "Entrainment in the Near and Far Field of Fire Plumes," *Combustion Science and Technology*, Vol. 39, pp. 305-311.
- Cetegen, B.M., and Ahmed, T., 1993, "Experiments on the periodic Instability of Buoyant Plumes and Pool Fires," *Combustion and Flame*, Vol. 93, pp. 157-184.
- Cox, G., and Chitty, R., 1980, "A Study of the Deterministic Properties of Unbounded Fire Plumes," *Combustion and Flame*, Vol. 39, pp. 191-209.
- Cox, G., and Chitty, R., 1985, "Some Source-Dependent Effects of Unbounded Fires," *Combustion and Flame*, Vol. 60, pp. 219-232.
- Currie, I.G., 1989, *Fundamental Mechanics of Fluids*, second ed., McGraw-Hill, Inc. New York.
- Delichatsios, M.A., and Orloff, L., 1984, "Entrainment Measurements in Turbulent Buoyant Jet Flames and Implications for Modeling," *Twentieth Symposium (International) on Combustion*, The Combustion Institute, Pittsburgh, pp. 367-375.
- Delichatsios, M.A., 1987, "Air Entrainment into Buoyant Jet Flames and Pool Fires," *Combustion and Flame*, Vol. 70, pp. 34-46.
- Faeth, G.M., 1984, ME598A Class notes - Laser Doppler Anemometry, Penn State University, University Park, PA.
- Gore, J.P., and Skinner, S.M., 1991, "Mixing Rules for State Relationships of Methane and Acetylene/air Diffusion Flames," *Combustion and Flame*, Vol. 87, pp. 357-364.
- Gore, J.P., 1993, ME 525 Combustion Classnotes, Purdue University, W. Lafayette, Indiana.
- Hamins, A., Yang, J.C., and Kashiwagi, T., 1992, "An experimental investigation of the pulsation frequency of flames," *Twenty-fourth Symposium (International) on Combustion*, The Combustion Institute, Pittsburgh, pp. 1695-1702.
- Hill, B.J., 1972, "Measurement of local entrainment rate in the initial region of axisymmetric turbulent air jets," *Journal of Fluid Mechanics*, Vol. 51, pp. 773-779.

Keane, R.D., and Adrian, R.J., 1990, "Optimization of particle image velocimeters. Part I: Double pulsed systems," *Meas. Sci. Technol.*, pp. 1202-1215.

Klassen, M., 1992, The Structure and Radiation of Liquid Pool Flames, Ph. D. Thesis, The University of Maryland, College Park, MD.

Koseki, H., and Yumoto, T., 1988, "Air Entrainment and Thermal Radiation from Heptane Pool Fires," *Fire Technology*, February, pp. 33-47.

Köylü, Ü.Ö., and Faeth, G.M., 1991, "Carbon Monoxide and Soot Emissions from Liquid-Fueled Buoyant Turbulent Diffusion Flames," *Combustion and Flame*, Vol. 87, pp. 61-76.

Kuo, K.K., 1986, Principles of Combustion, John Wiley & Sons, Inc., New York.

Liepmann, D., and Gharib, M., 1992, "The Role of Streamwise vorticity in the Near-field entrainment of round jets," *Journal of Fluid Mechanics*, Vol. 245, pp. 643-658.

Lourenco, L., and Krothapalli, A., 1995 "On the Accuracy of Velocity and Vorticity Measurements with PIV," *Experiments in Fluids*, Vol. 18, no. 6, pp. 421-438.

McCaffrey, B.J., 1979, "Purely Buoyant Diffusion Flames: Some Experimental Results," NBSIR 79-1910, U.S. National Bureau of Standards, Washington, D.C.

McCaffrey, B.J., and Cox, G., 1982, "Entrainment and Heat Flux of buoyant Diffusion Flames," NBSIR 82-2473, U.S. National Bureau of Standards, Washington, D.C.

McCaffrey, B.J., 1983, "Momentum Implications for Buoyant Diffusion Flames," *Combustion and Flame*, Vol. 52, pp. 149-167.

Megaridis, C.M., 1993, University of Illinois at Chicago, personal communication.

Moffat, R.J., 1982, "Contributions to the Theory of Single-Sample Uncertainty Analysis," *Journal of Fluids Engineering*, Vol. 104, pp. 250-260.

Morton, B.R., 1965, "Modeling Fire Plumes," *Tenth Symposium (International) on Combustion*, The Combustion Institute, pp. 973-982.

Nakakuki, A., 1994, "Heat Transfer in Small Scale Pool Fires," *Combustion and Flame*, Vol. 96, pp. 311-324.

Panton, R.L., 1984, Incompressible Flow, John Wiley & Sons, New York.

Ramadhyani, S., 1995, ME608 Numerical Methods in Heat, Mass and Momentum Transfer Classnotes. Purdue University, West Lafayette, Indiana.

Reuss, D.L., Adrian, R.J., Landreth, C.C., French, D.T., and Fansler, T.D., 1989, "Instantaneous Planar Measurements of Velocity and Large-Scale Vorticity and Strain Rate in an Engine Using Particle-Image-Velocimetry," *SAE Technical Paper Series*, 890616, SAE.

Ricou, F.P., and Spalding, D.B., 1961, "Measurements of entrainment by axisymmetrical turbulent jets," *Journal of Fluid Mechanics*, Vol. 11, pp. 21-32.

Schlichting, H., 1979, *Boundary Layer Theory*, McGraw-Hill Book Company, Inc., New York.

Sneddon, I.N., 1957, *Elements of Partial Differential Equations*, McGraw-Hill Book Company, Inc., New York.

Taylor, G.I., 1958, "Flow induced by jets," *Journal of the Aero/Space Sciences*, July, pp. 464-465.

Thomas, P.H., Baldwin, R., and Heselden, A.J., 1965, "Buoyant Diffusion Flames: Some Measurements of Air Entrainment, Heat Transfer, and Flame Merging," *Tenth Symposium (International) on Combustion*, The Combustion Institute, Pittsburgh, pp. 983-996.

Tomita, E., Hamanmoto, Y., Tsutsumi, H., and Yoshiyama, S., 1995, "Visualization of Transient Hydrogen Jet Flame and Ambient Air Entrainment Motion," *Eighth International Symposium on Transport Phenomena in Combustion*, 9A-5, San Francisco.

Toner, S.J., Zukoski, E.E., and Kubota, T., 1987, "Entrainment, Chemistry, and Structure of Fire Plumes," NBS-GCR-87-528, National Bureau of Standards, Washington, D.C.

TSI, 1992, *Seminar on Laser Doppler Velocimetry and Particle Image Velocimetry*, St. Paul, MN.

Walker, N.L., and Moss, J.B., 1984, "Laser Doppler Anemometry Measurement in and around a Turbulent Buoyant Flame," *Combustion Science and Technology*, Vol. 41, pp. 43-53.

Weckman, E.J., 1989, "Simplified Calculations of Total Flux and Entrainment Using Experimental Results from a Medium-Scale Pool Fire," *HTD-Vol.106, Heat Transfer Phenomena in Radiation, Combustion and Fires*, ASME, N.Y.

Weckman, E.J., and Sobiesiak, A., 1988, "The Oscillatory Behavior of Medium-Scale Pool Fires," *Twenty-Second Symposium (International) on Combustion*, The Combustion Institute, Pittsburgh, pp. 1299-1310.

Yumoto, T., and Koseki, H., 1982, "Gross Structure of Heptane Pool Fire: Some Experimental Results," *Fire Science and Technology*, Vol. 2, No. 2, pp. 91-97.

Zukoski, E.E., Kubota, T., and Cetegen, B.M., 1980, "Entrainment in Fire plumes," *Fire Safety Journal*, Vol. 3, pp. 107-115.

Zukoski, E.E., 1994, "Mass Flux in Fire Plumes," *Fire Safety Science - Proceedings of the fourth International Symposium*, pp. 137-147.

APPENDICES

Appendix A Dimensionless Numbers

The mass, momentum, and energy equations for a low Mach number, variable density flow with negligible viscous effects are (Baum and McCaffrey, 1988):

$$\frac{\partial \rho^*}{\partial t^*} + \nabla^* \cdot (\rho^* \bar{u}^*) = 0 \quad (\text{A.1})$$

$$\rho^* \frac{\partial \bar{u}^*}{\partial t^*} + \rho^* \bar{u}^* \cdot \nabla^* \bar{u}^* + \nabla^* \tilde{P}^* - (\rho^* - \rho_\infty^*) \bar{g}^* = 0 \quad (\text{A.2})$$

$$\rho^* C_p^* \frac{\partial T^*}{\partial t^*} + \rho^* C_p^* \bar{u}^* \cdot \nabla^* T^* - Q^* = 0 \quad (\text{A.3})$$

where asterisks represent dimensional variable and except for the asterisks the symbols have meaning identical to that given in the nomenclature. To nondimensionalize the equations, introduce the characteristic values for the dependent and independent variables and write the dimensional variables as:

$$\begin{aligned} \rho^* &= \rho_{ch} \rho \\ t^* &= t_{ch} t \\ \bar{u}^* &= \bar{u}_{ch} \bar{u} \\ \tilde{P}^* &= \tilde{P}_{ch} \tilde{P} \\ \rho_\infty^* &= \rho_{ch} \rho_\infty \\ \bar{g}^* &= g_{ch} \bar{g} \\ T^* &= T_{ch} T \\ C_p^* &= C_{pch} C_p \\ \nabla^* &= \frac{\nabla}{L_{ch}} \\ Q^* &= \frac{Q_0}{L_{ch}^3} Q \end{aligned} \quad (\text{A.4})$$

where subscript “ch” means characteristic parameter, and variables without asterisks are dimensionless. Substituting eq. (A.4) into eqs. (A.1-A.3) yields:

$$\frac{\partial \rho}{\partial t} + \frac{u_{ch} t_{ch}}{L_{ch}} \nabla \cdot (\rho \bar{u}) = 0 \quad (A.5)$$

$$\rho \frac{\partial \bar{u}}{\partial t} + \frac{u_{ch} t_{ch}}{L_{ch}} \rho \bar{u} \cdot \nabla \bar{u} + \frac{t_{ch}}{\rho_{ch} u_{ch}} \frac{P_{ch}}{L_{ch}} \nabla \tilde{P} - \frac{g_{ch} t_{ch}}{u_{ch}} (\rho - \rho_{\infty}) \bar{g} = 0 \quad (A.6)$$

$$\rho C_p \frac{\partial T}{\partial t} + \frac{u_{ch} t_{ch}}{L_{ch}} \rho C_p \bar{u} \cdot \nabla T - \frac{t_{ch}}{\rho_{\infty} C_{pch} T_{ch}} \frac{Q_0}{L_{ch}^3} Q = 0 \quad (A.7)$$

There are four nondimensional number groups:

$$\pi_1 = \frac{u_{ch} t_{ch}}{L_{ch}} \quad (A.8)$$

$$\pi_2 = \frac{t_{ch}}{\rho_{ch} u_{ch}} \frac{P_{ch}}{L_{ch}} = \frac{P_{ch}}{\rho_{ch} u_{ch}^2} \frac{u_{ch} t_{ch}}{L_{ch}} = \frac{P_{ch}}{\rho_{ch} u_{ch}^2} \pi_1 \quad (A.9)$$

$$\pi_3 = \frac{g_{ch} t_{ch}}{u_{ch}} = \frac{g_{ch} L_{ch}}{u_{ch}^2} \frac{u_{ch} t_{ch}}{L_{ch}} = \frac{g_{ch} L_{ch}}{u_{ch}^2} \pi_1 \quad (A.10)$$

$$\pi_4 = \frac{t_{ch}}{\rho_{\infty} C_{pch} T_{ch}} \frac{Q_0}{L_{ch}^3} = \frac{Q_0}{\rho_{\infty} C_{pch} T_{ch} u_{ch} L_{ch}^2} \frac{u_{ch} t_{ch}}{L_{ch}} = \frac{Q_0}{\rho_{\infty} C_{pch} T_{ch} u_{ch} L_{ch}^2} \pi_1 \quad (A.11)$$

If t_{ch} and P_{ch} are defined as:

$$t_{ch} = \frac{L_{ch}}{u_{ch}} \quad (A.12)$$

$$\text{and } P_{ch} = \rho_{ch} u_{ch}^2 \quad (A.13)$$

then π_1 and π_2 become unity and only two nondimensional groups are left:

$$\pi_3 = \frac{g_{ch} L_{ch}}{u_{ch}^2} \quad (A.14)$$

$$\pi_4 = \frac{Q_0}{\rho_{\infty} C_{pch} T_{ch} u_{ch} L_{ch}^2} \quad (A.15)$$

According to Delichatsios (1987), the buoyancy force per unit mass of hot gases at the flame temperature is:

$$g_{ch} = \frac{(T_f - T_\infty)(X_A - X_R)}{T_\infty} g \quad (A.15)$$

where T_f is flame temperature; T_∞ is the ambient temperature; X_A is combustion efficiency; X_R is radiative loss fraction; and g is the gravitational acceleration.

Delichatsios (1987) relates the nondimensional temperature rise in the flame to the heat of combustion as:

$$\frac{T_f - T_\infty}{T_\infty} \approx \frac{\Delta H_c}{C_p T_\infty (S + 1)} \quad (A.16)$$

where ΔH_c is the heat of combustion of the fuel, C_p is the specific heat at ambient temperature, and S is the mass based stoichiometric ratio.

Define:

$$L_{ch} = D$$

$$\rho_{ch} = \rho_\infty$$

$$C_{pch} = C_p$$

$$T_{ch} = T_f - T_\infty$$

$$u_{ch} = \sqrt{\frac{(T_f - T_\infty)(X_A - X_R)gD}{T_\infty}} \approx \sqrt{\frac{\Delta H_c(X_A - X_R)gD}{C_p T_\infty (S + 1)}} \quad (A.17)$$

Substituting eq. (A.17) into eq. (A.15) yields:

$$\pi_4 = \frac{Q_0}{\rho_\infty [\Delta H_c / (S + 1)] D^2 \sqrt{\{\Delta H_c / [(S + 1) C_p T_\infty]\} g D (X_A - X_R)}} \quad (A.18)$$

which is identical to the fire Froude number in Delichatsios (1987). Substituting eq. (A.15) and eq. (A.17) into eq. (A.14) leads to:

$$\pi_3 = T_\infty \frac{(T_f - T_\infty)(X_A - X_R)gD}{T_\infty [gD(T_f - T_\infty)(X_A - X_R)]} = 1 \quad (A.19)$$

Therefore, the fire Froude number is an appropriate parameter for correlating normalized entrainment with distance.

Appendix B Estimation of Combustion Efficiency

In the following, soot and carbon monoxide generation factors given by Köylü and Faeth (1991) for toluene combustion in air are used to evaluate the combustion efficiency of the present toluene fire.

The major conclusions of the study of Köylü and Faeth (1991) are that carbon monoxide and soot generation factors are uniform throughout the overfire region and that they are strongly correlated, with $\eta_{CO} = 0.34 \eta_s$. Generation factor η is defined as the mass of CO or soot generated per unit mass of fuel carbon burned. In the overfire region of toluene pool fire, the soot generation factor is reported in the aforesaid study to be about $\eta_s = 0.15$. Further assuming that all carbon atoms in the fuel burned are converted into only carbon monoxide, carbon dioxide, or soot, carbon dioxide generation factor can be obtained in the following manner.

$$\text{soot generation factor } \eta_s = 0.15 \text{ (kg/kg carbon in the fuel)} \quad (\text{B.1})$$

$$\text{CO generation factor } \eta_{CO} = 0.34\eta_s \quad (\text{B.2})$$

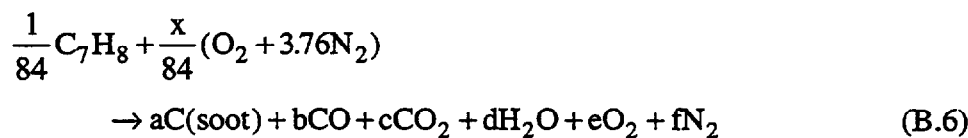
$$\text{CO}_2 \text{ generation factor } \eta_{CO_2} = (1 - \eta_s - \frac{12}{28}\eta_{CO})\frac{44}{12} \quad (\text{B.3})$$

Substituting eq. (B.1) for η_s in eqs. (B.2) and (B.3) yields

$$\eta_{CO} = 0.051 \quad (\text{B.4})$$

$$\eta_{CO_2} = 3.037 \quad (\text{B.5})$$

The formula for reaction based on 1 kg of carbon is



where x is the ratio of total air entrainment rate up to the upper interface to the fuel burning rate. The coefficients a , b , c , and d can be determined based on eqs (B.1), (B.2), and (B.3), independent of x :

$$\begin{aligned} a &= 0.0125 \\ b &= 0.0018 \\ c &= 0.0690 \\ d &= 0.0476 \end{aligned} \tag{B.7}$$

It is easy to show that

$$e = x/84 - 0.0967 \tag{B.8}$$

and

$$f = 0.0448 x \tag{B.9}$$

The combustion efficiency, X_A , required for the determination of the fire Froude number, is calculated based on the above analysis. According to Gore (1992), combustion efficiency is defined as the ratio of the enthalpy change in actual combustion to the enthalpy change in an ideal complete combustion process, when both the reactants and products are at standard state,

$$X_A = \frac{(\Delta H)_{\text{actual}}}{(\Delta H)_{\text{complete}}} \tag{B.10}$$

Since both the reactants and products are at standard state, the enthalpy change of the reaction is just the difference between the sum of the formation enthalpies of reactants and the sum of the formation enthalpies of products,

$$\Delta H = \sum v_p \Delta H_{f,p}^\circ - \sum v_r \Delta H_{f,r}^\circ \tag{B.11}$$

where ΔH_f° is the standard heats of formation of the species. As the heat of formation of elemental species is zero, the enthalpy change for one mole of toluene based on eq. (B.6) is:

$$(\Delta H)_{\text{actual}} = 84(b\Delta H_{f,\text{CO}}^\circ + c\Delta H_{f,\text{CO}_2}^\circ + d\Delta H_{f,\text{H}_2\text{O}}^\circ) - \Delta H_{f,\text{C}_7\text{H}_8}^\circ \tag{B.12}$$

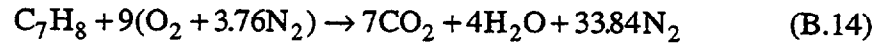
From Kuo (1986): $\Delta H_{f,\text{CO}}^\circ = -26.42$ kcal/mole, $\Delta H_{f,\text{CO}_2}^\circ = -94.054$ kcal/mole,

$\Delta H_{f,\text{H}_2\text{O}}^\circ = -68.32$ kcal/mole, and $\Delta H_{f,\text{C}_7\text{H}_8}^\circ = 11.95$ kcal/mole,

thus

$$(\Delta H)_{\text{actual}} = -834.2 \text{ kcal} \quad (\text{B.13})$$

The chemical formula for complete combustion of toluene is



and the enthalpy change is

$$(\Delta H)_{\text{complete}} = 7\Delta H_{\text{f},\text{CO}_2}^{\circ} + 4\Delta H_{\text{f},\text{H}_2\text{O}}^{\circ} - \Delta H_{\text{f},\text{C}_7\text{H}_8}^{\circ} = -943.6 \text{ kcal} \quad (\text{B.15})$$

which is actually the heating value for combustion of toluene. By eq. (B.10), the combustion efficiency

$$X_A = 88.4\% \quad (\text{B.16})$$

Appendix C Properties of LDV Probe and Measuring Volumes

The region within which the LDV measures the velocity normal to the fringe pattern is defined by the minimum of the probe volume defined by the sending optics responsible for forming the fringes and the view area and depth of field of the collection optics (Faeth, 1984). In the following, the dimensions of the probe volume are calculated first followed by the dimensions for the volume imaged by the collection optics. As seen at the end of this calculation, the present measuring volume is defined by the collection optics.

Dual-beam, single-channel LDV is the most widely used configuration among many variations of LDV systems. When the two parallel laser light beams are brought to a focus by a convex lens, they form an ellipsoidal region, usually called the probe volume, where the velocity of the flow is measured. The properties of this region which affect velocity measurement are determined by the wavelength of the laser light, the diameter of the laser beams, D_e , the distance between the beams, D , and the focusing length of the lens, f . One very important derived parameter is the beam angle κ . The two beams intersect each other at an angle of 2κ .

In the LDV measurement reported in this thesis,

$$D_e = 1.3 \text{ mm},$$

$$D = 50 \text{ mm},$$

$$f = 604 \text{ mm}, \text{ and}$$

$$\kappa = \tan^{-1}\left(\frac{D/2}{f}\right) = \tan^{-1}\left(\frac{50/2}{604}\right) = 2.37^\circ \text{ (TSI, 1992)}.$$

the wavelength of the laser light is $\lambda = 514.5 \text{ nm}$.

The most important property of the probe volume is the maximum number of fringes within the volume, which is in turn determined by the probe volume height D_p , and the fringe spacing d_f . The height of the probe volume (TSI, 1992):

$$D_p = \frac{4\lambda f}{\pi D_e \cos \kappa} = \frac{4 \times 514.5 \text{ nm} \times 604 \text{ mm}}{\pi \times 1.3 \text{ mm} \times \cos 2.37^\circ} = 0.3046 \text{ mm},$$

and the waist of probe volume

$$d_e = \frac{4\lambda f}{\pi D_e} = \frac{4 \times 514.5 \times 604}{\pi \times 1.3} = 0.3044 \text{ mm},$$

which is almost the same as the probe height.

The fringe spacing

$$d_f = \frac{\lambda}{2 \sin \kappa} = \frac{514.5 \text{ nm}}{2 \times \sin 2.37^\circ} = 6.22 \mu\text{m}.$$

Thus the number of fringes in the probe volume

$$N_f = \frac{D_p}{d_f} = \frac{0.30 \text{ mm}}{6.22 \mu\text{m}} = 48.$$

The length of the probe volume is

$$L_p = \frac{4\lambda f}{\pi D_e \sin \kappa} = \frac{4 \times 514.5 \text{ nm} \times 604 \text{ mm}}{\pi \times 1.3 \text{ mm} \times \sin 2.37^\circ} = 7.4 \text{ mm}.$$

The measuring volume, where light scattered by particles passing through the fringe pattern is collected by the detector, is the overlap region between probe volume and the region observed by the detector. It is not necessarily identical to the probe volume because of the limitation imposed by the relationship between the sending optics and the receiving optics.

The properties of the detector system are associated with the focal length and the aperture of the collecting lens, f_c and D_c , the focal length of the detector lens, f_d , and the aperture of the detector, d_d (Faeth, 1984). In the present measurement, $f_c = 604 \text{ mm}$, $D_c = 50 \text{ mm}$, $f_d = 100 \text{ mm}$, and $d_d = 0.2 \text{ mm}$. The F-number of the collecting lens is $F_c = f_c / D_c = 604 / 50 = 12.08$. The diameter of the region observed by the photodetector is the projection of the aperture diameter in the focal plane of the collecting lens.

$$d_{ma} = d_a \frac{f_c}{f_a} = 0.2\text{mm} \times \frac{604\text{mm}}{200\text{mm}} = 0.604\text{mm}$$

The length of this region is defined by the depth of field of the collecting optics, which is proportional to the square of F_c .

$$l_{ma} = 8F_c^2\lambda = 8 \times 12.08^2 \times 514.5\text{nm} = 0.601\text{mm}$$

The actual measuring region is the overlap between the probe volume and the region observed by the receiving optics., the length of the measuring region is $\min[l_{ma}, L_p]$, and the height of the region is $\min[d_{ma}, d_p]$. With the LDV system used in this study they are l_{ma} , 0.601 mm and d_p , 0.30 mm, respectively. The spatial resolution of the LDV system is the largest dimension of the measuring volume. In the present system, it is the length of the region observed by the receiving optics, 0.601 mm. Since the mean flow field induced by the pool fire is assumed to be axisymmetric, it is expected that the variation of mean velocity over this length in a direction normal to a plane passing through the pool axis should be small, and no efforts are made to increase the spatial resolution of the system. Various methods can be used to increase the spatial resolution. The most commonly used ones are increasing the spacing between the two laser beams, a sending lens with shorter focal length, a receiving lens with shorter focal length, or off-axis alignment.

Appendix D Uncertainty Analysis of LDV Measurement

The experimental data is without value in the absence of uncertainty analysis of the measurement method. How truthful the signal can represent the actual velocity of the particle is discussed here.

There are two kinds of measurement errors common to most counter-type LDV systems: fringe bias and velocity gradient bias (Faeth, 1984). Fringe bias happens when for some reason such as too small a magnitude of the velocity component in the measuring direction a particle crossing fringes cannot send out signals, or is too small to be recorded. The effects of fringe bias can be virtually eliminated by use of frequency shifting.

Velocity gradient bias occurs if there is a gradient in the mean within the measuring region. The bias caused by velocity gradient in the direction perpendicular to both the sending optics axis and measuring volume height can be approximately evaluated by the following formula (Faeth, 1984):

$$\Delta U = \frac{d_e^2}{6} \left(\frac{d^2 U}{dx^2} \right)$$

With the maximum second derivative of velocity with respect to distance approximately $10 \text{ 1/s} \cdot \text{cm}$ and d_e equaling 0.3 mm ,

$$\Delta U = 0.0015 \text{ cm/s}$$

Thus, LDV has sufficient accuracy for the present purposes.

Velocity gradient bias also affects rms of velocity measurements. The change of rms due to velocity bias can be estimated as (Faeth, 1984):

$$\Delta \bar{U}' = \left[\frac{d_e^2}{3} \left(\frac{dU}{dx} \right)^2 \right]^{1/2}$$

In the present study, $\Delta \bar{U}'$ is about 0.5 cm/s .

Appendix E Some Parameters of PIV Measurement

E.1 Spatial Resolution

In analyzing double-exposure images to obtain information about velocity, the value of displacement between pairing particle images is an average over the interrogation box. The interrogation box corresponds to the volume of a rectangular prism within the flow field illuminated by the pulsed light sheet. The rectangular volume is determined by the light thickness ΔZ , and the interrogation box height dY and width dX divided by magnification ratio M . Usually dX equals dY , and they are designated by dI .

In order to capture the small-scale spatial structure of the flow field, the spatial resolution should be as high as possible, i.e., the interrogation spot should be as small as possible. However, the size of the interrogation box is limited by two parameters: the seeding density and the maximum displacement between pairing images of the identical particle, ΔX_{\max} . Keane and Adrian (1990) showed that the number of particle images in the interrogation box, N_I , should be larger than 15 in order to ensure acceptable validation rate of the velocity measurements, and that the interrogation box length, dI , should be at least 4 times ΔX_{\max} .

There are several ways to increase spatial resolution, such as increasing the magnification ratio, using smaller seeding particles and using higher resolution recording medium.

E.2 Seeding Density

Expressions for the source density N_s and image density are given in several papers (Adrian, 1984; Adrian and Yao, 1985; Adrian, 1986; Adrian, 1991) as:

$$d_e = (M^2 d_p^2 + d_s^2)^{1/2}$$

$$d_s = 2.44(M+1)f$$

$$N_I = C\Delta Z \frac{\pi d_I^2}{4M^2}$$

where C : number density of seeding particles in flow;

ΔZ : light sheet thickness;

d_e : image diameter;

d_I : Interrogation box dimension;

M : Magnification ratio.

N_s represents the number of particles corresponding to one particles image. If $N_s \gg 1$, the seeding density is so high that the recording device cannot distinguish between the individual particles, and the mode of velocity measurement changes to Laser Speckle Velocimetry (LSV). Only when N_s is less than 1, the PIV mode is preserved. However, C should be large enough to ensure that N_I is larger than 15 to ensure good data validation rate.

E.3 Particle Size

In order to include an adequate number of particle images when the images are large, the interrogation box dimension has to be increased, and this results in lower spatial resolution. Besides, Adrian and coworkers (1985) showed that the uncertainty of PIV measurement is proportional to the image size. Larger particles will decrease the accuracy of the velocity measurement because uncertainty of locating the centers of images is proportional to the image size. Hence, smaller particles should be used. A necessary condition on seeding particles is that they follow the fluid flow faithfully. This requirement also leads to the need for smaller seeding particles. However, the particles

should be large enough to scatter sufficient light for forming images on the recording medium.

Due to diffraction of the lens, the image diameter is not linearly proportional to particle size. According to Adrian and Yao (1985):

$$d_e = (M^2 d_p^2 + d_s^2)^{1/2}$$

$$d_s = 2.44(M+1)f\#\lambda$$

where d_e : image diameter;

M : magnification ratio;

d_p : seeding particle diameter;

d_s : image caused by diffraction;

$f\#$: f number of the camera;

λ : wavelength of the light.

With the PIV system used in this study. $M=0.1428$, $d_p=0.5\ \mu\text{m}$, $f\#=2.8$, $\lambda=514.5\ \text{nm}$,

$$d_s = 2.44 \times 1.1428 \times 2.8 \times 0.5145 = 4\ (\mu\text{m}),$$

$$Md_p = 0.1428 \times 0.5 = 0.0714\ (\mu\text{m}),$$

$$d_e \approx 4\ \mu\text{m}.$$

However, in real measurement, it is observed that the particle image actually occupies several pixels. The calculated value is smaller for two possible reasons: 1) the coefficient is larger than 2.44 with the present PIV system; 2) Blooming effect: when one pixel is saturated, the charge leaks to neighboring pixels.

E.4 Pulse Timing

The pulse interval should be chosen depending upon the maximum velocity and the expected spatial resolution. Keane and Adrian (1990) suggested that the displacement of particle images should be less than 25% of the interrogation box:

$$Mu_{\max}\Delta t \leq \frac{d_I}{4},$$

thus,

$$\Delta t \leq \frac{d_I}{4Mu_{\max}}$$

The pulse duration is fixed for a pulse laser. When a CW laser is used, the pulse duration should be short enough to ensure that the image streak is no more than one diameter according to Adrian (1986).

E.5 Laser Sheet Thickness

The laser sheet thickness is one dimension of the spatial resolution. The main criterion in choosing this parameter is that the out-of-plane movement of the particle should be less than a quarter of the light sheet thickness during the pulse interval:

$$w\Delta t \leq \frac{\Delta Z}{4}$$

where w : Velocity component normal to the light sheet plane;

Δt : the interval between laser light pulses;

ΔZ : light sheet thickness.

E.6 Velocity Bias

In order to eliminate the ambiguity in the direction of the pairing particle images, velocity bias is introduced using a rotating mirror synchronized to the chopper through a digital delay. Since velocity bias increases the in-plane displacement between pairing particle images, it usually decreases SNR. Hence, velocity bias should be preferably small, yet large enough to offset the maximum reverse flow velocity to ensure the correct order of the pairing particle images.

E.7 Dynamic Range

The dynamic range is the ratio between maximum measurable velocity and the minimum measurable velocity. It is affected by the magnification ratio, the velocity bias, the chosen spatial resolution, the size of the seeding particles, and the time interval between two light pulses.

With the configuration of the PIV system used in this study and the chose interrogation resolution box (40 pixel \times 40 pixel = 2 mm \times 2 mm), velocity up to 40 cm/s can be measured. With the velocity bias, the theoretical minimum measurable velocity is zero. However, it is limited by the accuracy of the equipment in practice.

The uncertainty analyses of PIV in Adrian (1986) shows that

$$\frac{\sigma_u}{u_{\max}} = \frac{\sigma_{\Delta x}}{\Delta X_{\max}} + \frac{u \sigma_{\Delta t}}{\Delta X_{\max}}$$

Assuming that the uncertainty associated with pulse interval is negligible, the expression can be reduced to:

$$\frac{\sigma_u}{u_{\max}} \approx \frac{\sigma_{\Delta x}}{\Delta X_{\max}} = \frac{C d_{\tau}}{\Delta X_{\max}}$$

where C: uncertainty coefficient associated with locating the center of the image;

$\sigma_{\Delta x}$: standard deviation in determining the distance between pairing images;

d_{τ} : image diameter;

ΔX_{\max} : maximum particle displacement;

u_{\max} : maximum velocity.

In the PIV system used in this study, assuming $C = 0.1$ (because locating the center of the image can be accurate to subpixel level), the measurement uncertainty is

$$\sigma_u = \frac{0.1 \times 6.8}{0.7} = 1(\text{mm/s}), \text{ and } \frac{\sigma_u}{u_{\max}} = \frac{1}{400} = 0.25\%$$

Neglecting magnification ratio results in underestimate of the measurement uncertainty.

Appendix F LDV Measurement Data

Table F.1 Data of the mean velocity around the 7.1 cm toluene pool fire with a floor.

Height (cm)	Radius (cm)	U_R (cm/s)	U_Z (cm/s)	RMS of U_R (cm/s)	RMS of U_Z (cm/s)
1.0	13.5	8.36	0.20	4.45	5.22
1.0	11.5	8.69	1.20	4.73	5.66
1.0	9.5	9.42	1.55	3.15	5.43
1.0	7.5	9.78	2.46	3.73	5.85
1.0	5.5	9.71	2.46	4.44	5.70
1.0	4.5	8.54	3.23	4.48	5.40
1.0	3.5	12.2	6.44	5.52	9.37
2.0	13.5	7.84	0.90	4.32	5.67
2.0	11.5	8.94	2.28	4.65	6.46
2.0	9.5	8.85	1.80	4.05	6.23
2.0	7.5	9.87	3.49	3.35	6.43
2.0	5.5	9.29	4.17	4.09	6.56
2.0	4.5	8.46	4.50	4.47	6.27
2.0	3.5	9.60	5.01	4.51	7.14
3.0	13.5	8.41	0.94	4.23	5.86
3.0	11.5	8.81	0.60	4.60	6.99
3.0	9.5	8.93	2.99	3.88	7.19
3.0	7.5	8.84	3.84	3.97	7.02
3.0	5.5	8.82	6.18	4.32	7.00
3.0	4.5	7.39	6.31	5.04	6.77
3.0	3.5	7.74	9.42	5.10	10.60
4.0	13.5	8.28	1.99	4.46	5.92
4.0	11.5	7.83	3.81	4.79	6.70
4.0	9.5	7.24	3.08	4.38	6.63
4.0	7.5	8.27	4.80	3.81	6.97
4.0	5.5	8.85	6.94	4.29	7.63
4.0	4.5	6.38	8.76	4.89	7.19
4.0	3.5	6.35	10.98	5.42	9.75
5.0	13.5	7.89	2.18	4.87	5.98

Table F.1 (continue)

5.0	11.5	7.42	5.57	4.56	6.69
5.0	9.5	6.82	4.60	4.71	7.06
5.0	7.5	7.64	5.99	4.12	7.14
5.0	5.5	8.23	8.38	4.28	11.39
5.0	4.5	5.68	9.35	4.85	9.35
5.0	3.5	6.28	22.71	5.64	28.18
6.0	13.5	8.05	2.58	4.34	5.67
6.0	11.5	6.59	5.66	4.91	6.70
6.0	9.5	6.99	4.61	4.53	6.22
6.0	7.5	6.98	6.81	4.36	7.00
6.0	5.5	6.78	12.44	4.74	11.18
6.0	4.5	4.18	11.29	5.69	7.62
6.0	3.5	5.91	25.45	5.51	29.71
7.0	13.5	7.97	2.53	4.28	5.15
7.0	11.5	6.35	6.65	4.91	6.74
7.0	9.5	6.62	4.96	4.50	6.91
7.0	7.5	6.49	7.69	4.66	6.82
7.0	5.5	6.52	11.10	4.94	7.71
7.0	4.5	3.98	12.63	5.80	7.98
7.0	3.5	5.61	32.93	6.19	33.64
8.0	13.5	6.73	3.82	4.54	5.40
8.0	11.5	6.69	8.48	4.73	6.41
8.0	9.5	6.66	7.14	4.58	7.25
8.0	7.5	6.40	8.27	4.44	6.90
8.0	5.5	5.86	10.0	4.84	8.23
8.0	4.5	3.83	15.26	6.26	9.58
8.0	3.5	5.3	35.0	7.01	37.4
9.0	13.5	6.95	4.94	3.99	5.29
9.0	11.5	5.86	7.46	4.82	6.95
9.0	9.5	5.59	8.97	4.85	7.29
9.0	7.5	6.31	10.81	4.62	6.88
9.0	5.5	6.26	16.65	4.96	9.63
9.0	4.5	3.33	15.7	7.00	11.20
9.0	3.5	5.00	42.72	7.89	42.04
10.0	13.5	6.68	6.21	4.05	5.61
10.0	11.5	6.53	9.34	4.65	6.16
10.0	9.5	5.81	10.59	4.33	6.33
10.0	7.5	4.99	11.24	4.87	6.84
10.0	5.5	4.97	18.0	5.57	12.3

Table F.1 (continue)

10.0	4.5	4.0	20.0	6.45	15.7
10.0	3.5	4.7	45.0	8.62	41.1
12.0	13.5	5.74	5.14	4.17	4.96
12.0	11.5	6.15	11.31	4.34	6.14
12.0	9.5	5.40	11.43	4.27	6.95
12.0	7.5	5.05	13.69	4.88	7.54
12.0	5.5	5.38	21.44	6.00	14.60
12.0	4.5	4.8	30.84	7.56	25.35
12.0	3.5	4.30	53.01	10.1	43.36
14.0	13.5	5.20	6.21	4.07	5.20
14.0	11.5	5.53	12.59	4.46	6.01
14.0	9.5	4.90	12.08	4.29	7.49
14.0	7.5	5.13	16.84	4.72	9.50
18.0	13.5	3.59	9.53	3.42	5.90
18.0	11.5	4.62	12.59	4.48	6.49
18.0	9.5	3.69	15.90	5.06	8.80
18.0	7.5	4.30	20.15	6.17	10.69
22.0	13.5	2.44	8.82	3.27	5.56
22.0	11.5	4.19	14.63	4.18	6.88
22.0	9.5	3.05	16.51	5.73	10.18
26.0	13.5	1.71	8.48	3.52	5.75
26.0	11.5	3.49	14.56	4.28	8.53
26.0	9.5	3.12	18.16	5.94	11.66
30.0	13.5	1.98	8.99	2.84	7.06
30.0	11.5	3.12	11.95	6.12	10.35

NIST-114
(REV. 11-94)
ADMAN 4.09

U.S. DEPARTMENT OF COMMERCE
NATIONAL INSTITUTE OF STANDARDS AND TECHNOLOGY

(ERB USE ONLY)

ERB CONTROL NUMBER	DIVISION
PUBLICATION REPORT NUMBER	CATEGORY CODE
PUBLICATION DATE	NUMBER PRINTED PAGES

MANUSCRIPT REVIEW AND APPROVAL

INSTRUCTIONS: ATTACH ORIGINAL OF THIS FORM TO ONE (1) COPY OF MANUSCRIPT AND SEND TO THE SECRETARY, APPROPRIATE EDITORIAL REVIEW BOARD.

TITLE AND SUBTITLE (CITE IN FULL)

A Study of Entrainment and Flow Patterns in Pool Fires Using Particle Imaging Velocimetry

CONTRACT OR GRANT NUMBER

60NANB2D1291

TYPE OF REPORT AND/OR PERIOD COVERED

Final Report March 1996

AUTHOR(S) (LAST NAME, FIRST INITIAL, SECOND INITIAL)

Zhou, X.C., Gore, J.P.

PERFORMING ORGANIZATION (CHECK (X) ONE BLOCK)

- ☐ NIST/GAITHERSBURG
☐ NIST/BOULDER
☐ JILA/BOULDER

LABORATORY AND DIVISION NAMES (FIRST NIST AUTHOR ONLY)

SPONSORING ORGANIZATION NAME AND COMPLETE ADDRESS (STREET, CITY, STATE, ZIP)

U.S. Department of Commerce
National Institute of Standards and Technology, Gaithersburg, MD 20899

PROPOSED FOR NIST PUBLICATION

- | | | |
|---|--|--|
| <input type="checkbox"/> JOURNAL OF RESEARCH (NIST JRES) | <input type="checkbox"/> MONOGRAPH (NIST MN) | <input type="checkbox"/> LETTER CIRCULAR |
| <input type="checkbox"/> J. PHYS. & CHEM. REF. DATA (JPCRD) | <input type="checkbox"/> NATL. STD. REF. DATA SERIES (NIST NSRDS) | <input type="checkbox"/> BUILDING SCIENCE SERIES |
| <input type="checkbox"/> HANDBOOK (NIST HB) | <input type="checkbox"/> FEDERAL INF. PROCESS. STDS. (NIST FIPS) | <input type="checkbox"/> PRODUCT STANDARDS |
| <input type="checkbox"/> SPECIAL PUBLICATION (NIST SP) | <input type="checkbox"/> LIST OF PUBLICATIONS (NIST LP) | <input checked="" type="checkbox"/> OTHER NIST-GCR |
| <input type="checkbox"/> TECHNICAL NOTE (NIST TN) | <input type="checkbox"/> NIST INTERAGENCY/INTERNAL REPORT (NISTIR) | |

PROPOSED FOR NON-NIST PUBLICATION (CITE FULLY)

☐ U.S.

☐ FOREIGN

PUBLISHING MEDIUM

- ☐ PAPER ☐ CD-ROM
☐ DISKETTE (SPECIFY) _____
☐ OTHER (SPECIFY) _____

SUPPLEMENTARY NOTES

ABSTRACT (A 2000-CHARACTER OR LESS FACTUAL SUMMARY OF MOST SIGNIFICANT INFORMATION. IF DOCUMENT INCLUDES A SIGNIFICANT BIBLIOGRAPHY OR LITERATURE SURVEY, CITE IT HERE. SPELL OUT ACRONYMS ON FIRST REFERENCE.) (CONTINUE ON SEPARATE PAGE, IF NECESSARY.)

An experimental and theoretical study of the flow fields induced by pool fires was completed. Pool burners of three diameters, namely 7.1 cm, 15 cm and 30 cm, were used. For the two smaller pool burners, the effects of a 51 cm sheet metal floor around the pool at the surface were also studied. Three fuel, methanol, toluene and heptane were burned as representatives of alcohols, paraffins and aromatics. The velocity field induced by the 7.1 cm toluene pool fire with the metal floor was mapped with a Laser Doppler Velocimetry (LDV) system. The transient characteristics of the velocities were studied by analyzing their discrete Probability Density Functions (PDFs) and their Power Spectral Densities (PSDs). The instantaneous fire induced flow fields around all the pool fires were studied using Particle Imaging Velocimetry (PIV). The PIV data for the 7.1 cm toluene pool fire were confirmed using the LDV data. Following a favorable comparison, PIV, which is a faster technique, was used for the remaining fires. Air entrainment rates were calculated based on the mean velocity fields and normalized using the fire Froude number, which was shown to be the appropriate nondimensional number using the governing equations for the buoyant diffusion flames. A theoretical model was utilized to predict the entrainment flow field with the volumetric heat release rate distribution and vorticity distribution assumed to be known a priori.

KEY WORDS (MAXIMUM OF 9; 28 CHARACTERS AND SPACES EACH; SEPARATE WITH SEMICOLONS; ALPHABETIC ORDER; CAPITALIZE ONLY PROPER NAMES)

entrainment; flow measurement; pool fires; velocity distribution.

AVAILABILITY

- ☐ UNLIMITED ☐ FOR OFFICIAL DISTRIBUTION - DO NOT RELEASE TO NTIS
☐ ORDER FROM SUPERINTENDENT OF DOCUMENTS, U.S. GPO, WASHINGTON, DC 20402
☒ ORDER FROM NTIS, SPRINGFIELD, VA 22161

NOTE TO AUTHOR(S): IF YOU DO NOT WISH THIS MANUSCRIPT ANNOUNCED BEFORE PUBLICATION, PLEASE CHECK HERE.

☐

ELECTRONIC INFORMS